Spring 1-1-2011

Development of Frequency Comb Velocity-Modulation Spectroscopy, Spectroscopy of HfF+ and the JILA eEDM Experiment

Laura Cathleen Sinclair
University of Colorado at Boulder, sinclail@jilau1.colorado.edu

Development of Frequency Comb Velocity-Modulation Spectroscopy, Spectroscopy of HfF^+ and the JILA eEDM Experiment

by

Laura C. Sinclair

B.S. California Institute of Technology, 2004

A thesis submitted to the

Faculty of the Graduate School of the

University of Colorado in partial fulfillment

of the requirements for the degree of

Doctor of Philosophy

Department of Physics

2011

This thesis entitled:
Development of Frequency Comb Velocity-Modulation Spectroscopy, Spectroscopy of HfF^+
and the JILA eEDM Experiment
written by Laura C. Sinclair
has been approved for the Department of Physics

Eric A. Cornell

Prof. Jun Ye

Date

The final copy of this thesis has been examined by the signatories, and we find that both the content and the form meet acceptable presentation standards of scholarly work in the above mentioned discipline.

Sinclair, Laura C. (Ph.D. Physics)

Development of Frequency Comb Velocity-Modulation Spectroscopy, Spectroscopy of HfF^+ and the JILA eEDM Experiment

Thesis directed by Prof. Eric A. Cornell

Broad bandwidth, precision spectroscopy of the molecular ions of interest to the JILA electron electric dipole moment experiment, HfF^+ and ThF^+, is necessary due to the limited amount of spectroscopic information available and the large theoretical uncertainties in the energy level structure (thousands of wavenumbers). This thesis covers the development of a novel spectroscopic technique, frequency comb velocity-modulation spectroscopy, that provides high resolution, broad spectral bandwidth, ion discrimination and high sensitivity simultaneously. Frequency comb velocity-modulation spectroscopy as well as single-frequency velocity-modulation spectroscopy have been used to identify five rotational bands of HfF^+. This work discusses the first spectroscopic information for HfF^+ which came from our measurement of the $^1\Pi_1 - ^1\Sigma^+$ (0,0) band recorded with single-frequency velocity-modulation spectroscopy with a sensitivity of $3\text{x}10^{-7}$ $\text{Hz}^{-1/2}$. The development of frequency comb velocity-modulation spectroscopy allowed us to cover a thousand wavenumbers of spectral bandwidth and to identify an additional four HfF^+ bands. The achieved sensitivity for frequency-comb velocity-modulation spectroscopy was $4\text{x}10^{-8}$ $\text{Hz}^{-1/2}$ $(\text{spectral element})^{-1/2}$ with 1500 simultaneous detection channels spanning 150 cm^{-1} of bandwidth. For a 30 minute acquisition time using 30 interleaved images to densely sample the whole spectrum, this corresponded to a $3\text{x}10^{-7}$ single-pass fractional absorption sensitivity for each of the 45,000 measurement channels. The spectroscopic information from all five HfF^+ rotational bands is presented and molecular constants for the $^1\Sigma^+$, $^3\Pi_1$, and $^1\Pi_1$ states were extracted.

To Dr. Jack Blumenthal, mentor and softball coach

and to my siblings, Betsy and Andy, for reminding me to "keep calm and carry on"

Acknowledgements

I would like to thank my advisor, Eric Cornell, for sharing his joy of science, for his advice and ability to refocus our efforts when needed, and for his patience and kindness when things really didn't work. I would also like to thank Jun Ye for co-advising all of the frequency comb work. To have Jun step in with his expertise in frequency combs was critical to our success. Working with Jun and Eric was a fantastic experience although at times a terrifying experience due to the brain power in the room, and I'm very grateful for it.

I would like to thank experimental JILA eEDM-ers, past and present, Tyler Coffey, Kevin Cossel, Matt Grau, Dan Gresh, Aaron Leanhardt, Huanqian Loh, Patrick Maletinsky, Russ Stutz and Tyler Yahn. Special thanks go to Russ and Aaron for the early days in B238 and to Kevin for the late nights making frequency comb velocity-modulation spectroscopy work. John Bohn and his student, Ed Meyer, provided theoretical guidance from the early days onward and many corny physics jokes.

Without the larger JILA scientific community, this work would not have been possible. I'm grateful to Carl Wieman for stepping in as our advisor for those bad weeks of 2004. Florian Adler and Mike Thorpe provided a great deal of help in the initial design of frequency comb velocity-modulation spectroscopy for which I am grateful. Without the expertise of the JILA machine and electronic shops this work would have been much more challenging. Thank you, Todd Ascinar, for saving us multiple times with speedy repairs of our glass work and, Dave Alchenberger, for re-polishing our ti:sapph crystal. The guidance of Debbie Jin in the Cornell-Jin meetings as well as discussions with the members of the Jin, Cornell

and Wieman groups were very helpful. Likewise, the cold molecule meetings with the Ye molecule folks and the Lewandowski group provided many fruitful discussions.

Finally, thanks are due to my parents, siblings, siblings-in-law, and husband for their unwavering support.

Contents

Chapter

Tables

Table

Figures

Figure

Chapter 1

Introduction

"At first sight, the search for an edm in a molecule would seem unprofitable." – Sandars, 1967 [5]

1.1 Electron EDM as a probe of physics beyond the Standard Model

The existence of an electron electric dipole moment breaks both time invariance and parity invariance, as shown in Figure 1.1. The size of the electron EDM predicted by the Standard Model is tiny, while various extensions to the Standard Model predict values that are more than 10 orders of magnitude larger [1]. (See Table 1.1 for a list of predicted values.) Because of this, electron EDM measurements do not have a Standard Model background that needs to be accounted for. This is in contrast to experiments such as the parity non-conservation measurements using cesium, where there is a non-zero Standard Model component [6]. The zero background nature of the electron EDM in the Standard Model combined with the current predictions for the extensions to the Standard Model mean that a reduction in the current limit ($1.05\text{x}10^{-27}$ [9]) by an order of magnitude or two would put serious constraints on those models.

Most electron EDM experiments using atoms and molecules are conducted in the same way. (A summary of the state of electron EDM experiments is given in R. Stutz's thesis [7].) An electron spin resonance experiment to determine the spin-flip frequency is performed between two spin states with an electric and usually a magnetic field present. The sign of

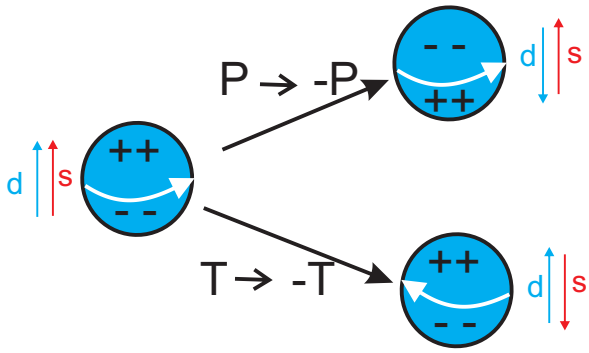

Figure 1.1: An Electron EDM violates both time and parity invariance. The dipole moment of the electron must lie either parallel or anti-parallel to the electron's spin. Here the electron EDM is represented by the blue arrow labeled d and also graphically by the charge separation on the sphere. The electron's spin is represented by the red arrow labeled s and graphically by the white arrow representing a ring of current. Under a reversal of time, the sign of the spin is reversed while the sign of the electron's dipole moment stays the same. Under a reversal of parity, the sign of the dipole moment is flipped while the spin stays the same. The amount of CP-violation and thus T-violation given CPT invariance required to give a non-negligible electron EDM cannot be accounted for with the Standard Model.

Model	$d_{electron}$ [e-cm]
Standard Model	$< 10^{-40}$
Canonical CP Violation	10^{-26}
Left-Right Symmetric	$10^{-26} - 10^{-28}$
Higgs dynamics	$> 10^{-27}$
Supersymmetry	$< 10^{-27}$

Table 1.1: Summary of predictions of electron EDM values for various extensions to the Standard Model. [1]

the magnetic field or electric field is then flipped and the splitting between the two spin states is measured again; if there is a permanent electron EDM, the spin-flip frequency is different for the magnetic and electric fields configured as parallel versus antiparallel [8]. In this type of experiment the sensitivity figure-of-merit is $E_{eff}\tau\sqrt{N}$, where E_{eff} is the electric field the electron experiences, τ is the spin resonance coherence time, and N is the number of spin-flips that can be measured in a reasonable amount of time. Recent results from the Hind's group with YbF have lowered the current limit to 1.05x10^{-27} e-cm [9] from the limit of 1.6x10^{-27} e-cm on the electron EDM that was set by the Cummins group in 2002 using a Tl beam [10].

1.2 The Advantage of Molecular Ions and the JILA eEDM experiment

To improve upon the current limit, the figure-of-merit $E_{eff}\tau\sqrt{N}$ must be increased. In 1967, Sandars first proposed using molecules for EDM measurements due to the very large effective electric fields that could be achieved [5]. While molecules offer the prospect of greatly increased effective electric fields, the additional complexity of their rich structure also poses additional experimental challenges. A number of experiments are currently underway using neutral polar diatomic molecules [9, 11, 12, 13, 14], and very recently, the Hinds group set a new limit on the electron EDM using YbF [9]. A table of recently completed and ongoing eEDM experiments, Table 1.2, demonstrates different approaches to improving the

Table 1.2: Comparison of recent and ongoing eEDM experiments (ongoing experiment values often represent order of magnitude estimates). The figure-of-merit for evaluating the sensitivity of an eEDM experiment is $E_{eff}\tau\sqrt{N}$, where E_{eff} is the effective electric field on the unpaired electron, τ is the coherence time, and N is the number of measurements that can be counted in some reasonable experimental integration time.

location	ref	species	E_{lab} [V/cm]	E_{eff} [V/cm]	τ [s]	N [1/s]	eEDM limit [e-cm]
Berkeley	[10]	Tl	$1.23\text{x}10^5$	$7\text{x}10^7$	$2\text{x}10^{-3}$	10^9	$1.6\text{x}10^{-27}$
Amherst	[15]	Cs	$4\text{x}10^3$	$4.6\text{x}10^5$	$1.5\text{x}10^{-2}$	-	$5.5\text{x}10^{-26}$
LBNL	[16]	Cs	10^5	10^7	1	10^9	$1.9\text{x}10^{-22}$
Texas		Cs	10^5	10^7	1	-	-
Penn State	[17]	Cs	10^5	10^7	1	-	-
Yale	[11, 18, 19, 20, 21]	PbO	10	$2.5\text{x}10^{10}$	$8\text{x}10^{-5}$	-	-
Imperial	[8, 9]	YbF	$7\text{x}10^4$	$2.9\text{x}10^{10}$	10^{-3}	-	$10.5\text{x}10^{-28}$
Oklahoma	[12, 22, 23]	PbF	$7\text{x}10^4$	$2.9\text{x}10^{10}$	-	-	-
ACME	[13, 24]	ThO	10^2	10^{11}	$2 \text{ x } 10^{-3}$	10^5	-
Michigan	[14]	WC	-	$5.4\text{x}10^{10}$	10^{-3}	-	-
JILA	[25]	HfF^+-ThF^+	5	$3\text{-}9\text{x}10^{10}$	0.2-1	$\sim$10	-

figure-of-merit for experiments using both atomic and molecular systems.

To achieve large, i.e. GV/cm, effective internal electric fields, the molecule must be polarized. For some molecules, such as YbF, rotational states of opposite parity must be mixed to fully polarize the molecule, leading to a requirement of kV/cm lab electric fields [8]. The lab electric field needs to fully polarize a molecule does not necessarily need to be that large. Molecules with an electronic state containing closely spaced levels of opposite parity due to the coupling of the electronic angular momentum to the rotation of the molecule, Ω-doubling, can be fully polarized in fields as small as a few volts per cm [26].

The presence of Ω-doubling offers another key advantage over atomic systems – an internal chop. First realized by DeMille in their use of the $^3\Sigma^+$ state of PbO [11], the upper and lower manifold of the Ω-doublet have an identical Zeeman splitting as long as the g-factors are not significantly impacted by mixing with different higher lying states. However, the splitting due to the electron's electric dipole moment interacting with the effective electric field is equal in magnitude for both the upper and lower manifolds, but opposite in sign.

Molecular ions offer the additional promise of long coherence times since they are

easier to trap than neutral molecules. As long as the molecule has the desired ground state or long-lived metastable state, a given molecule can be interrogated for longer than in a beam experiment, although at the cost of a reduction in number of spin-flips measured simultaneously (N). (See Table 1.2.) For molecular ions, a state which is polarizable with only a few volts per cm is necessary due to the additional challenges of working in a trap with rotating fields that limit the electric fields that can be applied. Meyer et al. took the constraints of working with molecular ions into account and proposed using molecular ions with $^3\Delta_1$ ground states or low-lying metastable states, specifically HfH^+, HfF^+ and PtH^+ [26]. Further consideration of $^3\Delta$ state molecules has also led to the proposal to use ThF^+ [24]. Since HfF^+ and ThF^+ have been successfully created and trapped, the JILA eEDM experiment has chosen to work with these two species [25, 7]. Many additional technological challenges that come with doing precision measurements using molecules inside an ion trap are discussed in Leanhardt et al. [25] as well as Stutz [7].

1.3 The Trouble with Molecular Ions: The Need for Spectroscopic Information

One of the challenges in using molecular ions for precision measurement is a lack of available spectroscopic data. For the eEDM experiment, multiple states will be needed for state preparation and spin readout. Figure 1.2 shows a schematic of some of the energy levels of interest for HfF^+. Knowledge of the exact energies of these states will guide design choices for other aspects of the eEDM experiment. For example, if the $^3\Phi_2$ of HfF^+ state is too low in energy, the quantum efficiencies of photomultiplier tubes (PMTs) will make using laser-induced fluorescence impractical.

When this work was begun, no experimental data existed for either HfF^+ or ThF^+. Recent work using pulsed-field-ionization zero-kinetic-energy measurements (PFI-ZEKE) from the Heaven group has provided information about the lowest lying states of HfF^+ [3] and ThF^+. Theoretical calculations exist for the states of HfF^+, but due to the challenges of

including so many electrons in the calculations, the uncertainties are thousands of wavenumbers [2, 27]. We chose to focus on HfF^+ first rather than ThF^+ due to the fact that the states of ThF^+ are even less certain.

The large theoretical uncertainties in the energy levels of HfF^+ and ThF^+ coupled with the need for information about multiple electronic states necessitates a method of spectroscopy that covers a broad spectral bandwidth. The requirement for sufficient signal strength to cover a wide spectral range in a reasonable amount of time puts a lower limit on the number of ions needed. As a result, spectroscopy of HfF^+ or ThF^+ needs to occur in an apparatus other than the experimental apparatus for the electron EDM measurement as the latter was designed for precise control of a small population of ions [25, 7]. Furthermore, many methods of producing molecular ions also produce their neutral counterparts often in high concentrations. Spectroscopic tools that discriminate between ionic and neutral species reduce crowding of the spectrum and prevent strong neutral transitions from overwhelming weak ionic signals. With molecular transitions, the ability to resolve individual rotational lines is key to state identification, and thus high resolution is needed.

1.4 Overview of Thesis

Chapter Two briefly covers our unsuccessful attempt to perform low-resolution spectroscopy without any ion-discrimination using a hollow cathode lamp of HfF+. Chapter Three discusses velocity modulation spectroscopy and our first measurements of electronic transitions in HfF^+. Chapter Four details our development of a novel spectroscopic technique that provides high-resolution, broad spectral-bandwidth, ion-discrimination and high sensitivity. Chapter Five summarizes our current knowledge about the structure of HfF^+ and its implications for the JILA eEDM experiment. Chapter Six concludes the thesis.

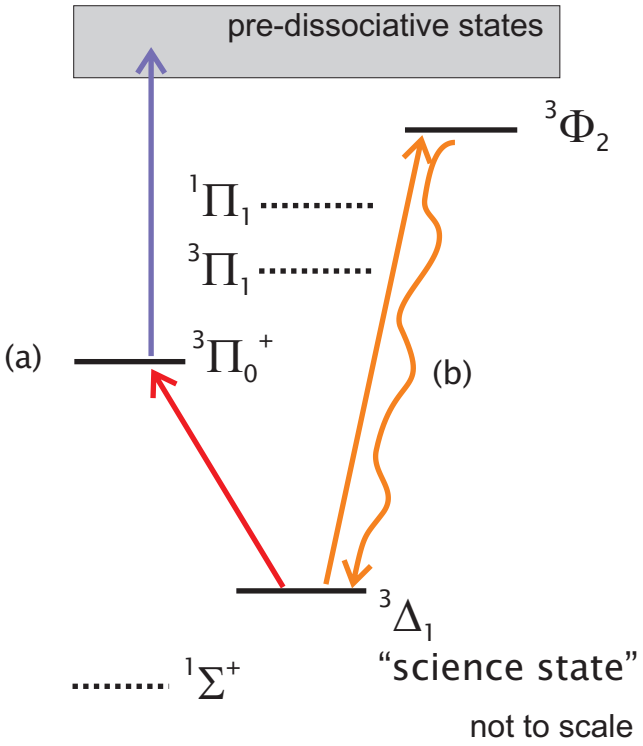

Figure 1.2: Energy levels of HfF^+ relevant to the eEDM experiment. Two different schemes for spin readout, state selective photodissociation (a) and laser induced fluorescence (LIF) (b), are shown. States shown as dashed lines including the $^1\Sigma^+$ ground state may be utilized for state preparation. The exact energies of these states will help to determine the best method for spin readout.

Chapter 2

Spectroscopy with a Hollow Cathode Lamp

Hollow cathode lamp (HCL) spectroscopy provides very broad spectral bandwidth with a minimal amount of technological investment. After the need for a method of ion spectroscopy outside of the electron EDM measurement apparatus was realized, these properties made HCL spectroscopy an appealing choice. An initial attempt at spectroscopy of HfF^+ was therefore conducted by resolving the emission from the hollow cathode lamp with a grating monochromator. Four thousand wavenumbers around 14,500 cm^{-1} were scanned with a resolution of $\sim$ 0.6 cm^{-1} (0.04 nm) to search for transitions arising from HfF^+. Although transitions were seen that corresponded to locations of Hf and possibly HfF transitions, the remaining unassigned features proved too complicated to extract the locations of transitions of HfF^+. A restrospective comparison of the data with a now known HfF^+ transition illustrates this difficulty. (See Figure 2.3 and associated discussion.)

A schematic of the system is shown in Figure 2.1. A hollow copper cathode was placed in a glass tube with a stainless steel anode on either side. In order to minimize contamination of the spectra with copper lines and to avoid damage to the copper cathode, a hafnium sleeve was press fit inside the copper cathode and then a small amount of HfF_4 powder was added. The discharge heats the HfF_4, creating a sufficient vapor pressure, which is then ripped apart to form HfF, HfF^+, as well as Hf and Hf^+. (With the hafnium sleeve absent, atomic copper and atomic copper ion transitions were both observed in the emission spectra.) Argon was continually flowed through the discharge cell with a pressure of approximately 750 mtorr.

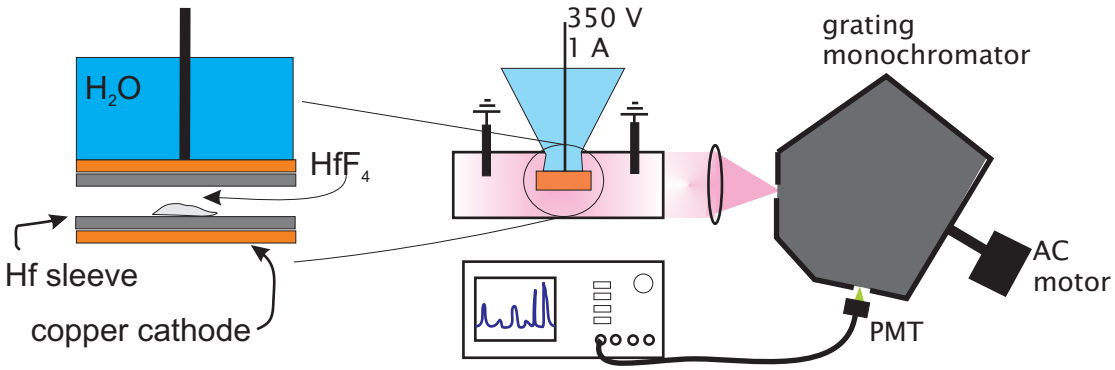

Figure 2.1: Qualitative sketch of the hollow cathode lamp apparatus. The glow from the discharge at the center of the hollow cathode (orange square) is imaged into the grating monochromator. As the AC motor scans the grating, the light at different wavelengths is imaged onto the photomultiplier tube and recorded by the oscilloscope. The cross-section of the cathode on the left shows the Hf sleeve press fit inside the copper cathode with the HfF_4 powder placed inside.

Four 100 ohm ballast resistors each capable of handling 50 W were used to provide a total ballast resistance of 100 ohms with the capacity to handle 200 W in order for the discharge to run stably at 350 V with 1 A of current. The large amount of power dissipated required water cooling of the copper cathode.

The fluorescence that passed through the exit slit of the monochromator was collected with a photomultiplier tube (Hamamatsu R3896). The slits on the monochromator were closed as far as possible to achieve the highest possible wavelength resolution, 0.04 nm. An external motor was connected to the handle of the monochromator to scan it in a controlled fashion and the PMT output was recorded with an oscilloscope. The NIST table of strong atomic lines for argon, helium, and copper were used to calibrate the monochromator leading to a frequency accuracy of $\sim$1.5 cm^{-1} (0.1 nm).

The complete frequency range scanned over is shown in Figure 2.2. In the spectral region covered, numerous transitions from argon, singly charged argon, fluorine, hafnium, and zirconium (the most significant contaminant in the hafnium sleeve) listed in the NIST strong lines tables are present, yet they account for only a fraction of the total features observed. One of the challenges of doing spectroscopy this way is that there is no way to discriminate between the signal from neutral molecules and atoms, such as HfF or Hf, and ionic molecules and atoms, such as HfF^+ or Hf^+. Furthermore, the low resolution, 0.04 nm, prevents resolution of individual rotational transitions for a given molecular electronic transition and makes discrimination between atomic lines and molecular bandheads difficult.

Figure 2.3 shows two separate regions of the recorded spectra that illustrate some of the challenges in assignment of the measured lines. In Figure 2.3 (b), the locations of the band origins of two HfF bands (solid cyan line), obtained using laser induced fluorescence of a beam of HfF at a later date, allow for the tentative identification of the peaks immediately to the blue as the R-branch band head of those transitions (dashed cyan line). The high rotational temperatures expected in the discharge suggest that most prominent feature will be due to the band head, in this case of the R-branch to the blue (dashed cyan line), and not

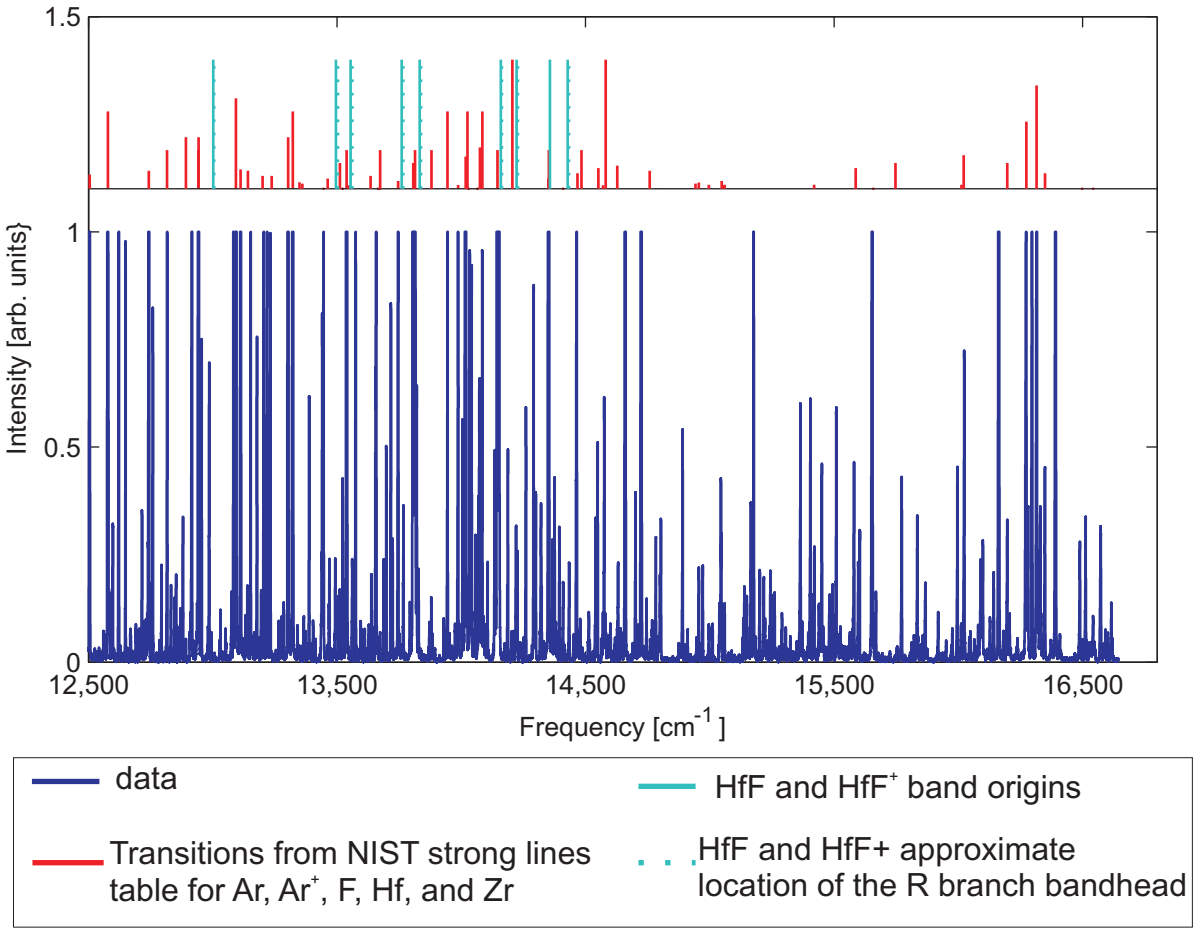

Figure 2.2: Fluorescence from the hollow cathode lamp versus frequency. Locations of strong lines from the most likely atomic sources of fluorescence in this frequency range as well as several HfF bands and one HfF^+ band at 13,000 cm^{-1} are also shown and are offset for clarity. The position of both the band origin and the R-branch band head are indicated for the HfF and HfF^+ bands found using other spectroscopic techniques. Note that a majority of the features shown are not accounted for by the atomic lines published in the NIST strong lines tables.

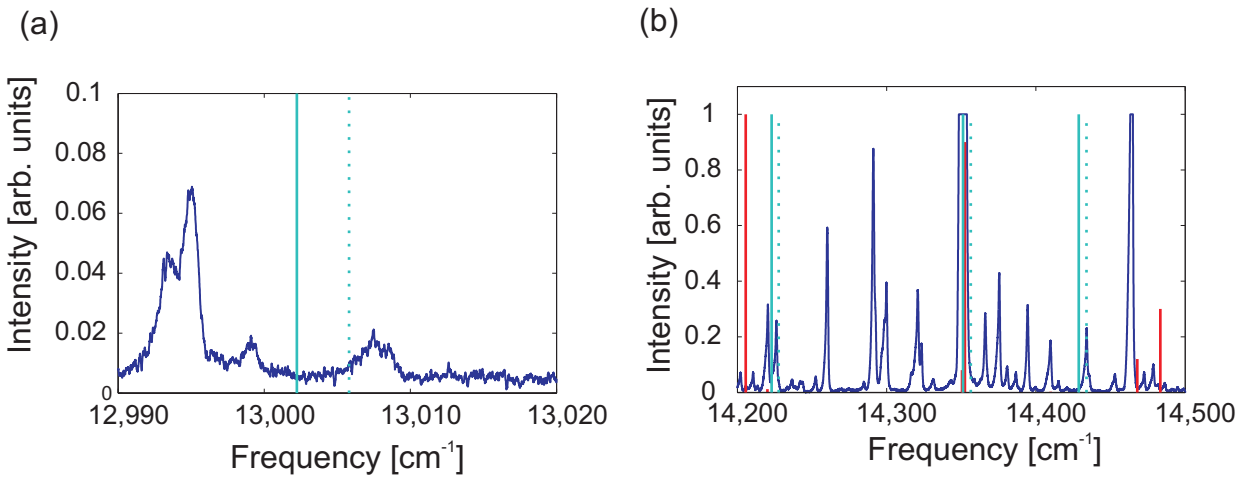

Figure 2.3: Regions of hollow cathode lamp spectra that contain known HfF^+ (a) or HfF (b) bands. Panel (a) shows data from hollow cathode lamp containing HfF_4 in the region of the $^1\Pi_1 - ^1\Sigma^+$ (0,0) band of HfF^+, which has a band origin of $\sim$ 13002.3 cm^{-1} (cyan line) and an R-branch band head at $\sim$ 13005 cm^{-1} (dashed cyan line), as well as other unidentified bands. The feature at $\sim$ 13,008 cm^{-1} is too blue to be the bandhead and lacks a sharp edge on the blue side. Panel (b) shows a region containing three HfF bands identified using laser-induced fluorescence in a supersonic beam (cyan lines) as well as a strong argon line (red line) and many unidentified features. The dashed cyan lines indicate the approximate location of the R-branch band heads for the HfF bands, which show reasonable agreement with the data.

the Q-branch around the band origin (solid cyan line). Despite the identification of these features, in the 300 cm^{-1} spanned by the plot in Figure 2.3, there are still approximately nineteen features unassigned.

Looking backwards from our velocity-modulation experiments (See Chapter 3), in Figure 2.3 (a), we can also examine the frequency range of the data for the $^1\Pi_1 - ^1\Sigma^+$ (0,0) band. Although multiple features are present around 13,000 cm^{-1}, there is not a band present that corresponds to the HfF^+ band whose band origin is indicated by the solid cyan line and whose R-branch band head is indicated by the dashed cyan line. The lack of a bandhead near the HfF^+ bandhead in the HCL data suggests that the sensitivity in these scans was too low to measure electronic transitions of HfF^+, especially since the $^1\Pi_1 - ^1\Sigma^+$ (0,0) transition is one of the strongest [2]. The gain and integration time per point were chosen such that the many unassigned features did not saturate the PMT and thus could have been increased. Increasing the sensitivity would not have reduced the forest of unassigned features and so only small windows of the spectral region covered would yield additional information.

Although the hollow cathode lamp provided broad spectral coverage quickly with some evidence for HfF production, the low resolution and lack of ion-specificity made this a poor spectroscopic tool for identifying electronic transitions of HfF^+. These measurements highlighted the need for ion-specific, high resolution, and high sensitivity measurements across a broad spectral range. Chapters three and four discuss our attempts to answer this need.

Chapter 3

Velocity-Modulation Spectroscopy with a Diode Laser

One of the great challenges of spectroscopy of ionic molecules is the presence of abundant neutral species. The development of velocity-modulation spectroscopy (VMS) in Richard Saykally's group [28] overcame this problem by providing ion-specific spectroscopy as well as high sensitivity. Over the past thirty years, this technique has been used and refined by many groups to achieve high sensitivity for the study of a wide range of molecular ions in the visible and infrared [29].

To achieve high sensitivity and ion specificity, velocity-modulation spectroscopy relies on the modulation of the ions' drift velocity in an alternating current discharge. The modulation of the drift velocity of the ions relative to a laser passing through the sample of ions results in a modulated Doppler shift and thus in a modulated absorption. After lock-in detection at the discharge frequency, the absorption signal has a dispersive-looking lineshape with the zero-crossing at the transition frequency. The characteristic lineshape of velocity modulation spectroscopy can be seen in Figure 3.6 (b).

The ionic and neutral species are both produced at twice the discharge frequency by the creation of the discharge every half cycle. Asymmetries in the discharge configuration can result in a non-negligible absorption signal from neutral molecular and atomic transitions at the discharge frequency. Counter-propagating beams can be used to remove this common-mode absorption signal as well as other common-mode technical noise as the sign of the demodulated ion absorption signal depends on the instantaneous velocity of the ions relative

to the direction of propagation of the laser.

3.1 Experiment Design

Velocity-modulation requires the detection of absorption in a laser that passes through the sample of ions modulated by an alternating-current discharge. Figure 3.1 shows the optical layout of our system to achieve this. A SDL diode laser tunable from 769 - 792 nm is split with a polarizing beam cube such that it passes through the discharge in both directions with the beams crossing in the center of the discharge. Each beam is then focused onto a balanced photodetector (ThorLabs PDB130A). Polarization optics are used to balance the power of the beams to approximately one part in a thousand. The difference signal between the two beams is demodulated at the discharge frequency (10 kHz) with a SRS lock-in detector and the analog output is recorded by the computer. The wavelength for each point was recorded by a wavemeter that was occasionally calibrated against the rubidium D_2 line at $\sim$780 nm.

To further reduce the noise caused by background drifts and electrical and optical pick-up from the discharge, we implemented a double demodulation scheme following Lan, Tholl, and Farley [30]. A chopper wheel running at 10 Hz was added to the optical path. The difference signal was then first demodulated on one lock-in at the discharge frequency (10 kHz) with a short enough time constant (1 ms) to be insensitive to the chopper wheel. That demodulated signal was then fed to a second lock-in detector and demodulated at the chopper frequency of 10 Hz with the time constant set to reach the desired sensitivity (0.3 - 10 s).

A key component of a velocity-modulation spectroscopy scheme is the discharge as it both produces the sample of interest and provides the modulation of the ions' drift velocity. The discharge apparatus consists of a center tube made of either alumina or quartz to withstand the oven temperature and of two endcaps each housing an electrode. (See Figure 3.2.) The center tube is housed within an oven for the production of a sufficient vapor pressure

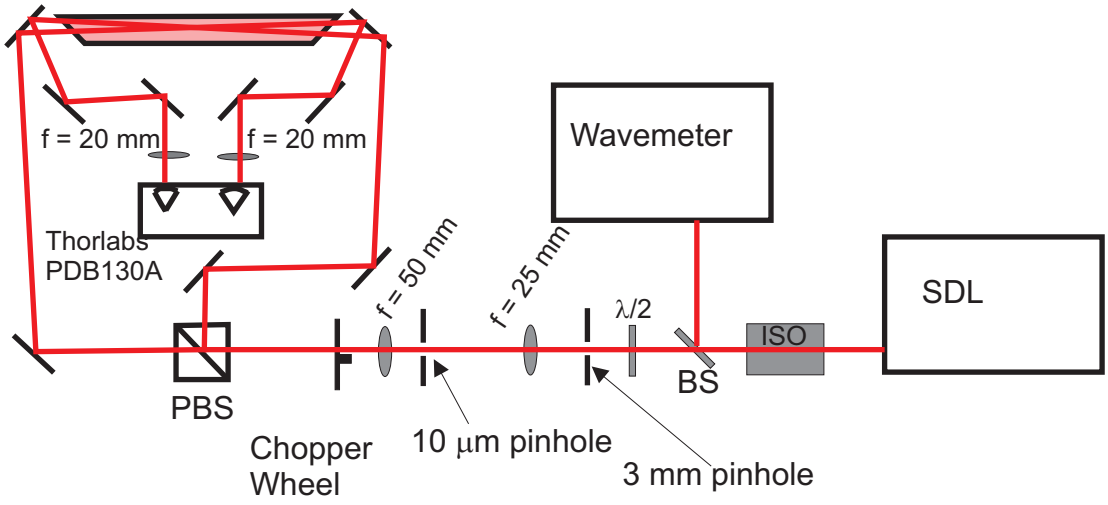

Figure 3.1: Optical layout for velocity-modulation spectroscopy. The light from the diode laser is spatially filtered, is split and balanced by polarization optics, and passes through the discharge in both directions before being focused onto the balanced photodetector.

of HfF_4. Several generations of endcap and electrode designs were tested before the final configuration was settled upon. The discharge assembly needed removable endcaps so that the HfF_4 could be place inside the central tube. (The initial oven could only accommodate a straight tube.) Concerns about needing to clean or replace the windows on the endcaps also motivated a design in which the endcaps were easy to remove. Based on previous design attempts, we knew the electrode surface needed to be far enough from the glass of the endcap to prevent melting of the glass from localized heating due to the discharge. Water cooling of the electrode was also needed to prevent excessive heating of the glass-to-metal seal and to prevent sputtering of the stainless steel. The endcaps also needed connections for the helium buffer gas that needed to be continuously flowed through the system.

To meet these requirements, a hollow stainless steel electrode with a wire spot-welded to the inside was connected via a glass-to-metal seal to a glass flange (Figure 3.2 (a).) The glass portion of the electrode can then be clamped to the endcap to achieve a seal that holds vacuum. The stainless electrode is one inch in diameter and the BK7 glass tube of the endcap that surrounds it is 2 inches in diameter to provide a sufficient distance between electrode and glass. The two inch diameter BK7 tube was then fused onto a two inch diameter tube in a tee configuration; the matching diameter was chosen to ensure the robustness of the endcap. The two inch diameter tee is then tapered down to a half inch outer diameter tube on either end so that it can be attached to the central discharge tube and to reduce the probability of the window getting coated. At the window end of the endcap, a $\frac{3}{8}$" thick piece of BK7 is attached with a high temperature wax (Crystalbond). On each endcap there are also two threaded connectors for the gas flow. On both endcaps, gas flows in on the connector closest to the window to help keep it clean. On one endcap, the second gas connection serves as the main inlet and on the other, it serves as the outlet. (See Figure 3.2 (b).)

A schematic of the discharge electronics is shown in Figure 3.3. A function generator drives two 2 kW commercial audio amplifiers at $\sim$10 kHz. Two homebuilt step-up transformers with a turn ratio of 25:1 provide the impedance matching to drive the $\sim 2k\Omega$ discharge

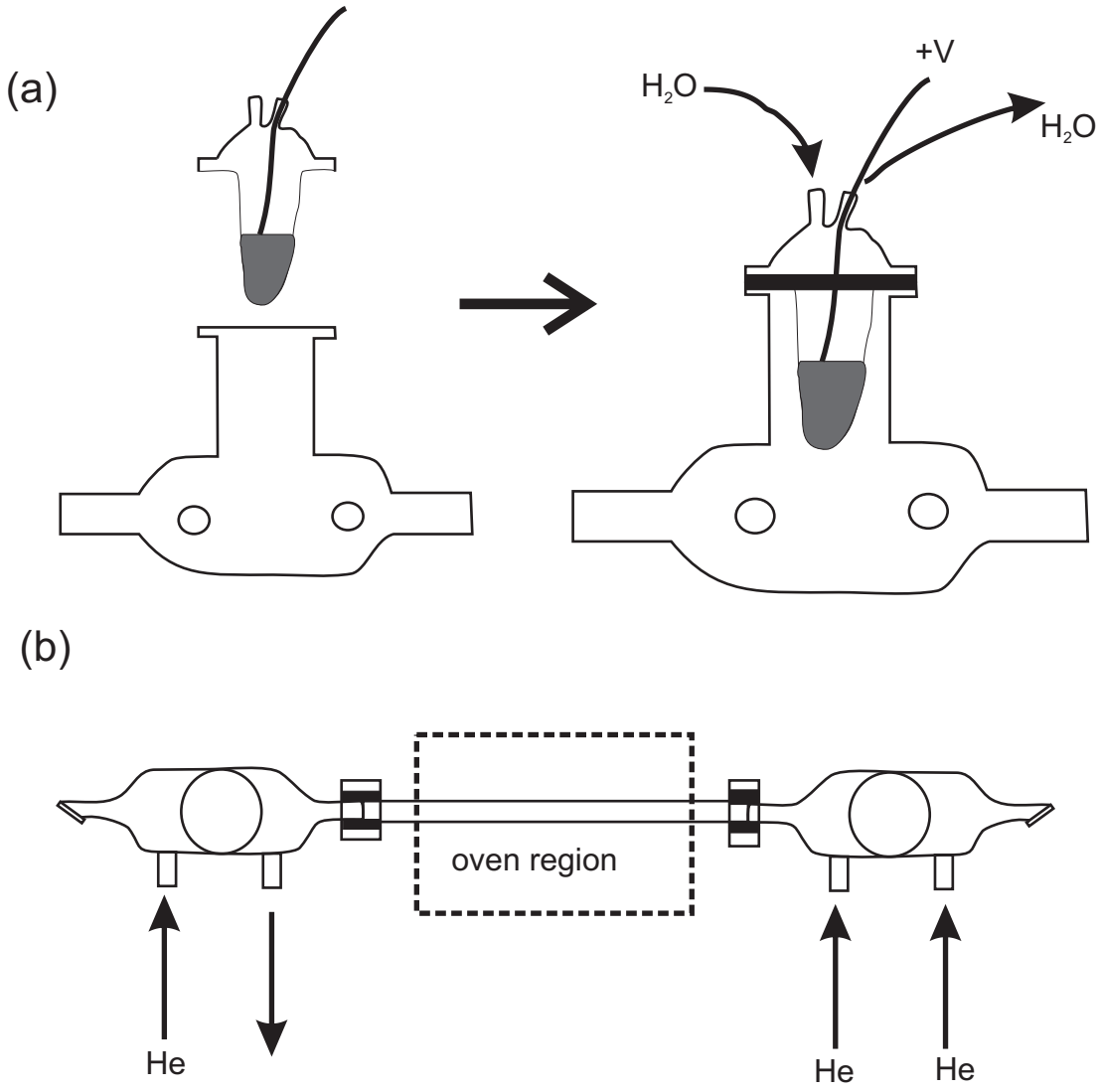

Figure 3.2: Schematic of discharge electrode and endcap. (a) Side view of endcap with water cooled electrode. The hollow stainless steel electrode is connected via a glass-to-metal seal to the rest of the endcap with a wire spot welded into the inside to provide the electrical connection. (b) Top view of endcaps showing the Brewster angle windows and ultratorr connections to the central quartz or alumina tube.

given the 8 Ω output impedance of the audio amplifiers. (The impedance matching is imperfect due to changes in the discharge impedance from the initial design.) The transformers on the secondary side are wired such that the voltage drop from each electrode to ground is one-half the voltage drop across the discharge. 100 Ω ballast resistors are used on the discharge side as well as two sense resistors of 1 Ω that are used to monitor the discharge current. A low value of 100 mA_{pk-pk} was chosen due to a concern that higher currents would result in the HfF^+ molecules being ripped into their atomic constituents. (Later measurements discussed in Chapter 4 used much higher currents ranging from 250 to 500 mA_{pk-pk}.) For these measurements the voltage across the primary side of the transformers was $\sim$ 22 V_{rms} leading to a voltage drop of $\sim$1.1 kV across the discharge.

3.2 Characterizing the System

Since no electronic transitions of HfF^+ had been measured at the time of the design of the velocity-modulation system, a previously studied N_2^+ band as well as a neutral hafnium transition were used for testing. Production of N_2^+ ions allowed for determination of the discharge settings and for the phase of the lock-in detection. Multiple lines from the (7,4) $A^2\Pi_u - X^2\Sigma_g^+$ band previously recorded by Collet et al [4] and Liu et al [31] were measured as a first test of the system. The N_2^+ lines enabled us to test everything except for the production of HfF_4 vapor and thus HfF^+ with the oven.

In order to characterize the oven performance, we used a transition in neutral hafnium at 784.8 nm. In order to be able to see a neutral transition, we rely on concentration-modulation instead of the velocity-modulation of the ions. Since the discharge is responsible for producing the HfF, HfF^+, Hf and Hf^+ from the HfF_4 vapor, the abundance of these species and thus the absorption from them is modulated at twice the discharge frequency (2x10 kHz). Asymmetries in the discharge may even produce a concentration-modulation signal at the discharge frequency, which is suppressed by using counter-propagating beams as the concentration-modulation is common mode between the two beams. To deliberately

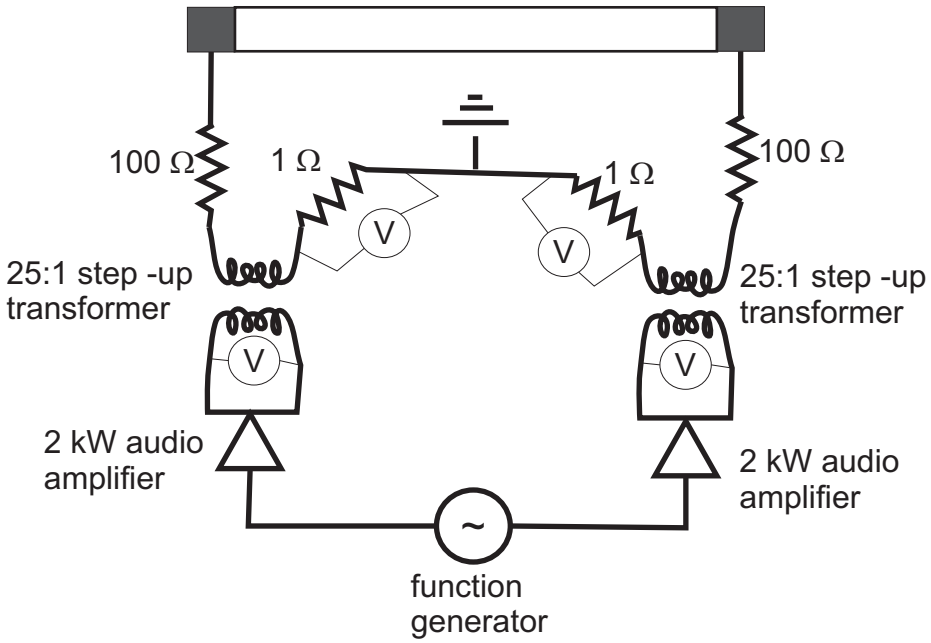

Figure 3.3: Schematic of discharge electronics. A function generator drives two 2 kW audio amplifiers at ∼10 kHz. Two homebuilt step-up transformers provide the impedance matching for the discharge. For the diode laser VMS measurements typical values were a discharge current of ∼100 mA_{pk-pk} and ∼22 V_{rms} across the primary side of the transformer.

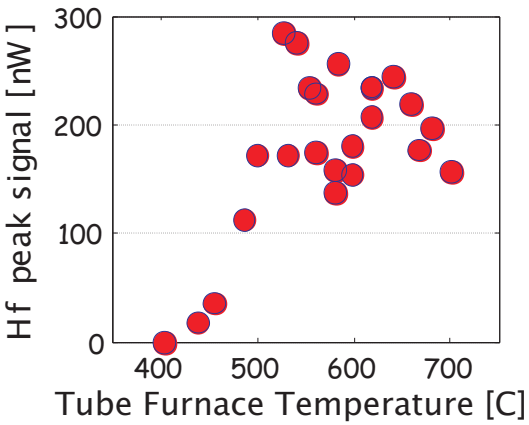

Figure 3.4: Strength of hafnium line versus temperature. The 550 °C temperature necessary to produce a reasonable vapor pressure of HfF_4 is much lower than initially expected.

measure the absorption from the concentration-modulation of hafnium at twice the discharge frequency, we therefore must detect only one of the beams rather than the difference of the counterpropagating beams. The strength of the hafnium line was then measured as a function of oven temperature to determine the appropriate operating temperature of 550 °C as shown in Figure 3.4. As one source quoted a sublimation temperature of HfF_4 of 968 °C [32] and we could not obtain a vapor curve, we purchased an oven capable of reaching 1500 C anticipating a need for high temperatures to produce a reasonable vapor pressure of HfF_4. The much lower temperature of 550 °C eventually allowed for the use of more compact home-built ovens. These temperature measurements were later repeated with one of the HfF^+ lines to confirm that the optimal operating temperature for HfF^+ measurements was the same as for Hf.

The sensitivity of the velocity-modulation system was characterized both with and without the discharge running. With the discharge off, the fractional noise was $8\text{x}10^{-8} Hz^{-1/2}$; while with the discharge on, the fractional noise is $3\text{x}10^{-7} Hz^{-1/2}$. This corresponds to approximately a factor of 5 above shot-noise with the discharge off and a factor of 20 above shot-noise with the discharge on. The fractional noise with the discharge off is most likely

due to air currents. For most of the data shown here, the discharge tube was located 17 inches above the optics table in the high temperature oven resulting in air currents being particularly problematic. Pick-up at the discharge frequency causes offsets on the lock-in that fluctuate and thus the noise with the discharge running is greater. For all of the noise measurements, the noise was greater than the noise-equivalent-power of the detector (15 pW/$\sqrt{Hz}$).

3.3 First Experimental Data of HfF^+ Spectra

Scans with the diode laser were started after the system had been characterized with N_2^+ and Hf starting with the wavelength region around 770 nm. HfF_4 was loaded into the bottom of the central discharge tube and the oven was heated to 550 °C. Helium buffer gas was flowed through the discharge continuously such that the total pressure was 5 torr. For these scans, the discharge current was $\sim$ 100 mA_{pk-pk} and the voltage drop across the discharge was $\sim$ 1 kV. A series of lines with first-derivative lineshapes characteristic of ions was seen near 13,000 cm^{-1}. The lines disappeared when the oven was turned off, which meant it was not due to one of the N_2^+ bands located in this wavelength range. This series of lines was tentatively identified as belonging to a HfF^+ band, which was confirmed by the fit.

Figure 3.5 shows the scans covering the HfF^+ band. 60 cm^{-1} of bandwidth was covered with rotational transitions with up to J=50 seen as the discharge plus the oven results in a relatively high temperature. The high rotational temperature provides many lines for the fit. Subsequent scans were acquired to see the band origin with higher sensitivity. High sensitivity around the band origin was necessary to identify the low J lines, which have low thermal population, so that the values of Ω could be assigned to the upper and lower states.

The electronic states of HfF^+ can be approximated as Hund's case (a) or in the case of strongly spin-orbit mixed states, Hund's case (c) [26]. As described in Ref. [35], for Hund's case (a), the interaction of the nuclear rotation ($\mathbf{N}$) with the electronic motion, both spin

(**S**) and orbital (**L**), is very weak while the electronic motion is coupled very strongly to the internuclear axis. For Hund's case (a), both the orbital angular momentum (**L**) and the spin (**S**) process around the internuclear axis with projection Λ and Σ respectively along the internuclear axis with $\Omega = \Lambda + \Sigma$. The total angular momentum, **J**, is then given by the coupling of the electronic motion ($\mathbf{L} + \mathbf{S}$) to the nuclear rotation (**N**). Since J cannot have values smaller than Ω, for a given Ω, J = Ω, $\Omega + 1$, $\Omega + 2$,... As the rotational energy is proportional to J(J+1) and transitions from one vibronic state to another are only allowed for $J = 0, +/-1$, examination of rotational bands for the presence of transitions for low values of J can thus lead to identification of the value of Ω for the upper and lower states [35].

Hund's case (c) is very similar to Hund's case (a) except that in this case the interaction between **L** and **S** is stronger than the interaction with the internuclear axis [35]. In Hund's case (c), Λ and Σ are not well-defined quantum numbers but rather **L** and **S** couple to form the resultant vector $\mathbf{J_a}$, which has a projection $\mathbf{\Omega}$ along the internuclear axis. $\mathbf{J_a}$ couples to the nuclear rotation to form the total angular momentum, **J** as in case (a). Again as in case (a), J cannot be smaller than Ω, leading to J = Ω, $\Omega + 1$, $\Omega + 2$,... and giving us the same tool to identify Ω for the upper and lower states from a rotational band [35]. Despite the strong spin-orbit mixing for some of the states of HfF^+ and ThF^+ such as the $^1\Pi_1$ and $^3\Pi_1$ [64], we still denote all of the states using the molecular term symbol, $^{2S+1}\Lambda_\Omega$, as if Λ is a good quantum number.

As hafnium has five isotopes with relative abundances of 35.10%(180), 13.63%(179), 27.30%(178), 18.6%(177), and 5.21%(176) [33], we expected to see some isotope structure in the measured spectrum. Initially, when this data was acquired, we did not anticipate seeing the odd isotopes due to the hyperfine structure washing out the lines. Later measurements discussed in Chapters 4 and 5 demonstrated that the hyperfine splittings are small enough that we see all five isotopes.

The presence of multiple isotopes allows us to determine the change in vibrational

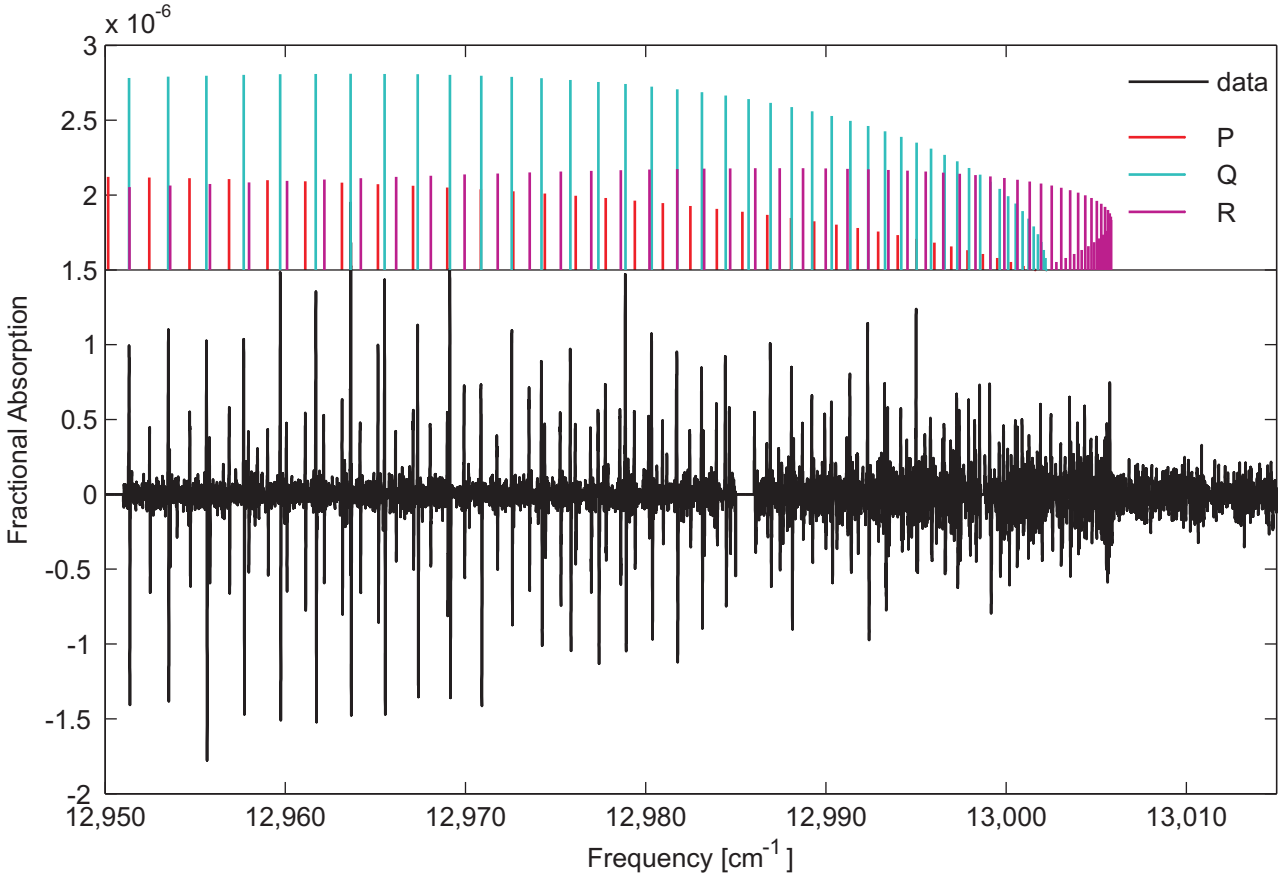

Figure 3.5: Compilation of scans covering HfF^+ band with isotope averaged fit (offset for clarity). Note that the high rotational temperature (800 K) results in a large number of lines present.

quantum number with some assumption of reasonable vibrational energies. In this case, $\Delta v = v' - v'' = 0$ as there is no sign of vibrational isotope splitting for $\Delta v > 0$, where v' and v' are the vibrational quantum numbers of the upper and lower states respectively . Because $\Delta v = 0$, we did an isotope averaged fit rather than fitting to lines from only one isotope of hafnium, i.e. $^{180}HfF^+$, as only in portions of the spectra was there partially resolved isotope structure. For part of the spectrum, the electronic, vibrational and rotational isotope shifts cancel or nearly cancel resulting in a single lineshape. (See Figure 3.6 (b).) Attempts to fit the lineshapes and to extract the positions of each individual isotope were unsuccessful.

Lines belonging to the P (J″-J′=1), Q (J″-J′=0) and R (J″-J′=-1) branches were identified. All three branches were then fit to the following:

$$E(J'', J') = \nu_0 + (B' - \frac{P}{2} * (p+2q))J'(J'+1) + D'J'^2(J'+1)^2 - B''J''(J''+1) - D''J''^2(J''+1)^2 \tag{3.1}$$

where $P = -1$ for $\Delta J = 0$ and $P = 1$ for $\Delta J = +/-1$, ν_0 is the energy difference between the $v = 0$ levels of the electronic states, B′ and B″ are the rotational constants of the upper and lower states respectively, (p+2q) is the Ω-doubling of the upper state (this parameterization is discussed in Ref. [34]), and D′ and D″ are the respective anharmonic distortion terms of the upper and lower state. Higher order Ω-doubling terms were not included as D′ was already consistent with zero. The values obtained by the fit are given in Table 3.1 and the locations of the P, Q, and R branches from the fit are shown graphically in Figure 3.5 along with a compilation of the data. The values for B″ and B′ are consistent with the species being HfF^+ as opposed to a species with the mass of N_2^+. The rotational constant in wavenumbers is given by

$$B = \frac{h}{8\pi^2 c\mu r_e^2} \tag{3.2}$$

where h is Planck's constant, μ is the reduced mass, c is the speed of light in cm/s and r_e is the equilibrium bond length [35]. Petrov et al. [2] had calculated values of r_e ranging from 1.78 to 1.87 $\mathring{A}$ for different electronic states of HfF^+, leading to values of B ranging from

Table 3.1: Isotope averaged values of fit of line positions with 1σ errors.

parameter	value [cm^{-1}]
B″	0.30489(10)
B′	0.28117(10)
D″	1(1) x 10^{-7}
D′	1(1) x 10^{-7}
(p+2q)	3.55(2) x 10^{-4}
ν_0	13002.229(3)

0.281 to 0.310 cm^{-1}. A more detailed comparison with theory follows in Chapter 5.

The presence or absence of low J lines allows for the determination of Ω for the upper and lower state. If the R(0) line is present, $\Omega'' = 0$ and $\Omega' \leq 1$. If the P(1) line is missing, then $\Omega' > 0$. Additional confirmation comes from looking at the Q(0) and Q(1) line locations. If Q(0) is missing, $\Omega'' > 0$ or $\Omega' > 0$ and if Q(1) is present, $\Omega'' \leq 1$ and $\Omega' \leq 1$. The region of the spectrum containing the low J lines is shown in Figure 3.6. With R(0) and Q(1) present and P(1) and Q(0) missing, $\Omega'' = 0$ and $\Omega' = 1$.

From comparison with theory [2], it would initially appear that the $\Omega'' = 0$ and $\Omega' = 1$ transitions is the $^3\Pi_1 - ^1\Sigma^+$ (0,0) transition since the predicted value for T_0 is only 300 cm^{-1} away from the theory prediction. However, the sign of the Ω-doubling corresponds not to the $^3\Pi_1 - ^1\Sigma^+$ transition, but to the $^1\Pi_1 - ^1\Sigma^+$ transition [64]. The identification of more states of HfF^+ as discussed in Chapter 4 led to the confirmation that this is actually the $^1\Pi_1 - ^1\Sigma^+$ (0,0) band. The structure of HfF^+ as identified so far is discussed in Chapter 5.

3.4 Extending Velocity-Modulation Spectroscopy

The fact that the $^1\Pi_1 - ^1\Sigma^+$ (0,0) is 2100 cm^{-1} from the predicted value [2] highlights one of the limitations of doing VMS with a cw laser when there is no prior spectroscopic information. Even with cw lasers that are relatively easy to scan, it takes a long time to cover several thousand wavenumbers of bandwidth. With the diode laser, we sampled small

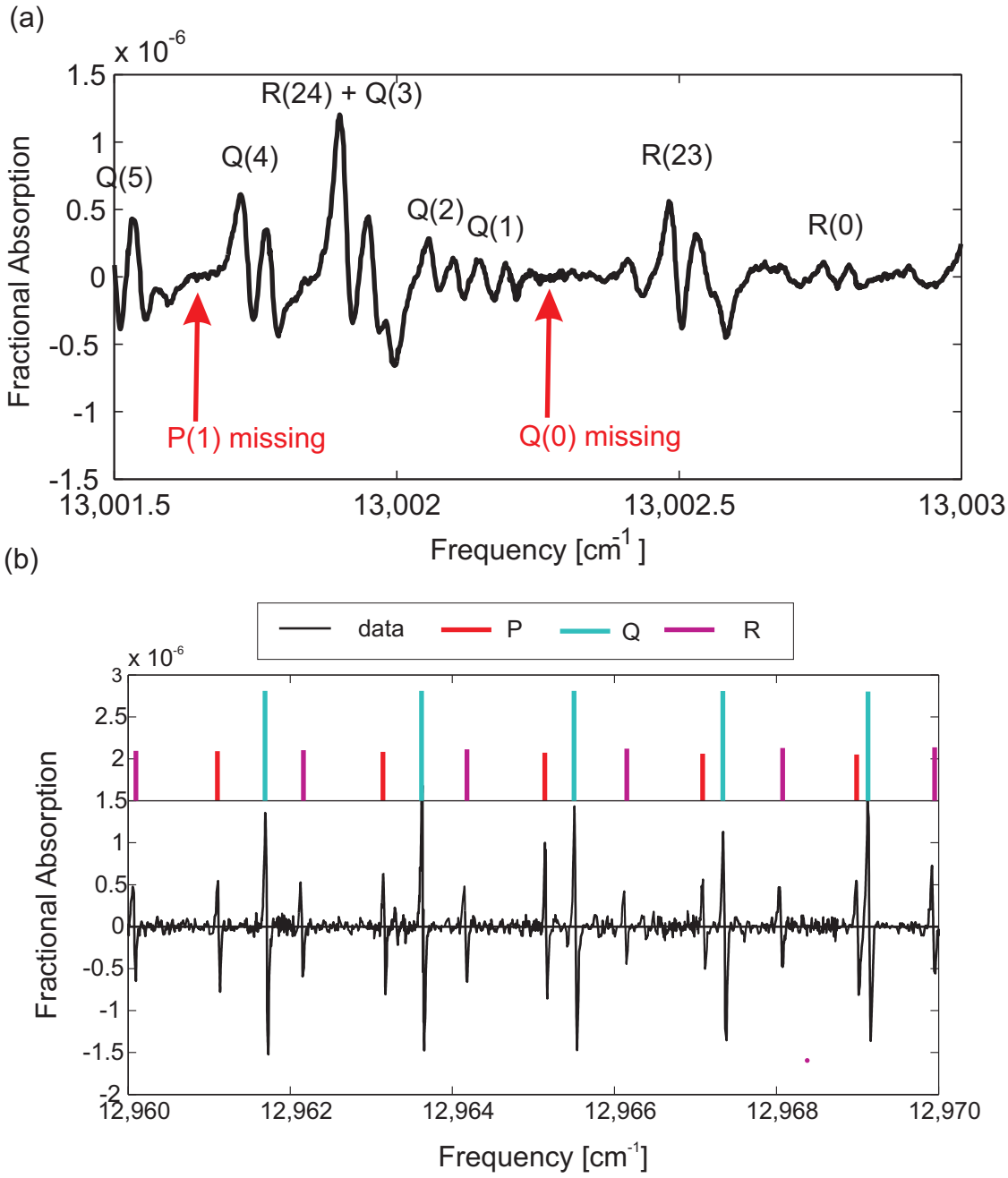

Figure 3.6: (a) Confirmation of an Ω=0 to Ω=1 transition. The red arrows point to the locations of the P(1) and Q(0) predicted by the fit. The visibility of the R(0) and Q(1) lines confirms that the sensitivity is high enough to see the P(1) and Q(0) lines if they were present. (b) Region of HfF^+ band in which isotope shifts cancel. In this region of the spectra the rotational isotope shift is canceled by the electronic and vibrational isotope shifts. The difference in energy for an electronic transition for $^{178}HfF^+$ relative to $^{180}HfF^+$ is given by $\Delta E = (1 - \frac{\mu_{180}}{\mu_{178}})E_{rot} + (\Delta T_{0,iso} + \Delta\omega_{\nu,iso})$, where μ_{180} and μ_{178} are the respective reduced masses, E_{rot} is the rotational contribution to the transition energy, and $(\Delta T_{0,iso} + \Delta\omega_{\nu,iso})$ is the sum of the electronic and vibrational isotope shift. From this we see that $(\Delta T_{0,iso} + \Delta\omega_{\nu,iso}) \sim -0.04$ cm^{-1}, which matches the structure seen in (a) where at the band origin $E_{rot} \sim 0$.

regions of the accessible bandwidth as is shown in Figure 3.7, but did not fully cover the wavelength range of the laser. The sampling approach was made to try to leverage the high rotational temperature, which results in each band covering $\sim$100 cm^{-1} with lines spaced by less than 0.5 cm^{-1}. By sampling the spectrum in non-contiguous 1 cm^{-1} sections, we in effect gain information about a much wider frequency range as we would see multiple lines if there is a band in the vicinity. However, once potential lines are seen, the whole band still needs to be scanned out. Instead of pushing to cover a wider energy range with cw lasers, we switched to frequency comb velocity-modulation spectroscopy which is discussed in Chapter Four.

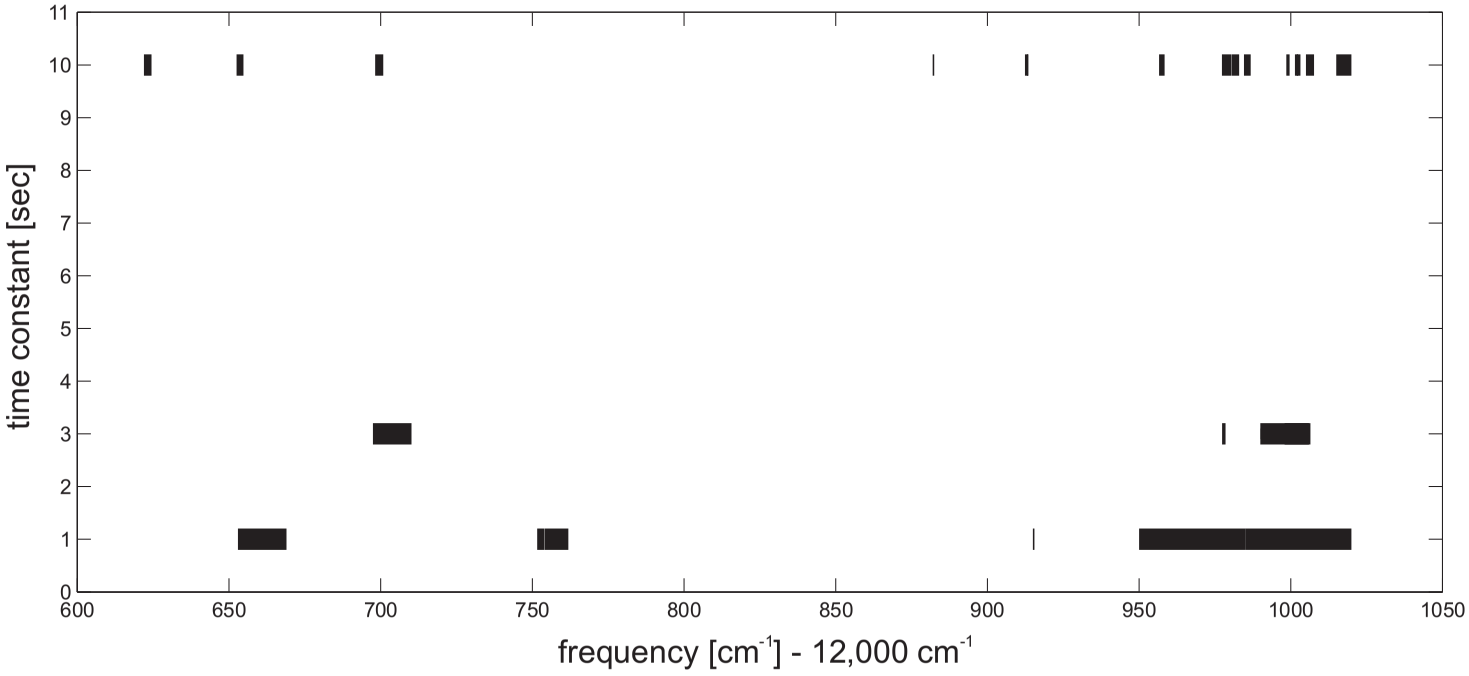

Figure 3.7: Summary of wavelength ranges and time constants of scans taken with the diode laser. All data was taken at a $\sim$ 100 mA_{pk-pk} discharge current with a voltage drop of $\sim$ 1 kV across the discharge and a sensitivity of 3x10^{-7} $Hz^{-1/2}$. No HfF^+ bands other than the one spanning 12,950-13,000 cm^{-1} were identified in the wavelength range covered. The low current of these scans compared to those in Chapter Four limited the size of the HfF^+ absorption signal.

Chapter 4

Development of Frequency Comb Velocity-Modulation Spectroscopy[1]

The application of optical frequency combs to a variety of spectroscopic techniques has resulted in ultrahigh sensitivity systems with simultaneous high resolution, absolute frequency accuracy, and spectral bandwidth, all with dramatic reduction in data acquisition times [37, 38, 39, 40, 41, 42, 43]. Compared to broadband incoherent light sources or tunable cw lasers, frequency combs offer both broad spectral bandwidth and spectrally narrow lines with well-defined frequencies given by $f_n = f_0 + n * f_{rep}$ set by only two parameters, the carrier-envelope-offset frequency, f_0, and the repetition rate, f_{rep} [44]. Applications of direct frequency comb spectroscopy have included breath analysis [45], tomography of supersonically-cooled molecular jets [46], demonstration of high-sensitivity molecular fingerprinting with ammonia [42] and detection of impurities in semi-conductor specialty gases [47]. The development and use of these spectroscopic techniques has been focused on neutral atomic and molecular species as opposed to ionic species. Prior to the research discussed below, no techniques have been capable of ion-specific high-sensitivity modulation spectroscopy on every parallel detection channel over a broad spectral range [36]. The integration of velocity modulation spectroscopy [29, 28] and cavity-enhanced direct frequency comb spectroscopy [39, 43] provides a way to achieve very broad spectral bandwidth ion-sensitive spectroscopy without sacrificing high-resolution or high-sensitivity.

[1]Portions of this chapter have been previously published in Sinclair et al. [36].

4.1 Overview

High resolution spectroscopy of molecular ions is typically performed using velocity-modulation spectroscopy (VMS), first demonstrated in Saykally's group [29, 28]. Velocity-modulation spectroscopy achieves high sensitivity via lock-in detection of the absorption signal from a laser which passes through a sample of ions with a modulated Doppler shift due to an alternating current discharge [28]. Although recent experiments have pushed to higher sensitivity [48, 49] as well as higher accuracy [50, 51], these systems still rely on slow scans of continuous wave (cw) lasers. In addition, broad spectral bandwidth has been achieved via emission spectroscopy [52, 53], but without the methods of enhancing sensitivity of the current experiment. Velocity-modulation spectroscopy of HfF^+ including some of the limitations was discussed in Chapter Three. Cavity-enhanced direct frequency comb spectroscopy has demonstrated broad simultaneous bandwidth with high resolution and high sensitivity [39, 43], and thus is an ideal candidate to integrate large instantaneous bandwidth with high-resolution VMS by enabling lock-in detection simultaneously on every comb tooth.

To integrate these two powerful spectroscopic techniques, several key features are needed, as sketched in Figure 4.1. An alternating-current discharge tube for the production and modulation of molecular ions must be placed within an optical enhancement cavity, with the cavity length actively stabilized such that the frequency comb light can be coupled into the cavity. The cavity needs a ring geometry to provide a single direction of propagation of the light relative to the instantaneous motion of the ions, which enables lock-in detection at the discharge frequency (10 kHz). For frequency accuracy that is not limited by the imaging system resolution, the imaging system must be able to resolve each individual comb mode. Finally, the detector used must be able to demodulate the intensity of each comb mode at the discharge frequency of 10 kHz to recover the absorption signal. The design considerations as well as the acquisition of a thousand wavenumbers of the spectra of HfF^+

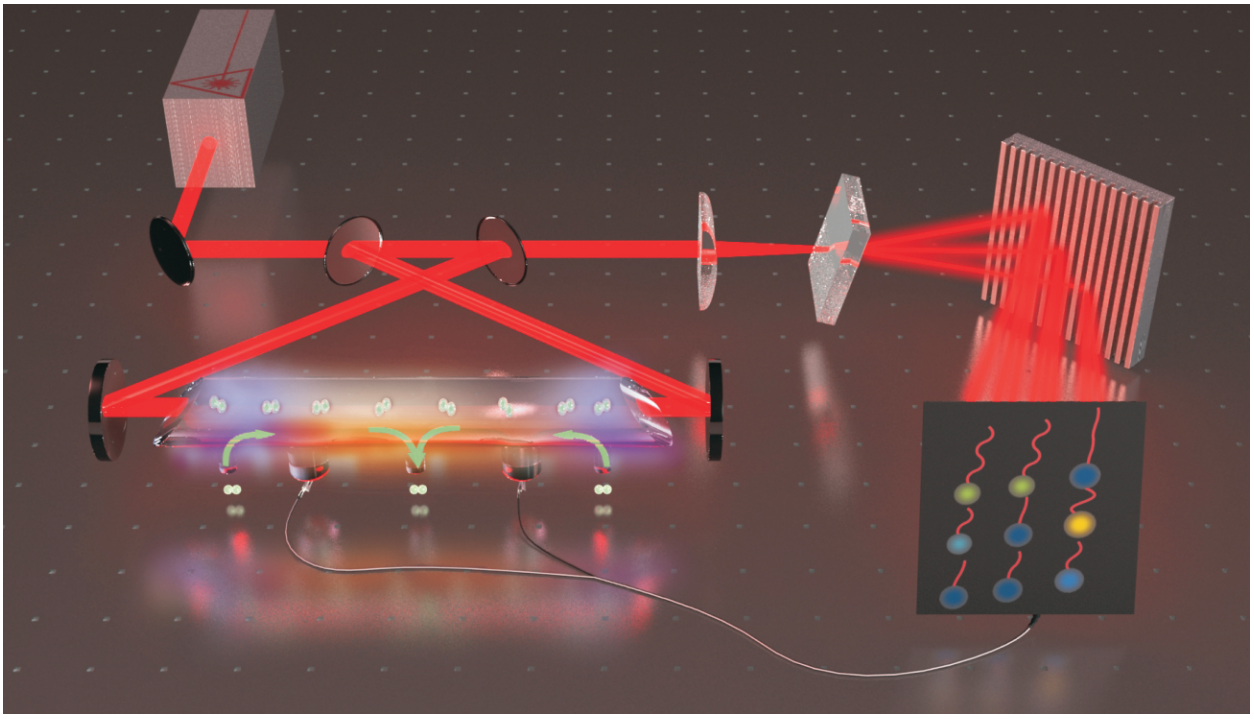

Figure 4.1: Qualitative sketch of a frequency comb velocity-modulation spectroscopy system. Light from the frequency comb is coupled into a bow-tie ring cavity containing an AC discharge tube. The AC discharge modulates the ions' Doppler shift and thus the ion absorption signal. The transmitted light is dispersed by a VIPA etalon and a grating to produce a 2-dimensional image in which every comb tooth is resolved and detected. A fast demodulation camera performs lock-in detection of each comb tooth at the discharge modulation frequency to recover ion-specific absorption signals across each comb mode. (Figure courtesy B. Baxley(JILA).)

are both discussed in this chapter. The analysis of the HfF^+ bands measured is discussed in Chapter Five.

4.2 Experiment Design

4.2.1 Cavity Design

To increase the effective absorption path length, a ring cavity was placed around the discharge tube. The ring geometry provides a well defined direction of propagation of the laser relative to the instantaneous velocity of the ions and allows for the use of counter-propagating beams for additional noise suppression. The existence of the discharge tube inside the cavity places limitations on the achievable finesse. Additionally, the presence of the discharge tube windows causes spectral filtering of the comb bandwidth coupled into the cavity due to group velocity dispersion.

For the cavity, a bow-tie configuration was chosen as shown in Figure 4.2. On either side of the approximately 1 meter discharge tube are 100 cm radius of curvature mirrors. On the short arm of the bow-tie are the flat input and output couplers with 98% reflectivity. The higher the finesse, the more sensitive the system but issues of intra-cavity losses and group velocity dispersion become more problematic. The reflectivity of the input couplers was chosen as a compromise between matching the losses due to the Brewster angle windows to maximize the transmitted intensity and maximizing the finesse. The ratio of cavity-enhanced signal to single-pass absorption signal for a ring cavity is given by $\mathscr{F}/\pi$, where $\mathscr{F}$ is the cavity finesse. The finesse of the cavity is given by

$$\mathscr{F} = \frac{\pi\sqrt{g_{rt}}}{1 - g_{rt}} \tag{4.1}$$

where $g_{rt} = R\sqrt{T_{cav}}$ is the probability a photon makes one round trip (round trip gain), R is the reflectivity of the input couplers, and T_{cav} is the transmissivity of the Brewster windows

[54]. The ratio of transmitted intensity to incident intensity is given by

$$\frac{I_{trans}}{I_{inc}} = \frac{(1-R)^2 T_{cav}}{(1-R\sqrt{T_{cav}})^2} \tag{4.2}$$

[54]. For the current system $T_{cav} \sim 0.97$ due to imperfect alignment of the Brewster angle windows on the discharge tube and thus $\mathscr{F} \sim 88$ and $I_{trans}/I_{inc} \sim 32\%$. I_{trans}/I_{inc} has been measured to be $\sim 30\%$ with the single-frequency reference laser (thus avoiding issues of spectral filtering for the measurement).

The free spectral range (FSR) of the cavity, ignoring intra-cavity dispersion, is given by FSR $\approx$ c/L, where c is the speed of light and L is the length of the cavity. We wanted to match every comb mode, spaced by 2.97 GHz, to every 25^{th} cavity resonance, which resulted in a cavity FSR of $\sim$119 MHz. By making the bow-tie as compact as possible, we achieved the required optical path length of 254 cm. Fine tuning of the cavity length to match the comb's repetition rate is achieved via mounting one input coupler on a translation stage. Additional, finer control is possible via a long-travel (80 μm) piezoelectric transducer (PZT) on the translation stage. The long-travel PZT has enough range to keep the cavity length and thus the FSR matched to the repetition rate of the comb as the repetition rate is scanned to fully sample the spectrum.

Once the required optical pathlength and desired cavity configuration were known, we wanted to confirm that we had designed a stable resonator and to calculate the radius of curvature and beam diameter of the cavity mode at different locations of the cavity. Knowledge of the radius of curvature and beam waist at the input coupler is necessary for matching the incident light to the cavity mode. We also wanted to know the size of the beam at the focus inside the discharge tube as well as at the two curved mirrors to get a sense of the size of the beam through the discharge region.

The so-called ABCD matrices and the q-parameter of the beam can be used to calculate the waist and radius of curvature of the beam as a function of position. The beam waist,

ω(z), at a given position, z, is given by

$$-Im(q) = \frac{\lambda}{\pi\omega^2(z)} = \frac{1}{B}\sqrt{1 - (\frac{A+D}{2})^2} \tag{4.3}$$

where λ is the wavelength of the light, and the radius of curvature at a given position, z, is given by

$$Re(q) = \frac{1}{R(z)} = \frac{D-A}{2B} \tag{4.4}$$

[54]. For any point in the cavity, we can also define a quantity m = (A+D)/2, where if $-1 \leq$ m ≤ 1, the resonator is stable. In order to find the q-parameter, the ABCD matrix can be calculated by using the propagation through a medium with index of refraction n with length d, $\begin{pmatrix} 1 & \frac{d}{n} \\ 0 & 1 \end{pmatrix}$, and the reflection from a spherical mirror with curvature R, $\begin{pmatrix} 1 & 0 \\ \frac{2}{R} & 1 \end{pmatrix}$, where R is positive if the center of curvature lies in the positive direction of the incident ray propagation. For example, the ABCD matrix for the focus between the two curved mirrors is given by:

$$\begin{pmatrix} A & B \\ C & D \end{pmatrix} = \begin{pmatrix} 1 & \frac{1}{2}L_{disch} \\ 0 & 1 \end{pmatrix} \begin{pmatrix} 1 & \frac{t}{n_{fs}} \\ 0 & 1 \end{pmatrix} \begin{pmatrix} 1 & \frac{1}{2}(L1 - L_{disch}) - t \\ 0 & 1 \end{pmatrix} \begin{pmatrix} 1 & 0 \\ \frac{-2}{R} & \end{pmatrix} \begin{pmatrix} 1 & L2 \\ 0 & 1 \end{pmatrix}$$
$$\begin{pmatrix} 1 & L3 \\ 0 & 1 \end{pmatrix} \begin{pmatrix} 1 & L2 \\ 0 & 1 \end{pmatrix} \begin{pmatrix} 1 & 0 \\ \frac{-2}{R} & 1 \end{pmatrix} \begin{pmatrix} 1 & \frac{1}{2}(L1 - L_{disch}) - t \\ 0 & 1 \end{pmatrix} \begin{pmatrix} 1 & \frac{t}{n_{fs}} \\ 0 & 1 \end{pmatrix} \begin{pmatrix} 1 & \frac{1}{2}L_{disch} \\ 0 & 1 \end{pmatrix}$$

where L_{disch} = 101 cm is the length of the discharge tube; t=0.1 cm is the thickness of the window; n_{fs} = 1.5 is the index of refraction of fused silica at 800 nm; L1=110 cm is the distance between the two curved mirrors (M2 and M3 in Figure 4.2); R=100 cm is the radius of curvature of the two curved mirrors; L2 = 67 cm is the distance between the curved mirror and the input coupler; and L3 = 7 cm is the distance between the two input couplers. From this we get that the beam diameter at the waist at the center of the discharge tube is $\sim$250 μm, at the curved mirrors it is $\sim$615 μm, and at the waist between the two input

Table 4.1: Distances between optical elements in enhancement cavity and between the mode-matching optics and the enhancement cavity. Optical elements are labeled in Figure 4.2.

Optical elements	Distance [cm]
M2 and M3	110
M1 and M2	67
M3 and M4	67
M1 and M4	8
f=70 mm lens and f=50 mm lens	17
f=50 mm lens and PBS	47
PBS and M1	44
PBS and M4	44

couplers it is $\sim$500 μm. Also, the value of m = -0.92, so the resonator is stable.

To couple light into one mode of the cavity, both the beam waist and radius of curvature of the incident beam must be matched to the waist and radius of curvature of the cavity mode at the input coupler. ABCD matrices were used to calculate the propagation of the beam from the collimated output of the fiber to the input coupler. Matlab's ability to solve systems of nonlinear equations was utilized to determine the appropriate distances for two lenses to be placed before the cavity by matching the real and imaginary parts of the q-parameter of the cavity to the incident light at the input coupler. Both lenses needed to go before the beamsplitter so that the beam would be well matched to the cavity for both clockwise and counterclockwise propagation. (See Figure 4.2.) Two lenses were needed due to the space constraints and the very gentle focus to match the two parameters.

One of the additional complications of this system is the presence of astigmatism. With the bow-tie cavity, the angle of incidence for the curved mirrors is 15° and thus the effective radius of curvature in the tangential plane (plane of incidence) is given by $R_e = Rcos(\theta)$, while in the sagittal plane (perpendicular to the plane of incidence) it is given by $R_e = R/cos(\theta)$. For $\theta = 15°$ and R=100 cm, R_e = 104 cm in the sagittal plane and R_e = 97 cm in the tangential plane. Additionally, the optical path through the Brewster window is

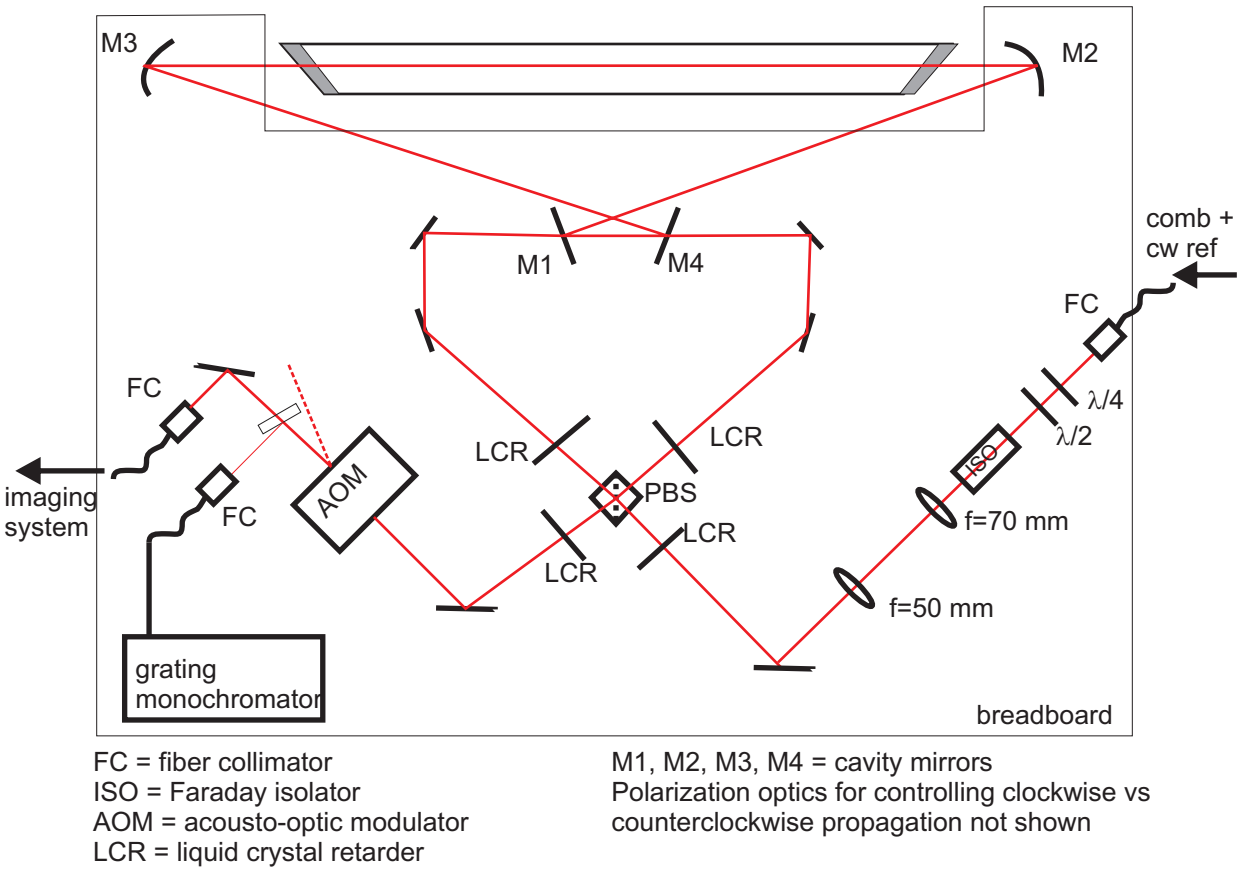

Figure 4.2: Optical layout for frequency comb velocity-modulation spectroscopy. Light from the frequency comb passes through $\lambda/2$ and $\lambda/4$ clean-up waveplates and a optical isolator to achieve the appropriate polarization and prevent back reflections to the comb. The two lenses are placed to match the mode of the collimated comb light from the fiber to the mode of the optical cavity at the input couplers (M1 and M4). Depending on the polarization of the light before the polarizing beam splitter (set by a LCR) light travels either clockwise or counter-clockwise through the cavity. M2 and M3 are 99.99% reflectivity mirrors with a 100 cm radius of curvature, and M1 and M4 are 98% reflective flat input couplers. A translation stage and long travel PZT on M4 coupled with a fast PZT on M2 allow for tuning of the cavity length to match the free spectral range of the cavity to the repetition rate of the comb. After traveling through the cavity, the outcoupled light passes through the AOM (used for measuring the DC intensity on the lock-in camera) and then to the imaging system. A glass wedge is used to pick-off a small amount of the outcoupled light to measure the transmitted spectrum with a grating spectrograph.

different in the two planes, but this is a smaller effect than the difference in effective radius of curvature. Despite this difference, the incident light is mode-matched to the cavity using spherical lenses and as a consequence there will always be some coupling into higher-order modes. With a single-frequency laser, i.e. no spectral filtering, 85-90% of the light is coupled into the lowest order mode (TEM_{00}).

In order to determine the spectral bandwidth of the frequency comb that can be coupled into the cavity simultaneously, we need to reconsider the free spectral range of the cavity taking intra-cavity dispersion into account. The free spectral range of the cavity is given by

$$FSR(\omega) = \frac{c}{L + c\frac{\partial\phi}{\partial\omega}} \tag{4.5}$$

where c is the speed of light, L is the optical path length of the cavity and $\frac{\partial\phi}{\partial\omega}$ is the intra-cavity dispersion [55, 56]. The variation of the FSR as a function of frequency is then given by

$$\frac{\partial FSR(\omega)}{\partial\omega} = -FSR(\omega)^2\frac{\partial^2\phi}{\partial\omega^2} \tag{4.6}$$

where $\frac{\partial^2\phi}{\partial\omega^2}$ is the group delay dispersion (GDD). The variation in the cavity FSR is non-negligible primarily due to the presence of the discharge tube windows inside the cavity. The discharge tube windows are 1 mm thick fused silica, which has a group velocity dispersion (GVD) of 36 fs^2/mm at 800 nm. The fused silica windows replaced the BK7 windows described in Chapter Three to reduce the window thickness from 3 mm to 1 mm. Using the GVD for fused silica at 800 nm, an initial FSR of 120 MHz, and a 1 MHz cavity linewidth, the change in frequency for a cavity resonance to be a cavity linewidth away from the bare cavity resonance occurs across a $\sim$ 6 THz spectral width. As is shown in Figure 4.3, $\sim$ 6.5 THz (15 nm at 830 nm) of the full comb spectrum is transmitted through the cavity. (By using a grating to select the portion of the full comb bandwidth for locking the frequency comb to the cavity, different 6.5 THz portions of the full comb bandwidth can be coupled into the cavity.) As is discussed in the next section, the imaging system has a spectral bandwidth of $\sim$ 4.4 THz (10 nm at 830 nm) so this is sufficient.

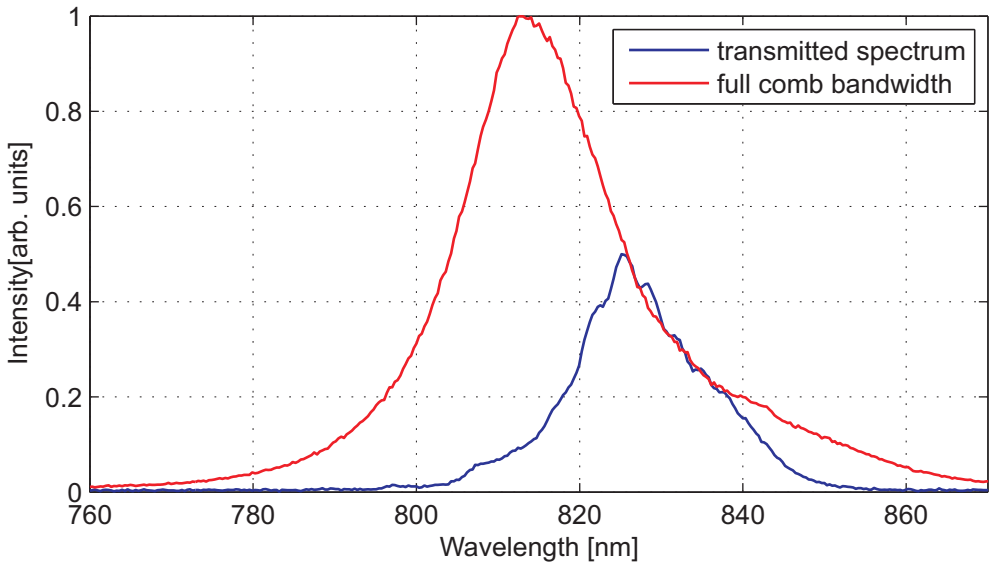

Figure 4.3: Full comb-spectrum and transmitted comb-spectrum measured with grating spectrometer. The transmitted spectrum is less than the full comb bandwidth due to the spectral filtering that results from the two Brewster angle windows on the discharge tube. By using a grating to select different regions of the full comb spectrum for producing the locking signal, the spectral region of the transmitted spectrum can be changed.

4.2.2 Imaging System

The cavity-transmitted light is coupled via fiber to a two-dimensional lock-in imaging system designed for massively parallel detection. A 1 GHz resolution crossed-dispersion system consisting of a titled VIPA etalon [57, 58] and a grating is used to resolve each individual comb mode [40, 45]. A Heliotis C2 "smart pixel" lock-in camera [59, 60], which uses a combination of CCD and CMOS technology, is used to demodulate and read out each pixel at the discharge modulation frequency. The lock-in camera uses a microlens array to achieve close to a hundred percent filling factor even though the active area is only ten percent of the total area. The use of the microlens array also makes the camera sensitive to horizontal tilt and thus careful alignment of the camera is required. A schematic of the imaging system is shown in Figure 4.4.

A VIPA is a high resolution element that consists of a plate with an entrance stripe with an anti-reflection coating, a highly reflective coating above the entrance stripe (R$\geq$99.9%), and an exit surface that is partially reflective (R$\sim$99.6%). Unlike a usual etalon, all incident wavelengths are transmitted. Similar to an etalon, the VIPA generates repeating mode orders with the free spectral range set by the plate thickness (94 GHz for this experiment). A grating is then used to resolve overlapping mode orders of the VIPA, and thus only requires a resolution at the level of the VIPA FSR. A detailed discussion of the design considerations for a VIPA etalon and grating crossed-dispersion system is found in Chapter 6 of M. Thorpe's thesis [56]. In this system, the first VIPA used was designed for 100 MHz resolution and thus was coated for $\mathscr{F} \sim 1000$. Due to the technical challenges of constructing a high resolution VIPA, the actual resolution was only on the order of 1 GHz, but alignment through it often resulted in aberrations and in a low efficiency of $\sim 1\%$. With a second VIPA designed for 1 GHz resolution ($\mathscr{F} \sim 100$), alignment was much easier and 10% of the light is transmitted through the VIPA.

The imaging system was designed with the goal of placing a comb mode onto a single

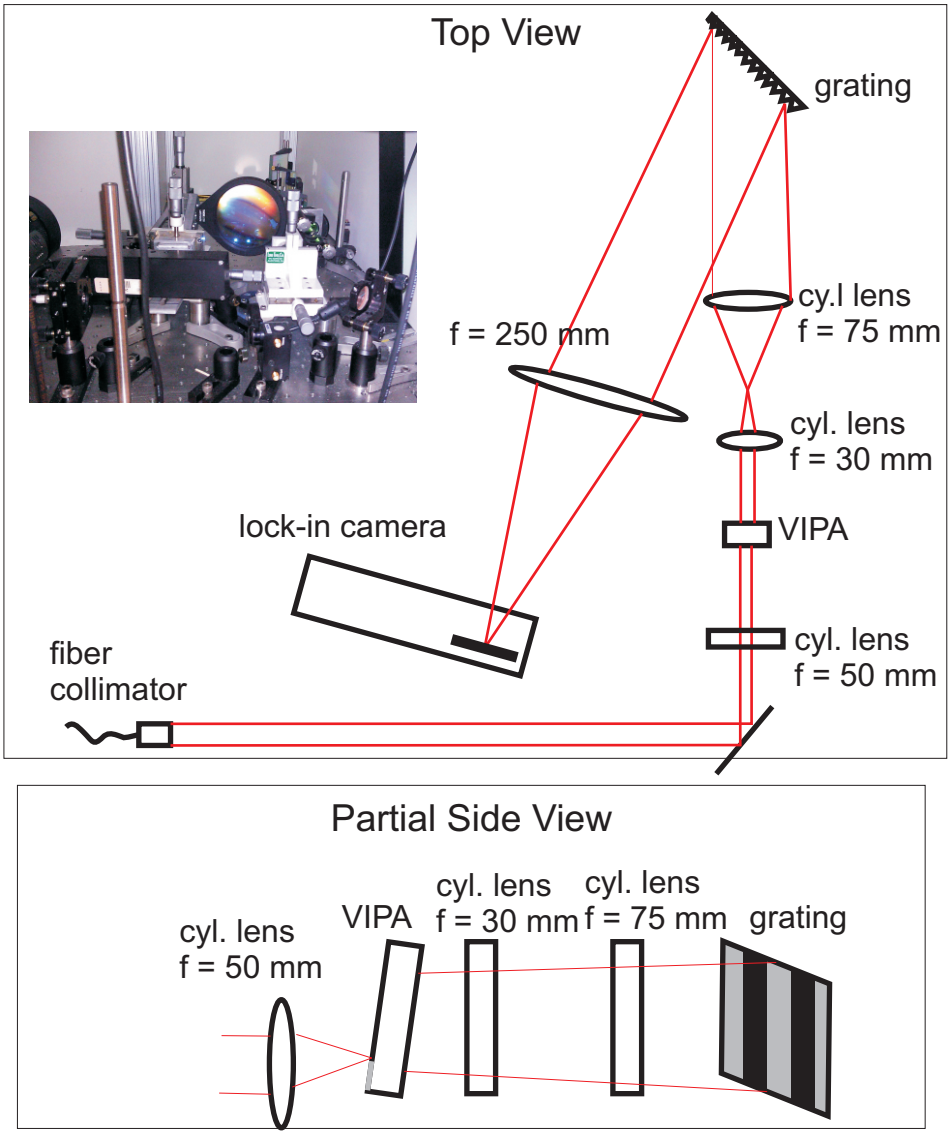

Figure 4.4: Schematic of imaging system. The VIPA provides high resolution, 1 GHz, but low free spectral range, 100 GHz. The grating resolves the 100 GHz FSR of the VIPA. The first f = 50 mm cylindrical lens focuses the light into the VIPA at the junction of the anti-reflective and high reflectivity coatings. After the VIPA, the cylindrical telescope expands the beam to fill the grating. The f=250 mm imaging lens then maps the differences in wavevector to differences in position at the detector plane of the camera. The inset shows a picture of the actual optics.

pixel, which has dimensions of 86.3 x 50 μm, and of spacing the comb modes in the grating (horizontal) direction by every other pixel to maximize the total number of comb modes imaged while retaining the ability to individually resolve them. In the VIPA (vertical) direction, prior experience led us to choose an imaging lens with $f \sim 250$ mm so that one FSR nearly fills the vertical direction of the camera. In the grating (horizontal) direction, the beam diameter after the VIPA is 2 mm, leading to a $b_i = 5$ mm beam diameter after the horizontal telescope. The beam diameter at the focus on the lock-in camera is then given by $\mathrm{b}_{camera} = \frac{4\lambda}{\pi}\frac{f_{imaging}}{b_i} = \frac{4*800nm}{\pi}\frac{250mm}{5mm} \approx 51$ μm. When measured using a conventional CCD camera with 13 x 13 μm pixels, the horizontal width was found to be ~ 65 μm. In the VIPA direction, the width was found to be ~ 50 μm.

The maximum resolution of a grating is given by $\Delta\lambda = \lambda/N$, where λ is the wavelength of the light and N number of grating lines illuminated. At 800 nm, given the 1800 lines/mm pitch of the grating and a 5 mm diameter beam, the maximum resolution is $\sim$ 42 GHz, which is sufficiently below the VIPA free spectral range of 94 GHz. To place the comb modes separated by one FSR on every other pixel, necessitates a 172.6 μm spacing for modes spaced by 0.22 nm at a center wavelength of 800 nm. The grating equation gives the angle of the first order off of the grating as follows:

$$sin(\beta) = G\lambda - sin(\alpha) \tag{4.7}$$

where G is the grating pitch of 1800 lines/mm, λ is the wavelength of the light, and α is the incident angle. From this we get that the change in angle as a function of wavelength is

$$\Delta\beta \approx \frac{G}{cos(\beta)}\Delta\lambda \tag{4.8}$$

. Using ray-tracing matrices, the position from the center axis is given by

$$x_f = f_{imaging}G\Delta\lambda/cos(\beta) \tag{4.9}$$

where $f_{imaging}$ is the focal length of the imaging lens, d_i is the distance from the grating to the imaging lens, $\Delta\lambda$ is the change in wavelength, and β is the angle of the first order off of

the grating. Given $f_{imaging}$ = 250 mm, G=1800 lines/mm, and $\Delta\lambda$ = 0.22 nm, an angle of $\beta = 55°$ is needed to produce x_f = 172.6 μm. From the grating equation, for λ = 800 nm, this requires an angle of incidence of 38°. Using the CCD camera, the comb modes had a horizontal spacing of $\sim$ 170 μm and a vertical spacing of $\sim$ 200 μm.

After the characterization with the conventional CCD camera, the comb light was then imaged onto the lock-in camera by applying a well-calibrated 10 kHz amplitude modulation to the light using the AOM shown in Figure 4.2. The resulting image of the incident comb light is shown in Figure 4.5. As can be seen in Figure 4.5, the chirp in the VIPA spacing results in some comb modes spanning more than a single pixel. The identification of the center of each comb mode and resulting summing scheme are discussed in the following section on spectrum generation.

A calibration of the lock-in camera was performed by measuring the shot-noise with both a LED and the cw Ti:sapph laser. In both cases, the light was modulated at 10 kHz as the lock-in camera does not measure the DC intensity. Since the readout noise is non-negligible, the noise in counts is the sum in quadrature of the readout and shot-noise contributions,

$$noise = \sqrt{\sigma_{readout}^2 + \frac{1}{C}N} \tag{4.10}$$

where $\sigma_{readout}$ is the readout noise, C is the calibration factor in photons per count and N is the number of counts measured in a single frame. From this, C, the calibration factor, is 3000 photons per count.

Additionally, the maximum number of cycles of demodulation that the camera can perform at 10 kHz is limited to 150. Above this, the camera reads a lower value of the power than it should. Issues of camera saturation arising from 10 kHz electrical pickup necessitated running at between 10 and 50 demodulation cycles per frame so this was not a limitation on the acquisition of data. At 10 cycles of demodulation at 10 kHz, saturation occurs at 100 percent modulation depth with $\sim$ 800 pW on a pixel.

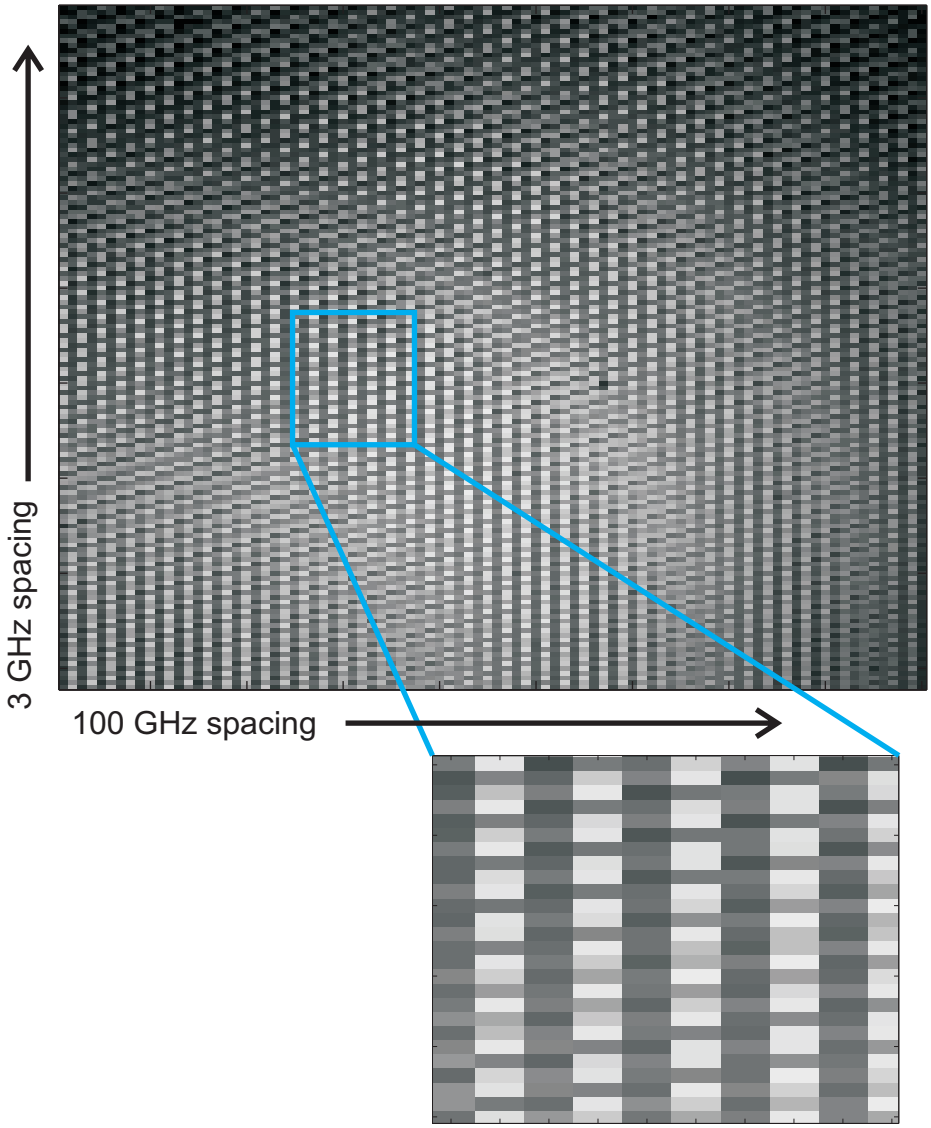

Figure 4.5: Image of the transmitted comb light. The comb modes are spaced by the repetition rate of the comb (2.97 GHz) in the vertical direction and by the FSR of the VIPA (94 GHz) in the horizontal direction. The size of a comb mode is the same as the pixel size and in the horizontal direction the grating resolution was chosen such that each FSR is spaced by one pixel to fit the maximum number of comb modes on the camera. Because of the spacing and the chirp of the spacing due to the VIPA, comb modes are sometimes split across more than one pixel as can be seen in the zoomed in portion of the figure.

4.2.3 Generating a Spectrum

Once a series of images each with comb modes spaced by 2.97 GHz but stepped by 100-200 MHz are acquired, the absorption signal for each comb mode must be extracted from each image and then that information is interleaved to produce a conventional looking velocity-modulation spectrum. The two stages of generating a spectrum are identifying the location of each comb mode on an image and putting the absorption signal from that location into the spectrum. In order to construct a spectrum from the data, the LabView data acquisition program records for each data image acquired: the signal at the discharge frequency (10 kHz) for both clockwise and counterclockwise propagation, a "chopper" image produced by applying a well-calibrated 10 kHz amplitude modulation to the transmitted light for both clockwise and counterclockwise propagation, the wavelength of the cw reference laser from the 30 MHz accuracy wavemeter, and the repetition rate of the comb from a frequency counter. For the data and "chopper" images, the data acquisition program averages over the number of frames and sets of frames taken by the camera, but not the number of demodulation cycles. The "chopper" images allow for the identification of the location of each comb mode as well as the determination of the DC intensity for each comb mode and thus the fractional absorption.

To identify the locations of each comb mode on an image, a global fit to the grid formed by the pixels is used. A global fit is necessary instead of simply counting by a fixed number of pixels from a given starting location due to the chirp in the comb mode spacing. (See Figure 4.5.) The fit starts with a small region and the fit region is expanded to eventually include the whole image for higher polynomial orders. For the full image, in the VIPA direction, the fit to the comb mode positions is quartic and in the grating direction, the fit to the comb mode positions is quadratic. For each region, the fitting program maximizes the sum of the weighted intensity of each predicted mode averaged over the number of predicted modes in that region. The weighting function consists of a quadratic arch centered on the predicted

comb mode location to minimize issues of comb modes split across two pixels. A portion of the global fit is shown in Figure 4.7 (a).

Once the location of each comb mode is known for the first image of the scan, all of the information acquired by the data acquisition program discussed above, in addition to the following, is utilized by a data analysis program to generate the spectrum. In order to compute the appropriate DC intensity, the modulation depth for the AOM that applies the 10 kHz modulation needs to be determined. Since the data acquisition program does not average over the number of demodulation cycles, the number of demodulation cycles[2] for both the data images and the "chopper" images must be input. The output from the global fit program is passed to the data analysis program as a 3-dimensional array of positions on the grid formed by the pixels where first dimension corresponds to an integer VIPA row index, the second dimension corresponds to the grating column index and the third dimension corresponds to the pixel location in either the VIPA or grating direction. As more than one FSR of the VIPA fits onto the camera, the pixel from which we start counting a single FSR can be chosen to avoid portions of the camera that have lower incident power or a poorer fit. In order to determine the absolute frequency of a given comb mode, the position of the cw reference laser on the first image and the value of the beatnote frequency between the cw reference laser and the frequency comb are input. From previous measurements, we know the sensitivity of the camera ($\sim$3000 photons/count) and the FSR of the VIPA (94 GHz).

The analysis program first extracts the appropriate number of comb spots from the global fit output and condense that 3-dimensional array output into a 2-dimensional array of size Lx2, where L is given by the number of comb modes per FSR times the number of columns in the grating direction that contain a full FSR. For each grating column, the code starts counting from the first spot that is above the user-input starting pixel. Because the code draws a flat line from which to start counting, it is important to keep track of whether

[2]For our specific Heliotis lock-in camera, the actual number of demodulation cycles is two less than the nominal value entered into the control program.

the first comb mode location above the start pixel for a given column is above or below the first comb mode location for the previous column. The nuances of keeping track of the comb modes are illustrated in Figure 4.6. Once this operation is completed, the index of the array of grating (x) and VIPA (y) locations corresponds to the relative frequency of each comb mode.

The analysis code also calculates the distance between each neighboring comb mode in the grating (x) and VIPA (y) directions for the first image. For the last comb mode location in each FSR it uses the distance between the previous mode and that mode. Rather than run the global fit code for each individual image, the locations for each subsequent image are interpolated using the distance between comb modes in the first image. The interpolation maps the frequency step taken by the cw laser to a step in pixel position via the following for the mth comb mode:

$$x_{final,m} = \frac{\Delta f}{f_{rep}} * \sqrt{\Delta x_m^2 + \Delta y_m^2} cos(arctan(\frac{\Delta y_m}{\Delta x_m})) + x_{initial,m} \tag{4.11}$$

$$y_{final,m} = \frac{\Delta f}{f_{rep}} * \sqrt{\Delta x_m^2 + \Delta y_m^2} sin(arctan(\frac{\Delta y_m}{\Delta x_m})) + y_{initial,m} \tag{4.12}$$

where $\Delta f = f_{cw,final} - f_{cw,initial}$, f_{cw} is the frequency of the cw reference laser, f_{rep} is the repetition rate of the comb, $\Delta x_m = x_{initial,m+1} - x_{initial,m}$, $\Delta y_m = y_{initial,m+1} - y_{initial,m}$, and m is the index of the comb mode.

For the first image it is also necessary to determine the absolute frequency of one comb mode in addition to the relative frequencies of all the modes determined earlier. To do this, the comb mode at index n that is located closest to the cw laser spot is found. The frequency difference between that comb mode and the cw laser is just the beatnote frequency, $f_{beatnote}$. Frequencies can then be assigned for every data point. The frequency of the mode with index m, for image i, is given by

$$f_{i,m} = (m - n) * f_{rep,i} + f_{cw,i} + f_{beatnote} \tag{4.13}$$

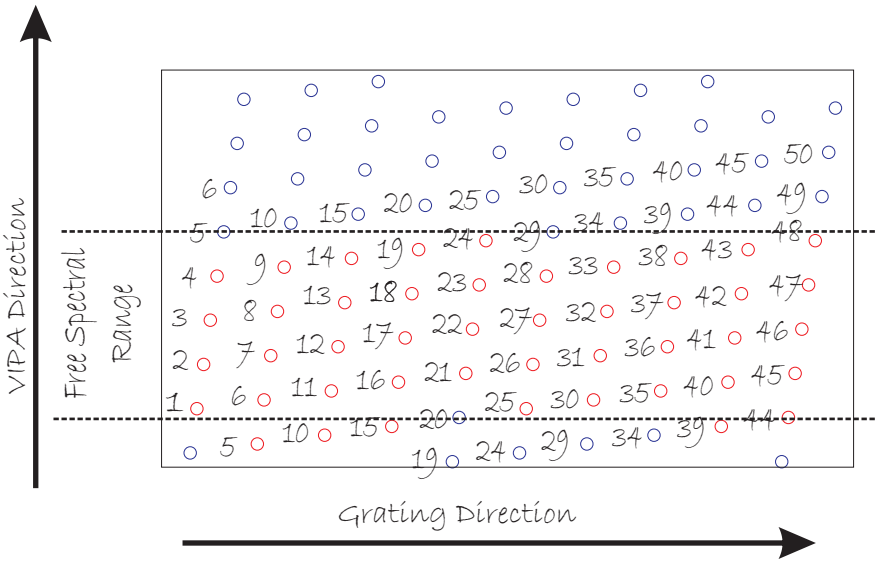

Figure 4.6: Sketch of selection of comb modes by spectrum generator code. In this simplified example, four comb modes fit within one free spectral range of the VIPA and the free spectral range is not an integer multiple of four leading to the chirp in the location in the VIPA direction. The red and blue circles represent the comb mode locations. The number adjacent to that comb mode represents the frequency offset of that mode scaled by the repetition rate. The red circles represent the locations of the comb modes which would be concatenated by the spectrum generator code.

where $f_{cw,i}$ is the frequency of the cw laser for that image and $f_{rep,i}$ is the repetition rate of the comb for that image.

The intensity for a given comb mode is determined by the sum over one to four pixels depending on the center of the mode with respect to the center of the pixel. If the center of the comb mode is in the left half of the pixel, the intensity is summed over that pixel and one pixel to the left in the grating direction. Likewise, if the center is in the right half of the pixel, the intensity is summed over that pixel and one pixel to the right in the grating direction. If the center is in the bottom 40% of the pixel, the intensity is summed over that pixel and one pixel below in the VIPA direction, and if the center is in the upper 40% of the pixel, the intensity is summed over that pixel and one pixel above in the VIPA direction. If the center is in the middle 20% of the pixel, just that pixel is summed over in the VIPA direction. The intensity at 10 kHz and the DC intensity are then given by the resulting double sum. After summation over the appropriate number of pixels, the intensity at 10 kHz is normalized by the DC intensity.

After normalizing the intensity, a running median is calculated for each image to remove noise that is common across neighboring comb teeth. The width of the range over which to calculate the median is determined via a user input and is typically 6 comb modes. Note that this is for each image, so that those 6 comb modes would span $\approx$ 18 GHz, which is much wider than any features we are trying to retain. The raw data and running median are shown for a test of our system with a N_2^+ band in Figure 4.7. Note that the high points in Figure 4.7 (b) correspond to N_2^+ absorption and are not removed by the median subtraction. After median subtraction, the spectra with $\sim$ 3 GHz spacing for each image are interleaved together. At this point, additional smoothing across neighboring frequencies can also be applied, which now reflects smoothing across points from different images. The final product as well as several intermediate steps of the spectrum generation are shown in Figures 4.7 and 4.8.

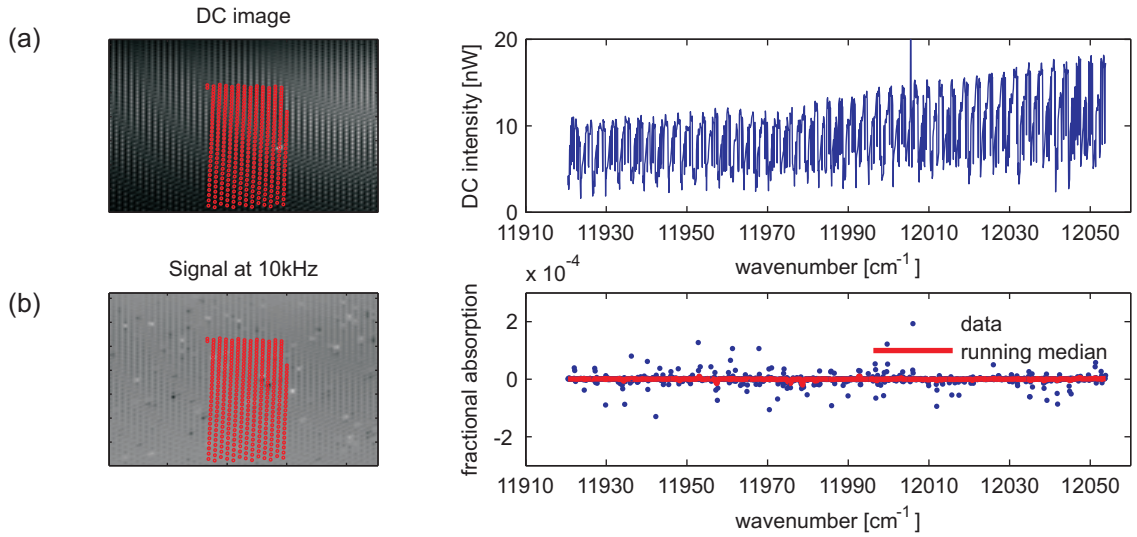

Figure 4.7: Data Analysis Part 1. (a) The DC intensity is shown as the initial 2-dimensional image, which is then fit to obtain the comb mode positions as shown in red circles over part of the image. This fit calibrates the DC intensity as a function of the comb frequency, which is shown on the right. An additional 10 kHz amplitude modulation was applied to the transmitted light to measure the DC intensity. In (b) the signal at 10 kHz (with only the discharge modulation) is shown for one image. The red circles on the two-dimensional image are the positions of the comb modes determined from the global fit to the DC intensity in (a). Note the bright and dark pixels, which represent the spectral signature of nitrogen absorption. The difference between the clockwise and counterclockwise signal extracted from the fit for one image is also shown with the points spaced by the repetition rate of the comb. The running median plotted with the data is subtracted from each image before they are interleaved.

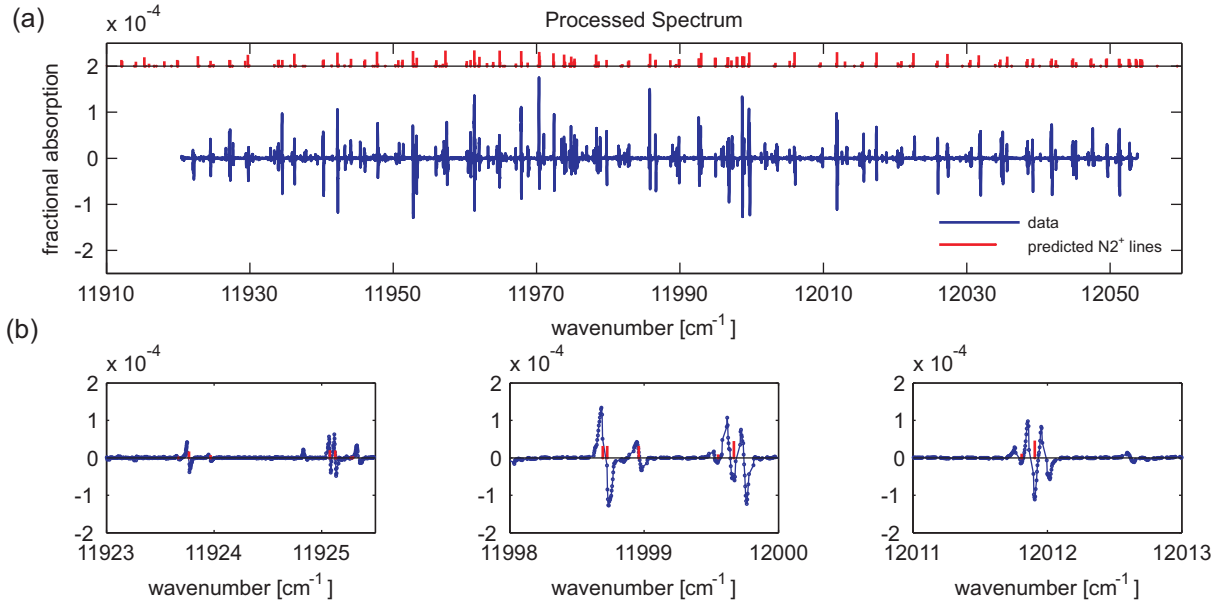

Figure 4.8: Data Analysis Part 2. The resulting processed spectrum (blue) from all the images (each processed similarly but with stepped cw laser frequency) is shown in (a). The predicted positions from molecular constants reported by Collet et al. [4] for the (4,2) N_2^+ band (red) are also shown in (a). The full recorded spectrum was acquired in 20 images with 1500 simultaneous channels in less than one hour, with a sensitivity of 3 x 10^{-7} fractional absorption per detection channel. The zoomed-in panels (b) show three different portions of the spectrum with data points indicating the actual sampling period.

4.2.4 Control of the Frequency Comb

A cw Ti:sapphire laser serves as a frequency reference for stabilizing the comb and provides a marker on the two-dimensional spectral image. The cw laser is locked to its internal reference cavity, and feedback to the comb's repetition rate locks a comb mode to the cw laser. The comb mode referenced to the cw laser is controlled by acting on both the comb laser cavity length (slow feedback via a PZT) and the pump power (fast feedback via an acousto-optic modulator) [61, 62]. The comb is not fully fixed because only one degree of freedom is locked, because the feedback mostly drives the repetition rate, the offset frequency is essentially left free running. The enhancement cavity is then locked to the comb via a dither lock (at 50 kHz) using the spectrally filtered reflection from the cavity. The enhancement cavity length is controlled by both a fast PZT mounted directly to one of the cavity mirrors following Briles et al [63] to achieve high bandwidth and a slow, long travel PZT mounted inside a translation stage to keep the cavity length in range of the fast PZT. We found it critical to feed forward a 10 kHz compensation voltage onto the lock of the enhancement cavity to compensate for the 10 kHz electrical pickup from the discharge, an effect seen in other cavity-based velocity-modulation experiments [51] as well. A detailed schematic of the optical layout is shown in Figure 4.12.

In Figure 4.9, the repetition rate of the comb is shown over the acquisition of multiple images to form a fully sampled spectrum. Since a single comb mode with frequency, $f_n = f_0 + n * f_{rep}$, is locked to the cw laser, the repetition rate change gives a measure of the drift of the carrier-offset-frequency, f_0, which is left free-running. From the noise in f_{rep} during a single measurement (lower panel Figure 4.9), we can determine the amount of uncertainty in the frequency of a comb mode that is m modes away from the comb mode that is locked to the cw laser. With 1500 comb modes in a single image and the cw reference always on the image as a marker, the maximal uncertainty is $\sim$ 300 kHz for a comb mode that is 1500 comb modes away from the fixed reference given the 200 Hz level fluctuations in f_{rep}, which

is well below the 30 MHz resolution of the wavemeter used to determine the frequency of the cw laser.

To achieve this level of quietness of f_0, control of the air currents around the pump beam and control of the cooling water flow through the comb laser were both necessary. A box was placed around the pump beam to reduce air currents. Appropriate cooling water flow further reduced the fluctuations in the repetition rate from 1-2 kHz to 100-200 Hz over the course of a measurement. A flow gauge and valve were installed on the chiller for the comb. The flow was lowered until the noise on f_{rep} when a comb mode was locked to the cw laser was no longer reduced. Reducing the flow too much causes inadequate cooling and long-term thermal drifts. Minimizing the drift in the offset frequency is necessary not only for accurate wavelength metrology, but also to keep the transmitted spectrum the same over the course of a measurement, especially over the timescale of switching directions.

4.3 Noise and the Sensitivity of the System

With the discharge running, 10 kHz electrical pickup, while minimized as much as possible by placement and isolation of the discharge electronics, remains a problem. A 10 kHz compensation voltage is fed forward onto the lock of the enhancement cavity to compensate for this. Despite this, residual 10 kHz noise from the discharge is present on the cavity transmitted light due to incomplete cancelation by the feed-forward mechanism resulting in baseline offsets. These offsets arise from frequency-to-amplitude-noise conversion in the enhancement cavity. Since the offsets have common values across neighboring comb modes, they are removed by subtracting the median value across a number of neighboring comb modes. This method of rejecting common mode noise, inherent in this comb-based spectroscopy, is not available for conventional cw systems.

The technical noise in our current system, due to incomplete common-mode noise rejection, lies above the readout noise on the camera, which in turn lies above the shot-noise limit. A summary of the relative contributions of the technical, camera, and shot-noise for

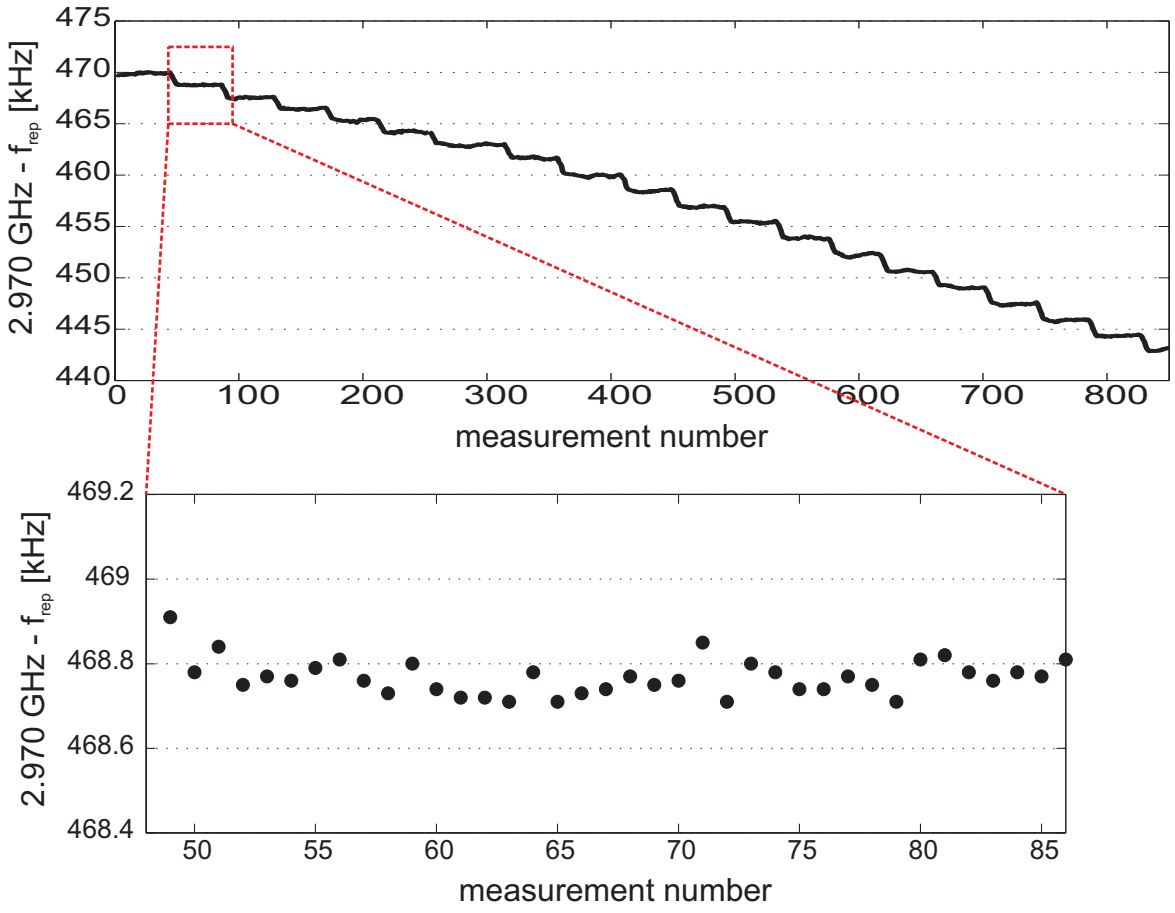

Figure 4.9: Repetition rate of the frequency comb during data acquisition. Each flat plateau occurs during a measurement of the 1500 simultaneous channels. The repetition rate is then stepped by scanning the cw laser such that each comb mode with frequency $f_n = f_0 + nf_{rep}$ is scanned over 3 GHz to fully sample the spectrum. As $n \sim 10^5$, stepping f_{rep} by 30 kHz steps the comb mode frequency by 3 GHz. In the lower panel, the fluctuation of f_{rep} during a single measurement is shown. The 200 Hz drift in f_{rep} corresponds to a maximal 300 kHz uncertainty in the comb modes not locked to the cw laser, which is well below the 30 MHz resolution of the wavemeter.

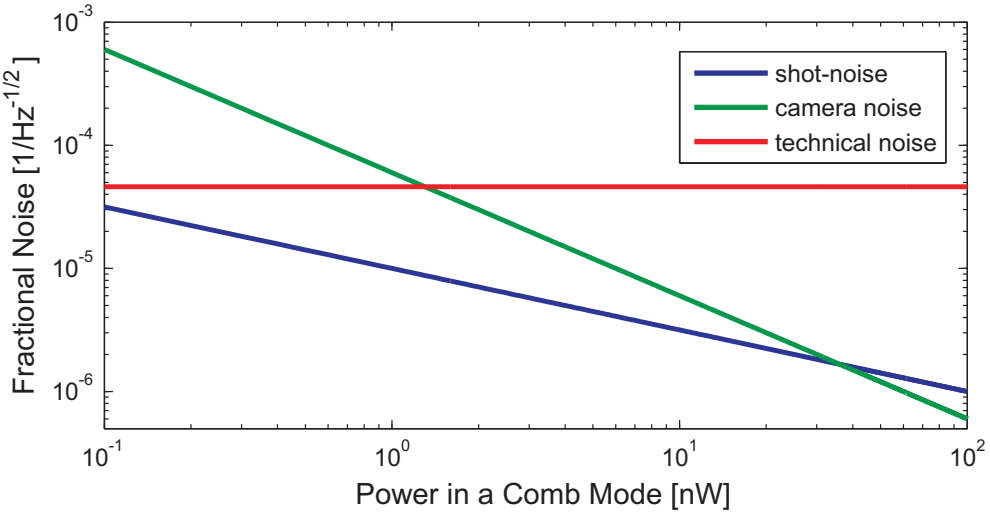

Figure 4.10: Noise contributions as a function of the power in a comb mode. The HfF^+ data was acquired with comb mode powers ranging from 1 nW to 20 nW. The sensitivity of the system is given by the fractional noise divided by a factor of 30 due to the enhanced path length. The values for the camera noise and technical noise are for switching rapidly, $\sim$ 3X s^{-1}, between clockwise and counterclockwise directions of propagation as single direction measurements stopped averaging down at $\sim$ 1 Hz bandwidth. (Actual time to switch directions is $\sim$ 1 ms, 300 ms is the time for data acquisition.)

varying comb mode powers is shown in Figure 4.10. Note that the sensitivity of the system is given by the fractional noise divided by $\mathscr{F}/\pi \sim 30$ as discussed earlier. Initial measurements of the noise with the light traveling in a single direction of propagation through the cavity did not average down for bandwidths below 1 Hz. Similar problems were seen in the camera noise as measured across different pixels with no light incident on the camera. By rapidly switching between clockwise and counterclockwise beam propagation through the ring cavity via polarization control and subtracting the two images, we are able to reduce the impact of drifts in the gain of each individual pixel on long time scales, remove other common mode noise, and further increase the rejection of neutral molecular signals while retaining the ion absorption signals.

Our achieved sensitivity is 3 x 10^{-7} single-pass fractional absorption for each measurement channel, with 1500 simultaneous channels covering 150 cm^{-1}, corresponding to 4 x 10^{-8} $Hz^{-1/2}$ (spectral element)$^{-1/2}$ absorption sensitivity. One full spectrum, consisting of 30 interleaved images takes 30 minutes to acquire. For other high-accuracy cw-laser velocity-modulation experiments using cavity-enhancement, the sensitivity is $\approx 10^{-5}$ [51], which is much lower than our current sensitivity due to the additional common-mode noise-suppression discussed earlier. We note that for a cw laser system to achieve the same level of sensitivity across the spectral bandwidth we cover in a single acquisition, it would need a sensitivity of 4 x 10^{-8} $Hz^{-1/2}$ and the ability to scan across 150 cm^{-1} continuously.

4.4 A Thousand of Wavenumbers of HfF^+

As a diagnostic tool, the fluorescence from the plasma in the discharge tube was imaged behind one of the high reflectivity cavity mirrors into a fiber collimator leading to a grating spectrograph (OceanOptics). The spectral region of fluorescence imaged was limited to wavelengths below the coating curve of the cavity mirror. By looking at the changes in fluorescence, we could tell when the oven was running low on HfF_4. Additionally, this was a more sensitive test of small leaks than the pressure gauge on the system due to the easily

identified N_2 signature. The spectral signature of a Helium-only discharge, a discharge with $\sim$ 10% N_2 present, and a discharge with the oven hot with HfF_4 present can be seen in Figure 4.11.

For the following spectra, a 2.5 meter long bow-tie enhancement-cavity with a finesse of 100 surrounds a 1 meter long discharge tube, which is driven at 10 kHz with $\approx$ 400 mA_{pk-pk}. The discharge tube contains HfF_4, which is heated to 800 K, and helium buffer gas is flowed through the discharge tube such that the total pressure is 5 torr. A Gigaoptics 3 GHz repetition rate Ti:saphhire comb is coupled into the 120 MHz free-spectral-range enhancement-cavity traveling either clockwise or counterclockwise around the bow-tie cavity, with every 25^{th} cavity resonance matched to a comb mode. Spectral filtering of the cavity due to group velocity dispersion (GVD) limits the transmitted bandwidth to 300 cm^{-1}. The windows on the discharge tube are at Brewster's angle to minimize intra-cavity loss and are thin to reduce GVD. A schematic of the system is shown in Figure 4.12.

A summary of the entire spectral region covered with multiple scans is shown in Figure 4.13. Multiple overlapping scans, taken across the whole region, were interpolated onto a 0.001 cm^{-1} grid and then averaged together. For each scan, the fluorescence from the discharge tube was monitored to ensure that HfF^+ was present. Additional scans with the oven off were taken in the regions in which molecular bands were seen as an initial check that they arose from HfF^+. From Figure 4.13, two obvious bands can be seen as well as a number of isolated sharp features that are most likely atomic transitions. In the region with the two obvious bands, we have identified four different HfF^+ bands as shown in Figure 4.14 with $\sim$ 150 as yet unidentified presumably HfF^+ lines in the same region as the four identified bands. The fits to all four bands are discussed in detail in Chapter Five. The lower panels in Figure 4.14 show the characteristic velocity-modulation lineshape of the HfF^+ lines. The structure around the strong lines is not the noise floor but additional HfF^+ lines. The fractional noise for the region with the HfF^+ bands was $4x10^{-8}$ $Hz^{-1/2}$ (spectral element)$^{-1/2}$ as can be seen in Figure 5.1 in Chapter Five.

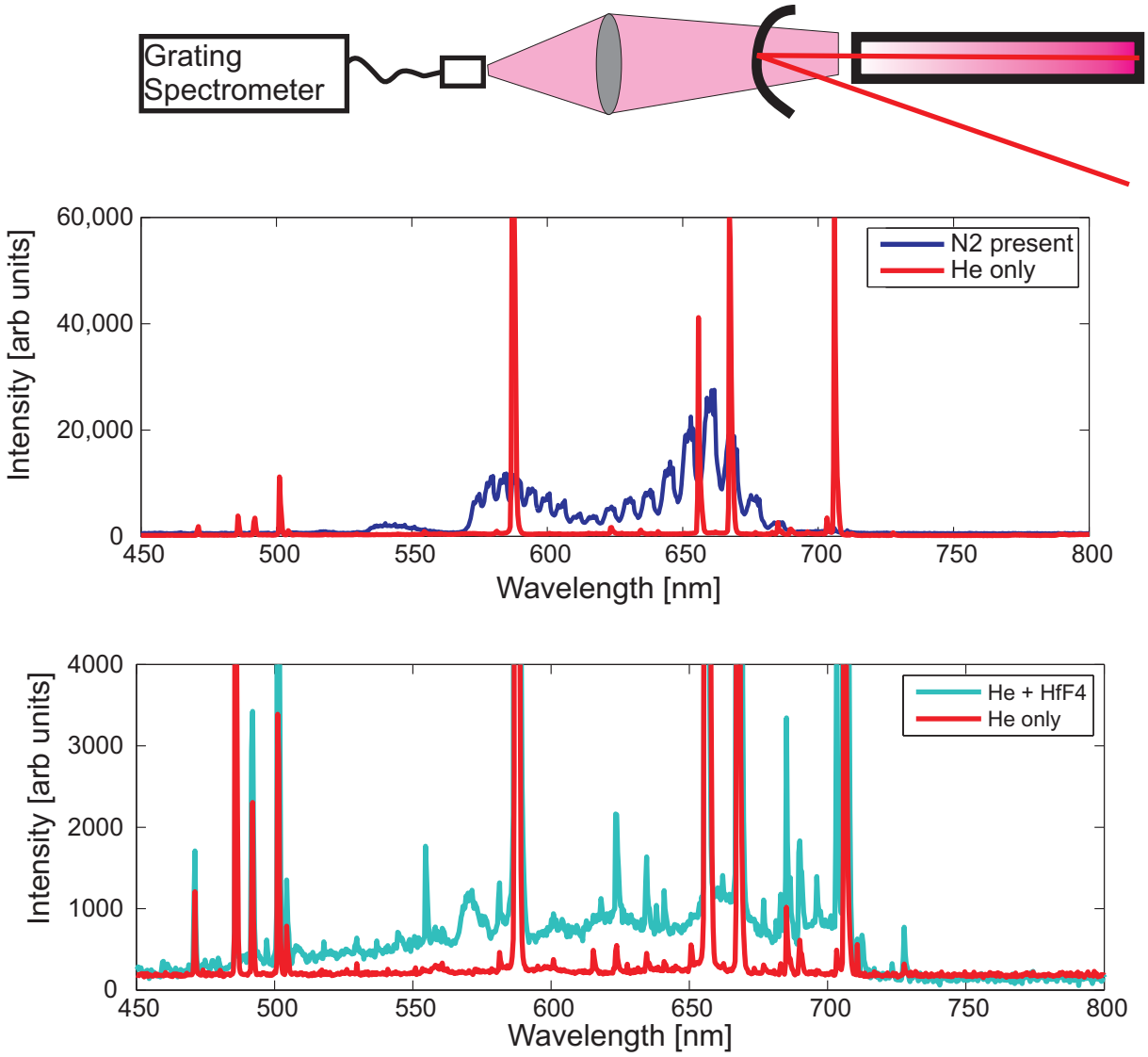

Figure 4.11: Fluorescence from the discharge as a diagnostic tool. The light from the center of the discharge tube passes through the mirror if it is below $\sim$ 700 nm and is focused into a fiber connected to the grating spectrometer. (a) N_2 signature versus a He only discharge. The sharp spikes in the He only case are atomic He transitions. Note the suppression of the He fluorescence when large amounts of N_2 are present. The clear N_2 signature can also be used when checking for leaks as it is quite distinctive albeit smaller even for significantly lower partial N_2 pressures. (b) Spectral signature the corresponds to the presence of HfF^+ is the broad background lifting off of the baseline. The additional sharp features are mostlhy atomic transitions of fluorine.

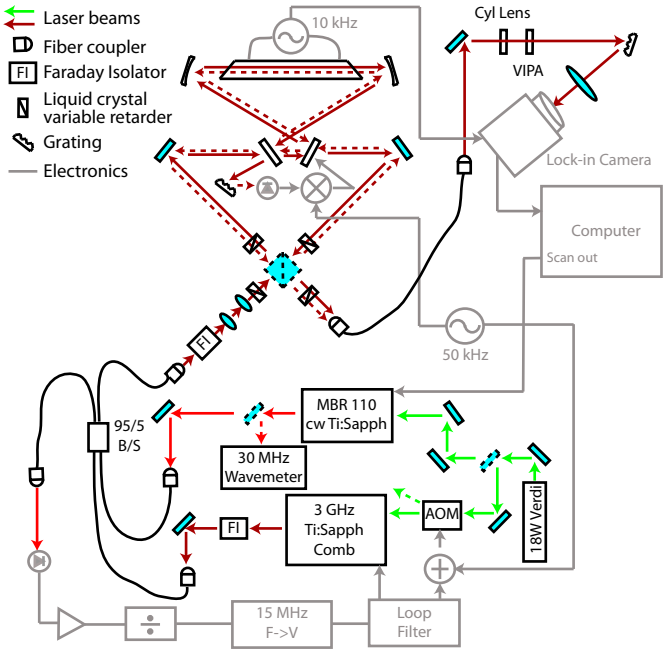

Figure 4.12: Schematic of the system. An 18 W Coherent Verdi pumps both the CW Ti:Sapphire laser, used as a frequency reference, and the 3 GHz repetition rate Ti:Sapphire comb. The CW laser is read by a wavemeter with an accuracy of 30 MHz. The comb is referenced to the CW laser via a beatnote with a single comb tooth. Feedback to the comb's repetition rate is achieved through the pump power (high bandwidth and small range) and through the comb cavity length (low bandwidth and large range). 95% of the comb light and 5% of the CW light are combined in a fiber which is coupled to the enhancement cavity. Liquid crystal retarders and a polarizing beam splitter are used to select the direction of light propagation around the enhancement cavity while maintaining all locks. The enhancement cavity is locked to the comb. Cavity transmitted light is dispersed by the 2-dimensional imaging system, qualitatively sketched in Fig. 4.6, and recorded by the lock-in camera, which demodulates each pixel at the discharge modulation frequency. The CW light serves as a reference marker on the lock-in camera image.

Although the scanned region covers from 11,700 cm^{-1} to 12,700 cm^{-1} no additional HfF^+ bands were seen outside the 12,100 to 12,300 cm^{-1} region. An additional unidentified band was seen around 12,400 cm^{-1}, but it was present with HfF^+ absent (oven shut off). At the edges of the scan range, the lower comb power resulted in higher fractional readout noise and a less stable lock which caused the fractional noise to increase as can be seen in Figure 4.13. To increase the spectral bandwidth covered, the frequency comb would need to be broadened and the intensity of each comb mode on the camera would need to be increased. Different options for doing this are discussed briefly in Chapter Six.

4.5 Coherent Subtraction

An additional way to increase signal-to-noise is to use coherent subtraction; i.e., using a balanced Sagnac-type interferometer as shown in the blue inset to Figure 4.16. With a ring cavity, it is possible to have counter-propagating beams through the sample and to cancel common-mode noise at the output of the dark port of the resulting interferometer. The signal-to-noise using coherent subtraction increases as the splitting ratio approaches 50% between the two beams until camera readout noise or shot-noise dominates. Figure 4.15 shows the improvement in signal-to-noise ratio as a function of splitting ratio when the common mode technical noise dominates the noise. We have tested coherent subtraction versus a single direction of propagation using a photodiode and single-channel lock-in detector with our CW laser and demonstrate a factor of 10 gain in the signal-to-noise (Figure 4.16). Coherent subtraction, unlike counter-propagating beams in a multipass cell, is sensitive to phase as well as amplitude of the light field; thus, the resulting lineshape is dependent on both absorption and dispersion and can vary if there are additional differential phase shifts between the two directions. These phase shifts in effect change the relative sensitivity to absorption and dispersion. We have made a simple model (dashed lines in Figure 4.16) that reproduces the lineshape modification. In our current experiment, the power per comb mode is too low for us to take advantage of this coherent subtraction approach, but this problem

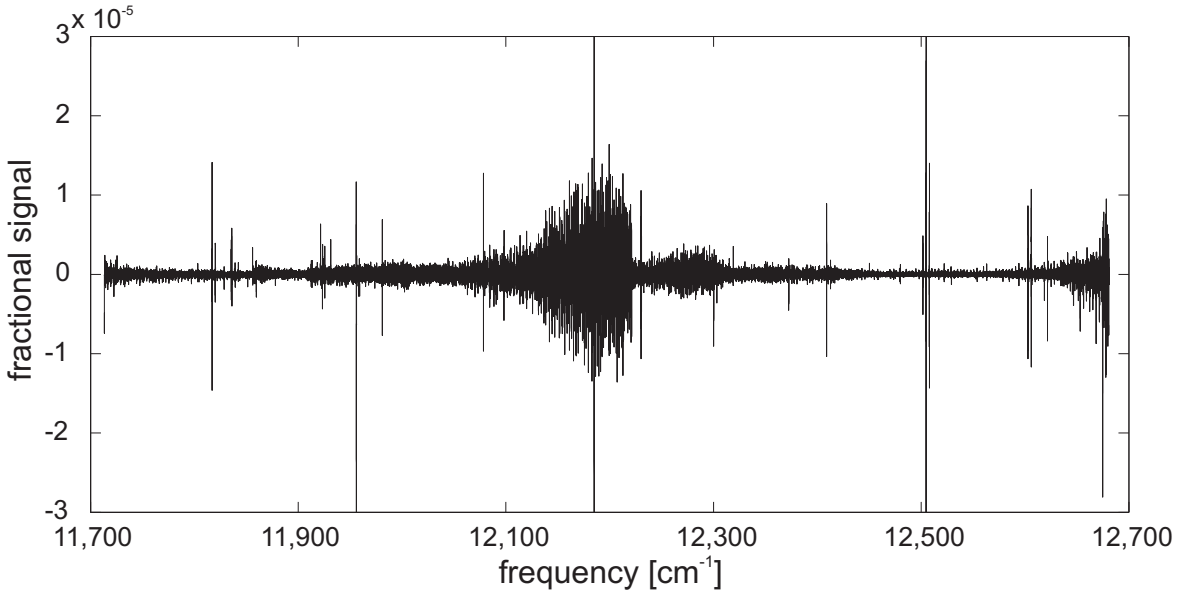

Figure 4.13: Full spectral region scanned with HfF^+ present. There are four HfF^+ bands that have been identified so far and these are highlighted in Figure 4.14. The isolated sharp features are most likely due to atomic transitions. The increased fractional signal at both edges is due to the camera noise starting to be the dominant noise source due to the decrease in comb power at the edges of the comb bandwidth. This summary plot was generated by interpolating multiple scans onto a 0.001 cm^{-1} grid and then averaging them together.

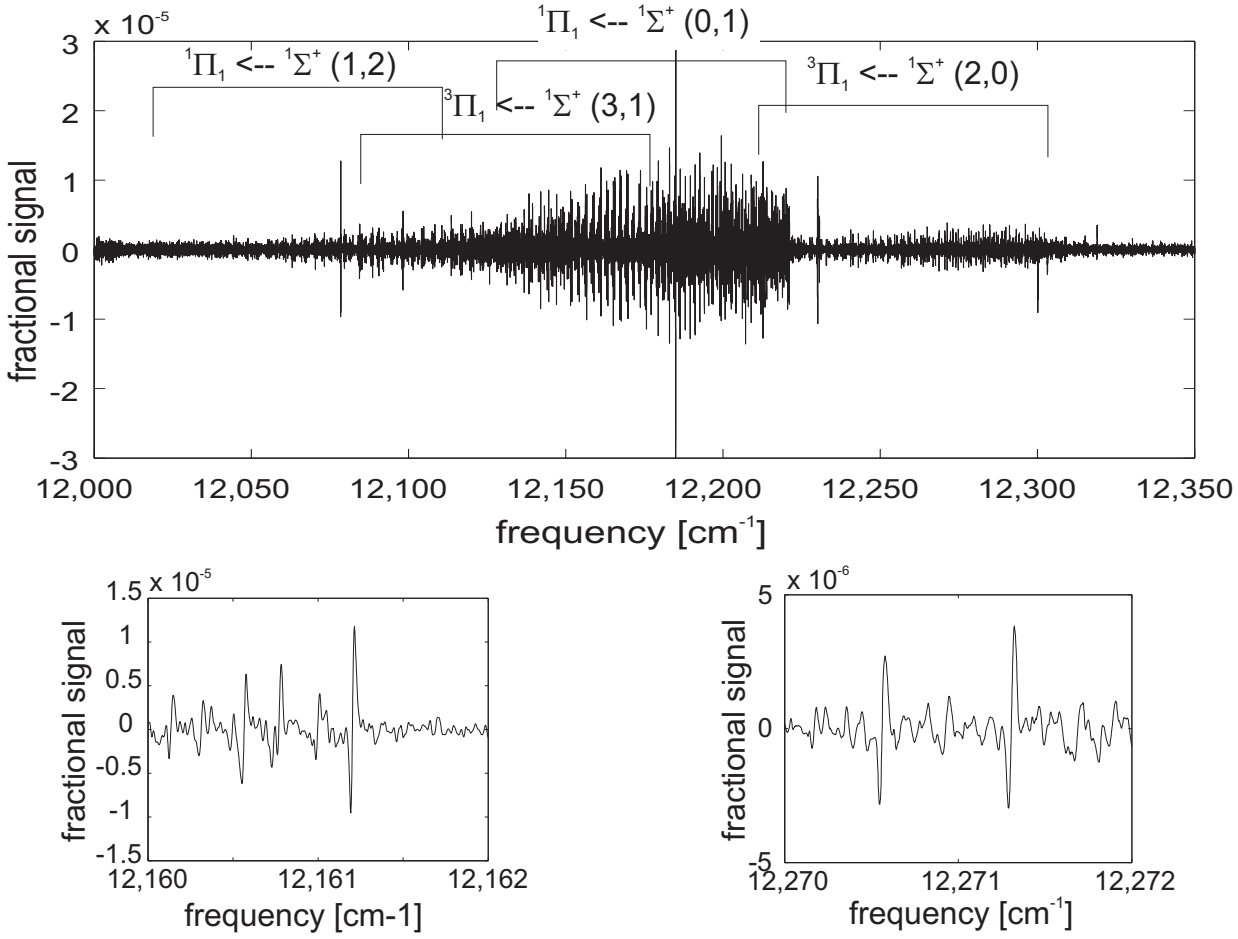

Figure 4.14: Region of spectrum with HfF^+ lines with smaller regions showing the characteristic velocity-modulation lineshape. Fits to the bands identified are discussed in Chapter Five. In the lower plots, the structure surrounding the strongest lines is due to additional HfF^+ molecular absorption. The fractional sensitivity measured without HfF^+ present is $3x10^{-7}$.

could be overcome in the future by using either a more sensitive camera or a comb with more power.

The lineshape simulations used to model the data in the coherent subtraction scheme were done by applying a cosine modulation in time to the center frequency for both the absorption (assumed Gaussian lineshape) and dispersion terms (obtained via Kramers-Kronig) and then taking the cosine transformation and selecting the appropriate modulation harmonic. This was done at a variety of laser frequencies to generate the lineshape. The amplitude and linewidth of the single direction simulation was scaled to the measured value and this value was fed into the coherent subtraction simulation. The constant phase offset (most likely due to the beamsplitter) added to the coherent subtraction simulation was chosen to fit the measured lineshape (about $\pi/20$ radians). The beamsplitter intensity splitting ratio between transmission and reflection was 52%/48%.

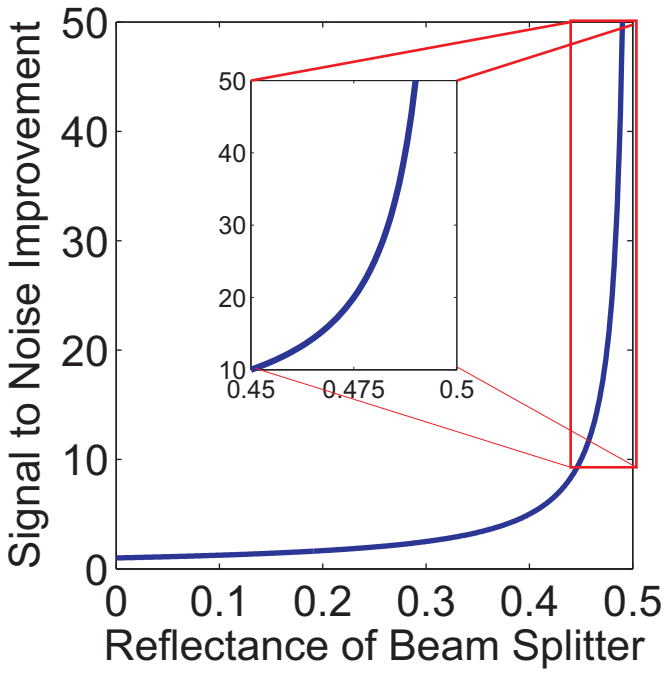

Figure 4.15: Improvement of signal-to-noise ratio as a function of splitting ratio. The signal-to-noise ratio improves dramatically as the intensity for the two directions of propagation becomes more similar as long as common-mode technical noise dominates the noise. If the single direction measurements are dominated by the shot-noise, the signal-to-noise ratio for coherent subtraction is the same as single direction propagation. If the camera noise begins to dominate due to the decrease in power as the splitting ratio approaches 50%, the signal-to-noise ratio will decrease. The challenge of achieving a splitting ratio of better than 52%/48% also limits the gains in signal-to-noise ratio improvement.

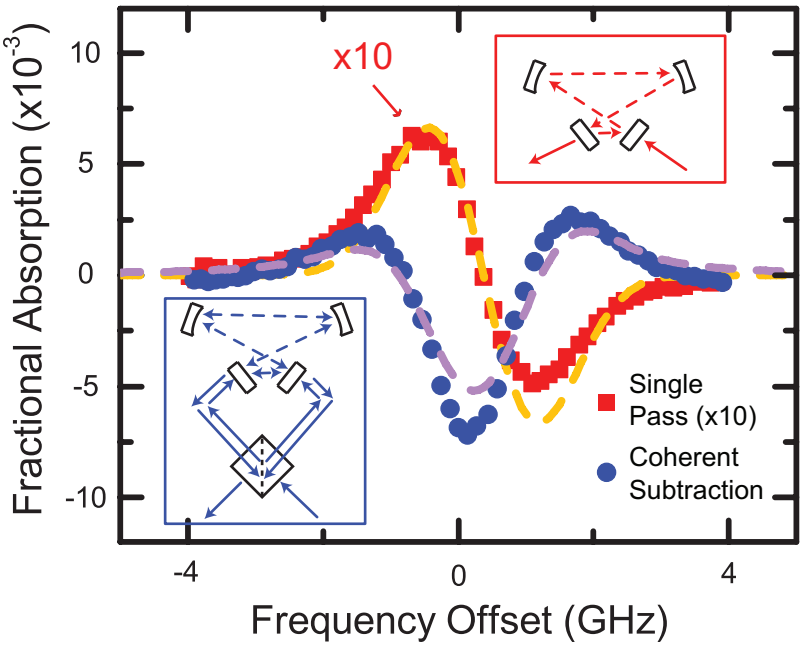

Figure 4.16: Comparison of coherent subtraction and single direction measurements The signal to noise for coherent subtraction (using a 52/48 beam splitter) surpasses that of single direction measurements by a factor of 10 in cases where we have sufficient optical power to dominate over the camera readout noise. Both measurements of a single N_2^+ line were made with the cw Ti:Sapphire laser. The dashed lines are a calculation of the expected lineshape. The slight modification in the lineshape for the coherent subtraction is due to an additional differential phase shift of approximately $\pi/20$ between the two counter-propagating beams.

Chapter 5

HfF^+ Structure[1]

Currently, five different bands of HfF^+ have been identified; one with single-frequency velocity-modulation spectroscopy, discussed in Chapter Three, and four with the frequency comb velocity-modulation system described in Chapter Four. The full spectrum acquired with the frequency comb velocity-modulation system can be seen in Figure 4.13, with Figure 5.1 showing the four bands we have identified so far; the fifth band acquired with single-frequency velocity-modulation spectroscopy can be seen in Figure 3.5 and Figure 3.6. Furthermore, we have a collection of as yet unassigned lines in the midst of the other bands in the frequency comb velocity-modulation data, indicating the presence of at least one more band at around 12200 cm^{-1}. As illustrated in Figure 5.1, the spectrum from about 12100-12300 cm^{-1} is extremely congested due to the presence of many bands, each with five isotopes, and the high temperature of our oven, which results in observed J″ values up to about 70. The power of frequency comb velocity-modulation spectroscopy is demonstrated by our ability to identify the overlapping $^1\Pi_1 - {}^1\Sigma^+(0,1)$ and $^3\Pi_1 - {}^1\Sigma^+(3,1)$ bands despite the difference in linestrengths and an offset in band origin of only $\sim$1 cm^{-1}. This chapter will discuss the fits to each of the bands and the molecular constants that can be extracted from them.

[1]Much of the discussion on the structure of HfF^+ will be discussed in a forthcoming publication from K.C. Cossel et al.

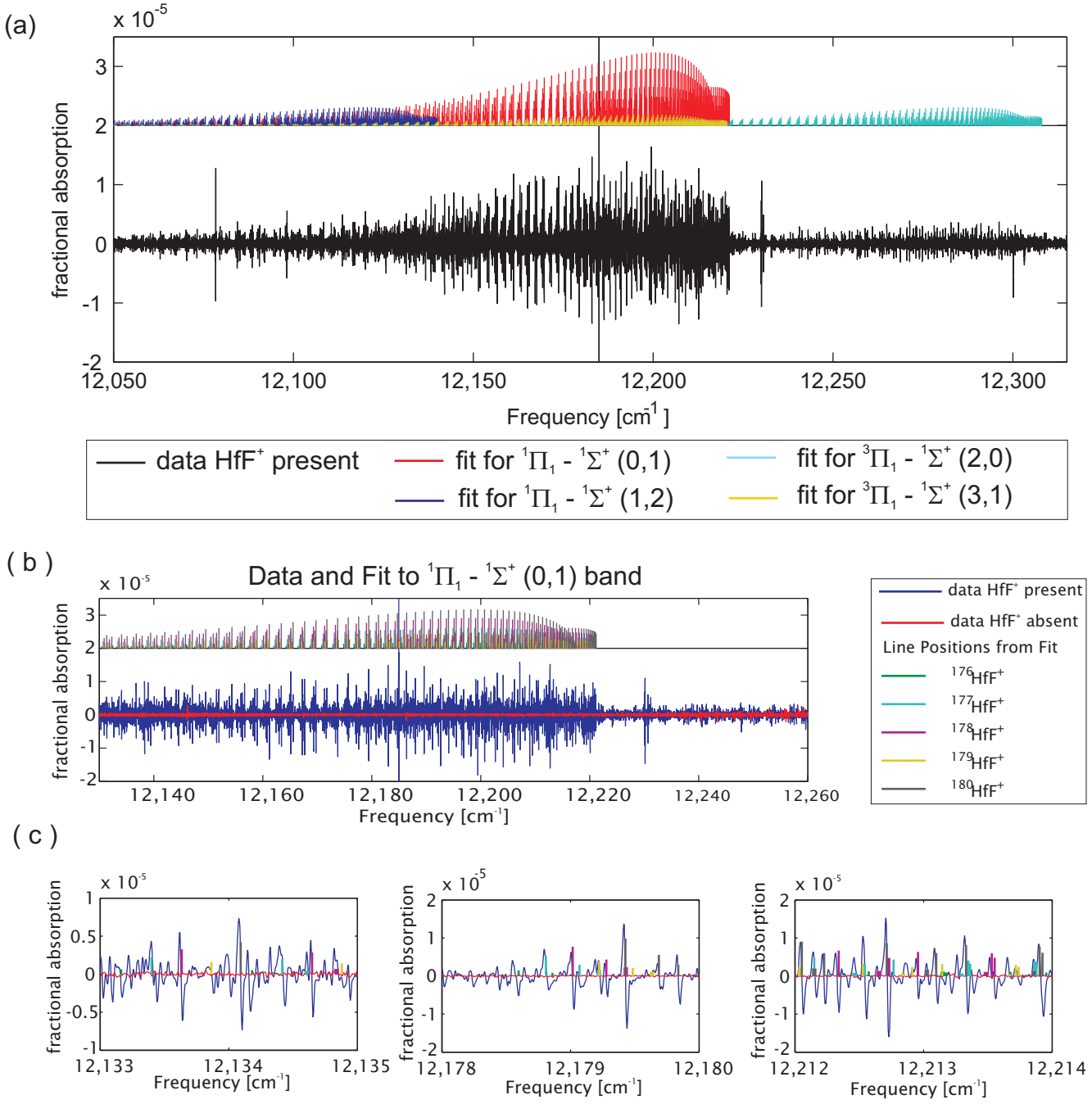

Figure 5.1: (a) Data and fits to the four HfF^+ bands identified with frequency comb velocity-modulation spectroscopy. Linestrengths for the fit positions are scaled by isotopic abundance, by an approximate rotational temperature of ~ 640 K, and by an overall transition strength to match the measured fractional absorption. (b) Region of the recorded spectra containing the $^1\Pi_1 - {}^1\Sigma^+(0,1)$ band as well as at least three other HfF^+ bands with the fit for the $^1\Pi_1 - {}^1\Sigma^+(0,1)$ band offset for clarity. (c) All five isotopes of HfF+ are present and resolved for transitions with $\Delta v \neq 0$. The additional structure with HfF^+ present (blue) consists of lines belonging to the other HfF^+ bands while the red line (HfF^+ absent) shows the level of sensitivity of the system in this region.

5.1 Fits to HfF^+ Bands

We fit each band with the energy expression,

$$E(J'', J') = \nu_0 + (B' - \frac{P}{2} * (p + 2q))J'(J' + 1) + (D' - \frac{P}{2} * (p_D + 2q_D))J'^2(J' + 1)^2 \quad (5.1)$$

$$- B''J''(J'' + 1) - D''J''^2(J'' + 1)^2 \quad (5.2)$$

where B′ and B″ are the rotational constants for a given vibrational level of the upper and lower state, D′ and D″ are the centrifugal distortion terms for a given vibrational level of the upper and lower state, $(p + 2q)$ is the Ω-doubling of the excited state [34] with $(p_D + 2q_D)$ the next higher-order of the Ω-doubling, and P is a parity term with $P = -1$ for $\Delta J = 0$ and $P = 1$ for $\Delta J = +/ - 1$. A summary of the fitted constants for each band is given in Table 5.1 and the molecular constants that can be derived for the states observed are given in Table 5.2. For the bands for which the centrifugal distortion term is consistent with zero due to a sufficiently large uncertainty, the corresponding higher-order term of the Ω-doubling was not included in the fit.

All five isotopes of Hf were resolved for transitions with $\Delta v \neq 0$ allowing for the extraction of molecular constants for a particular isotope. The rich isotope structure also yielded the change in vibrational quantum number for those bands. For the $^1\Pi_1$–!$^1\Sigma^+$ (0, 0) band, we were not able to fully resolve the isotope structure as discussed in Chapter Three. Therefore, we fit to estimated line centers and scaled the fitted constants by the reduced masses and isotopic abundances to obtain the final constants in Table 5.1. For this band we were able to establish that $\Delta\Omega = 1$ since we observed an R(0) line but no P(1) line, as can be seen in Figure 3.6. For the other four bands, the congestion of the spectrum prevented a similar confirmation of the values of Ω for the upper and lower states.

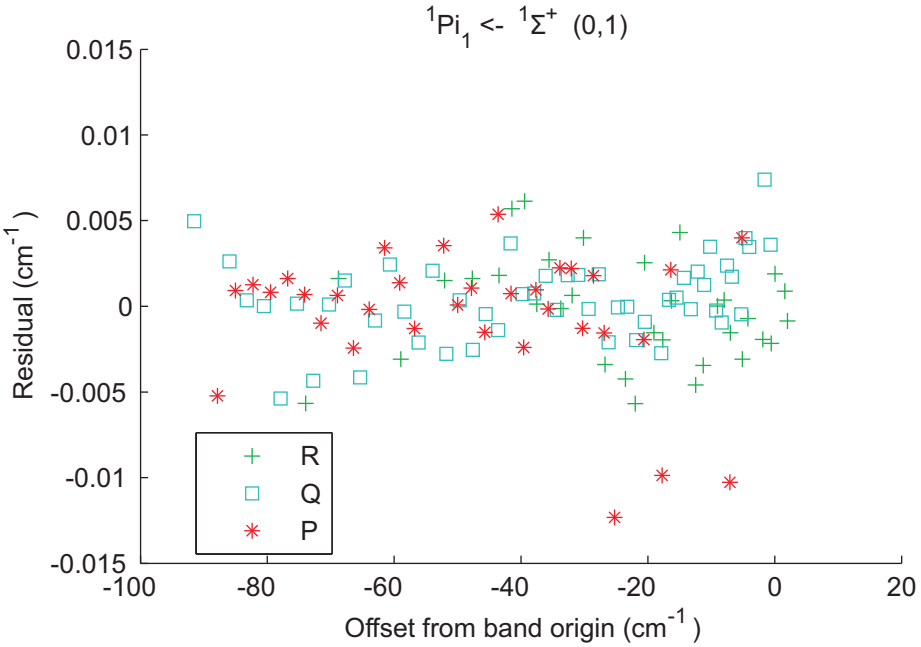

Figure 5.2: Residuals from the fit to the $^1\Pi_1 - {}^1\Sigma^+(0,1)$ band of $^{180}HfF^+$. The fit spans $\sim$100 cm^{-1} reaching J values as high as 70 due to the high rotational temperature. This fit provides high accuracy in the determination of the molecular constants.

Table 5.1: Fitted constants for observed transitions in $^{180}HfF^+$. Quoted uncertainties are 95% except for the $^3\Pi_1 - {}^1\Sigma^+(3,1)$ transition for which uncertainties are quoted at the level for which the manual fit would noticeably fail. Note that the values for the $^1\Pi_1 - {}^1\Sigma^+$ (0,0) transition were extracted from a fit to the average line positions as the individual isotopes are not fully resolved as discussed in Chapter Three. $^\circ$ $^3\Pi_1 - {}^1\Sigma^+(3,1)$ values assigned using a manual fit due to challenges of determining the line centers of the weaker lines in the dense spectrum. *Value fixed to the fitted value from the $^1\Pi_1 - {}^1\Sigma^+(0,1)$ transition. $^+$Isotope averaged value with the error due to the uncertainty in the electronic isotope shift.

	$^1\Pi_1 \leftarrow {}^1\Sigma^+(0,1)$	$^1\Pi_1 \leftarrow {}^1\Sigma^+(1,2)$	$^3\Pi_1 \leftarrow {}^1\Sigma^+(2,0)$	$^3\Pi_1 \leftarrow {}^1\Sigma^+(3,1)^\circ$	$^1\Pi_1 \leftarrow {}^1\Sigma^+(0,0)$
ν_0 [cm^{-1}]	12217.698(2)	12136.012(3)	12304.400(3)	12216.87(1)	13002.229(6)$^+$
B″ [cm^{-1}]	0.30335(3)	0.30180(5)	0.30481(4)	0.30335*	0.30474(20)
B′ [cm^{-1}]	0.28115(3)	0.27973(5)	0.28096(4)	0.27958(20)	0.28104(20)
D″ [10^{-7} cm−1]	1.88(8)	1.80(14)	1.78(12)	1.8(2)	1(2)
D′ [10^{-7} cm^{-1}]	1.81(8)	1.74(14)	1.78(11)	1.8(2)	1(2)
(p+2q) [10^{-4} cm^{-1}]	3.69(2)	2.68(4)	-3.82(1)	-3.8(2)	3.55(4)
(p_D+2q_D) [10^{-9} cm^{-1}]	9.7(7)	7.4(14)	-0.3(10)	-	-

5.2 Molecular Constants

The molecular constants that can be derived from the fit values listed in Table 5.1 are given in Table 5.2. These values enable the prediction of other transitions from the same states as well as comparison with theory.

The electronic rotational constant is given by [35]

$$B_e = B_\nu + \alpha_e(v + \frac{1}{2}), \tag{5.3}$$

where B_ν is the rotational constant for a given vibrational level and α_e is the vibrational correction and thus by measuring B_ν for multiple vibrational levels, we can extract α_e and B_e. Likewise, the electronic centrifugal distortion term is given by

$$D_e = D_\nu + \beta_e(\nu + \frac{1}{2}). \tag{5.4}$$

The energy of an electronically excited state as measured from the minima of the potential with a zero reference for the electronic ground state is given by

$$T_0 = \nu_0 - \omega_e'(v' + \frac{1}{2}) + \omega_e\chi_e'(v' + \frac{1}{2})^2 + \omega_e''(v'' + \frac{1}{2}) - \omega_e\chi e''(v'' + \frac{1}{2})^2 \tag{5.5}$$

where ν_0 is the band origin for a given transition, ω_e is the vibrational constant, and $\omega_e\chi e$ is the anharmonicity term. Initially, it would seem that the (0,0), (0,1), and (1,2) bands of $^1\Pi_1 - ^1\Sigma^+$ do not provide enough information to extract ω_e and $\omega_e\chi_e$ for both $^1\Pi_1$ and $^1\Sigma^+$ states as well as T_0 for the $^1\Pi_1$ state. However, assuming a Morse potential,

$$\omega_e\chi_e = \frac{\alpha_e^2\omega_e^2}{36B_e^3} + \frac{\alpha_e\omega_e}{3B_e} + B_e \tag{5.6}$$

[35]. Using this assumption, we obtain the molecular constants given in Table 5.2. The errors quoted represent the propagation of the statistical 95% uncertainty levels from the fit assuming a Morse potential and thus do not reflect any model dependent errors.

The vibrational constant, ω_e, can also be calculated from the relationship of the rotational constant to the centrifugal distortion,

$$\omega_e = \sqrt{\frac{4B_e^3}{D_e}} \tag{5.7}$$

Table 5.2: Derived constants for observed states in $^{180}HfF^+$. Values for T_0 are given from the minima of the potential not the lowest vibrational level. The error quoted is the statistical error and does not include any model dependent systematics. The dominant source of the statistical error is the uncertainty in α_e. The model dependent error would arise from $\omega_e\chi_e$ for which we see good agreement for the $^1\Sigma^+$ state with a non-model dependent value.

	$^1\Sigma^+$	$^1\Pi_1$	$^3\Pi_1$
T_0 [cm^{-1}]	0	13046.3(3)	10933(3)
B_e [cm^{-1}]	0.30568(8)	0.28186(4)	0.28441(50)
ω_e [cm^{-1}]	791.1(1)	702.6(7)	713(1)
$\omega_e\chi_e$ [cm^{-1}]	3.10(16)	2.70(15)	2.61(26)
α_e [10^{-3} cm^{-1}]	1.55(6)	1.42(6)	1.38(20)

[35]. From this definition of ω_e we obtain 780(17) cm^{-1} compared to 791.1(1) cm^{-1} as derived above for the $^1\Sigma^+$ state, 719(22) cm^{-1} compared to 713(1) cm^{-1} for the $^3\Pi_1$ state, and 703(16) cm^{-1} compared to 702.6(7) cm^{-1} for the $^1\Pi_1$ state. However, the uncertainty in the centrifugal distortion from the fits causes the uncertainty in the vibrational constant to be much greater than when it is calculated using the definition of $\omega_e\chi_e$ given in Equation (5.6). The good agreement of our value of $\omega_e\chi_e$ for the $^1\Sigma^+$ state using the Morse potential assumption with that of the Heaven group [3] as shown in Table 5.3 supports the Morse potential assumption, which allows us to achieve much more accurate values of the derived molecular constants.

5.3 Comparison with Theory and Other Experimental Data

A comparison of some of the derived molecular constants with theoretical calculations from Petrov et al. [2] is presented in Table 5.3. Initially, the predicted value of 12,686 cm^{-1} for the energy of the $^3\Pi_1$ state led to the identification of the band at $\sim 13,000$ cm^{-1} measured using single-frequency velocity-modulation spectroscopy as the $^3\Pi_1 - ^1\Sigma^+$ (0,0) band. However, if the band at $\sim 13,000$ cm^{-1} was the $^3\Pi_1 - ^1\Sigma^+$ (0,0) band, the Ω-doubling was expected to be negative as opposed to the positive value we measured [64].

The additional data from the frequency comb velocity-modulation spectroscopy resolved this confusion with the identification of the $\Delta v = 1$ band at 12,217 cm^{-1} with positive Ω-doubling and a higher energy upper state and the $\Delta v = 2$ band at 12,304 cm^{-1} with negative Ω-doubling and a lower energy upper state. The predicted energies of the $^1\Pi_1$ and $^3\Pi_1$ states are $\sim$1800 cm^{-1} above the predicted values, but the fine structure splitting between the two agrees with the predicted values to within the uncertainty of the derived energy from the fit. Preliminary theoretical calculations with a modified core potential shift the manifold of Π states so that their positions more closely match the measured values [64]. (This will be discussed further in a forthcoming publication from K.C. Cossel et al.) Additional unpublished work from E.R. Meyer has shown similar discrepancies in the state energies, but good agreement in B_e and α_e [65].

In addition to theoretical comparisons, in Table 5.3 molecular constants of the $v = 0$ level of the $^1\Sigma^+$ state can be compared to the experimental results from Barker et al. using pulsed-field-ionization zero-kinetic-energy measurements (PFI-ZEKE) to study the low-lying states of HfF^+ [3]. We find that values of B_e, ω_e, and $\omega_e\chi_e$ agree within the errors. The agreement in $\omega_e\chi_e$ supports our assumption of a Morse potential for calculations of ω_e, T_0 and $\omega_e\chi_e$. Due to directly measuring a large number of rotational lines for each HfF^+ band, our values of B_e are considerably more precise. In addition to the $^1\Pi_1 - ^1\Sigma^+$ (0,0) and (0,1) bands, we measure the energy of the $v = 1$ level of the $^1\Sigma^+$ state relative to the $v = 0$ level to be 784.841(6) cm^{-1}, which is again consistent with the Heaven group's value of 785.8(10) cm^{-1} [3].

5.4 Isotope Shifts

For the stronger transitions, we can fit not only the $^{180}HfF^+$ bands, but also those corresponding to other isotopes of Hf. Tables 5.4 and 5.5 contain the fit values for multiple isotopes for the $^1\Pi_1 \leftarrow ^1\Sigma^+(0,1)$ band and the $^3\Pi_1 \leftarrow ^1\Sigma^+(2,0)$ band, respectively. For the rotational constants for the $^1\Pi_1 \leftarrow ^1\Sigma^+(0,1)$ band, B''_{179}, B''_{178}, B''_{177}, B'_{179},B'_{178}, and B'_{177} all

Table 5.3: Comparison of derived molecular constants for $^{180}HfF^+$ with the theoretical calculations of Petrov et al. [2] and results from Barker et al. [3]. The theoretical values of B_e were computed from the equilibrium bond length.

	this work	theory [2]	other exp [3]	this work	theory	other exp
		T_0 [cm^{-1}]			B_e [cm^{-1}]	
$^1\Sigma^+$	0	0	0	0.30368(8)	0.3092	0.304(5)
$^3\Pi_1$	10933(3)	12686	–	0.2844(5)	0.2835	–
$^1\Pi_1$	13046.3(3)	14784	–	0.28186(4)	0.2805	–
		ω_e [cm^{-1}]			$\omega_e\chi_e$ [cm^{-1}]	
$^1\Sigma^+$	791.1(1)	751	791.2(10)	3.10(16)	–	2.95(20)
$^3\Pi_1$	713(1)	687	–	2.61(26)	–	–
$^1\Pi_1$	702.6(7)	679	–	2.70(15)	–	–

scale with the ratio of reduced masses as expected to within the error. The uncertainty in the values of D make comparison with the expected isotope shift impossible.

The ability to resolve all five isotopes of Hf for transitions with $\Delta v \neq 0$ aids in band identification as the vibrational isotope shift for $\Delta v = v' - v'' = 2$ versus $\Delta v = 1$ is obviously different. For those bands with sufficient signal strength and uncrowded spectral region, i.e. $^1\Pi_1 - ^1\Sigma^+(0,1)$ and $^3\Pi_1 - ^1\Sigma^+(2,0)$, we can fit to multiple isotopes and use the expected vibrational isotope scaling to extract the electronic isotope shift. While only the ^{180}HfF$^+$ band was fit for the $^3\Pi_1 - ^1\Sigma^+(3,1)$ and $^1\Pi_1 - ^1\Sigma^+(2,1)$ bands, the vibrational isotope shift seen is consistent with a $\Delta v = 2$ and $\Delta\nu = -1$ transition respectively.

From the differences in band origin, we can extract information about the electronic isotope shift of a transition by assuming that the vibrational isotope shift scales like the ratio of the square root of the reduced masses, which is an extremely good approximation. For a given isotope, the electronic energy

$$T_{0,i} = \nu_{0,i} - \Delta\omega_{\nu,i} \tag{5.8}$$

where

$$\Delta\omega_{\nu,i} = \omega'_{e,i}(v' + \frac{1}{2}) - \omega_e\chi'_{e,i}(v' + \frac{1}{2})^2 - \omega''_{e,i}(v'' + \frac{1}{2}) + \omega_e\chi''_{e,i}(v'' + \frac{1}{2})^2 \tag{5.9}$$

and thus the electronic isotope shift relative to ^{180}HfF$^+$ is given by

$$\Delta T_0 = T_{0,180} - T_{0,i} = \Delta\nu_0 - (1 - \sqrt{\frac{\mu_{180}}{\mu_i}})\Delta\omega_{\nu,180}. \tag{5.10}$$

For ^{178}HfF$^+$, from the $^1\Pi_1 - ^1\Sigma^+(0,1)$ band, $\Delta T_0 = -0.073(3)$ cm^{-1}. From observing the cancelation of the rotational isotope shift with the combination of the electronic and vibrational isotope shifts for the $^1\Pi_1 - ^1\Sigma^+(0,0)$ band as shown in Figure 3.6, the total electronic and vibrational isotope shift of ^{178}HfF$^+$ relative to ^{180}HfF$^+$ was -0.04 cm^{-1}. Using the values for the vibrational constant and anharmonicity term, this results in an electronic isotope shift of ΔT_0 = -0.064(7) cm^{-1} of ^{178}HfF$^+$ relative to ^{180}HfF$^+$, which is consistent with the shift found for the $^1\Pi_1 - ^1\Sigma^+(0,1)$ band. For the $^3\Pi_1 - ^1\Sigma^+(2,0)$ band, the electronic isotope shift between ^{180}HfF$^+$ and ^{178}HfF$^+$ is ΔT_0 = -0.048(4) cm^{-1}.

Table 5.4: Fitted constants for the $^1\Pi_1 \leftarrow^1 \Sigma^+(0,1)$ band for four different isotopes of HfF^+. The $^{176}HfF^+$ lines at 5.21% abundance were excluded from fitting due to their lower intensity. Quoted uncertainties are 95%.

	$^{180}HfF^+$	$^{179}HfF^+$	$^{178}HfF^+$	$^{177}HfF^+$
abundance [%]	35.10	13.63	27.30	18.6
ν_0 [cm^{-1}]	12217.698(2)	12217.198(4)	12216.997(2)	12216.818(4)
B″ [cm^{-1}]	0.30335(3)	0.30350(6)	0.30369(5)	0.30387(7)
B′ [cm^{-1}]	0.28115(3)	0.28129(7)	0.28146(4)	0.28163(7)
D″ [10^{-7} cm−1]	1.81(8)	1.70(19)	1.87(9)	1.90(17)
D′ [10^{-7} cm^{-1}]	1.81(8)	1.64(18)	1.80(9)	1.83(16)
2(p+2q) [10^{-4} cm^{-1}]	3.69(2)	3.72(5)	3.68(2)	3.72(4)
$2(p_D+2q_D)$ [10^{-9} cm^{-1}]	9.7(7)	10.4(25)	9.2(8)	10.4(14)

Table 5.5: Fitted constants for the $^3\Pi_1 \leftarrow^1 \Sigma^+(2,0)$ band for three different isotopes of HfF^+. The $^{179}HfF^+$ lines at 13.63% abundance and the $^{176}HfF^+$ lines at 5.21% abundance were not fit. Quoted uncertainties are 95%. * Values fixed based on expected rotational isotope shift.

	$^{180}HfF^+$	$^{178}HfF^+$	$^{177}HfF^+$
abundance [%]	35.10	27.30	18.6
ν_0 [cm^{-1}]	12304.400(3)	12305.183(2)	12305.581(3)
B″ [cm^{-1}]	0.30481(5)	0.30519(4)	0.30531*
B′ [cm^{-1}]	0.28096(4)	0.28131(4)	0.28142*
D″ [10^{-7} cm−1]	1.78(12)	1.89(12)	1.80(8)
D′ [10^{-7} cm^{-1}]	1.78(11)	1.88(11)	1.80(8)
2(p+2q) [10^{-4} cm^{-1}]	-3.82(1)	-3.82(1)	-3.84(2)
$2(p_D+2q_D)$ [10^{-9} cm^{-1}]	–	–	–

Chapter 6

Conclusion

In this work, different spectroscopic techniques have been both unsuccessfully (hollow cathode lamp spectroscopy) and successfully (single-frequency and frequency-comb velocity-modulation spectroscopy) used to identify bands of HfF^+. The first spectroscopic information for HfF^+ came from our measurement of the $^1\Pi_1 -^1 \Sigma^+$ (0,0) band measured with single-frequency velocity-modulation spectroscopy with a sensitivity of $3x10^{-7}$ Hz^{-1} as discussed in Chapter Three. Single-frequency velocity-modulation spectroscopy also enabled the characterization of the discharge and oven system. The development of a new powerful spectroscopic tool [36], frequency comb velocity-modulation spectroscopy (Chapter Four), allowed us to cover a thousand wavenumbers of spectral bandwidth and to identify an additional four HfF^+ bands. The achieved sensitivity for frequency-comb velocity-modulation spectroscopy was $4x10^{-8}$ $Hz^{-1/2}$ (spectral element)$^{-1/2}$ with 1500 simultaneous detection channels spanning 150 cm^{-1} of bandwidth. For a 30 minute acquisition using 30 interleaved images to densely sample the whole spectrum, this corresponded to a $3x10^{-7}$ single-pass fractional absorption sensitivity for each of 45,000 measurement channels. Identification of bands arising from multiple vibrational levels of the same electronic states of HfF^+ enables the prediction of additional $^3\Pi_1 -^1 \Sigma^+$ and $^1\Pi_1 -^1 \Sigma^+$ rotational bands with only a few wavenumbers of uncertainty. The spectroscopic information from all five HfF^+ rotational bands was presented in Chapter Five. Molecular constants for the $^1\Sigma^+$, $^3\Pi_1$, and $^1\Pi_1$ states were extracted, which can be compared with theory as well as other experimental results for

the $^1\Sigma^+$ and which may lead to improvements in the theoretical predictions for electronic states that couple well to the $^3\Delta_1$ metastable state. The resolution of all five isotopes of hafnium allows for examination of the isotope shifts and provides a confirmation that the bands do in fact arise from HfF^+.

As discussed in Chapter One, the science state of interest of HfF^+ for the JILA eEDM experiment is the metastable $^3\Delta_1$ state, not the $^1\Sigma^+$ ground state [25], and thus additional survey spectroscopy of HfF^+ is needed as all the bands currently identified arise from the $^1\Sigma^+$ ground state. Figure 6.1 summarizes the five bands identified so far as well as the spectral region currently covered with frequency comb velocity-modulation spectroscopy. The relative intensity covered with the single-frequency velocity-modulation measurements is not shown, but the relatively low discharge current of 100mA_{ppk} limited the strength of the absorption signal. Additionally, Figure 6.1 shows the potential location and relative intensity of other bands from 11,000 to 15,000 cm^{-1} with crude error bars representing the large theoretical uncertainties for band locations. Theory values were taken both from Petrov et al.[2] as well as recent preliminary work from Petrov et al.[64] and E.R. Meyer[65]. Work is on-going both to use single-frequency velocity-modulation spectroscopy with a cw Ti:sapph laser to sample portions of the spectral region from 11,000 to 15,000 cm^{-1} likely to contain states of interest and to broaden the ti:sapph comb to cover 11,000 to 15,000 cm^{-1} with the required power per comb mode. Since comb sources enable efficient non-linear optical generation, which allows for spectral broadening and access to spectral regions ranging from the UV to the mid-IR [66, 67, 47], modifications to the imaging system, such as an InGaAs camera, a streak camera similar to Thorpe et al. [39], or an optical frequency up-conversion system, would be all that would be required to push this technique even further to those wavelengths, thus opening the door to even more applications.

The impetus for the development of frequency comb velocity-modulation spectroscopy was the lack of experimental data on the electronic structure of molecular ions such as HfF^+ and ThF^+, which are ideal for a highly sensitive search for the electron electric dipole

moment [26]. Coupled with the large theoretical uncertainties (thousands of wavenumbers) [27], the lack of experimental data necessitated broad survey spectroscopy to understand and assign the molecular energy level structure. However, this technique has a wide range of potential applications because broad bandwidth, precision spectroscopy of molecular ions is of interest in precision measurement, astrochemistry, and physical chemistry. Beyond molecules of interest to eEDM experiments, precision spectroscopy of molecular ions such as H_3^+ [48] and CH_5^+ [68] can provide a test of ab initio theory and yield new insights into few-body quantum dynamics, respectively. In astrochemistry, numerous ions and radicals have been discovered in the interstellar medium and many more species have been hypothesized [69, 70]. It is believed that the source of the unidentified diffuse interstellar bands, currently the longest standing question in astronomical spectroscopy, is molecular (possibly ionic), but accurate identification will require matching the spectra of candidate species to astronomical observations over wide and often times disparate spectral windows [71, 72]. Additionally, understanding the chemistry of molecular clouds in circumstellar gases has been enabled by the identification of molecular ions in the laboratory [73]. Efficient survey spectroscopy of molecular ions is thus of interest beyond the JILA electron EDM experiment.

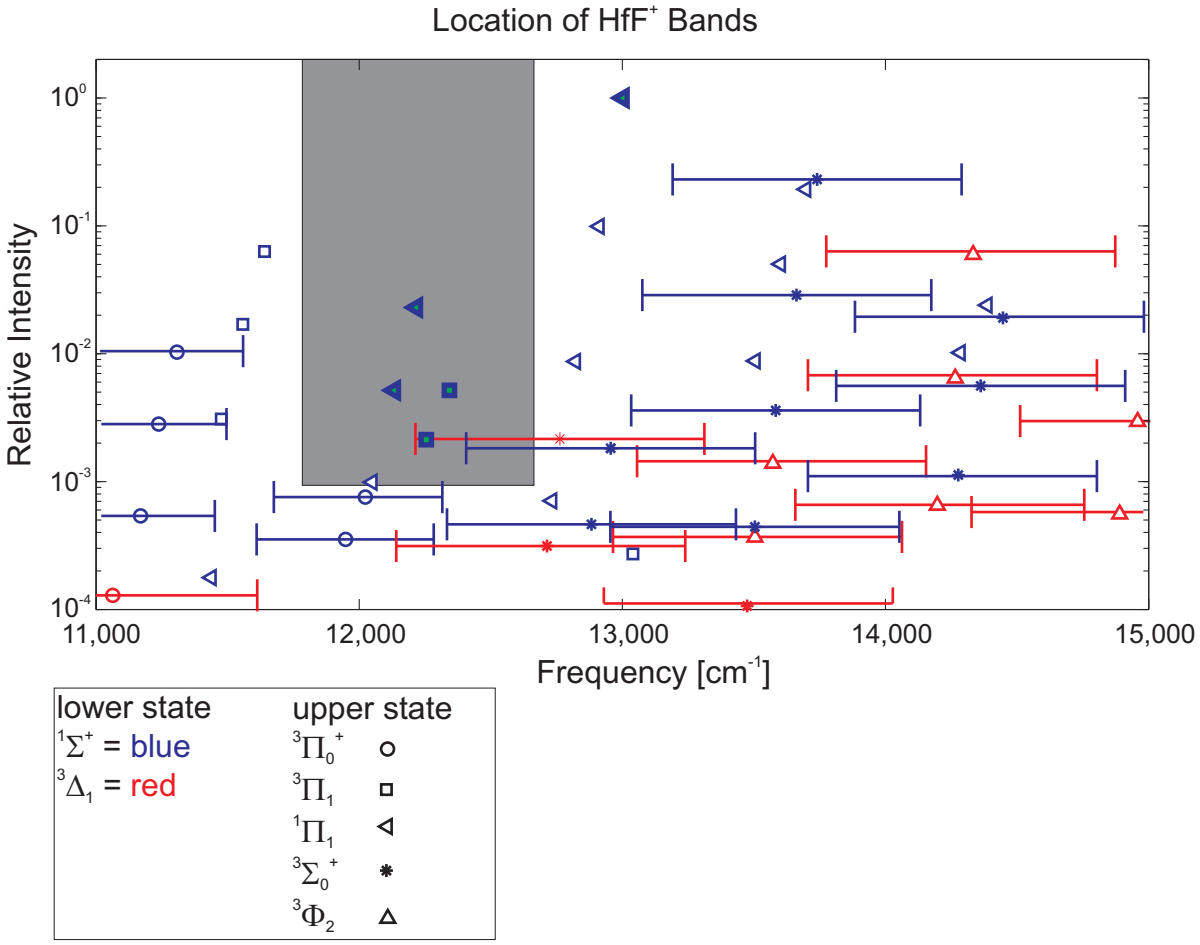

Figure 6.1: Identified and predicted HfF^+ rotational band locations from 11,000 to 15,000 cm^{-1} (909-668 nm) for up to v′ and v″ equal to 3. The relative intensity is scaled by the predicted dipole moment, by thermal factors assuming an approximate vibrational and electronic temperature based on a rotational temperature of 640 K, and by the Franck-Condon factors. The relative intensities for the four bands measured with frequency comb velocity-modulation spectroscopy agree with the experimental data and the uncertainty in the relative intensity for bands with no experimental data is a factor of 3-4. The color of the point indicates the lower state of the band, either $^1\Sigma^+$ (blue) or $^3\Delta_1$ (red), while the shape of the point indicates the upper state of the band. The five identified HfF^+ bands discussed in Chapter Five are shown in green with the outline bolded. For those bands which arise from states for which no experimental information about molecular constants exists, crude error bars for the energy uncertainty have been added. The gray region represents the spectral-range covered and relative sensitivity with frequency comb velocity-modulation spectroscopy. Even with the four bands of HfF^+ accounted for in the spectral region covered with the frequency comb, we still have ∼100 lines unidentified in the 12,100 to 12,200 cm^{-1} corresponding on this scale to a relative intensity of $2x10^{-3}$. While we have been unable to assign these lines due to the overlapping bands, it is possible that they belong to a fifth HfF^+ band such as the $^3\Sigma_0^+ -^3 \Delta_1$ band predicted 1000 cm^{-1} to the blue or the $^3\Pi_2 - 3\Delta_1$ band shifted up from the predicted relative intensity currently off the lower edge of what is plotted here.

Bibliography

[1] P. G. H. Sandars, "Electric dipole moments of charged particles," Contemporary Physics, vol. 42, pp. 97–111, Mar. 2001.

[2] A. Petrov, N. Mosyagin, and A. Titov, "Theoretical study of low-lying electronic terms and transition moments for HfF+ for the electron electric-dipole-moment search," Physical Review A, vol. 79, pp. 1–7, Jan. 2009.

[3] B. J. Barker, I. O. Antonov, V. E. Bondybey, and M. C. Heaven, "Communication: Spectroscopic measurements for HfF(+) of relevance to the investigation of fundamental constants.," The Journal of chemical physics, vol. 134, p. 201102, May 2011.

[4] D. Collet, J.-L. Destombes, I. Hadj Bachir, and T. Huet, "Rotational analysis of the vibrational hot bands of $N2^+$ ($A^2\Pi_u X^2\Sigma_g^+$) in the near-infrared region using velocity modulation spectroscopy," Chemical Physics Letters, vol. 286, pp. 311–316, Apr. 1998.

[5] P. Sandars, "Measurability of the Proton Electric Dipole Moment," Physical Review Letters, vol. 19, no. 24, pp. 1396–1398, 1967.

[6] S. C. Bennett and C. E. Wieman, "Measurement of the 6s→7s Transition Polarizability in Atomic Cesium and an Improved Test of the Standard Model," Physical Review Letters, vol. 82, pp. 4153–4153, May 1999.

[7] R. P. Stutz, Towards Measuring the Electron Electric Dipole Moment Using Trapped Molecular Ions. PhD thesis, University of Colorado Boulder, 2010.

[8] J. Hudson, B. Sauer, M. Tarbutt, and E. Hinds, "Measurement of the Electron Electric Dipole Moment Using YbF Molecules," Physical Review Letters, vol. 89, pp. 8–11, June 2002.

[9] J. J. Hudson, D. M. Kara, I. J. Smallman, B. E. Sauer, M. R. Tarbutt, and E. a. Hinds, "Improved measurement of the shape of the electron," Nature, vol. 473, pp. 493–496, May 2011.

[10] B. C. Regan, E. D. Commins, C. J. Schmidt, and D. DeMille, "New Limit on the Electron Electric Dipole Moment," Physical Review Letters, vol. 88, pp. 18–21, Feb. 2002.

[11] D. DeMille, F. Bay, S. Bickman, D. Kawall, D. Krause, S. Maxwell, and L. Hunter, "Investigation of PbO as a system for measuring the electric dipole moment of the electron," Physical Review A, vol. 61, pp. 1–8, Apr. 2000.

[12] N. Shafer-Ray, "Possibility of 0-g-factor paramagnetic molecules for measurement of the electrons electric dipole moment," Physical Review A, vol. 73, pp. 1–3, Mar. 2006.

[13] A. C. Vutha, W. C. Campbell, Y. V. Gurevich, N. R. Hutzler, M. Parsons, D. Patterson, E. Petrik, B. Spaun, J. M. Doyle, G. Gabrielse, and D. DeMille, "Search for the electric dipole moment of the electron with thorium monoxide," Journal of Physics B: Atomic, Molecular and Optical Physics, vol. 43, p. 074007, Apr. 2010.

[14] J. Lee, E. Meyer, R. Paudel, J. Bohn, and A. Leanhardt, "An electron electric dipole moment search in the X 3 Δ 1 ground state of tungsten carbide molecules," Journal of Modern Optics, vol. 56, pp. 2005–2012, Oct. 2009.

[15] S. A. Murthy, D. Krause, Jr., Z. L. Li, and L. R. Hunter, "New Limits on the Electron Dipole Moment from Cesium," Physical Review Letters, vol. 63, no. 9, pp. 965–968, 1989.

[16] J. Amini, C. Munger, and H. Gould, "Electron electric-dipole-moment experiment using electric-field quantized slow cesium atoms," Physical Review A, vol. 75, pp. 1–8, June 2007.

[17] F. Fang and D. S. Weiss, "Resonator-enhanced optical guiding and trapping of Cs atoms.," Optics letters, vol. 34, pp. 169–71, Jan. 2009.

[18] L. Hunter, S. Maxwell, K. Ulmer, N. Charney, S. Peck, D. Krause, S. Ter-Avetisyan, and D. DeMille, "Detailed spectroscopy of the a(1) [$^3\Sigma^+$] state of PbO," Physical Review A, vol. 65, pp. 1–4, Feb. 2002.

[19] D. Kawall, F. Bay, S. Bickman, Y. Jiang, and D. DeMille, "Precision Zeeman-Stark Spectroscopy of the Metastable a(1)[$^3\Sigma^+$] State of PbO," Physical Review Letters, vol. 92, pp. 2–5, Apr. 2004.

[20] M. Kozlov and D. DeMille, "Enhancement of the Electric Dipole Moment of the Electron in PbO," Physical Review Letters, vol. 89, pp. 20–23, Sept. 2002.

[21] A. Petrov, A. Titov, T. Isaev, N. Mosyagin, and D. DeMille, "Configuration-interaction calculation of hyperfine and P,T-odd constants on ^{207}PbO excited states for electron electric-dipole-moment experiments," Physical Review A, vol. 72, pp. 1–6, Aug. 2005.

[22] M. G. Kozlov, V. I. Fomichev, Y. Y. Dmitriev, L. N. Labzovsky, and A. V. Titov, "Calculation of the P- and T-odd spin-rotational Hamiltonian of the PbF molecule," J. Phys. B., vol. 20, pp. 4939–4948, 1987.

[23] Y. Dmitriev, "Calculation of the spin-rotational Hamiltonian including P- and P, T-odd weak interaction terms for HgF and PbF molecules," Physics Letters A, vol. 167, pp. 280–286, July 1992.

[24] E. Meyer and J. Bohn, "Prospects for an electron electric-dipole moment search in metastable ThO and ThF^+," Physical Review A, vol. 78, p. 010502, July 2008.

[25] A. E. Leanhardt, J. L. Bohn, H. Loh, P. Maletinsky, E. R. Meyer, L. C. Sinclair, R. P. Stutz, and E. A. Cornell, "On Measuring the Electron Electric Dipole Moment in Trapped Molecular Ions," arXiv:1008.2997v2, Aug. 2010.

[26] E. Meyer, J. Bohn, and M. Deskevich, "Candidate molecular ions for an electron electric dipole moment experiment," Physical Review A, vol. 73, p. 062108, June 2006.

[27] A. Petrov, N. Mosyagin, T. Isaev, and A. Titov, "Theoretical study of HfF+ in search of the electron electric dipole moment," Physical Review A, vol. 76, pp. 3–6, Sept. 2007.

[28] C. Gudeman, M. Begemann, J. Pfaff, and R. J. Saykally, "Velocity-Modulated Infrared Laser Spectroscopy of Molecular Ions: The v_1 Band of HCO^+," Physical Review Letters, vol. 50, pp. 727–731, 1983.

[29] S. K. Stephenson and R. J. Saykally, "Velocity modulation spectroscopy of ions.," Chemical Reviews, vol. 105, pp. 3220–34, Sept. 2005.

[30] G. Lan, H. D. Tholl, and J. W. Farley, "Double-modulation spectroscopy of molecular ions: Eliminating the background in velocity-modulation spectroscopy," Review of Scientific Instruments, vol. 62, no. 4, p. 944, 1991.

[31] Y. Liu, C. Duan, S. Wu, H. Zhuang, and Y. Chen, "The Rotational Structure of the (7, 4) and (7, 2) Bands of the $A^2\Pi_u - X^2\Sigma_g^+$ System of N_2^+ Studied by Velocity Modulation Laser Spectroscopy.," Journal of molecular spectroscopy, vol. 208, pp. 144–147, July 2001.

[32] D. L. Perry and S. C. Phillips, Handbook of Inorganic Compounds. Boca Raton: CRC Press, 1995.

[33] J. Emsley, The Elements, Oxford Chemistry Guides. New York: Oxford Univ. Press, 1995.

[34] J. M. Brown and A. J. Merer, "Lambda-type doubling parameters for molecules in Π electronic states of triplet and higher multiplicity," Journal of Molecular Spectroscopy, vol. 74, pp. 488–494, Mar. 1979.

[35] G. Herzberg, Molecular Spectra and Molecular Structure: Volume I - Spectra of Diatomic Molecules. Malabar, Florida: Krieger Publishing Company, 2nd edition ed., 1950.

[36] L. C. Sinclair, K. C. Cossel, T. Coffey, J. Ye, and E. A. Cornell, "Frequency Comb Velocity-Modulation Spectroscopy," Physical Review Letters, vol. 107, no. 9, p. 093002, 2011.

[37] A. Marian, M. C. Stowe, J. R. Lawall, D. Felinto, and J. Ye, "United time-frequency spectroscopy for dynamics and global structure.," Science, vol. 306, pp. 2063–8, Dec. 2004.

[38] F. Keilmann, C. Gohle, and R. Holzwarth, "Time-domain mid-infrared frequency-comb spectrometer.," Optics Letters, vol. 29, pp. 1542–4, July 2004.

[39] M. J. Thorpe, K. D. Moll, R. J. Jones, B. Safdi, and J. Ye, "Broadband cavity ringdown spectroscopy for sensitive and rapid molecular detection.," Science, vol. 311, pp. 1595–9, Mar. 2006.

[40] S. A. Diddams, L. Hollberg, and V. Mbele, "Molecular fingerprinting with the resolved modes of a femtosecond laser frequency comb.," Nature, vol. 445, pp. 627–30, Feb. 2007.

[41] I. Coddington, W. Swann, and N. Newbury, "Coherent Multiheterodyne Spectroscopy Using Stabilized Optical Frequency Combs," Physical Review Letters, vol. 100, p. 013902, Jan. 2008.

[42] B. Bernhardt, A. Ozawa, P. Jacquet, M. Jacquey, Y. Kobayashi, N. Picque, T. Udem, R. Holzwarth, G. Guelachvili, and T. W. Hansch, "Cavity-enhanced dual-comb spectroscopy," Nature Photonics, vol. 4, p. 55, 2009.

[43] F. Adler, M. J. Thorpe, K. C. Cossel, and J. Ye, "Cavity-enhanced direct frequency comb spectroscopy: technology and applications.," Annual Review of Analytical Chemistry, vol. 3, pp. 175–205, Jan. 2010.

[44] S. Cundiff and J. Ye, "Colloquium: Femtosecond optical frequency combs," Reviews of Modern Physics, vol. 75, pp. 325–342, Mar. 2003.

[45] M. J. Thorpe, D. Balslev-Clausen, M. S. Kirchner, and J. Ye, "Cavity Enhanced Optical Vernier Spectroscopy, Broad Band, High Resolution, High Sensitivity," Optics Express, vol. 16, June 2008.

[46] M. J. Thorpe, F. Adler, K. C. Cossel, M. H. de Miranda, and J. Ye, "Tomography of a supersonically cooled molecular jet using cavity-enhanced direct frequency comb spectroscopy," Chemical Physics Letters, vol. 468, pp. 1–8, Jan. 2009.

[47] K. C. Cossel, F. Adler, K. A. Bertness, M. J. Thorpe, J. Feng, M. W. Raynor, and J. Ye, "Analysis of trace impurities in semiconductor gas via cavity-enhanced direct frequency comb spectroscopy," Applied Physics B, vol. 100, pp. 917–924, July 2010.

[48] C. P. Morong, J. L. Gottfried, and T. Oka, "H3+ as the benchmark for rigorous ab initio theory," Journal of Molecular Spectroscopy, vol. 255, pp. 13–23, May 2009.

[49] J. L. Gottfried, B. J. McCall, and T. Oka, "Near-infrared spectroscopy of H_3^+ above the barrier to linearity," The Journal of Chemical Physics, vol. 118, no. 24, p. 10890, 2003.

[50] A. A. Mills, B. M. Siller, and B. J. McCall, "Precision cavity enhanced velocity modulation spectroscopy," Chemical Physics Letters, vol. 501, pp. 1–5, Dec. 2010.

[51] B. M. Siller, A. A. Mills, and B. J. McCall, "Cavity-enhanced velocity modulation spectroscopy," Optics Letters, vol. 35, no. 8, pp. 1266 – 1268, 2010.

[52] P. Martin and G. Guelachvili, "Velocity-Modulation Fourier-Transform Spectroscopy of Molecular Ions," Physical Review Letters, vol. 65, no. 20, pp. 2535–2538, 1990.

[53] N. Picque and G. Guelachvili, "High-resolution multimodulation Fourier-transform spectroscopy," Applied Optics, vol. 38, no. 7, pp. 1224–1230, 1999.

[54] A. E. Siegman, Lasers. Sausalito, CA: University Science Books, 1986.

[55] M. Thorpe, R. Jones, K. Moll, J. Ye, and R. Lalezari, "Precise measurements of optical cavity dispersion and mirror coating properties via femtosecond combs.," Optics Express, vol. 13, pp. 882–8, Feb. 2005.

[56] M. J. Thorpe, Cavity-enhanced direct frequency comb spectroscopy. PhD thesis, University of Colorado, 2009.

[57] S. Xiao and A. Weiner, "2-D wavelength demultiplexer with potential for $\geq$ 1000 channels in the C-band.," Optics Express, vol. 12, pp. 2895–902, June 2004.

[58] M. Shirasaki, "Large angular dispersion by a virtually imaged phased array and its application to a wavelength demultiplexer.," Optics Letters, vol. 21, pp. 366–8, Mar. 1996.

[59] S. Beer and P. Seitz, "A smart pixel array with massively parallel signal processing for real-time optical coherence tomography performing close to the physical limits," Research in Microelectronics and Electronics, 2005 PhD, vol. 2, pp. 135–138, 2005.

[60] S. Bourquin, R. P. Prasankumar, F. X. Kärtner, J. G. Fujimoto, T. Lasser, and R. P. Salathé, "High-speed femtosecond pump-probe spectroscopy with a smart pixel detector array.," Optics Letters, vol. 28, pp. 1588–90, Sept. 2003.

[61] K. Holman, R. Jones, A. Marian, and S. Cundiff, "Detailed studies and control of intensity-related dynamics of femtosecond frequency combs from mode-locked Ti:sapphire lasers," IEEE Journal of Selected Topics in Quantum Electronics, vol. 9, pp. 1018–1024, July 2003.

[62] D. Heinecke, A. Bartels, T. Fortier, D. Braje, L. Hollberg, and S. Diddams, "Optical frequency stabilization of a 10 GHz Ti:sapphire frequency comb by saturated absorption spectroscopy in ˆ{87}rubidium," Physical Review A, vol. 80, pp. 1–7, Nov. 2009.

[63] T. C. Briles, D. C. Yost, A. Cingöz, J. Ye, and T. R. Schibli, "Simple piezoelectric-actuated mirror with 180 kHz servo bandwidth.," Optics Express, vol. 18, pp. 9739–46, May 2010.

[64] A. Petrov and A. Titov, "private communication."

[65] E. R. Meyer, "private communication."

[66] A. Gambetta, R. Ramponi, and M. Marangoni, "Mid-infrared optical combs from a compact amplified Er-doped fiber oscillator.," Optics Letters, vol. 33, pp. 2671–3, Nov. 2008.

[67] F. Adler, K. C. Cossel, M. J. Thorpe, I. Hartl, M. E. Fermann, and J. Ye, "Phase-stabilized, 1.5 W frequency comb at 2.8 um," Optics Letters, vol. 34, no. 9, pp. 1330–1332, 2009.

[68] X. Huang, A. B. McCoy, J. M. Bowman, L. M. Johnson, C. Savage, F. Dong, and D. J. Nesbitt, "Quantum deconstruction of the infrared spectrum of CH_5^+.," Science, vol. 311, pp. 60–3, Jan. 2006.

[69] W. Klemperer, "Astronomical Chemistry," Annual Review of Physical Chemistry, vol. 62, pp. 173–184, 2011.

[70] T. P. Snow and V. M. Bierbaum, "Ion chemistry in the interstellar medium.," Annual Review of Analytical Chemistry, vol. 1, pp. 229–59, Jan. 2008.

[71] P. J. Sarre, "The diffuse interstellar bands: A major problem in astronomical spectroscopy," Journal of Molecular Spectroscopy, vol. 238, pp. 1–10, July 2006.

[72] J. P. Maier, G. a. H. Walker, D. a. Bohlender, F. J. Mazzotti, R. Raghunandan, J. Fulara, I. Garkusha, and a. Nagy, "Identification of H 2 Ccc As a Diffuse Interstellar Band Carrier," The Astrophysical Journal, vol. 726, p. 41, Jan. 2011.

[73] D. T. Halfen and L. M. Ziurys, "Laboratory Detection of FeCO + ($X^4\Sigma^-$) by Millimeter/Submillimeter Velocity Modulation Spectroscopy," The Astrophysical Journal, vol. 657, pp. L61–L64, Mar. 2007.

Appendix A

Hollow Cathode Lamp Data

All data acquired with the hollow cathode lamp as discussed in Chapter Two are plotted in 250 cm^{-1} segments. The first image is a summary of the spectral region covered.

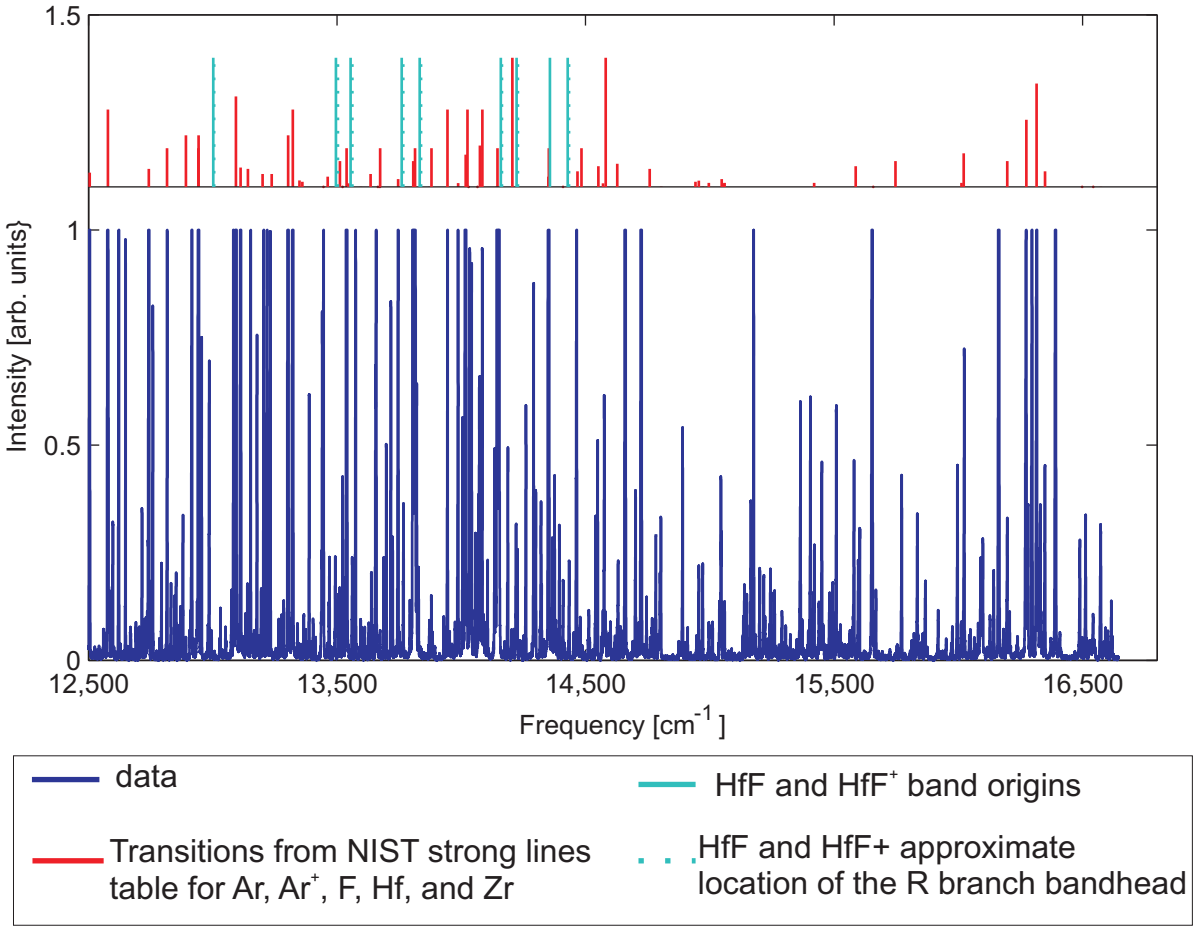
1.5
1
0.5
0
Intensity [arb. units]
12,500
13,500
14,500
15,500
16,500
Frequency [cm-1]
data
Transitions from NIST strong lines table for Ar, Ar+, F, Hf, and Zr
HfF and HfF+ band origins
HfF and HfF+ approximate location of the R branch bandhead

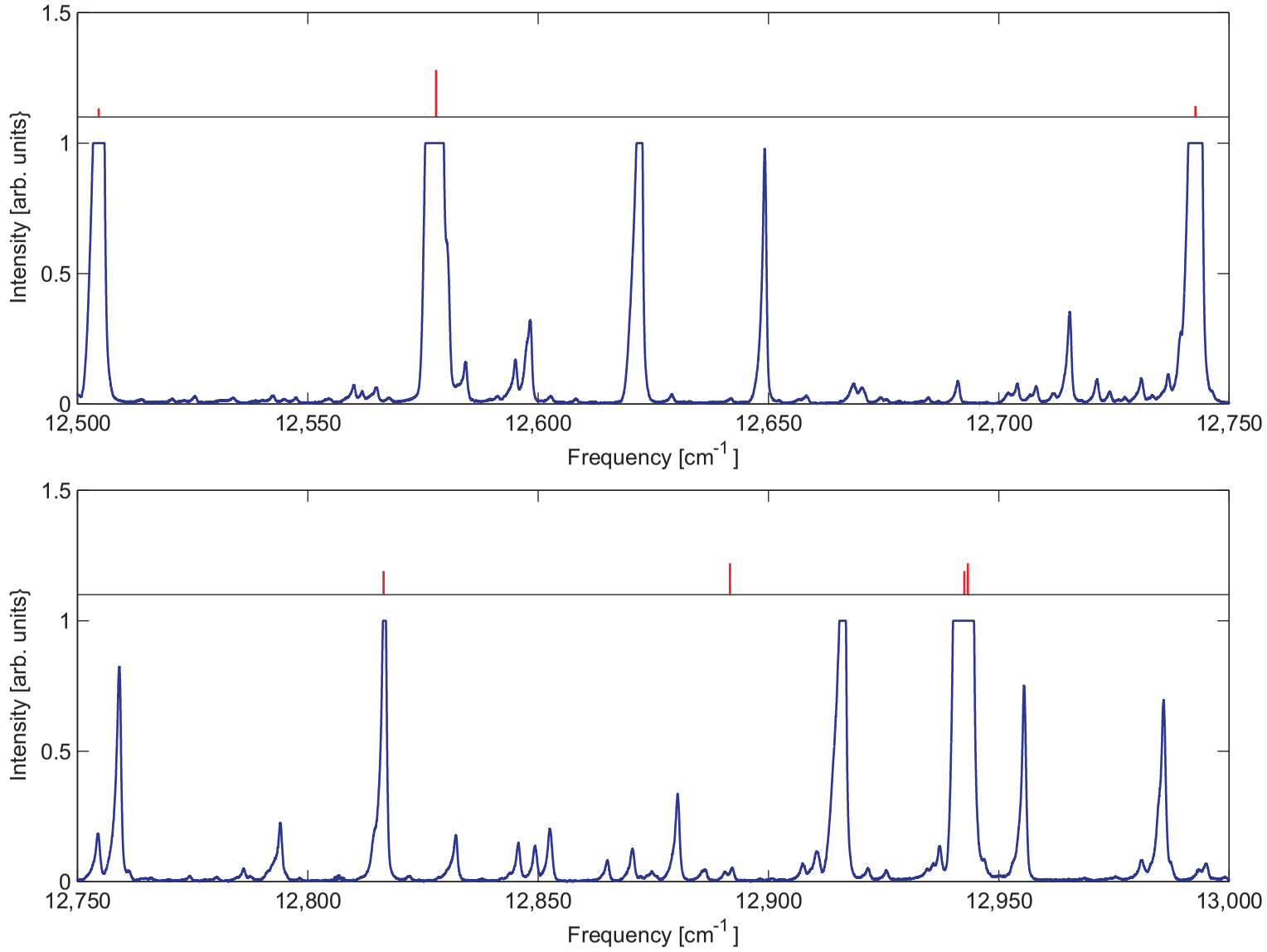
1.5
1
0.5
0
Intensity [arb. units}
12,500
12,550
12,600
12,650
12,700
12,750
Frequency [cm-1]
1.5
1
0.5
0
Intensity [arb. units}
12,750
12,800
12,850
12,900
12,950
13,000
Frequency [cm-1]
data
Transitions from NIST strong lines table for Ar, Ar+, F, Hf, and Zr
HfF and HfF+ band origins
HfF and HfF+ approximate location of the R branch bandhead

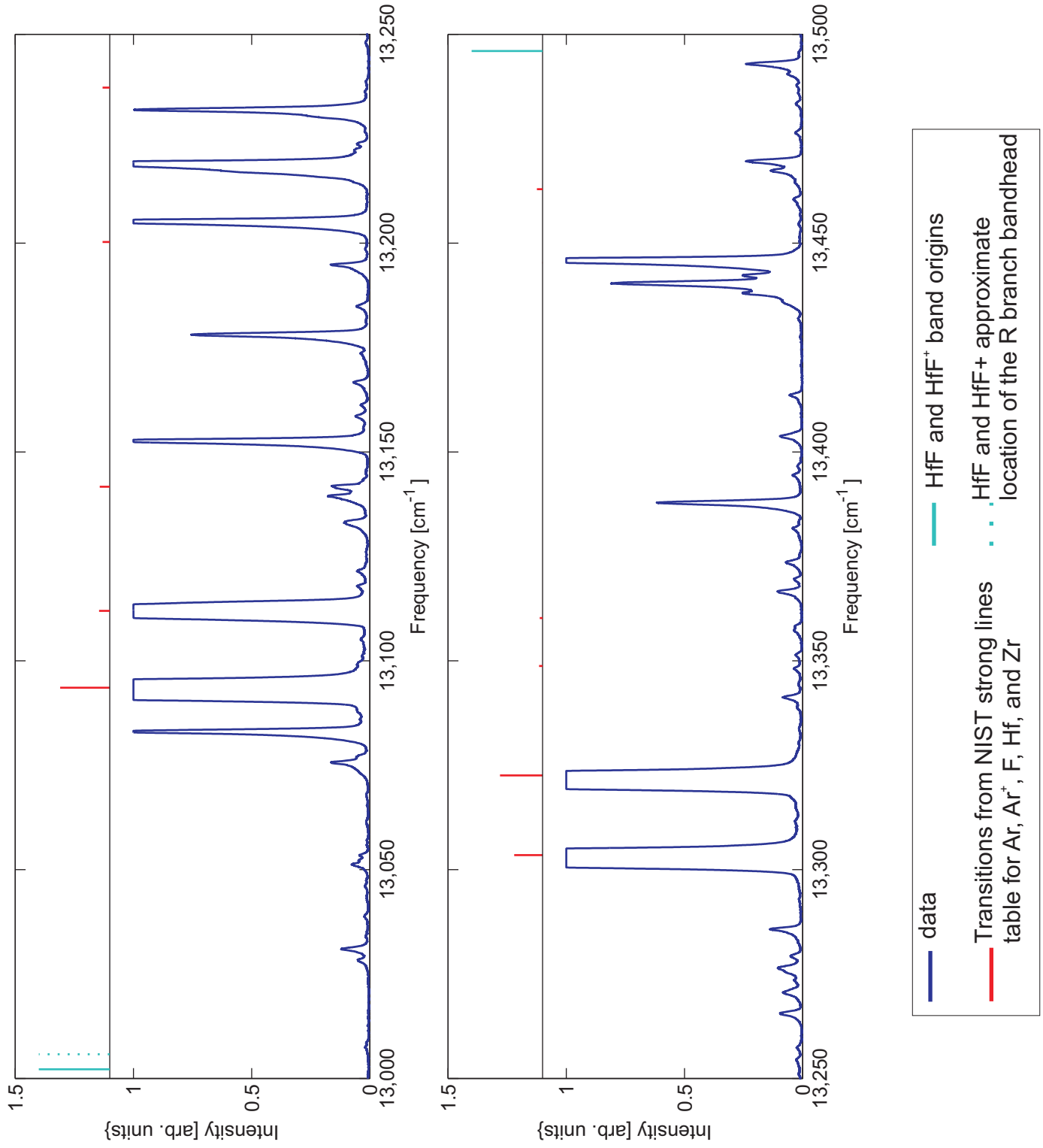
1.5
1
0.5
0
Intensity [arb. units]
13,000
13,050
13,100
13,150
13,200
13,250
Frequency [cm-1]
1.5
1
0.5
0
Intensity [arb. units]
13,250
13,300
13,350
13,400
13,450
13,500
Frequency [cm-1]
data
Transitions from NIST strong lines table for Ar, Ar+, F, Hf, and Zr
HfF and HfF+ band origins
HfF and HfF+ approximate location of the R branch bandhead

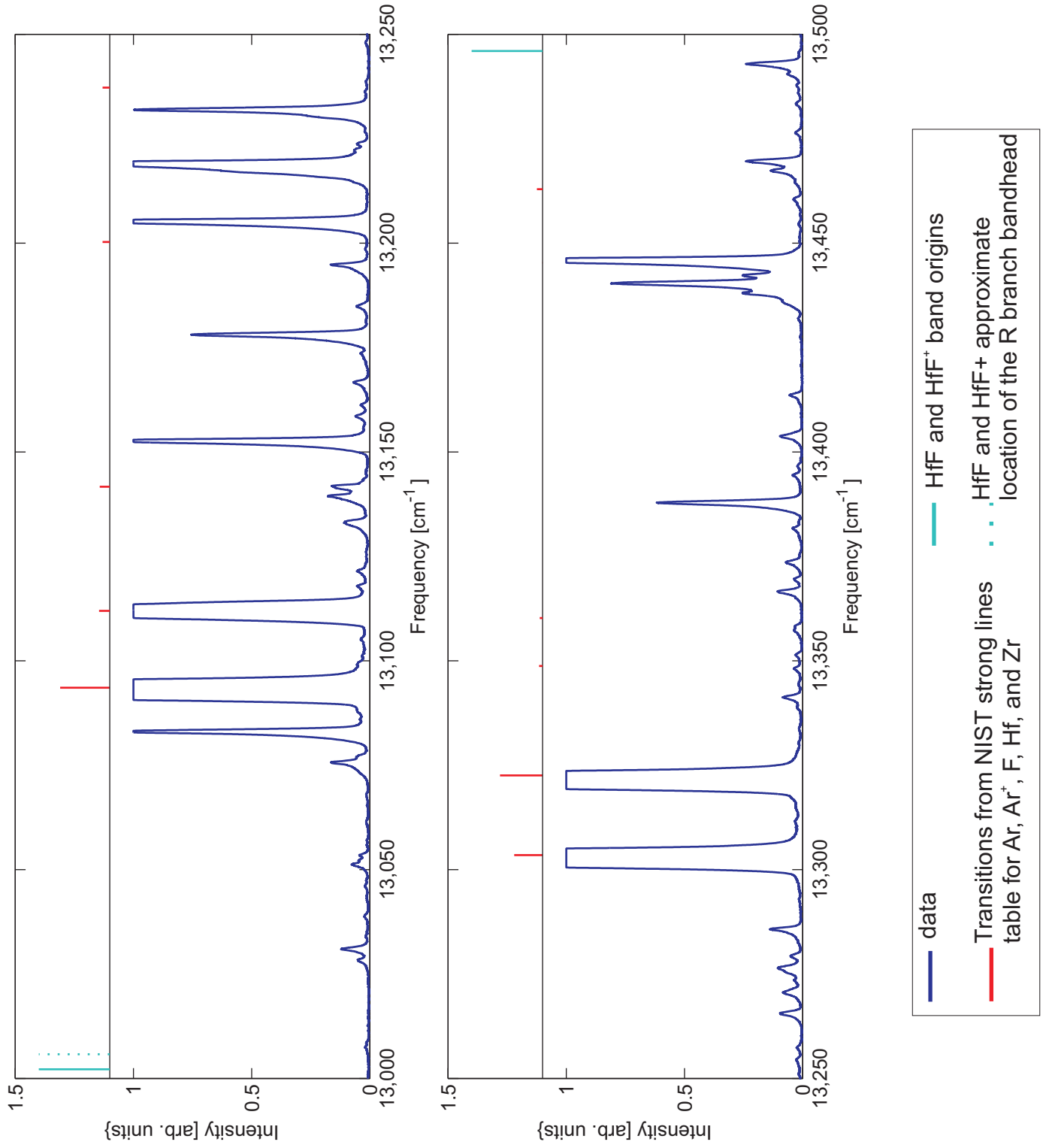
1.5
1
0.5
0
Intensity [arb. units]
13,000
13,050
13,100
13,150
13,200
13,250
Frequency [cm-1]
1.5
1
0.5
0
Intensity [arb. units]
13,250
13,300
13,350
13,400
13,450
13,500
Frequency [cm-1]
data
Transitions from NIST strong lines table for Ar, Ar+, F, Hf, and Zr
HfF and HfF+ band origins
HfF and HfF+ approximate location of the R branch bandhead

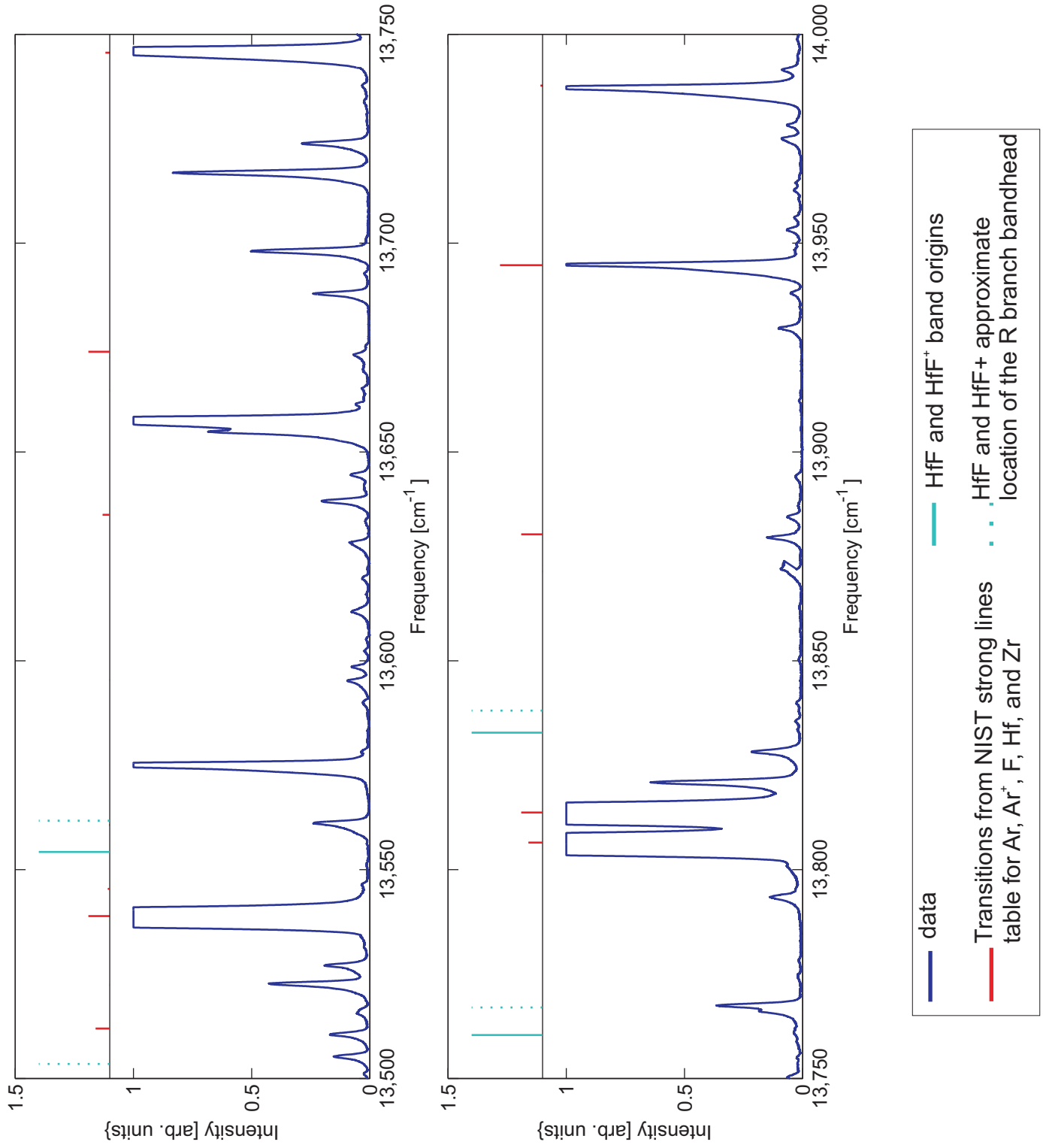
1.5
1
0.5
0
Intensity [arb. units]
13,500
13,550
13,600
13,650
13,700
13,750
Frequency [cm-1]
1.5
1
0.5
0
Intensity [arb. units]
13,750
13,800
13,850
13,900
13,950
14,000
Frequency [cm-1]
data
Transitions from NIST strong lines table for Ar, Ar+, F, Hf, and Zr
HfF and HfF+ band origins
HfF and HfF+ approximate location of the R branch bandhead

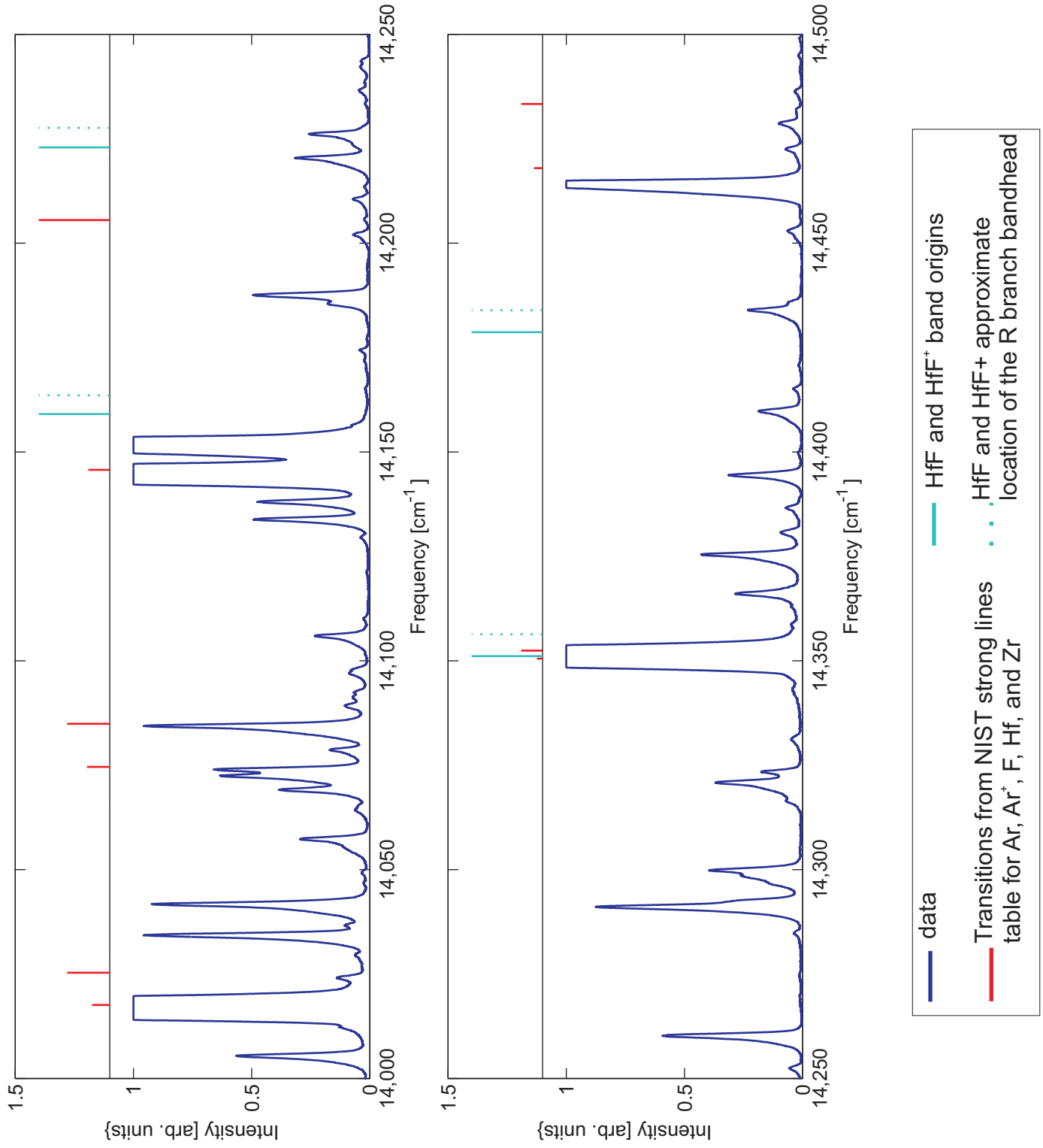
1.5
1
0.5
0
Intensity [arb. units]
14,000
14,050
14,100
14,150
14,200
14,250
Frequency [cm-1]
1.5
1
0.5
0
Intensity [arb. units]
14,250
14,300
14,350
14,400
14,450
14,500
Frequency [cm-1]
data
Transitions from NIST strong lines table for Ar, Ar+, F, Hf, and Zr
HfF and HfF+ band origins
HfF and HfF+ approximate location of the R branch bandhead

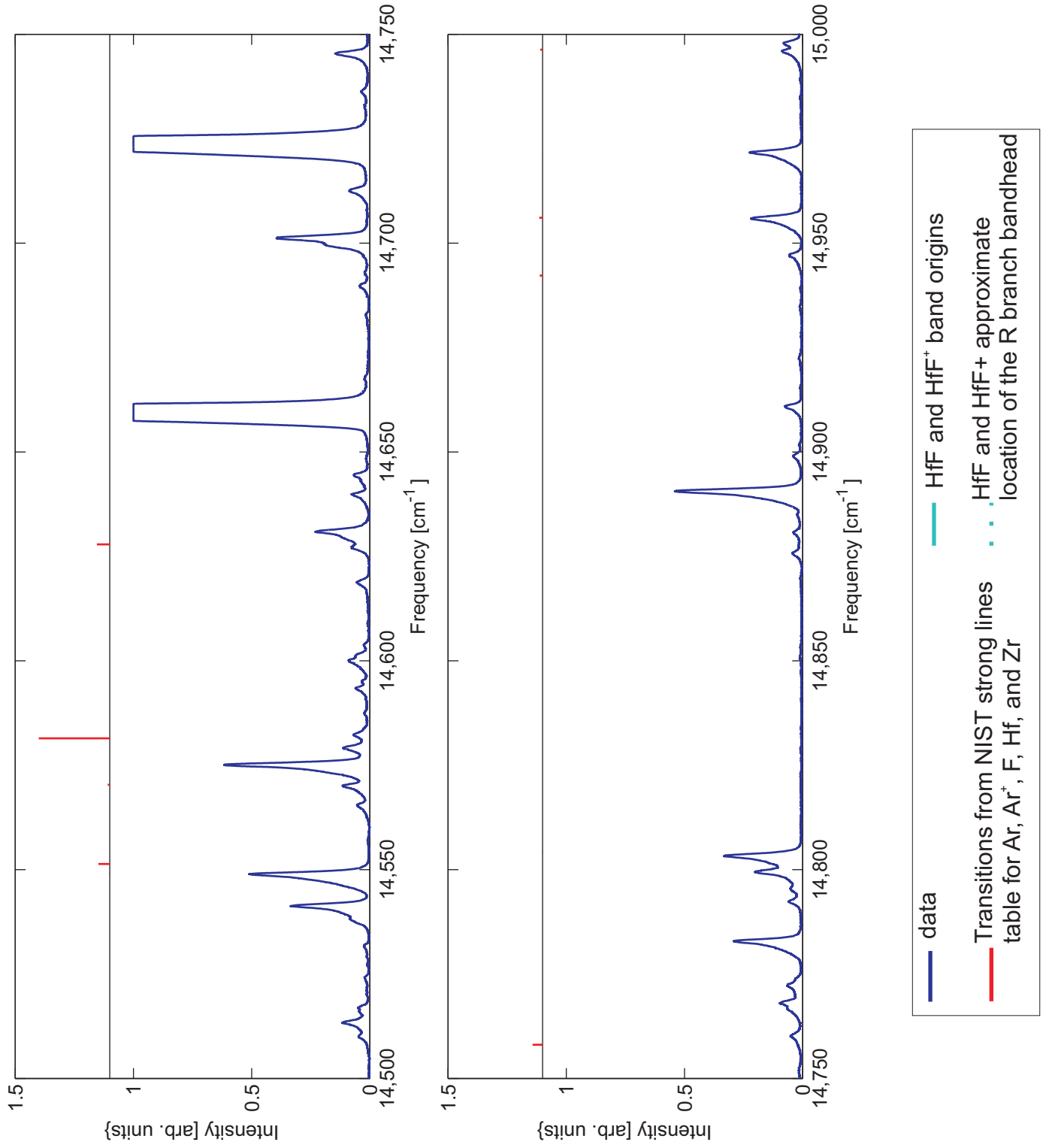
Intensity [arb. units]
Frequency [cm^{-1}]
data
Transitions from NIST strong lines table for Ar, Ar^{+}, F, Hf, and Zr
HfF and HfF^{+} band origins
HfF and HfF+ approximate location of the R branch bandhead

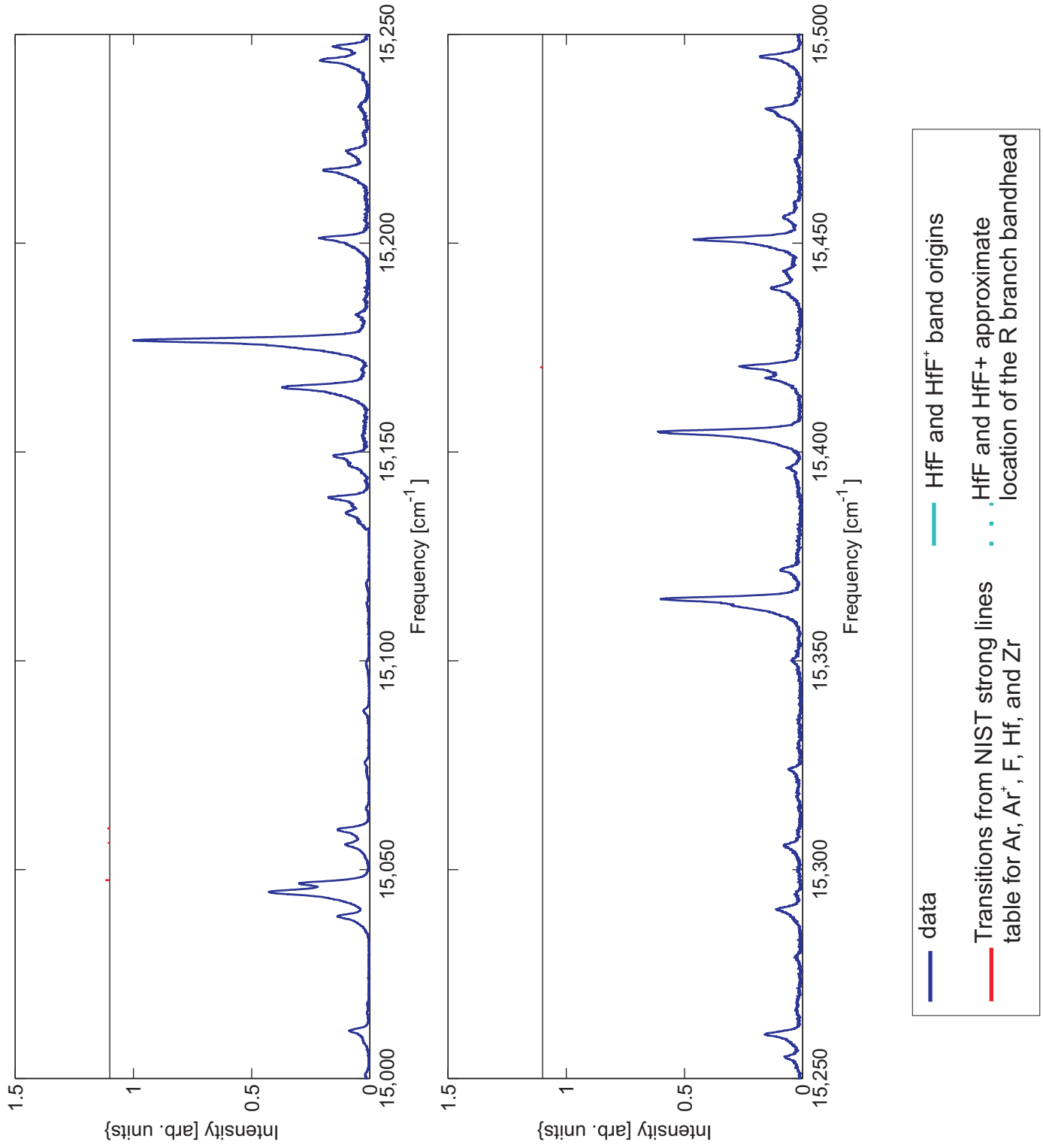
1.5
1
0.5
0
Intensity [arb. units]
15,000
15,050
15,100
15,150
15,200
15,250
Frequency [cm-1]
1.5
1
0.5
0
Intensity [arb. units]
15,250
15,300
15,350
15,400
15,450
15,500
Frequency [cm-1]
data
Transitions from NIST strong lines table for Ar, Ar+, F, Hf, and Zr
HfF and HfF+ band origins
HfF and HfF+ approximate location of the R branch bandhead

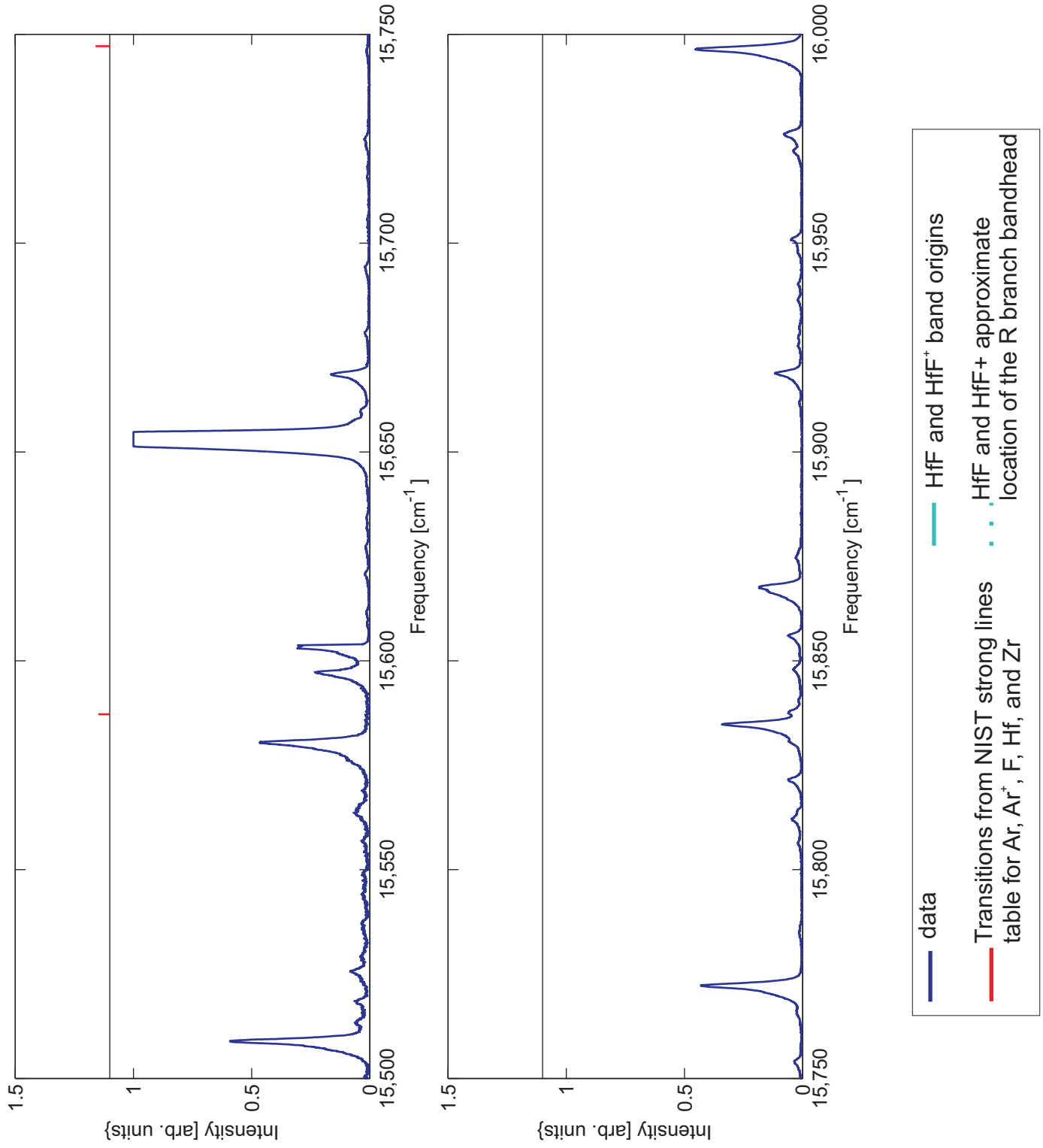
1.5
1
0.5
0
Intensity [arb. units]
15,500
15,550
15,600
15,650
15,700
15,750
Frequency [cm-1]
1.5
1
0.5
0
Intensity [arb. units]
15,750
15,800
15,850
15,900
15,950
16,000
Frequency [cm-1]
data
HfF and HfF+ band origins
Transitions from NIST strong lines table for Ar, Ar+, F, Hf, and Zr
HfF and HfF+ approximate location of the R branch bandhead

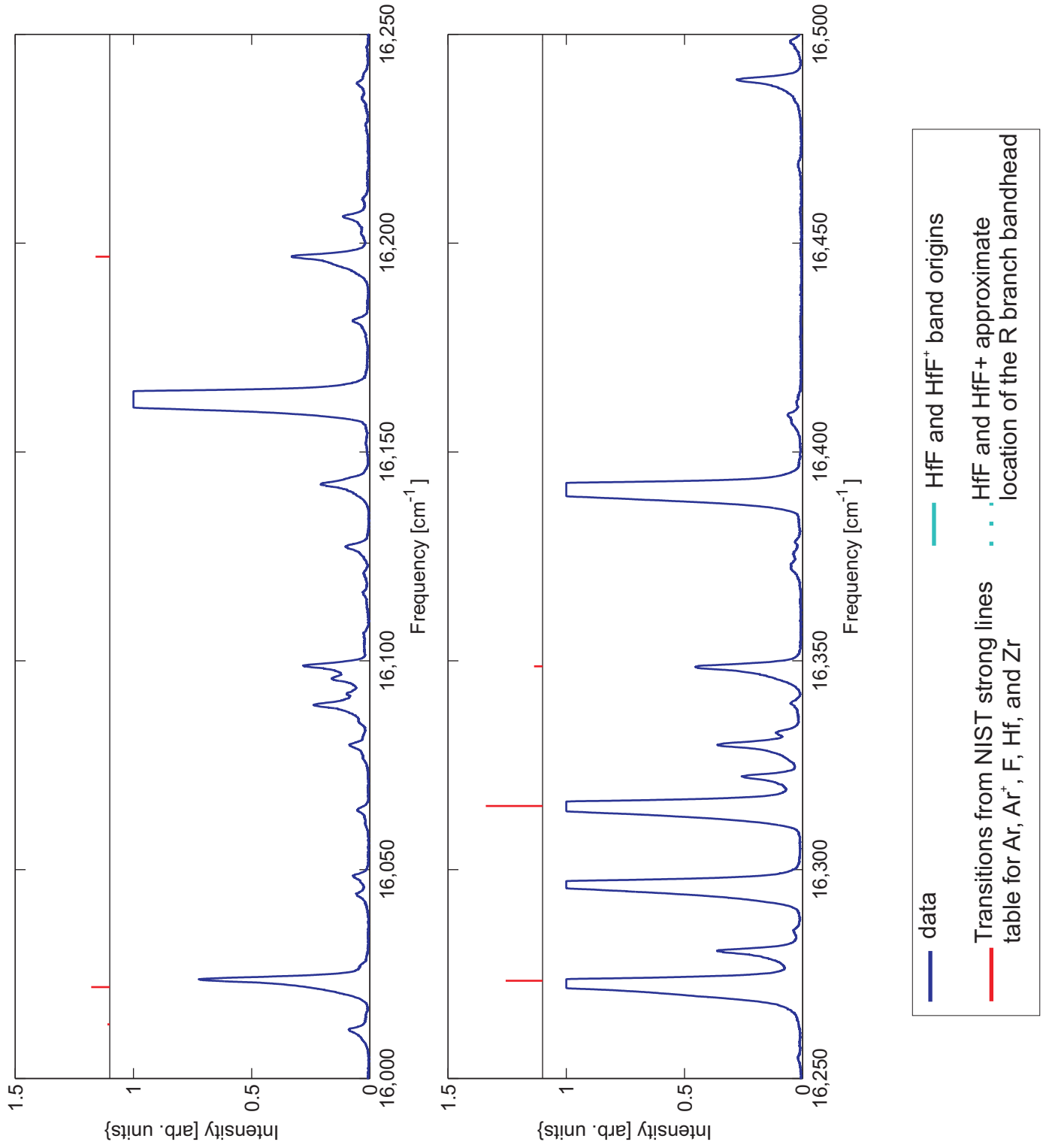
1.5
1
0.5
0
Intensity [arb. units]
16,000
16,050
16,100
16,150
16,200
16,250
Frequency [cm-1]
1.5
1
0.5
0
Intensity [arb. units]
16,250
16,300
16,350
16,400
16,450
16,500
Frequency [cm-1]
data
Transitions from NIST strong lines table for Ar, Ar+, F, Hf, and Zr
HfF and HfF+ band origins
HfF and HfF+ approximate location of the R branch bandhead

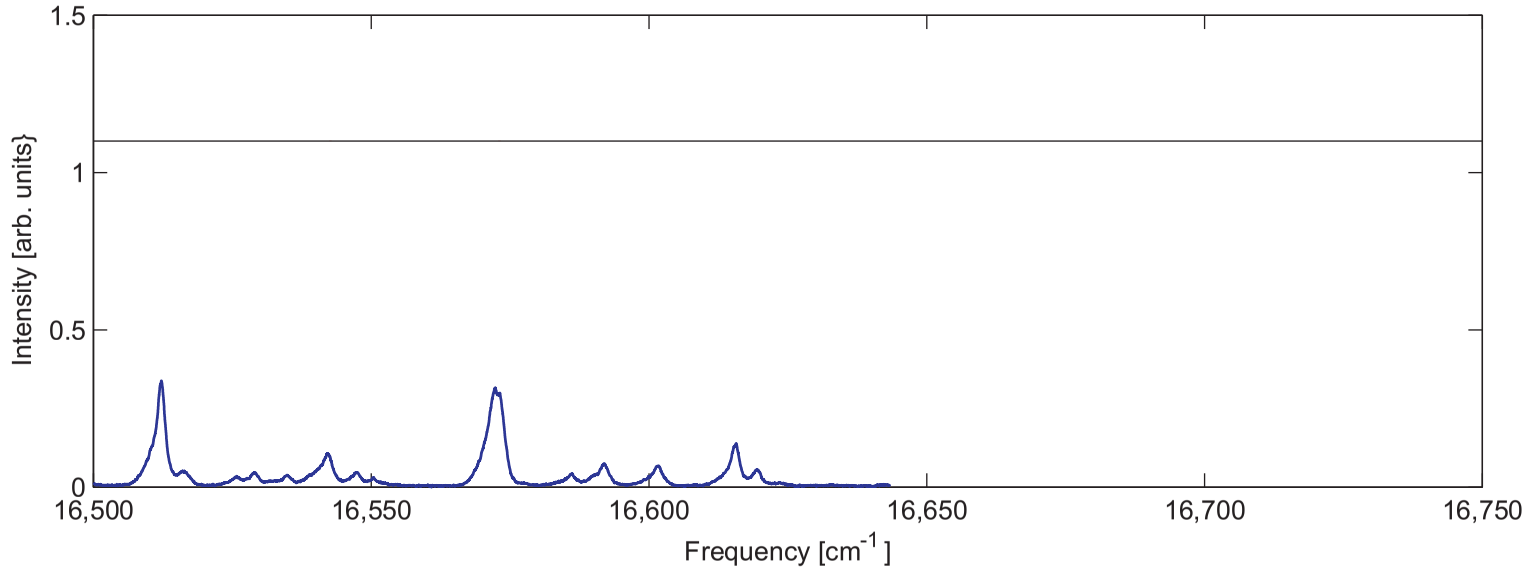

data

Transitions from NIST strong lines table for Ar, Ar^+, F, Hf, and Zr

HfF and HfF^+ band origins

HfF and HfF+ approximate location of the R branch bandhead

Appendix B

Velocity-Modulation Data

Single-frequency velocity-modulation spectroscopy data for the $^1\Pi_1 - ^1\Sigma^+$ band as discussed in Chapter Three are presented along with the line locations from the fit plotted in 5 cm^{-1} segments. The first image is a summary of the spectral region covered. Additional higher signal-to-noise scans were taken over select regions to determine the value of Ω' and Ω'' through the presence or absence of the low J lines.

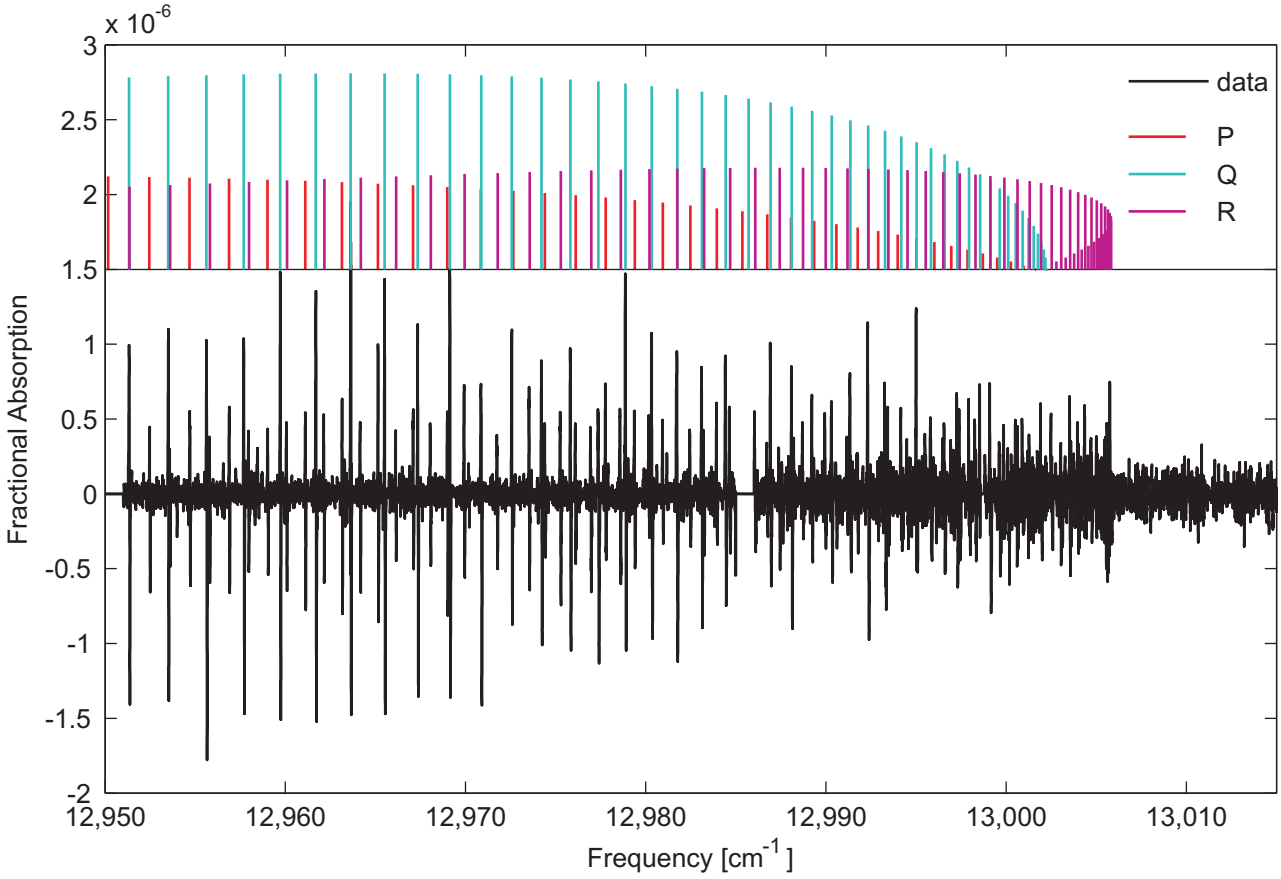
x 10^-6
3
2.5
2
1.5
1
0.5
0
-0.5
-1
-1.5
-2
Fractional Absorption
data
P
Q
R
12,950
12,960
12,970
12,980
12,990
13,000
13,010
Frequency [cm^-1]

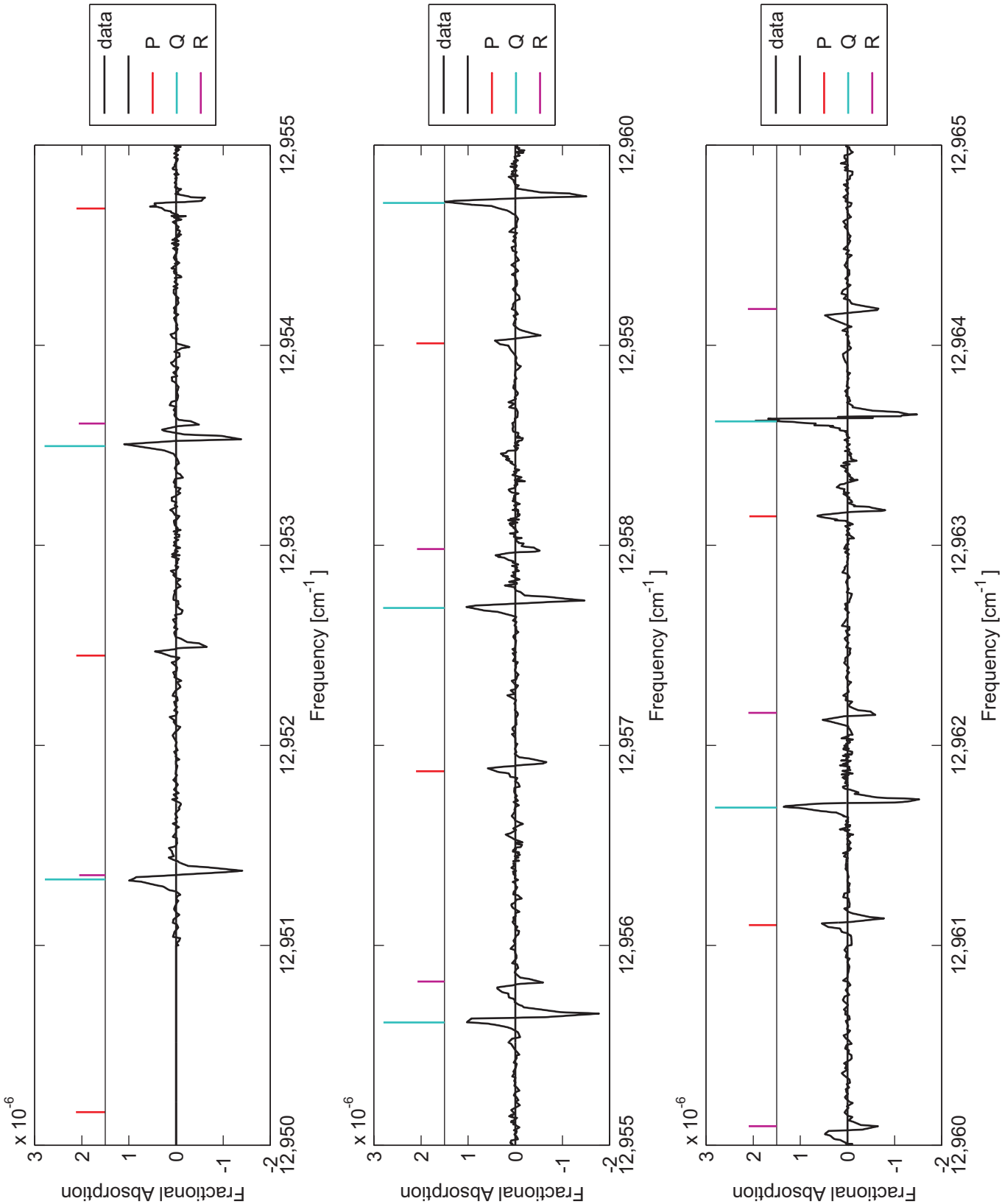
data
P
Q
R
x 10^-6
3
2
1
0
-1
-2
Fractional Absorption
12,950
12,951
12,952
12,953
12,954
12,955
Frequency [cm^-1]
12,955
12,956
12,957
12,958
12,959
12,960
12,960
12,961
12,962
12,963
12,964
12,965

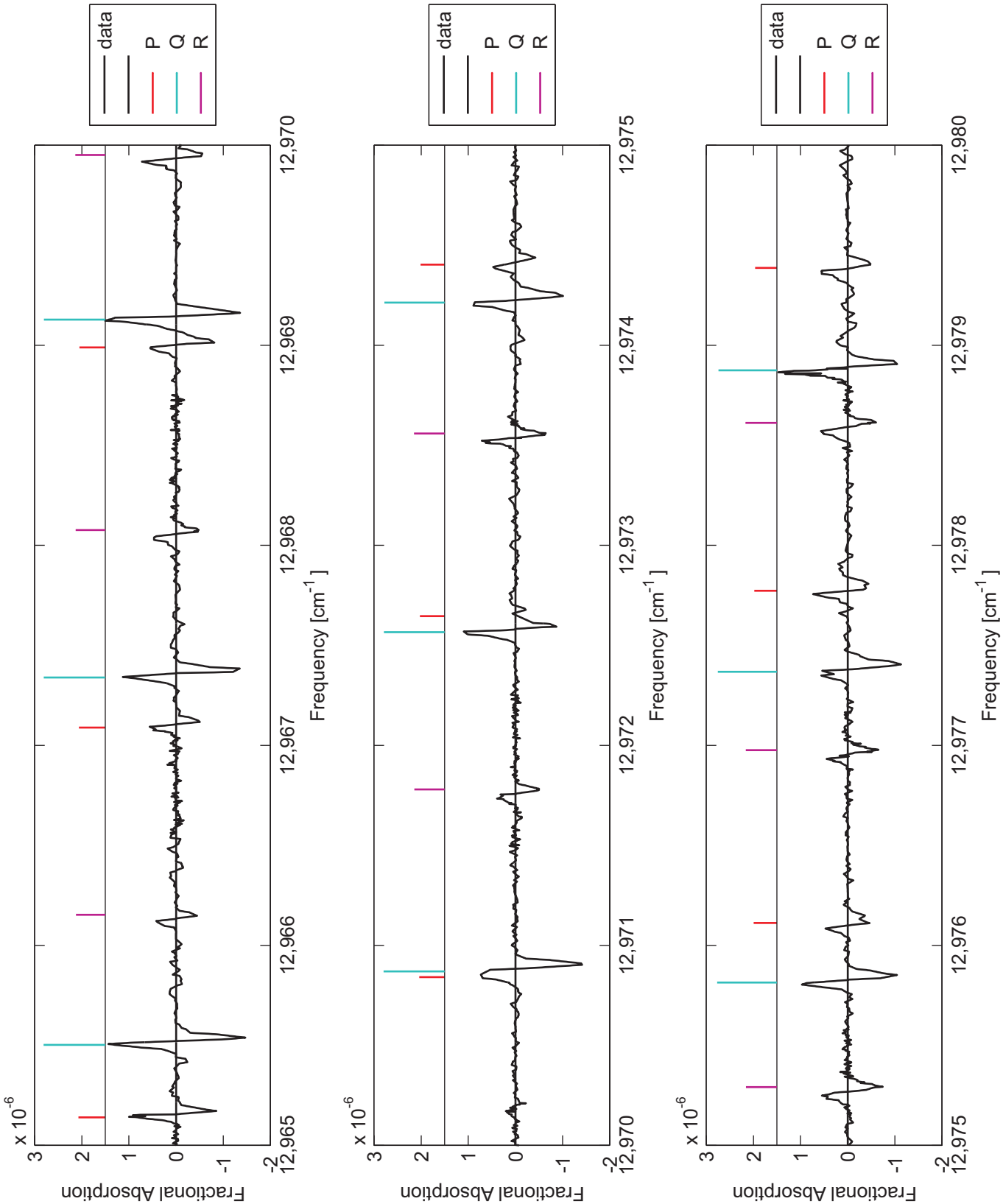
data
P
Q
R
x 10^-6
3
2
1
0
-1
-2
Fractional Absorption
12,965
12,966
12,967
12,968
12,969
12,970
Frequency [cm^-1]
data
P
Q
R
x 10^-6
3
2
1
0
-1
-2
Fractional Absorption
12,970
12,971
12,972
12,973
12,974
12,975
Frequency [cm^-1]
data
P
Q
R
x 10^-6
3
2
1
0
-1
-2
Fractional Absorption
12,975
12,976
12,977
12,978
12,979
12,980
Frequency [cm^-1]

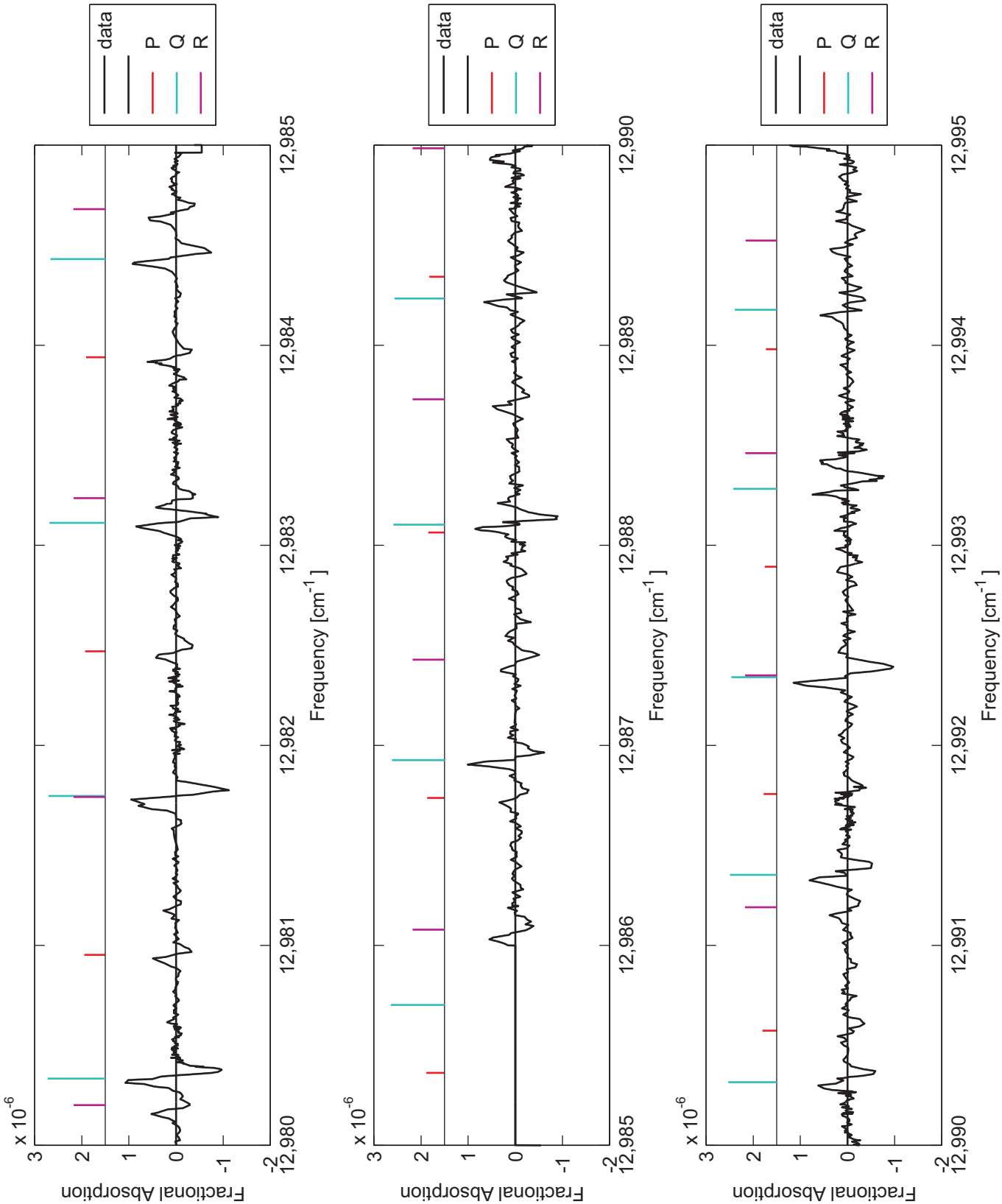
data
P
Q
R
x 10^-6
3
2
1
0
-1
-2
Fractional Absorption
12,980
12,981
12,982
12,983
12,984
12,985
Frequency [cm^-1]
12,985
12,986
12,987
12,988
12,989
12,990
12,990
12,991
12,992
12,993
12,994
12,995

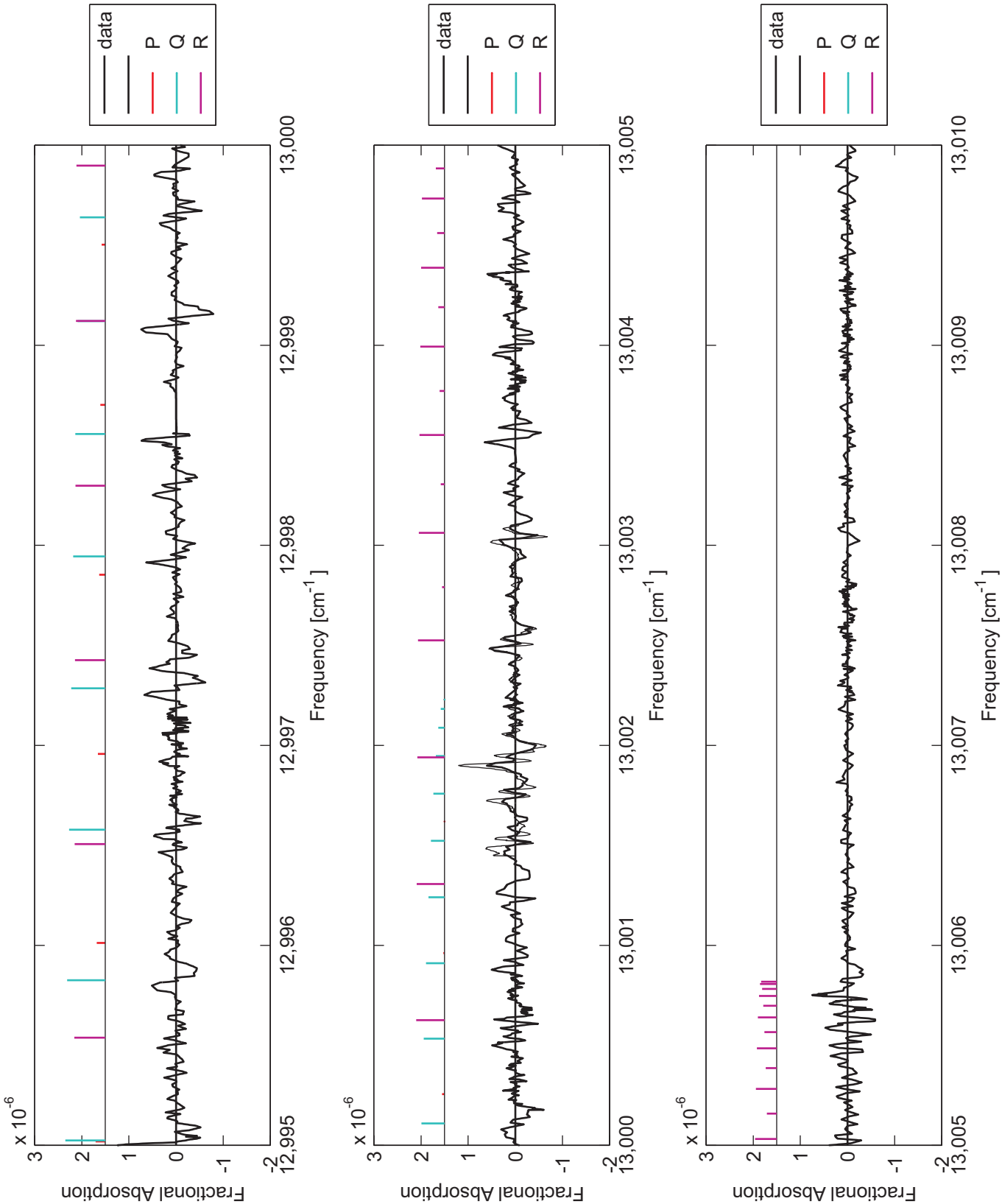
data
P
Q
R
x 10^-6
3
2
1
0
-1
-2
Fractional Absorption
12,995
12,996
12,997
12,998
12,999
13,000
Frequency [cm^-1]
13,000
13,001
13,002
13,003
13,004
13,005
13,005
13,006
13,007
13,008
13,009
13,010

Appendix C

Frequency Comb Velocity-Modulation Data

On the following pages, all of the data acquired with frequency comb velocity-modulation spectroscopy with HfF^+ present are plotted in 5 cm^{-1} segments. For the four HfF^+ rotational bands identified, the line positions from the fit are shown offset for clarity. The first figure shows a summary of the spectral region covered and a summary of the region containing the four identified bands. There are many unassigned weaker lines but at the time this thesis was completed it was not clear whether these indicate the presence of yet another band, or whether instead these lines are aliases from nearby high-intensity lines.

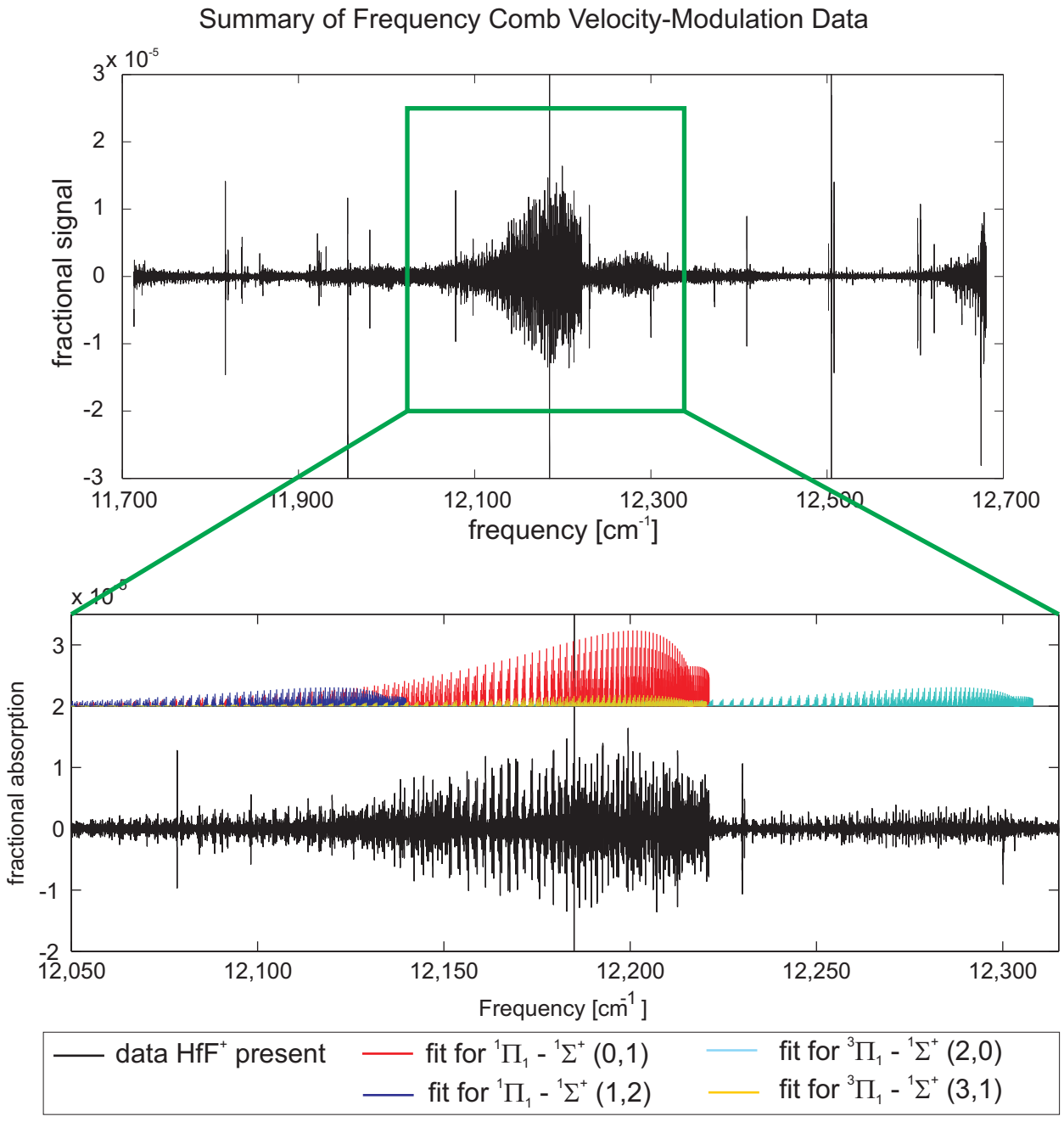
Summary of Frequency Comb Velocity-Modulation Data
x 10^-5
fractional signal
frequency [cm^-1]
fractional absorption
Frequency [cm^-1]
data HfF+ present
fit for 1Π1 - 1Σ+ (0,1)
fit for 1Π1 - 1Σ+ (1,2)
fit for 3Π1 - 1Σ+ (2,0)
fit for 3Π1 - 1Σ+ (3,1)

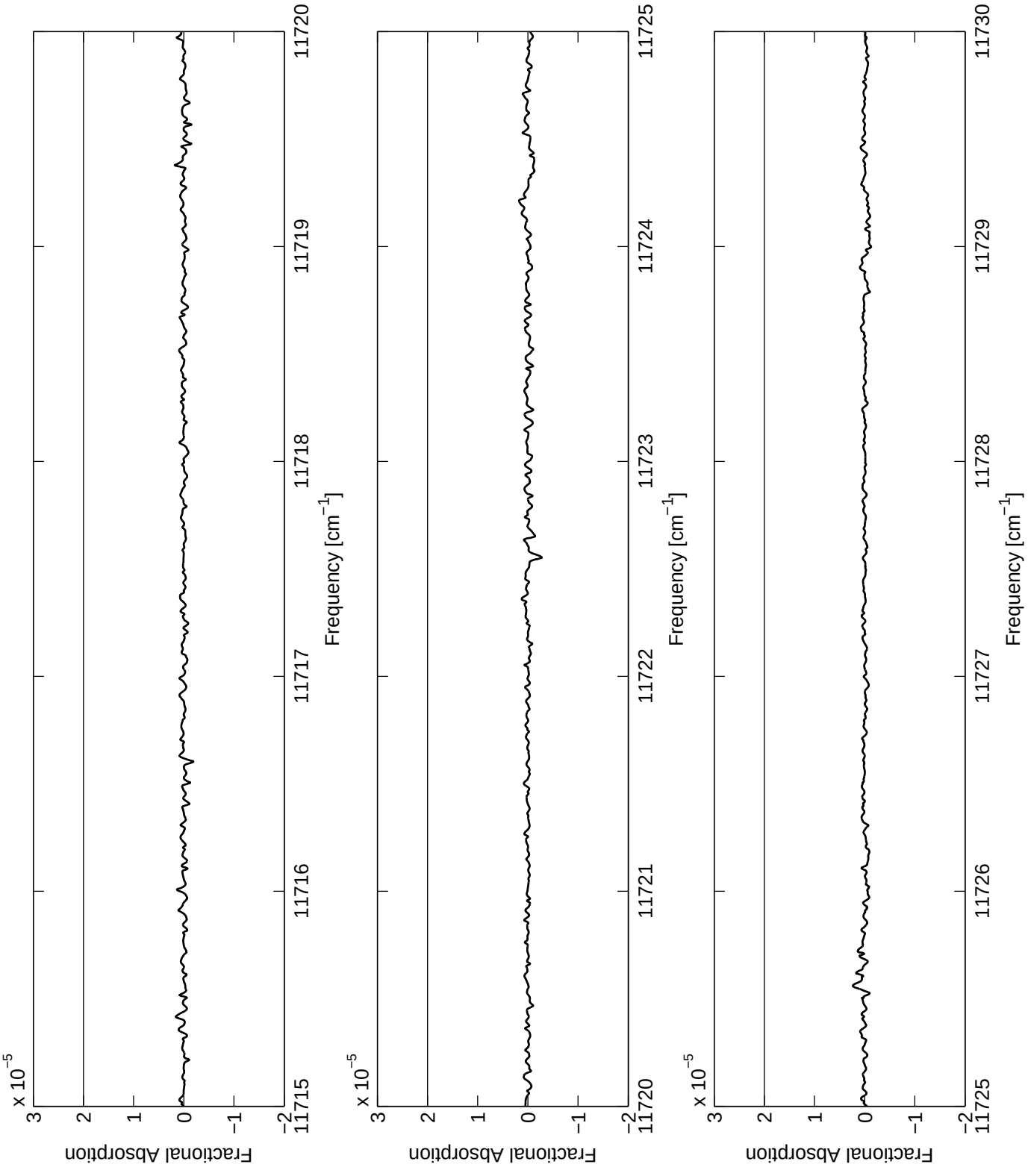
x 10^−5
3
2
1
0
−1
−2
Fractional Absorption
11715
11716
11717
11718
11719
11720
Frequency [cm^−1]
x 10^−5
3
2
1
0
−1
−2
Fractional Absorption
11720
11721
11722
11723
11724
11725
Frequency [cm^−1]
x 10^−5
3
2
1
0
−1
−2
Fractional Absorption
11725
11726
11727
11728
11729
11730
Frequency [cm^−1]

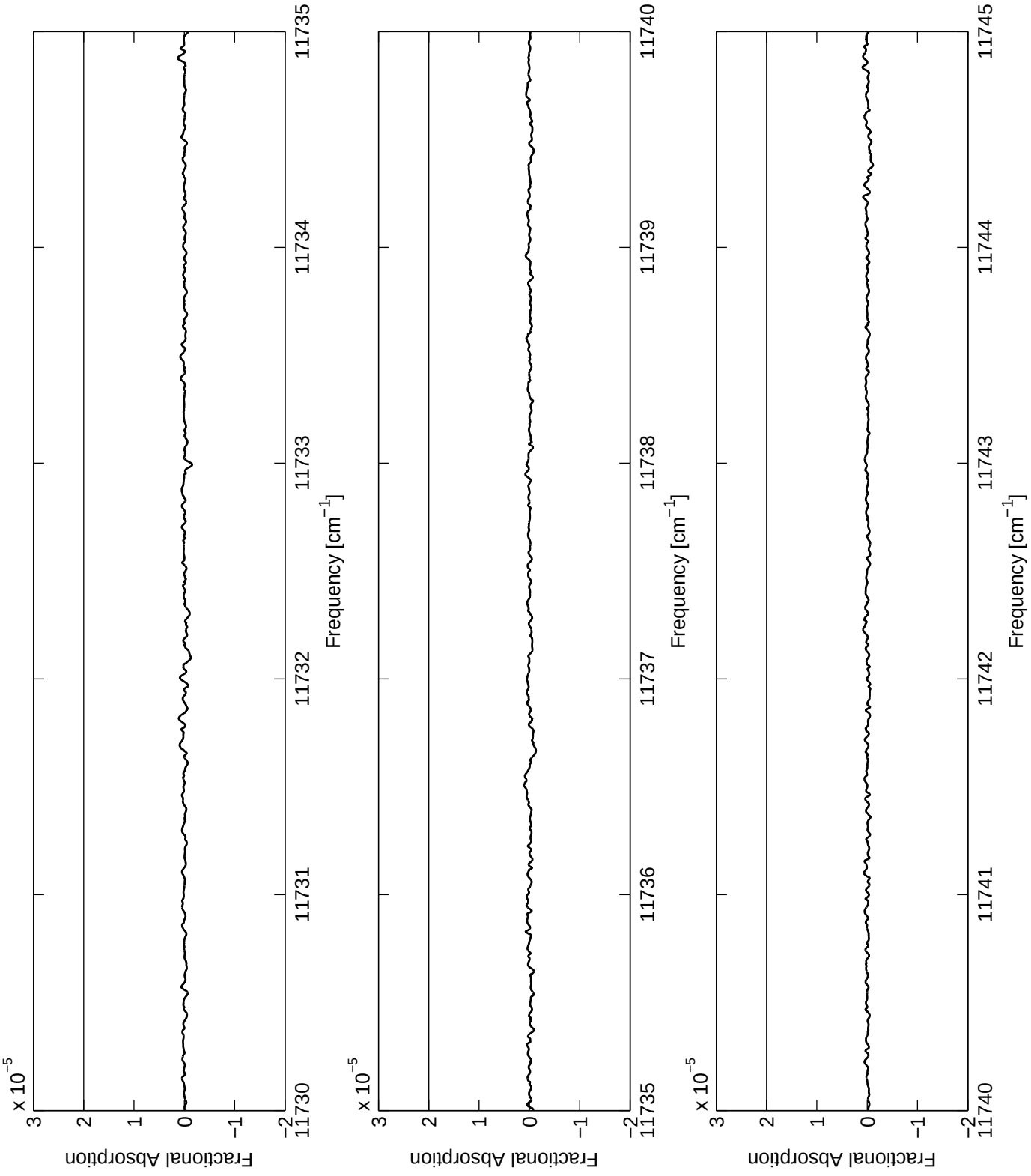
x 10^−5
3
2
1
0
−1
−2
Fractional Absorption
11730
11731
11732
11733
11734
11735
Frequency [cm^−1]
x 10^−5
3
2
1
0
−1
−2
Fractional Absorption
11735
11736
11737
11738
11739
11740
Frequency [cm^−1]
x 10^−5
3
2
1
0
−1
−2
Fractional Absorption
11740
11741
11742
11743
11744
11745
Frequency [cm^−1]

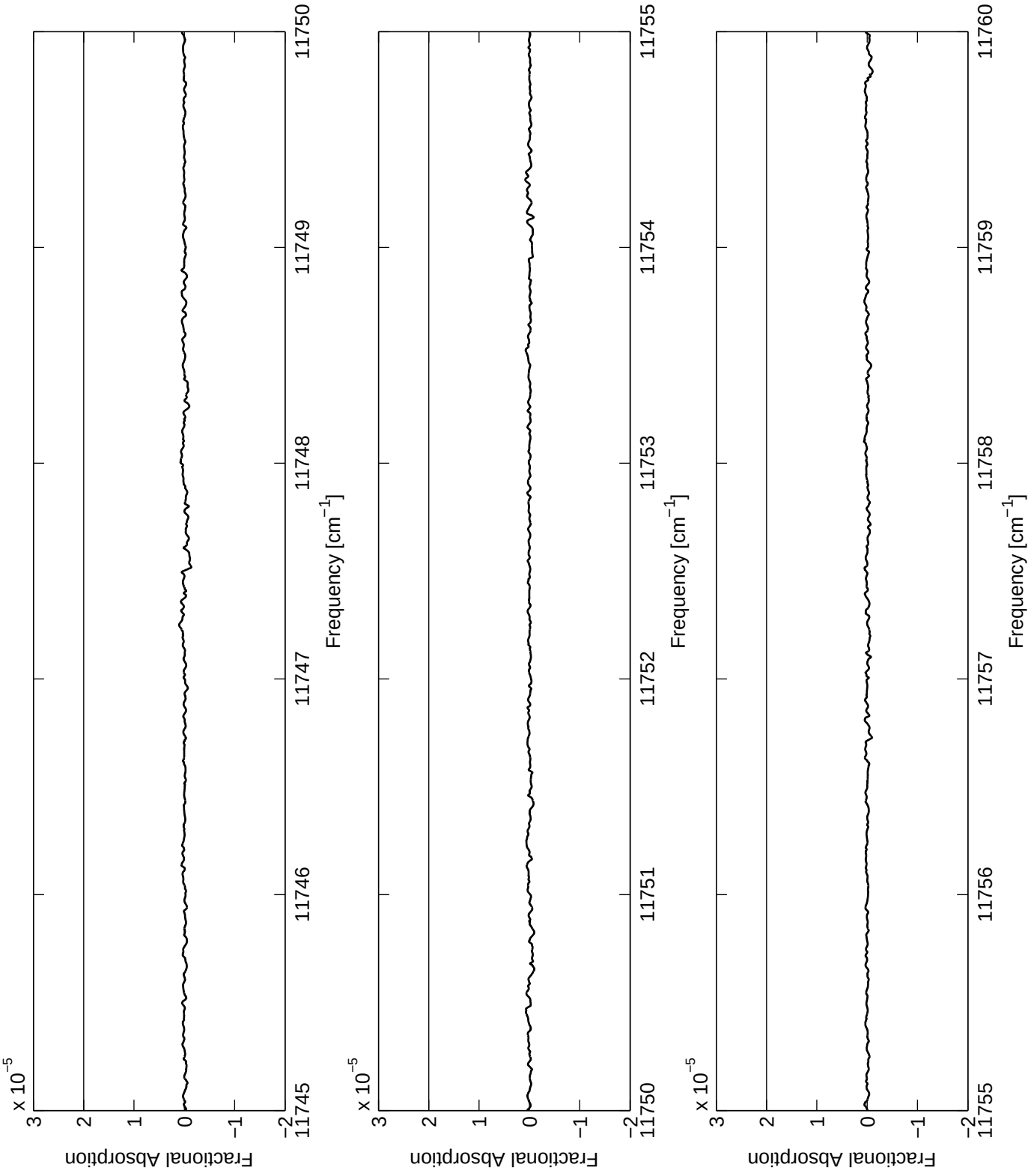
x 10^−5
3
2
1
0
−1
−2
Fractional Absorption
11745
11746
11747
11748
11749
11750
Frequency [cm^−1]
x 10^−5
3
2
1
0
−1
−2
Fractional Absorption
11750
11751
11752
11753
11754
11755
Frequency [cm^−1]
x 10^−5
3
2
1
0
−1
−2
Fractional Absorption
11755
11756
11757
11758
11759
11760
Frequency [cm^−1]

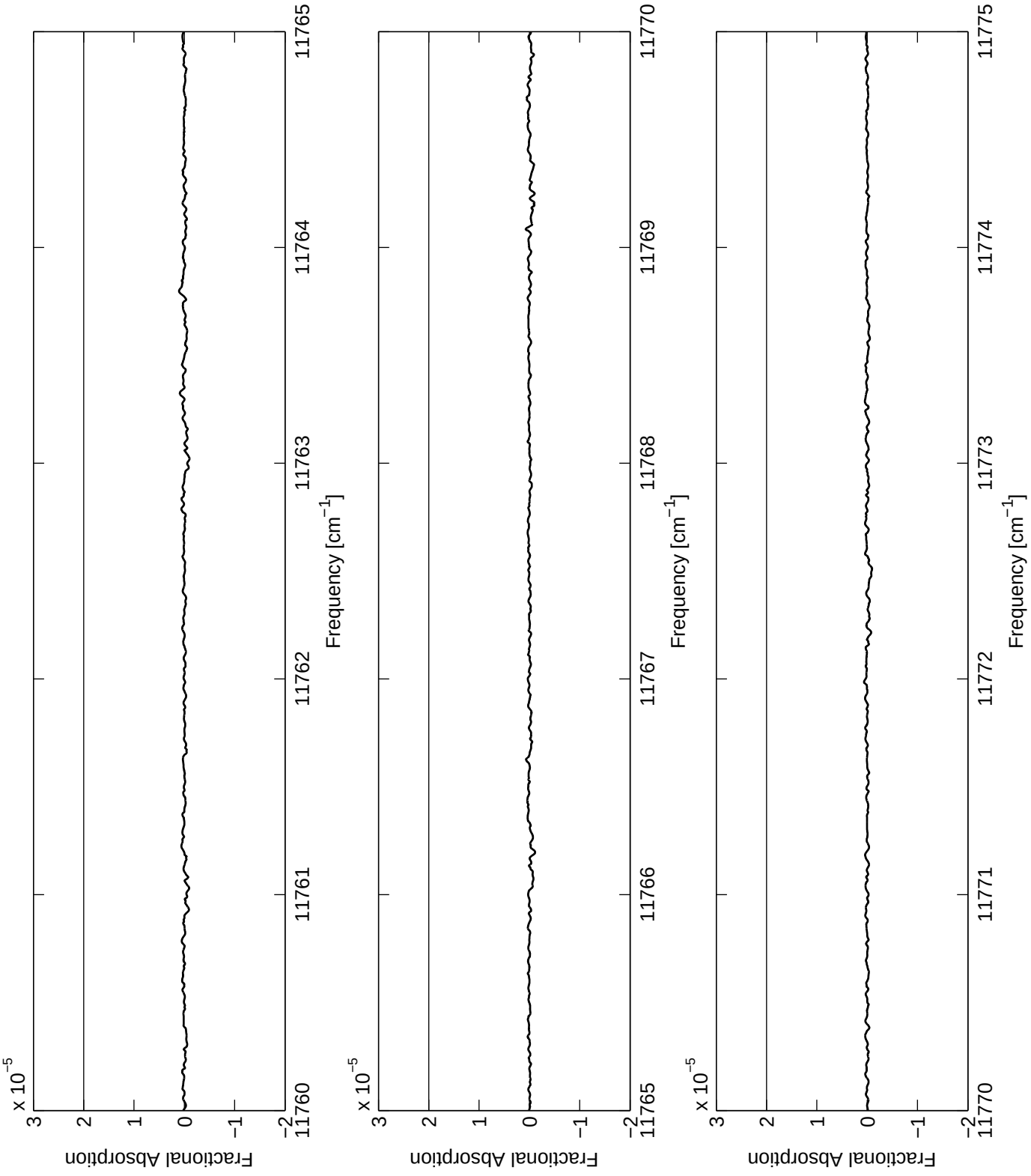
x 10^−5
3
2
1
0
−1
−2
Fractional Absorption
11760
11761
11762
11763
11764
11765
Frequency [cm^−1]
x 10^−5
3
2
1
0
−1
−2
Fractional Absorption
11765
11766
11767
11768
11769
11770
Frequency [cm^−1]
x 10^−5
3
2
1
0
−1
−2
Fractional Absorption
11770
11771
11772
11773
11774
11775
Frequency [cm^−1]

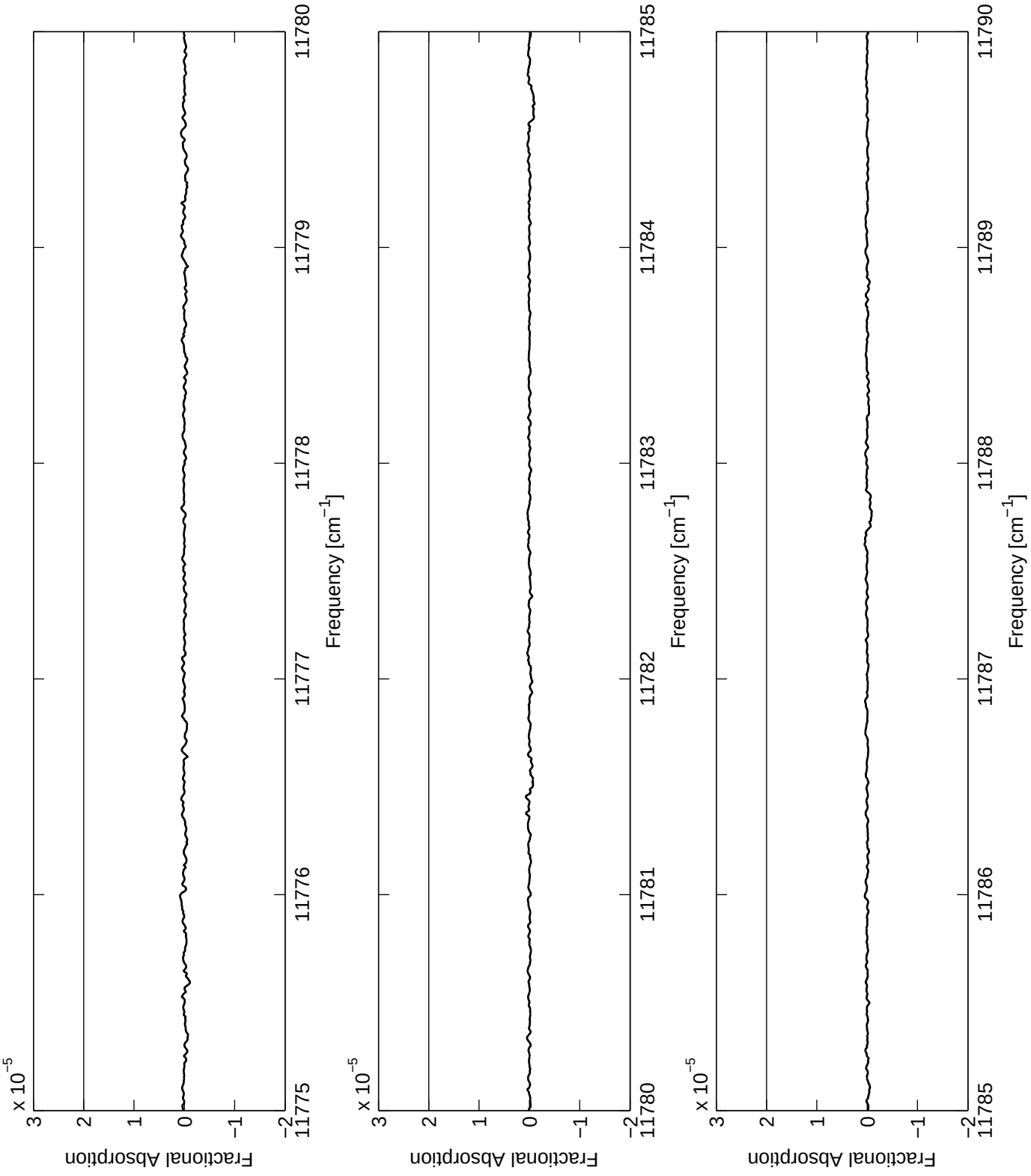
x 10^−5
3
2
1
0
−1
−2
Fractional Absorption
11775
11776
11777
11778
11779
11780
Frequency [cm^−1]
x 10^−5
3
2
1
0
−1
−2
Fractional Absorption
11780
11781
11782
11783
11784
11785
Frequency [cm^−1]
x 10^−5
3
2
1
0
−1
−2
Fractional Absorption
11785
11786
11787
11788
11789
11790
Frequency [cm^−1]

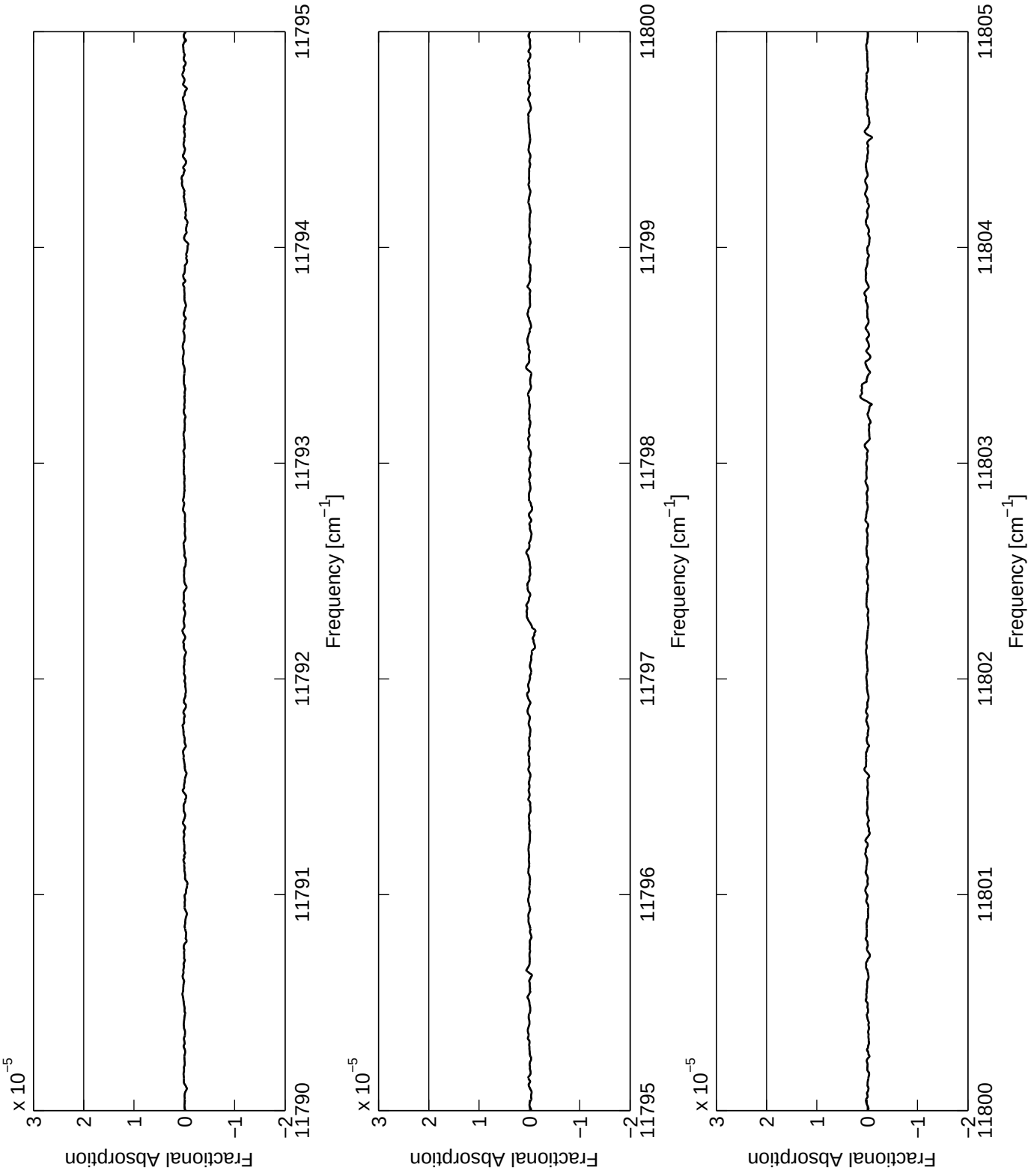
x 10^−5
3
2
1
0
−1
−2
Fractional Absorption
11790
11791
11792
11793
11794
11795
Frequency [cm^−1]
x 10^−5
3
2
1
0
−1
−2
Fractional Absorption
11795
11796
11797
11798
11799
11800
Frequency [cm^−1]
x 10^−5
3
2
1
0
−1
−2
Fractional Absorption
11800
11801
11802
11803
11804
11805
Frequency [cm^−1]

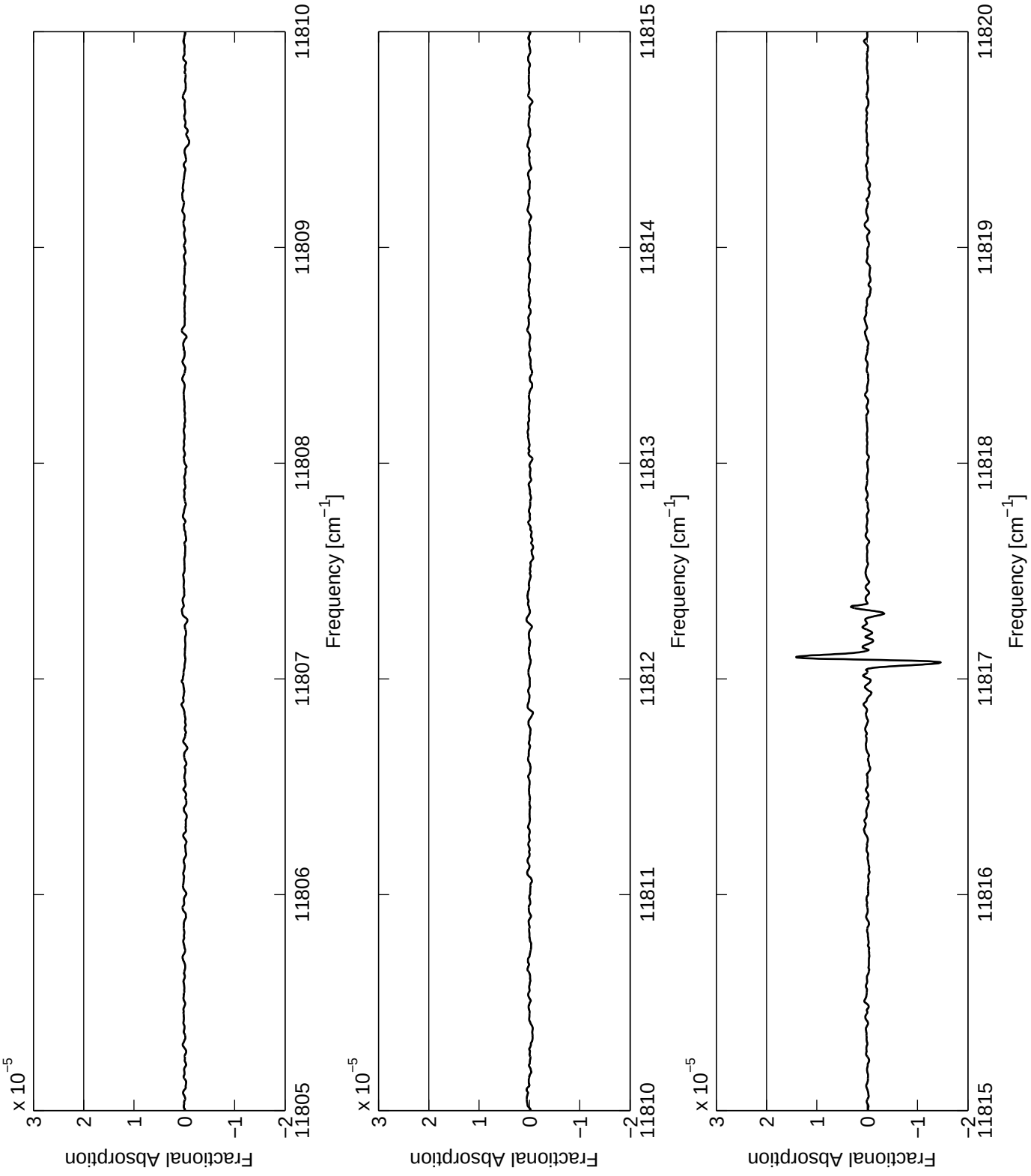
x 10^−5
3
2
1
0
−1
−2
Fractional Absorption
11805
11806
11807
11808
11809
11810
Frequency [cm^−1]
x 10^−5
3
2
1
0
−1
−2
Fractional Absorption
11810
11811
11812
11813
11814
11815
Frequency [cm^−1]
x 10^−5
3
2
1
0
−1
−2
Fractional Absorption
11815
11816
11817
11818
11819
11820
Frequency [cm^−1]

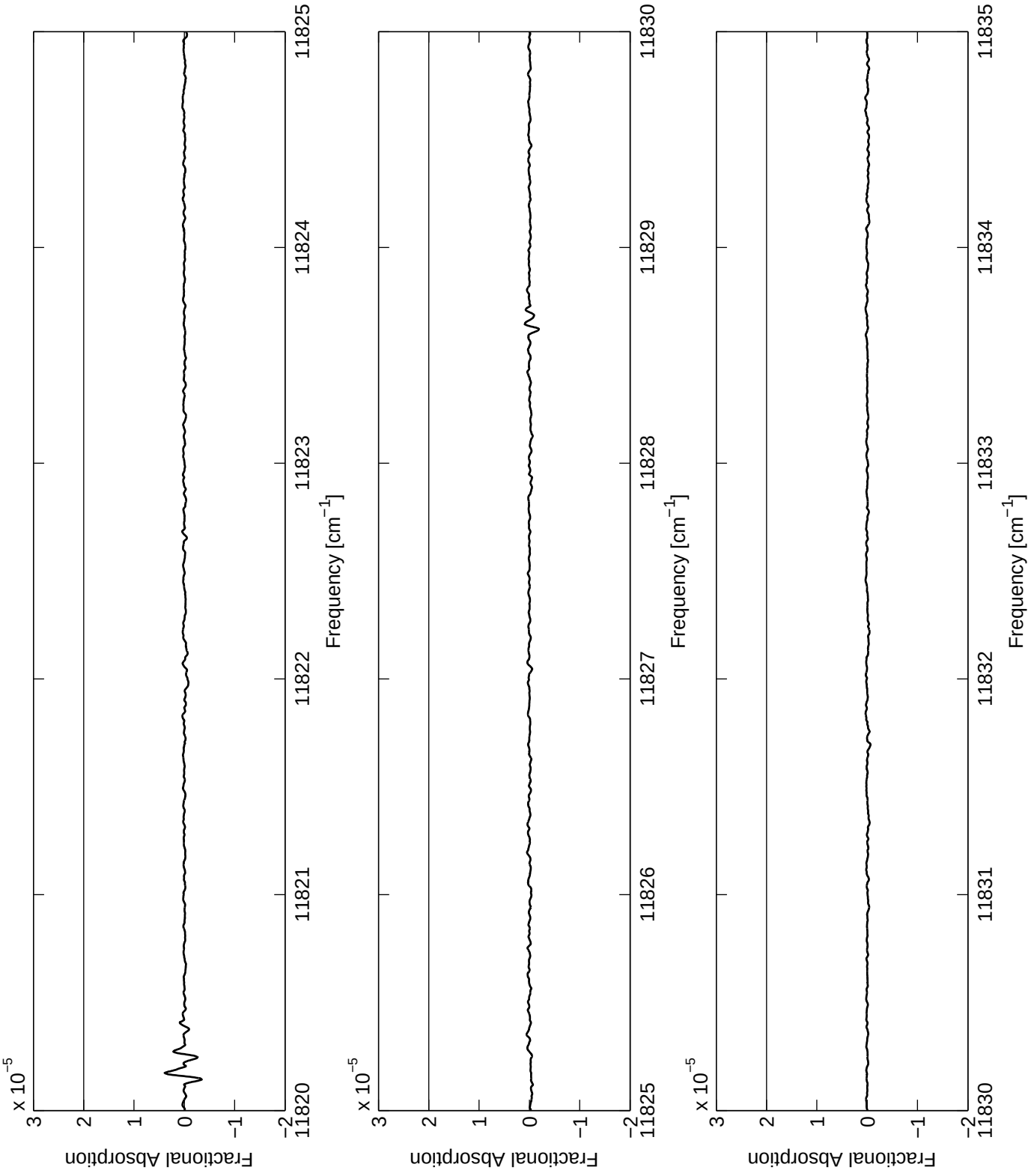
x 10^−5
3
2
1
0
−1
−2
Fractional Absorption
11820
11821
11822
11823
11824
11825
Frequency [cm^−1]
x 10^−5
3
2
1
0
−1
−2
Fractional Absorption
11825
11826
11827
11828
11829
11830
Frequency [cm^−1]
x 10^−5
3
2
1
0
−1
−2
Fractional Absorption
11830
11831
11832
11833
11834
11835
Frequency [cm^−1]

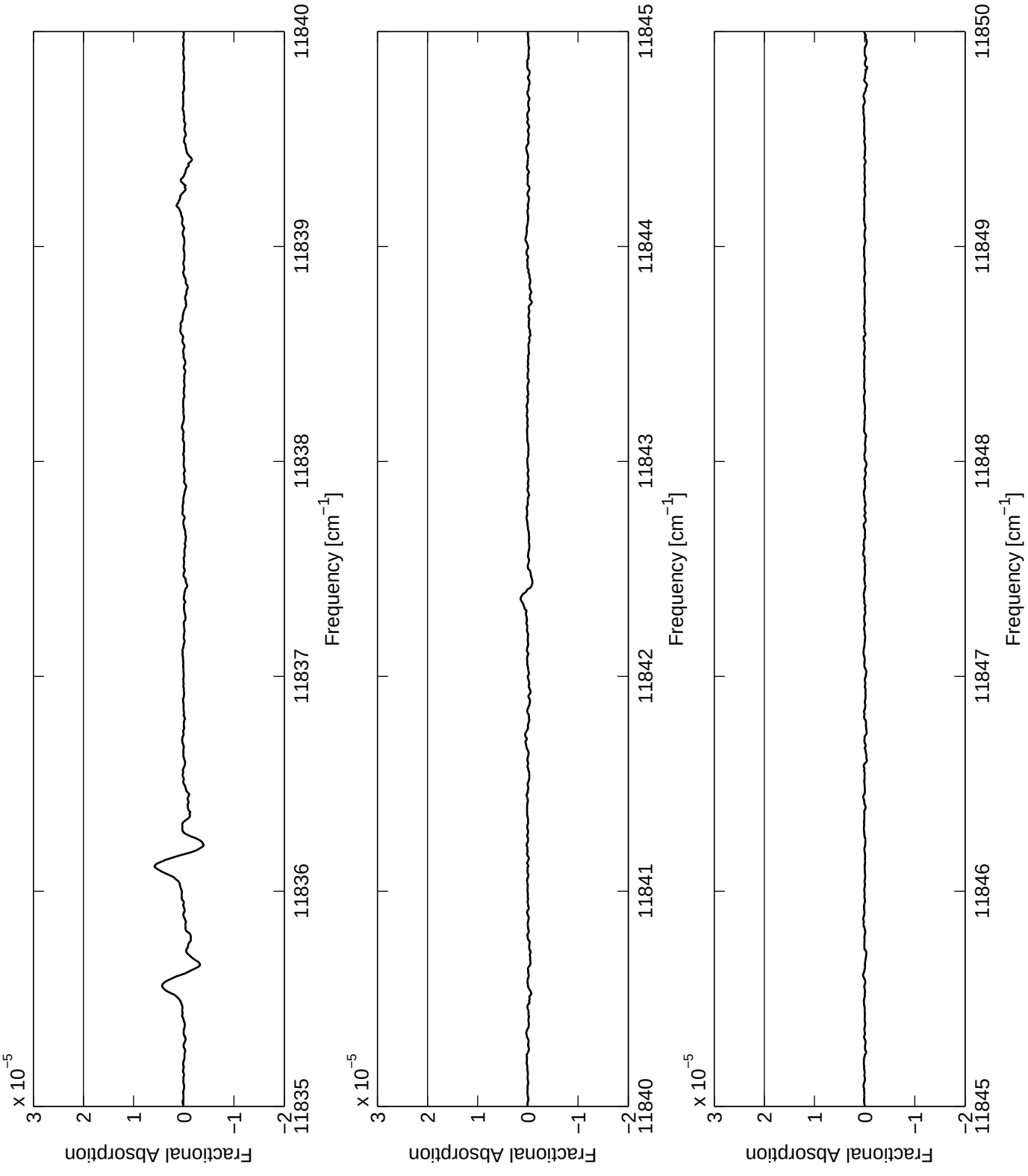
x 10^−5
3
2
1
0
−1
−2
Fractional Absorption
11835
11836
11837
11838
11839
11840
Frequency [cm^−1]
x 10^−5
3
2
1
0
−1
−2
Fractional Absorption
11840
11841
11842
11843
11844
11845
Frequency [cm^−1]
x 10^−5
3
2
1
0
−1
−2
Fractional Absorption
11845
11846
11847
11848
11849
11850
Frequency [cm^−1]

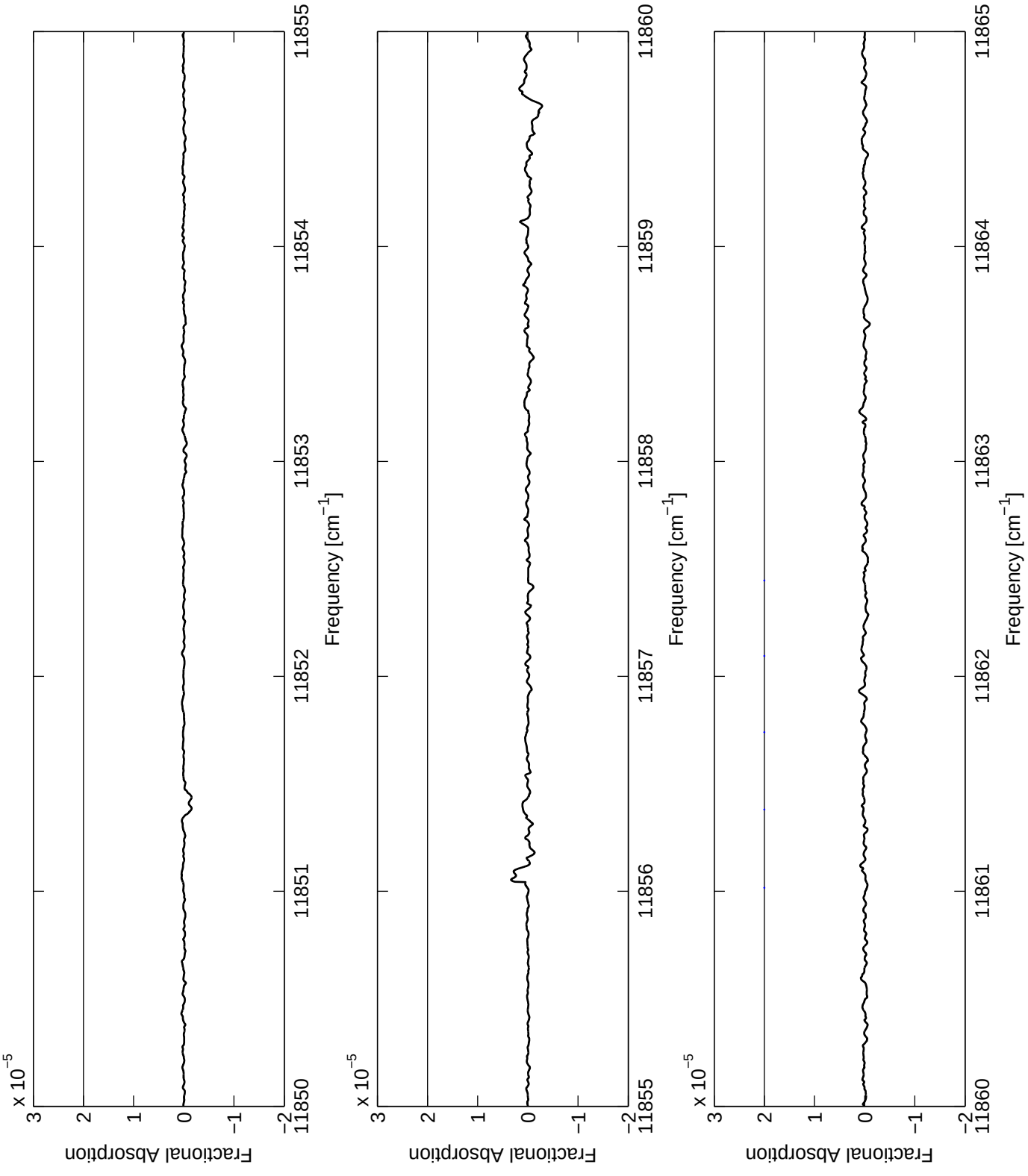
x 10^−5
3
2
1
0
−1
−2
Fractional Absorption
11850
11851
11852
11853
11854
11855
Frequency [cm^−1]
x 10^−5
3
2
1
0
−1
−2
Fractional Absorption
11855
11856
11857
11858
11859
11860
Frequency [cm^−1]
x 10^−5
3
2
1
0
−1
−2
Fractional Absorption
11860
11861
11862
11863
11864
11865
Frequency [cm^−1]

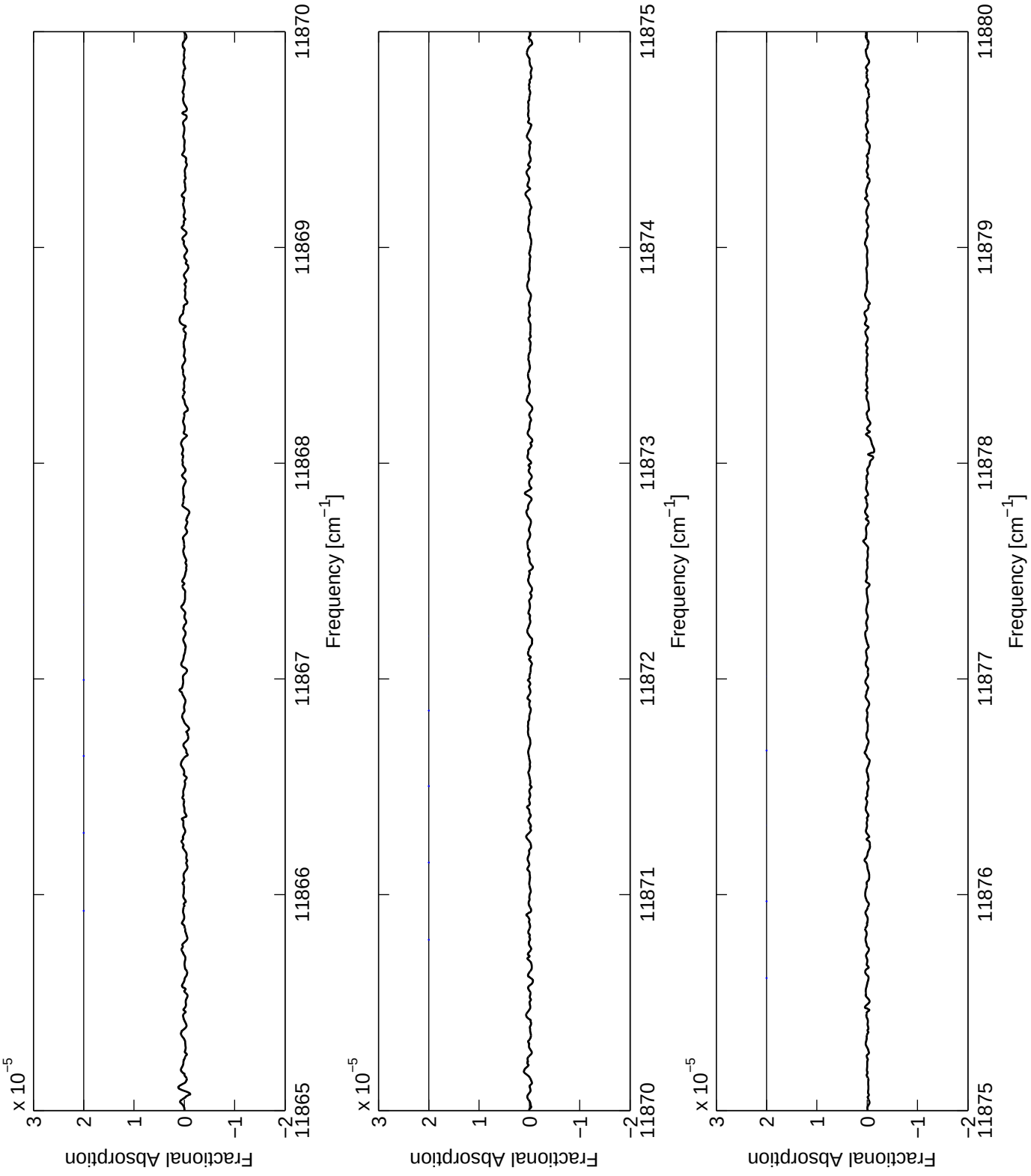
x 10^−5
3
2
1
0
−1
−2
Fractional Absorption
11865
11866
11867
11868
11869
11870
Frequency [cm^−1]
11870
11871
11872
11873
11874
11875
11875
11876
11877
11878
11879
11880

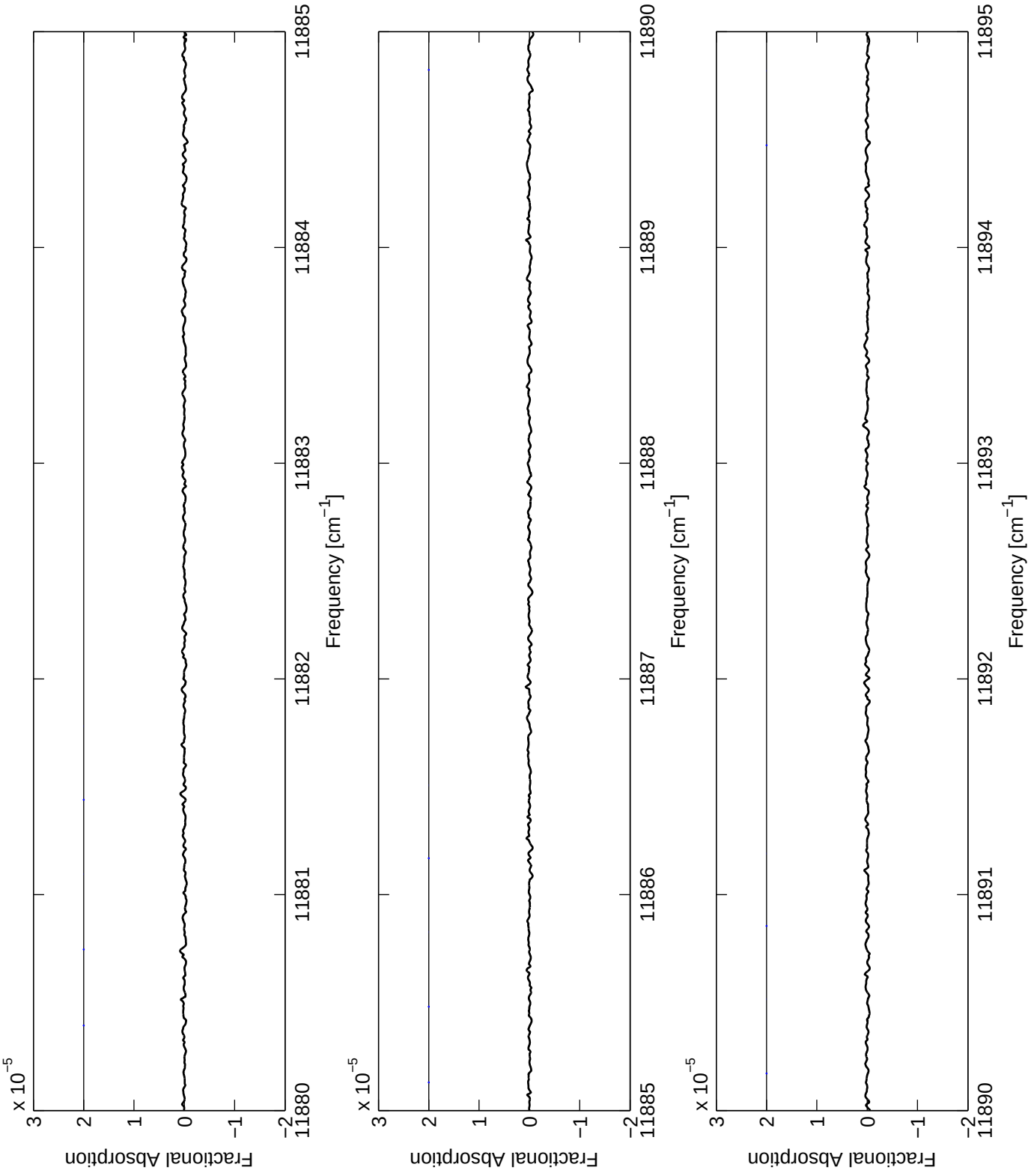
x 10^−5
3
2
1
0
−1
−2
Fractional Absorption
11880
11881
11882
11883
11884
11885
Frequency [cm^−1]
x 10^−5
3
2
1
0
−1
−2
Fractional Absorption
11885
11886
11887
11888
11889
11890
Frequency [cm^−1]
x 10^−5
3
2
1
0
−1
−2
Fractional Absorption
11890
11891
11892
11893
11894
11895
Frequency [cm^−1]

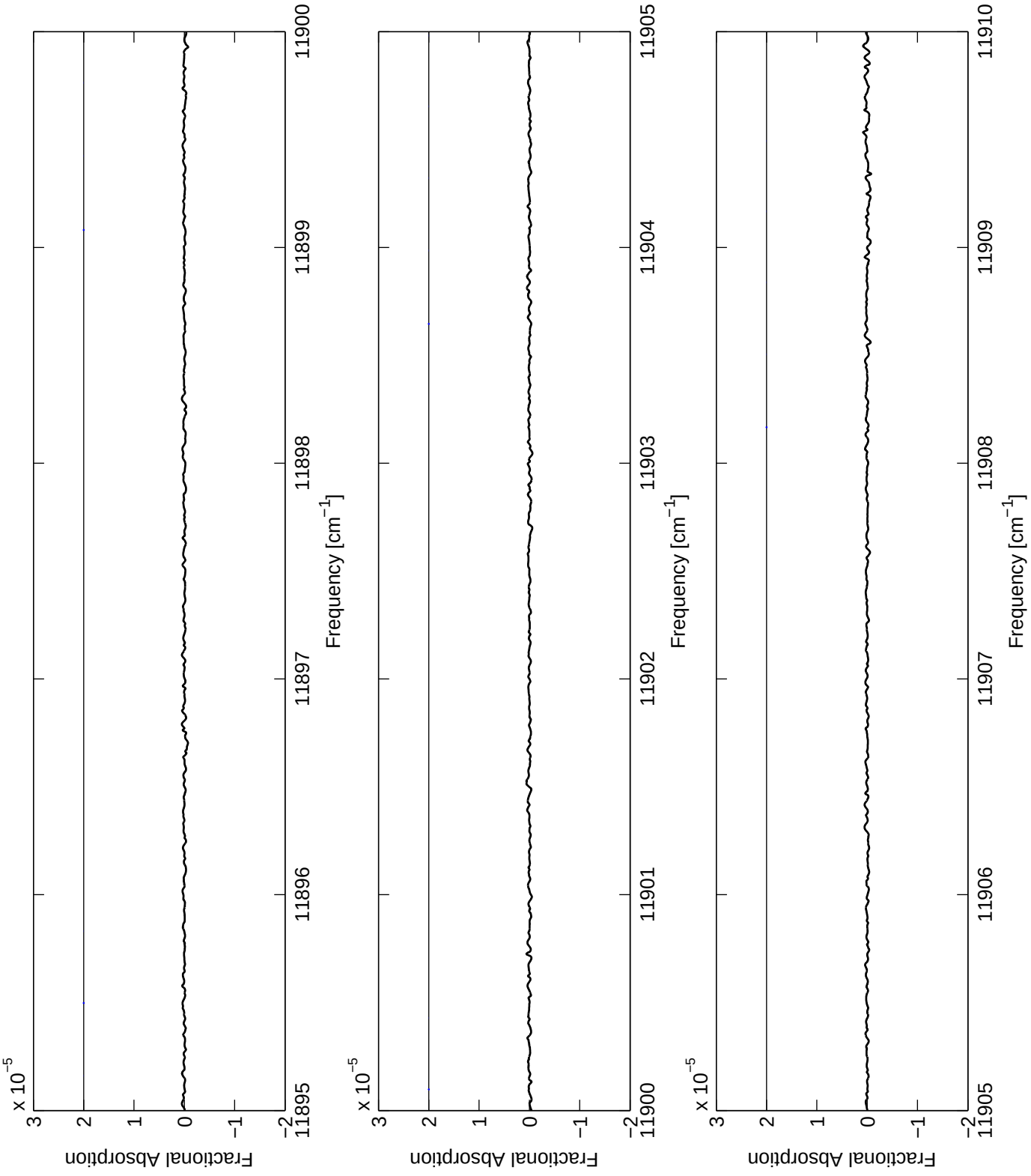
x 10^−5
3
2
1
0
−1
−2
Fractional Absorption
11895
11896
11897
11898
11899
11900
Frequency [cm^−1]
x 10^−5
3
2
1
0
−1
−2
Fractional Absorption
11900
11901
11902
11903
11904
11905
Frequency [cm^−1]
x 10^−5
3
2
1
0
−1
−2
Fractional Absorption
11905
11906
11907
11908
11909
11910
Frequency [cm^−1]

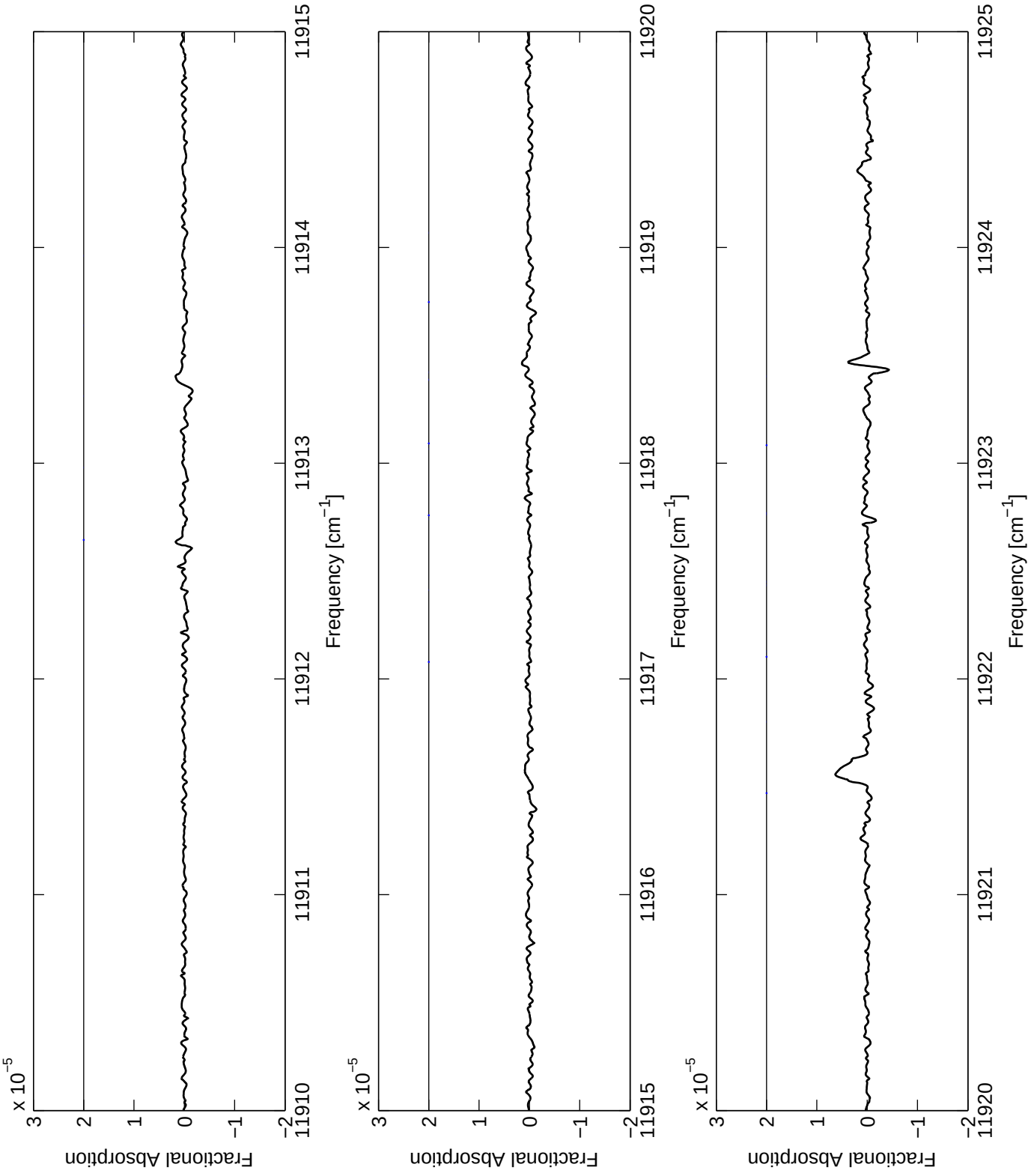
x 10^−5
3
2
1
0
−1
−2
Fractional Absorption
11910
11911
11912
11913
11914
11915
Frequency [cm^−1]
x 10^−5
3
2
1
0
−1
−2
Fractional Absorption
11915
11916
11917
11918
11919
11920
Frequency [cm^−1]
x 10^−5
3
2
1
0
−1
−2
Fractional Absorption
11920
11921
11922
11923
11924
11925
Frequency [cm^−1]

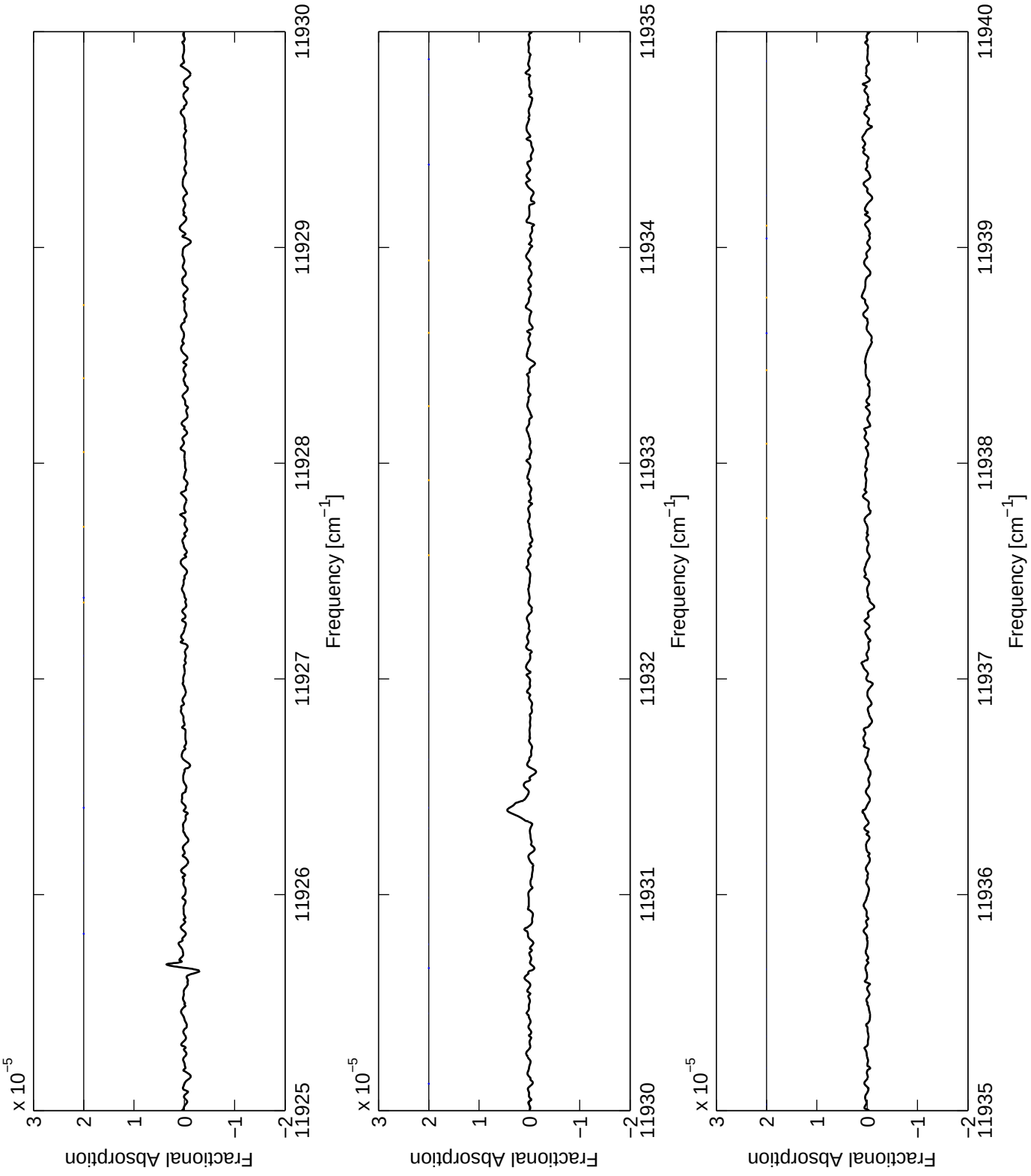
x 10^−5
3
2
1
0
−1
−2
Fractional Absorption
11925
11926
11927
11928
11929
11930
Frequency [cm^−1]
x 10^−5
3
2
1
0
−1
−2
Fractional Absorption
11930
11931
11932
11933
11934
11935
Frequency [cm^−1]
x 10^−5
3
2
1
0
−1
−2
Fractional Absorption
11935
11936
11937
11938
11939
11940
Frequency [cm^−1]

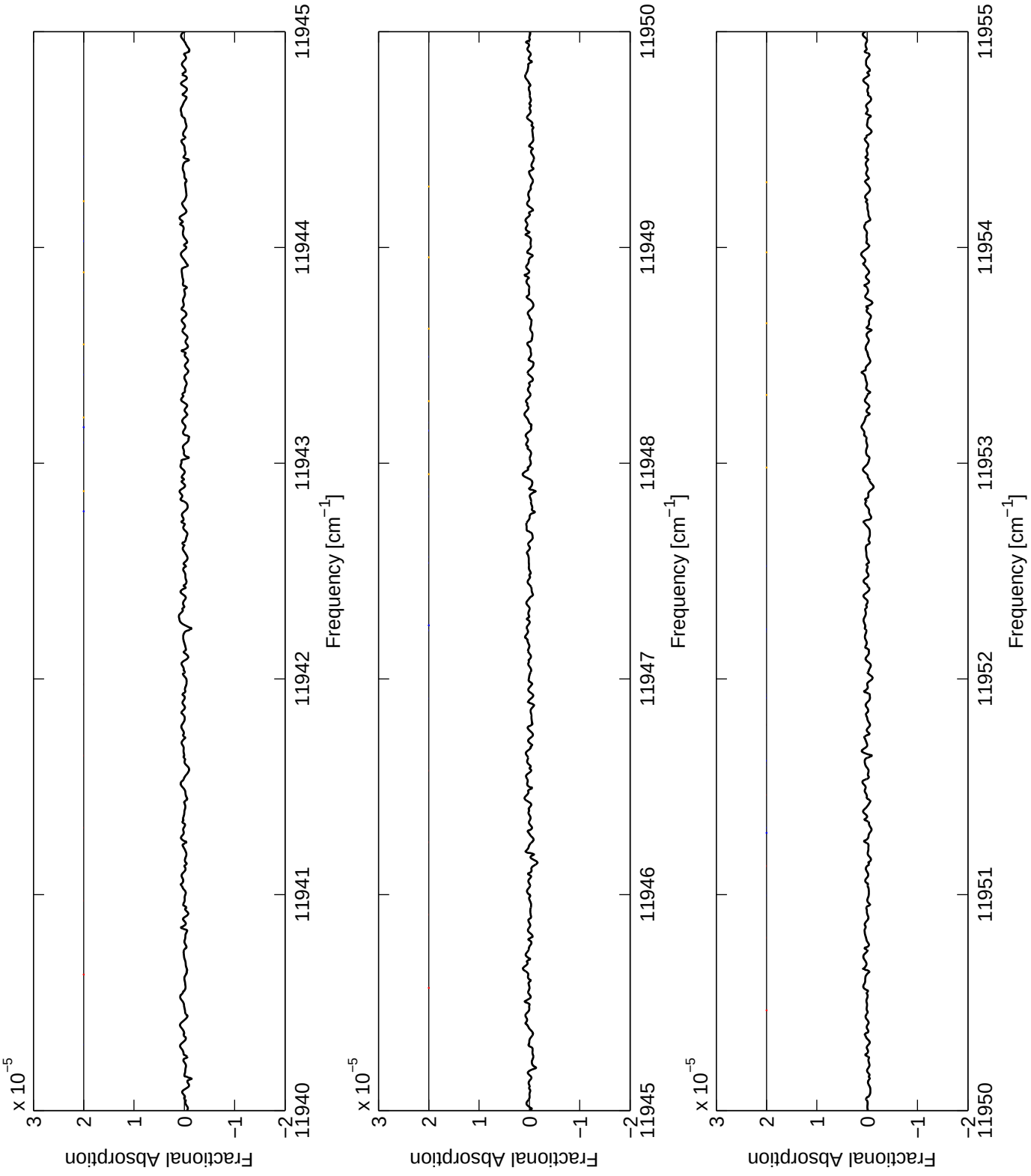
x 10^−5
3
2
1
0
−1
−2
Fractional Absorption
11940
11941
11942
11943
11944
11945
Frequency [cm^−1]
x 10^−5
3
2
1
0
−1
−2
Fractional Absorption
11945
11946
11947
11948
11949
11950
Frequency [cm^−1]
x 10^−5
3
2
1
0
−1
−2
Fractional Absorption
11950
11951
11952
11953
11954
11955
Frequency [cm^−1]

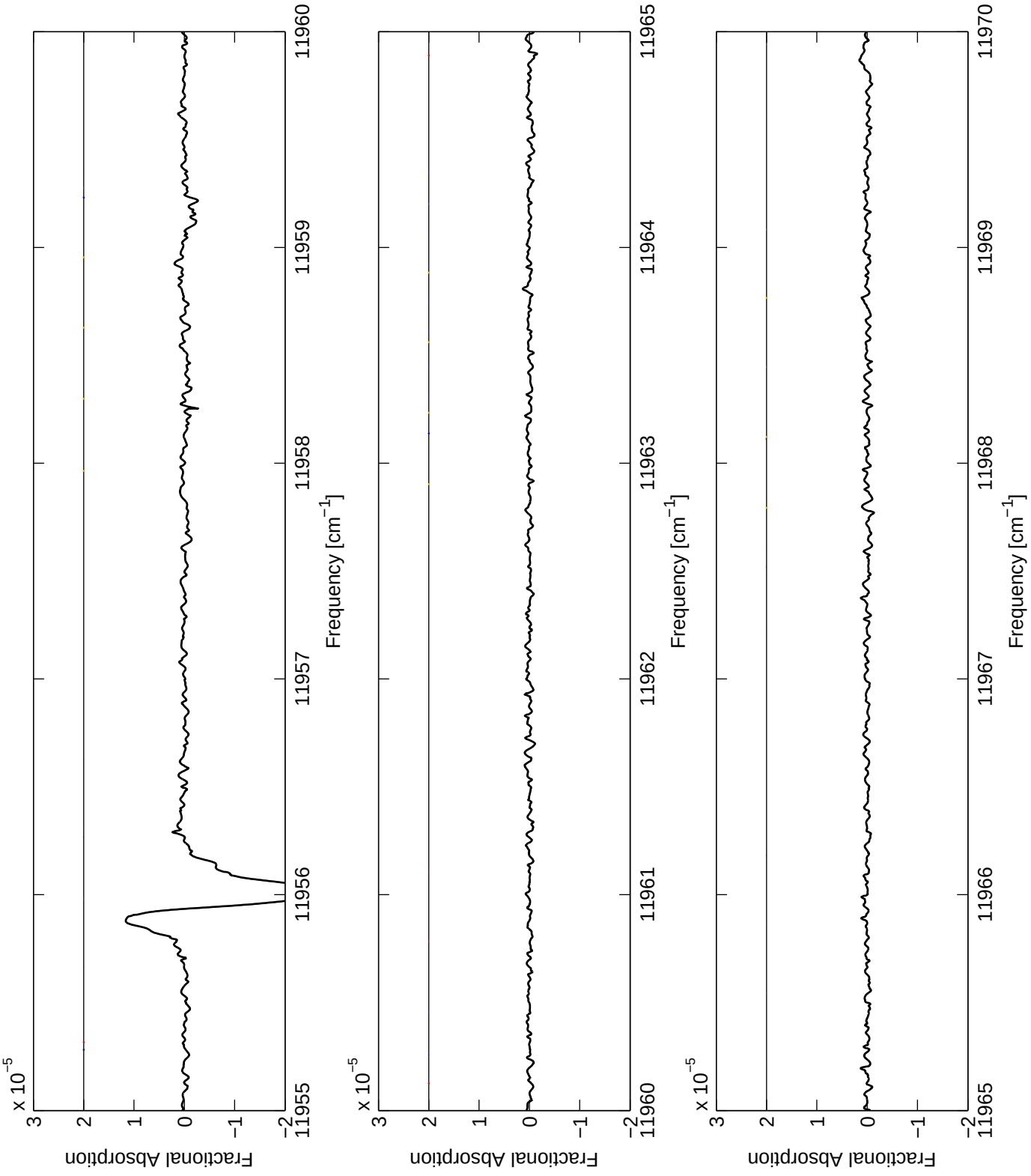
x 10^−5
3
2
1
0
−1
−2
Fractional Absorption
11955
11956
11957
11958
11959
11960
Frequency [cm^−1]
x 10^−5
3
2
1
0
−1
−2
Fractional Absorption
11960
11961
11962
11963
11964
11965
Frequency [cm^−1]
x 10^−5
3
2
1
0
−1
−2
Fractional Absorption
11965
11966
11967
11968
11969
11970
Frequency [cm^−1]

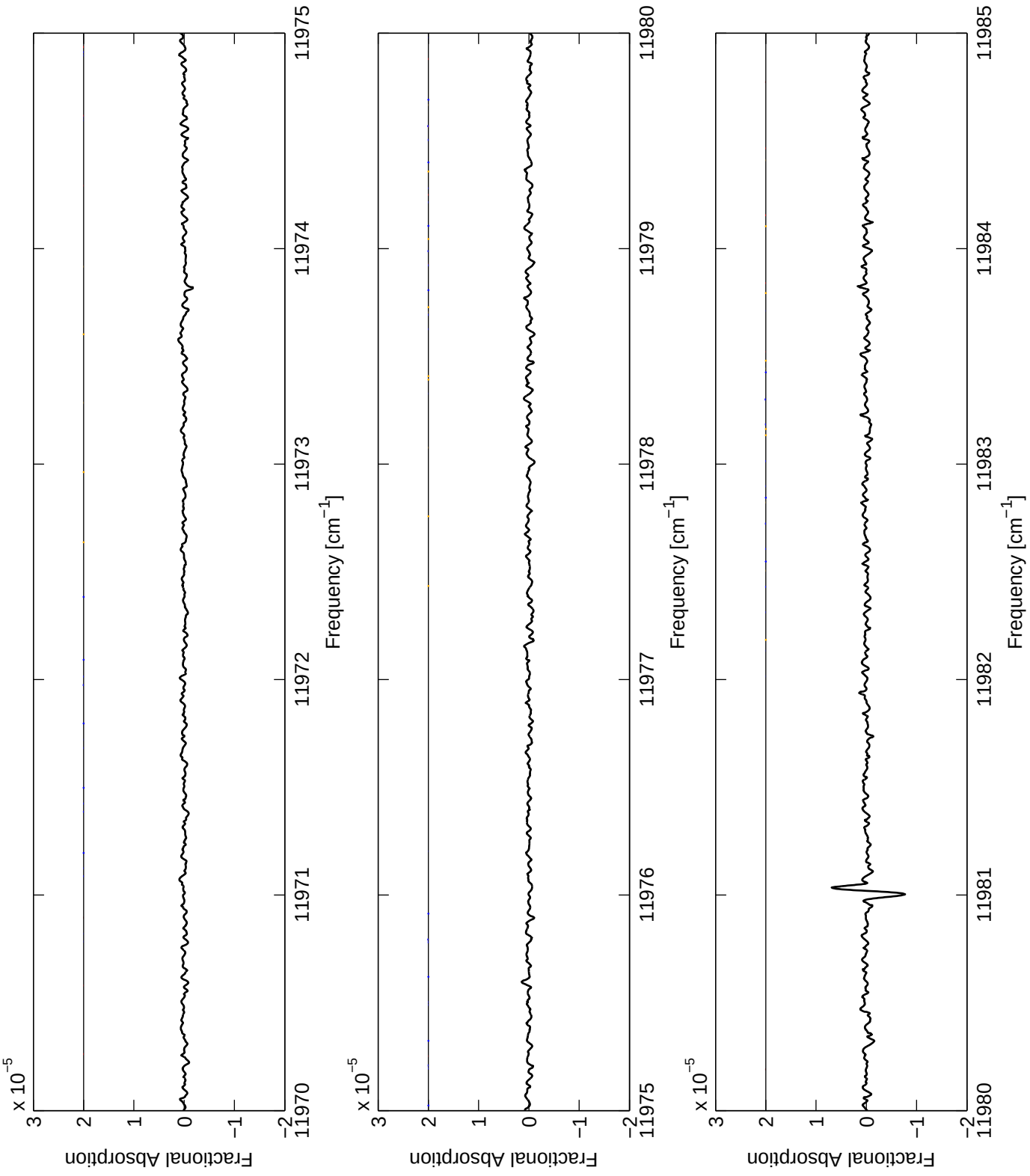
x 10^−5
3
2
1
0
−1
−2
Fractional Absorption
11970
11971
11972
11973
11974
11975
Frequency [cm^−1]
x 10^−5
3
2
1
0
−1
−2
Fractional Absorption
11975
11976
11977
11978
11979
11980
Frequency [cm^−1]
x 10^−5
3
2
1
0
−1
−2
Fractional Absorption
11980
11981
11982
11983
11984
11985
Frequency [cm^−1]

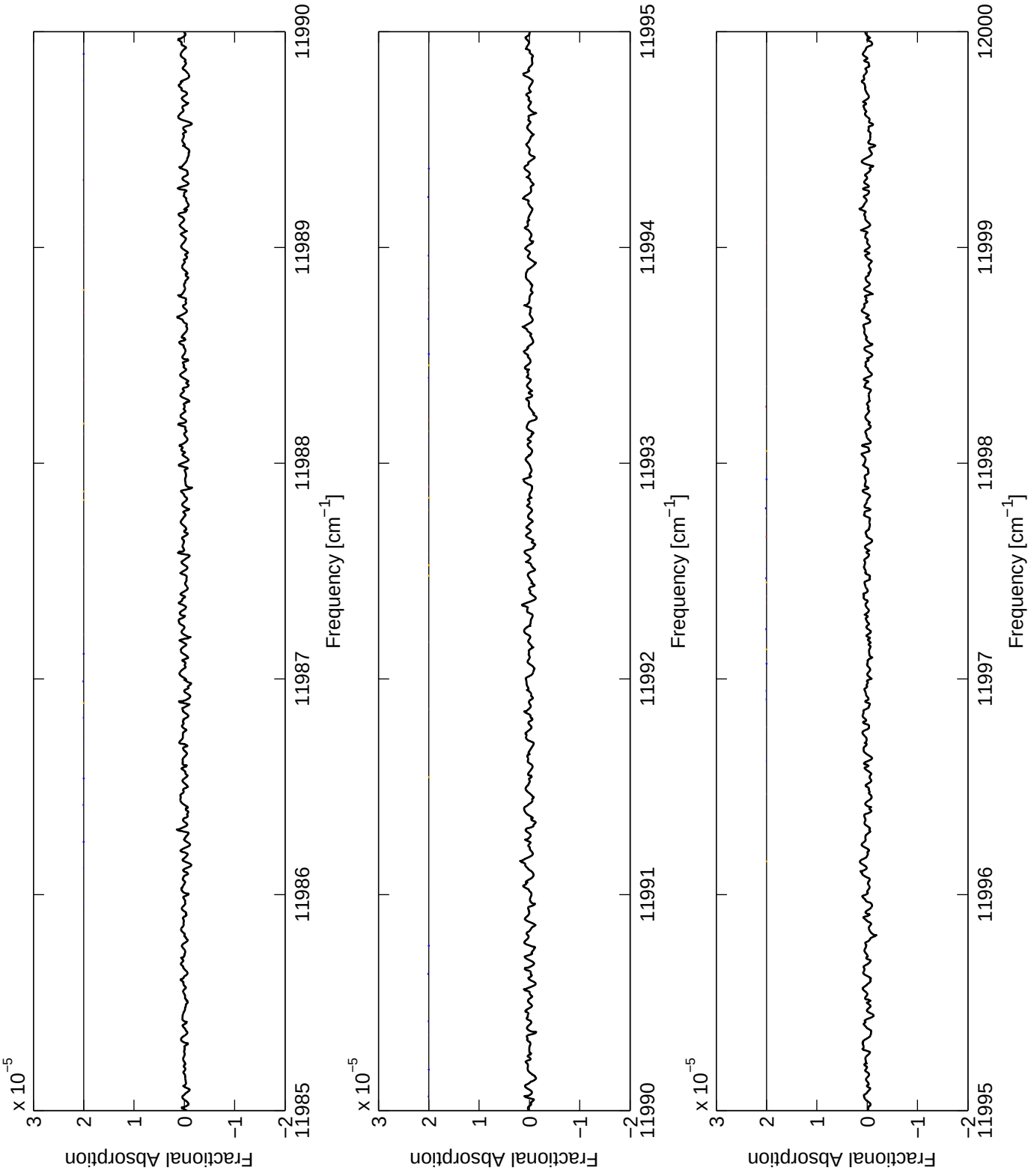
x 10^−5
3
2
1
0
−1
−2
Fractional Absorption
11985
11986
11987
11988
11989
11990
Frequency [cm^−1]
x 10^−5
3
2
1
0
−1
−2
Fractional Absorption
11990
11991
11992
11993
11994
11995
Frequency [cm^−1]
x 10^−5
3
2
1
0
−1
−2
Fractional Absorption
11995
11996
11997
11998
11999
12000
Frequency [cm^−1]

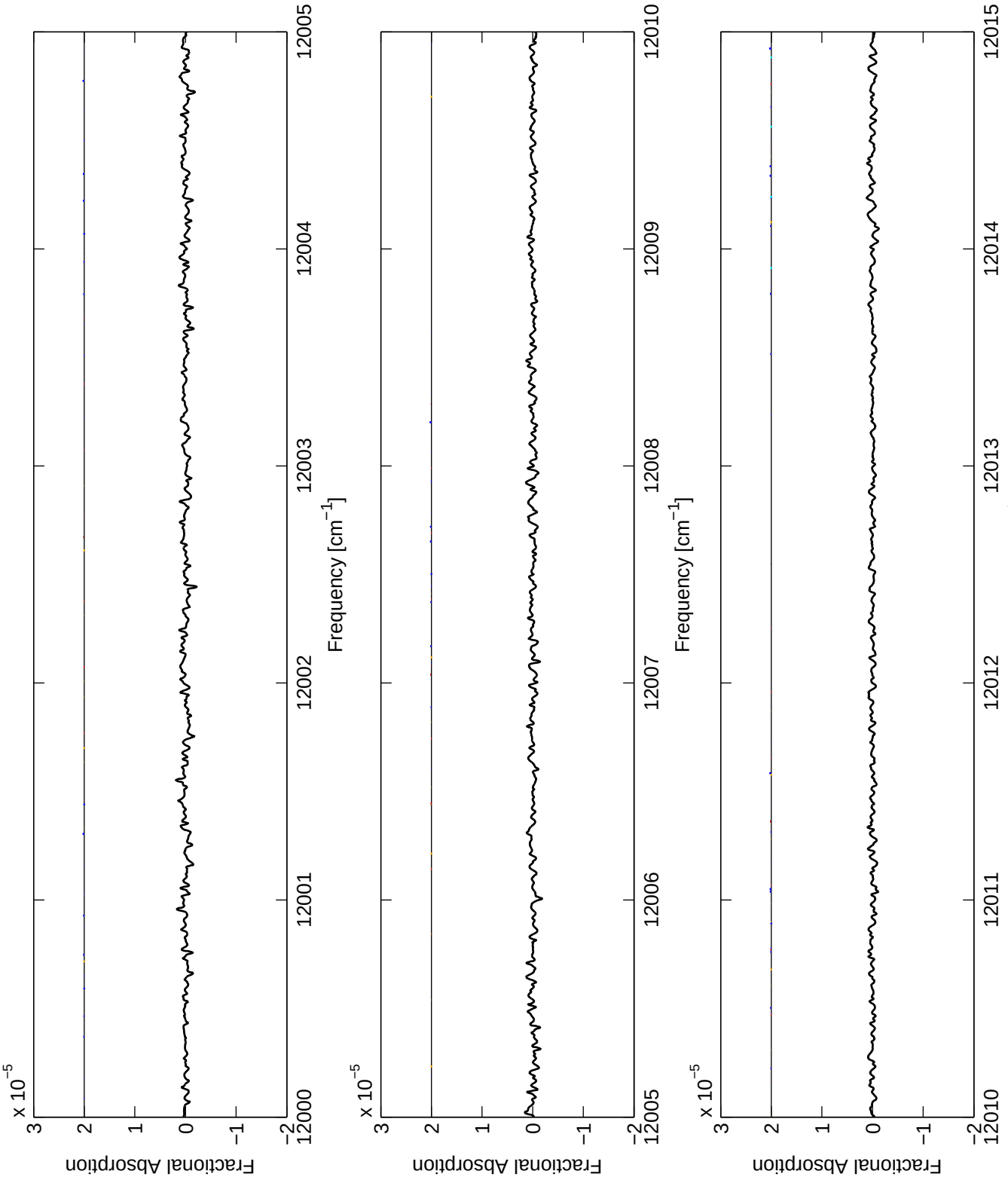
x 10^−5
3
2
1
0
−1
−2
Fractional Absorption
12000
12001
12002
12003
12004
12005
Frequency [cm^−1]
x 10^−5
3
2
1
0
−1
−2
Fractional Absorption
12005
12006
12007
12008
12009
12010
Frequency [cm^−1]
x 10^−5
3
2
1
0
−1
−2
Fractional Absorption
12010
12011
12012
12013
12014
12015
Frequency [cm^−1]

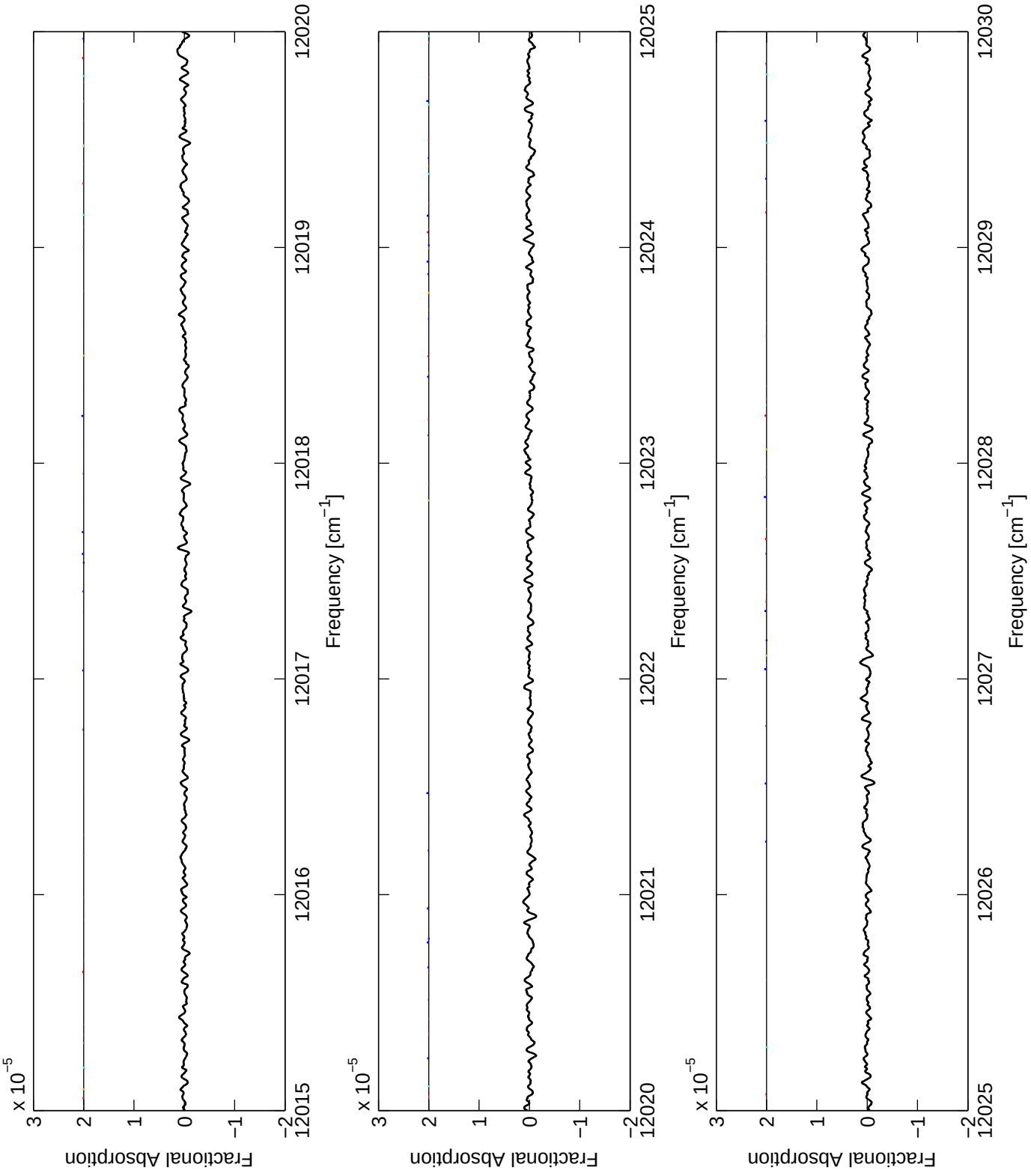
x 10^−5
3
2
1
0
−1
−2
Fractional Absorption
12015
12016
12017
12018
12019
12020
Frequency [cm^−1]
x 10^−5
3
2
1
0
−1
−2
Fractional Absorption
12020
12021
12022
12023
12024
12025
Frequency [cm^−1]
x 10^−5
3
2
1
0
−1
−2
Fractional Absorption
12025
12026
12027
12028
12029
12030
Frequency [cm^−1]

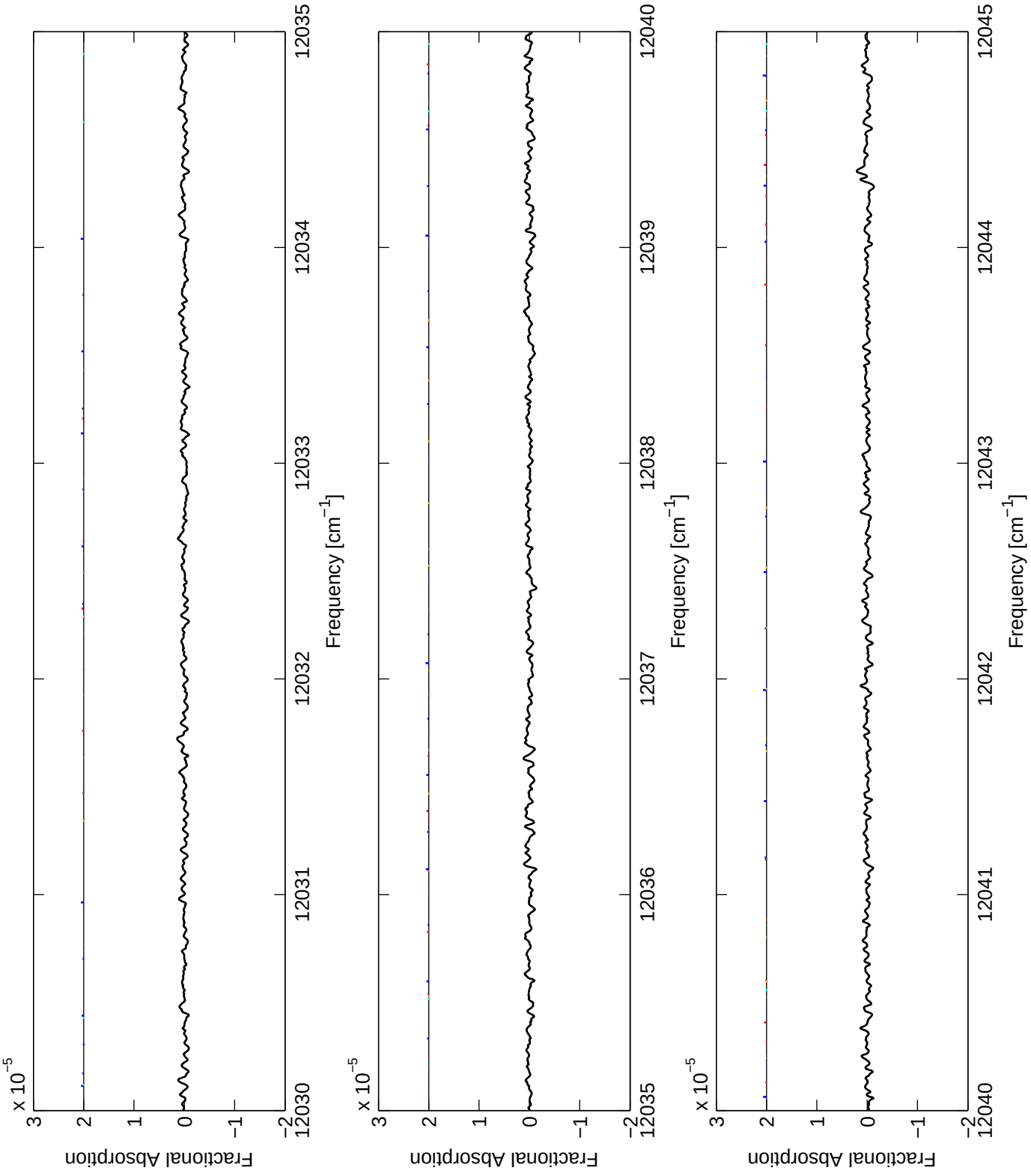
x 10^−5
3
2
1
0
−1
−2
Fractional Absorption
12030
12031
12032
12033
12034
12035
Frequency [cm^−1]
x 10^−5
3
2
1
0
−1
−2
Fractional Absorption
12035
12036
12037
12038
12039
12040
Frequency [cm^−1]
x 10^−5
3
2
1
0
−1
−2
Fractional Absorption
12040
12041
12042
12043
12044
12045
Frequency [cm^−1]

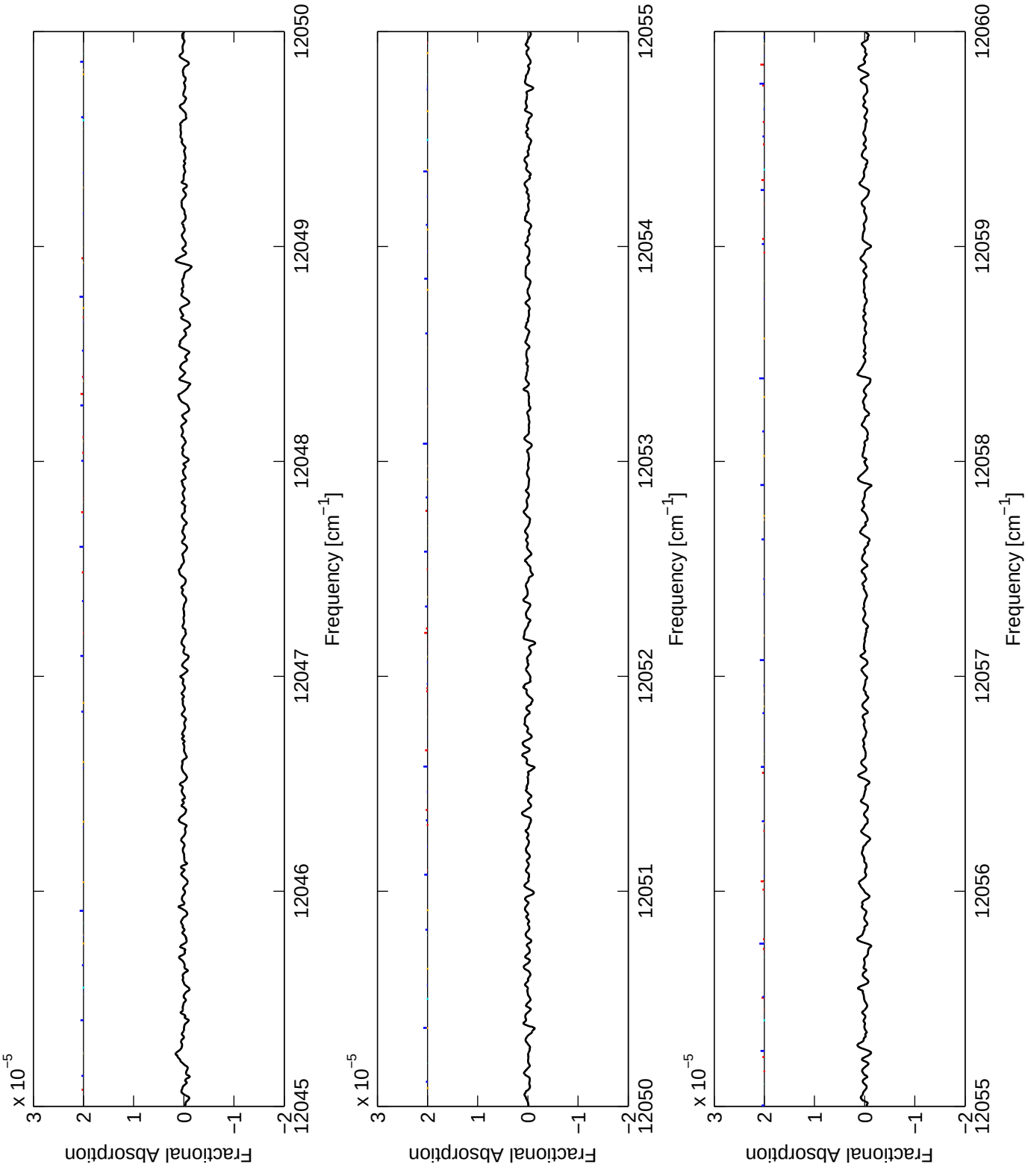
x 10^−5
3
2
1
0
−1
−2
Fractional Absorption
12045
12046
12047
12048
12049
12050
Frequency [cm^−1]
x 10^−5
3
2
1
0
−1
−2
Fractional Absorption
12050
12051
12052
12053
12054
12055
Frequency [cm^−1]
x 10^−5
3
2
1
0
−1
−2
Fractional Absorption
12055
12056
12057
12058
12059
12060
Frequency [cm^−1]

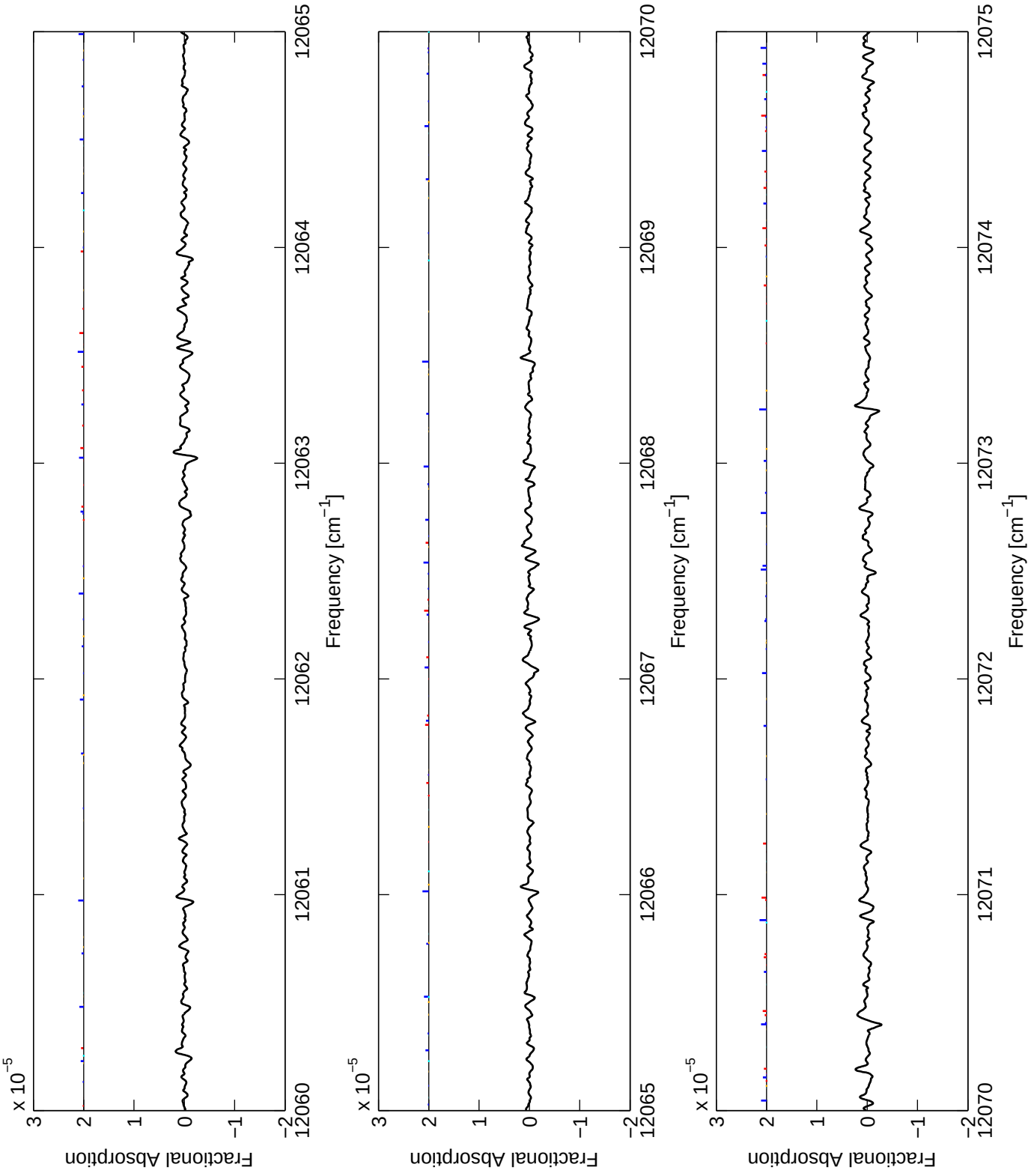
x 10^−5
3
2
1
0
−1
−2
Fractional Absorption
12060
12061
12062
12063
12064
12065
Frequency [cm^−1]
x 10^−5
3
2
1
0
−1
−2
Fractional Absorption
12065
12066
12067
12068
12069
12070
Frequency [cm^−1]
x 10^−5
3
2
1
0
−1
−2
Fractional Absorption
12070
12071
12072
12073
12074
12075
Frequency [cm^−1]

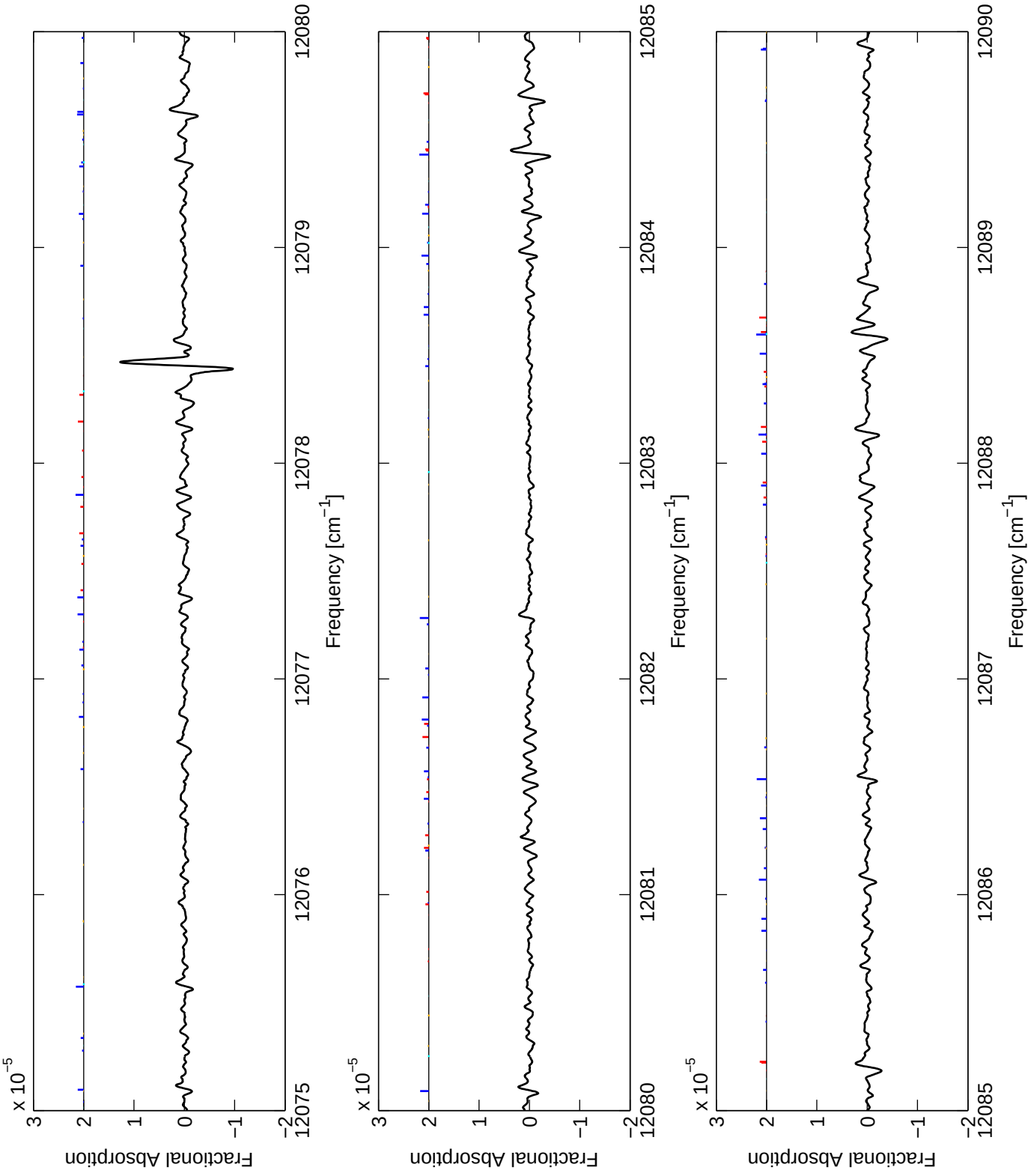
x 10^−5
3
2
1
0
−1
−2
Fractional Absorption
12075
12076
12077
12078
12079
12080
Frequency [cm^−1]
x 10^−5
3
2
1
0
−1
−2
Fractional Absorption
12080
12081
12082
12083
12084
12085
Frequency [cm^−1]
x 10^−5
3
2
1
0
−1
−2
Fractional Absorption
12085
12086
12087
12088
12089
12090
Frequency [cm^−1]

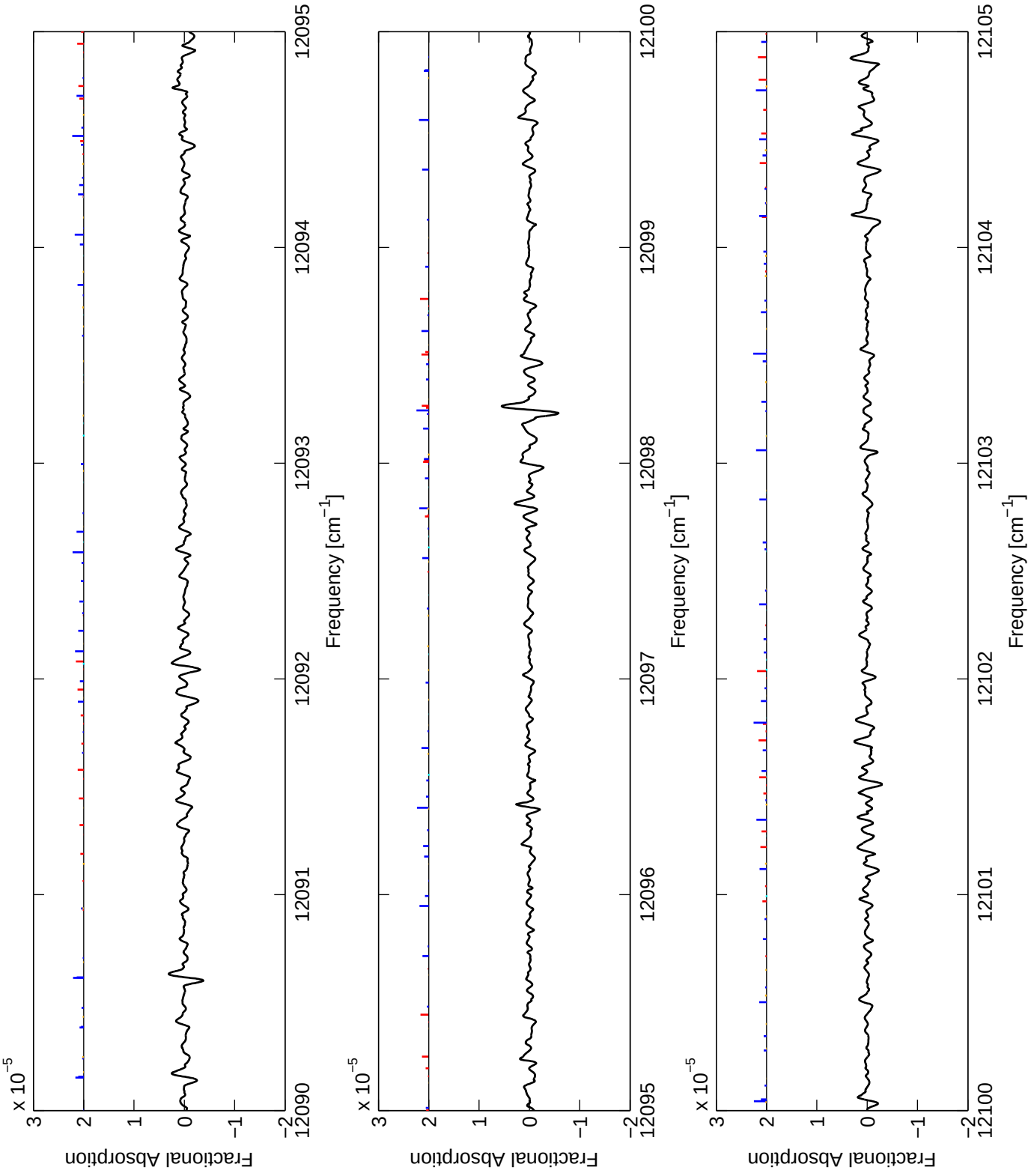
x 10^−5
3
2
1
0
−1
−2
Fractional Absorption
12090
12091
12092
12093
12094
12095
Frequency [cm^−1]
x 10^−5
3
2
1
0
−1
−2
Fractional Absorption
12095
12096
12097
12098
12099
12100
Frequency [cm^−1]
x 10^−5
3
2
1
0
−1
−2
Fractional Absorption
12100
12101
12102
12103
12104
12105
Frequency [cm^−1]

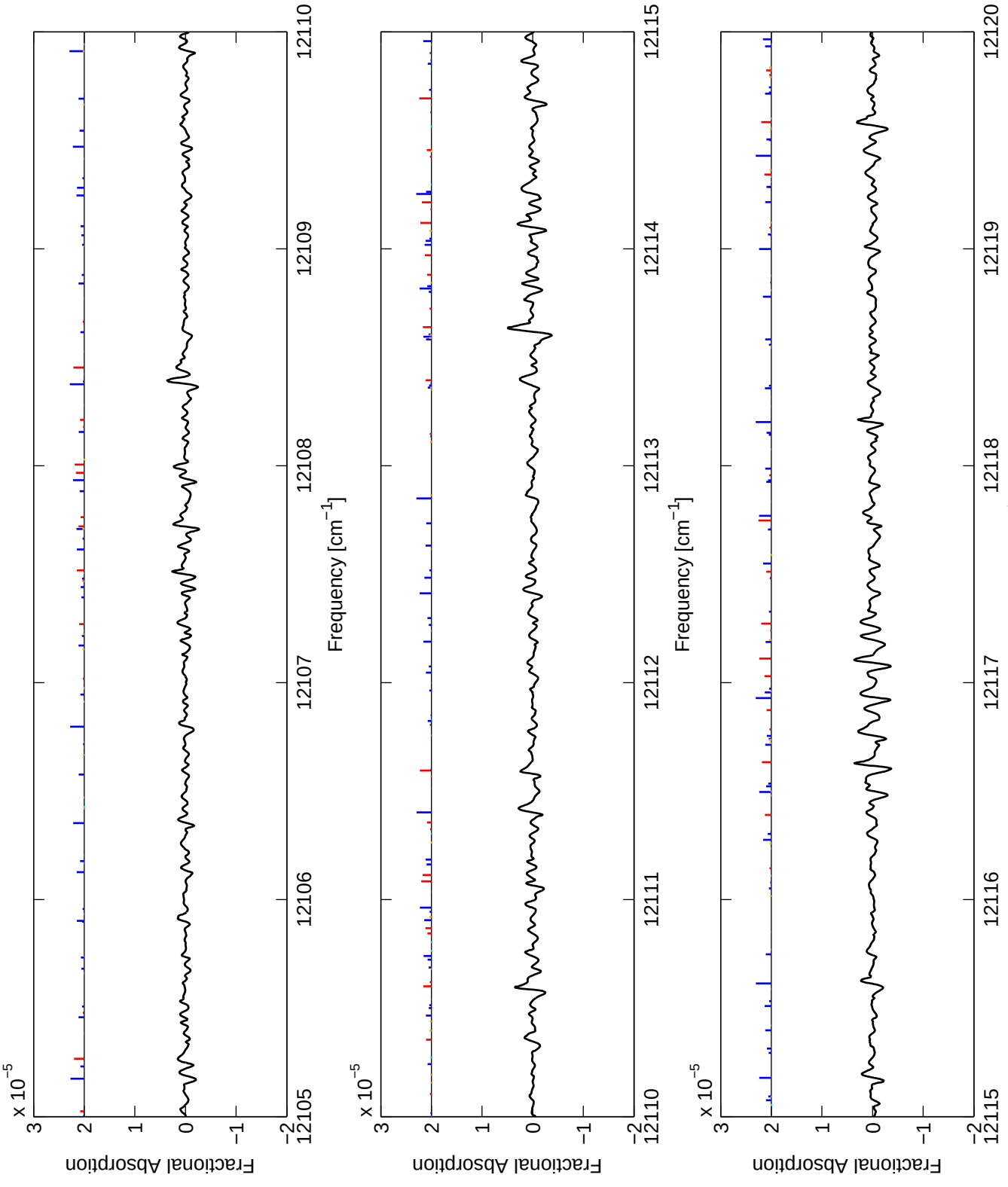
x 10^-5
3
2
1
0
−1
−2
Fractional Absorption
12105
12106
12107
12108
12109
12110
Frequency [cm^-1]
x 10^-5
3
2
1
0
−1
−2
Fractional Absorption
12110
12111
12112
12113
12114
12115
Frequency [cm^-1]
x 10^-5
3
2
1
0
−1
−2
Fractional Absorption
12115
12116
12117
12118
12119
12120
Frequency [cm^-1]

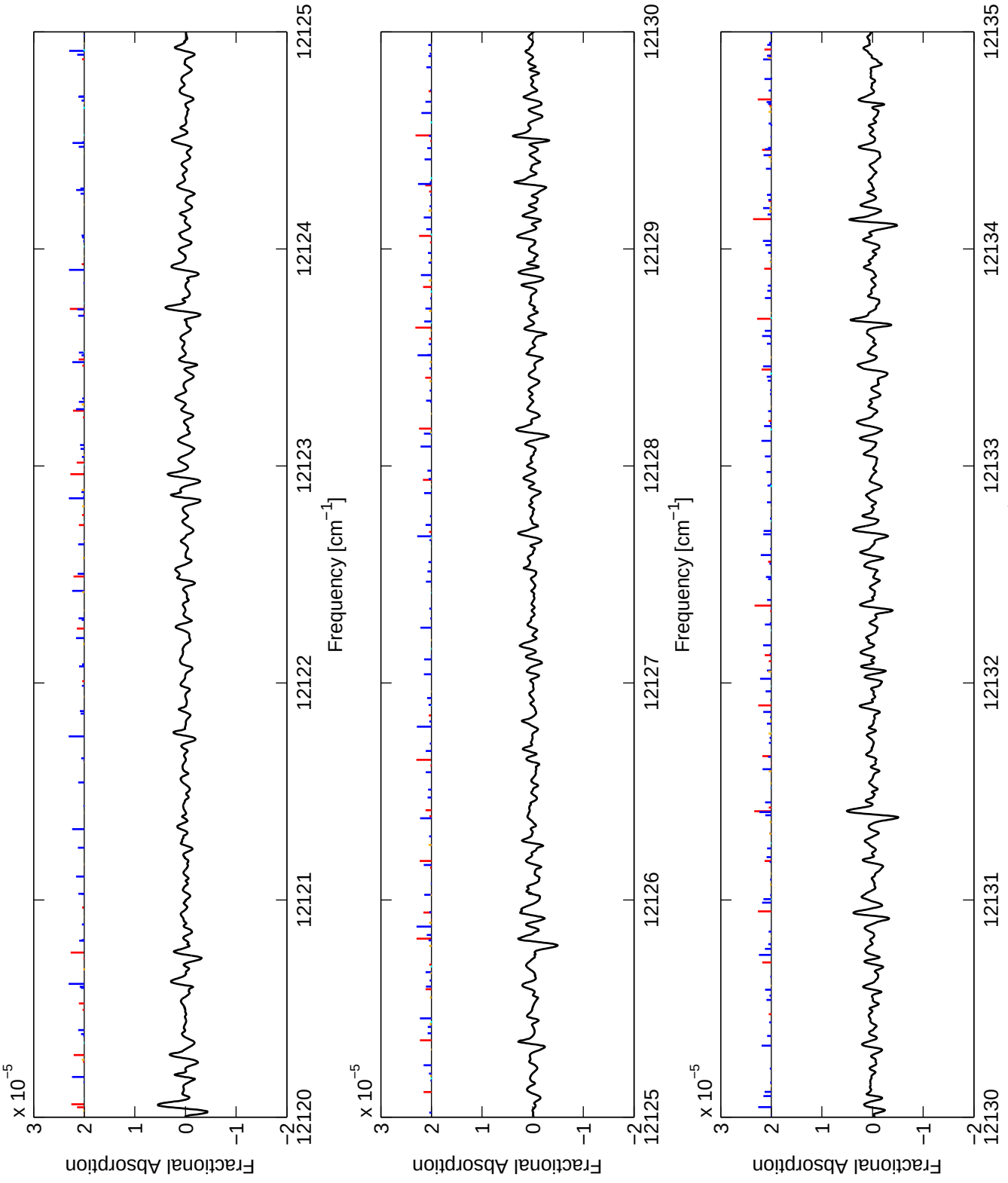
x 10^−5
3
2
1
0
−1
−2
Fractional Absorption
12120
12121
12122
12123
12124
12125
Frequency [cm^−1]
12125
12126
12127
12128
12129
12130
12130
12131
12132
12133
12134
12135

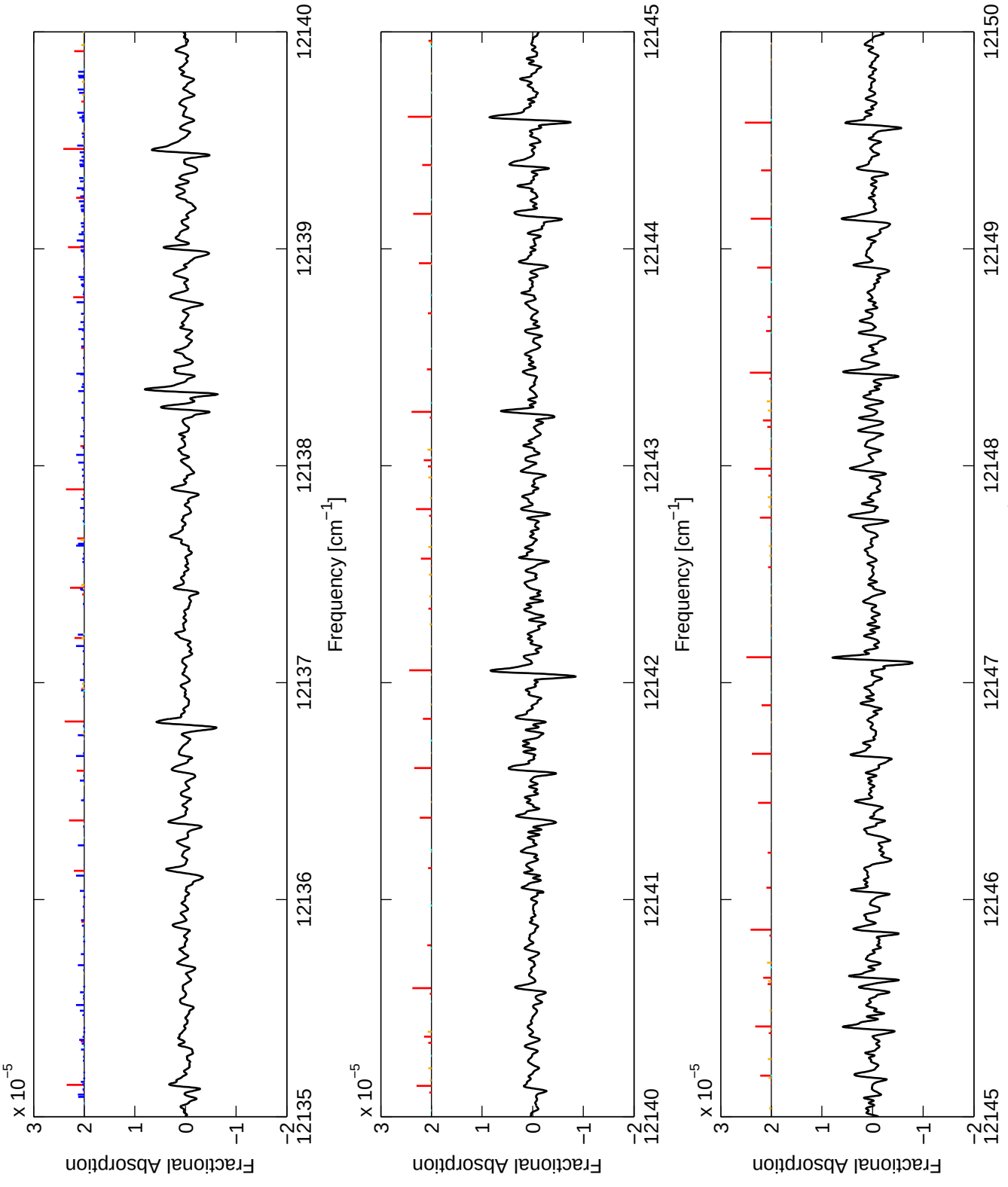
x 10^−5
3
2
1
0
−1
−2
Fractional Absorption
12135
12136
12137
12138
12139
12140
Frequency [cm^−1]
x 10^−5
3
2
1
0
−1
−2
Fractional Absorption
12140
12141
12142
12143
12144
12145
Frequency [cm^−1]
x 10^−5
3
2
1
0
−1
−2
Fractional Absorption
12145
12146
12147
12148
12149
12150
Frequency [cm^−1]

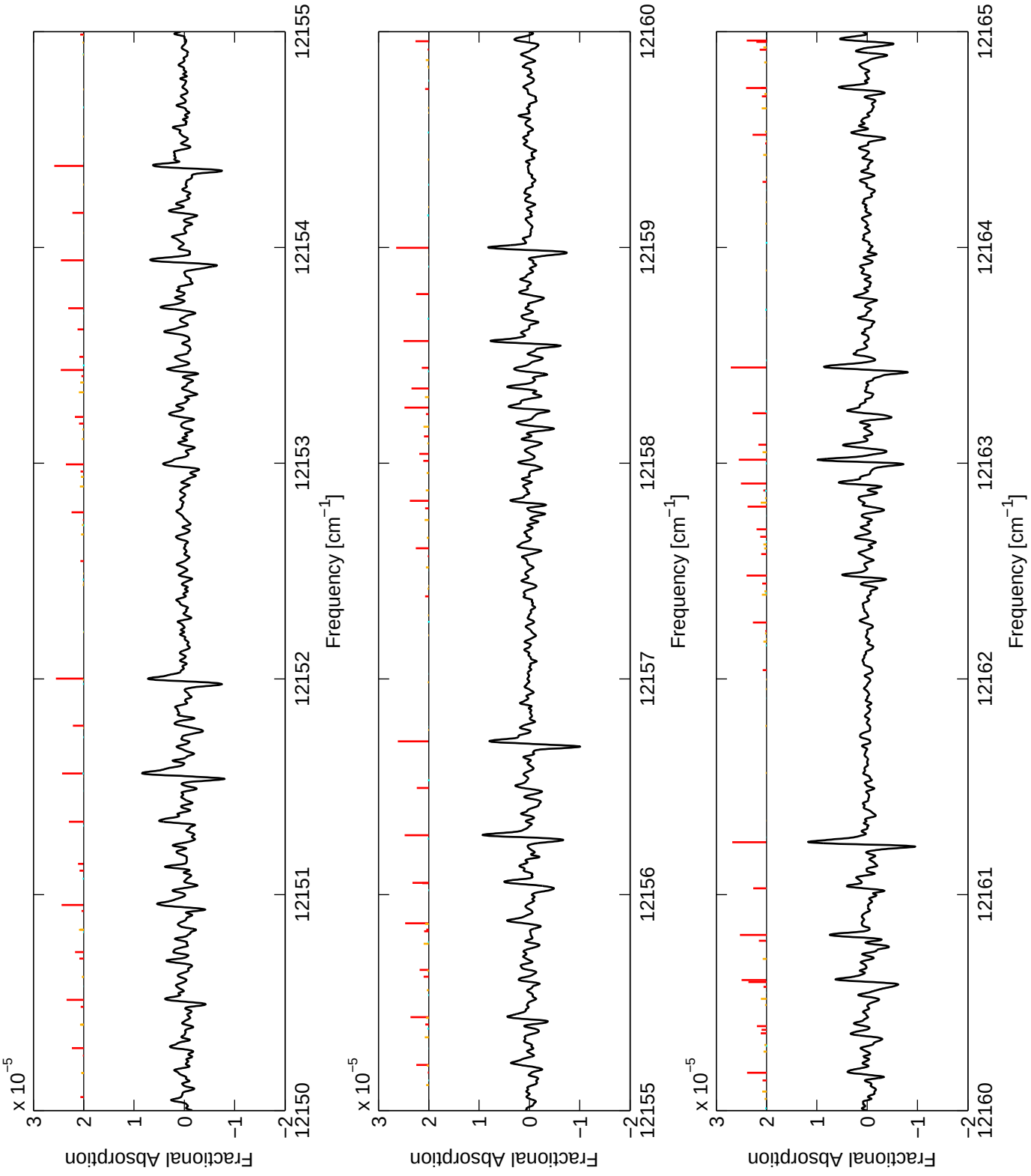
x 10^−5
3
2
1
0
−1
−2
Fractional Absorption
12150
12151
12152
12153
12154
12155
Frequency [cm^−1]
x 10^−5
3
2
1
0
−1
−2
Fractional Absorption
12155
12156
12157
12158
12159
12160
Frequency [cm^−1]
x 10^−5
3
2
1
0
−1
−2
Fractional Absorption
12160
12161
12162
12163
12164
12165
Frequency [cm^−1]

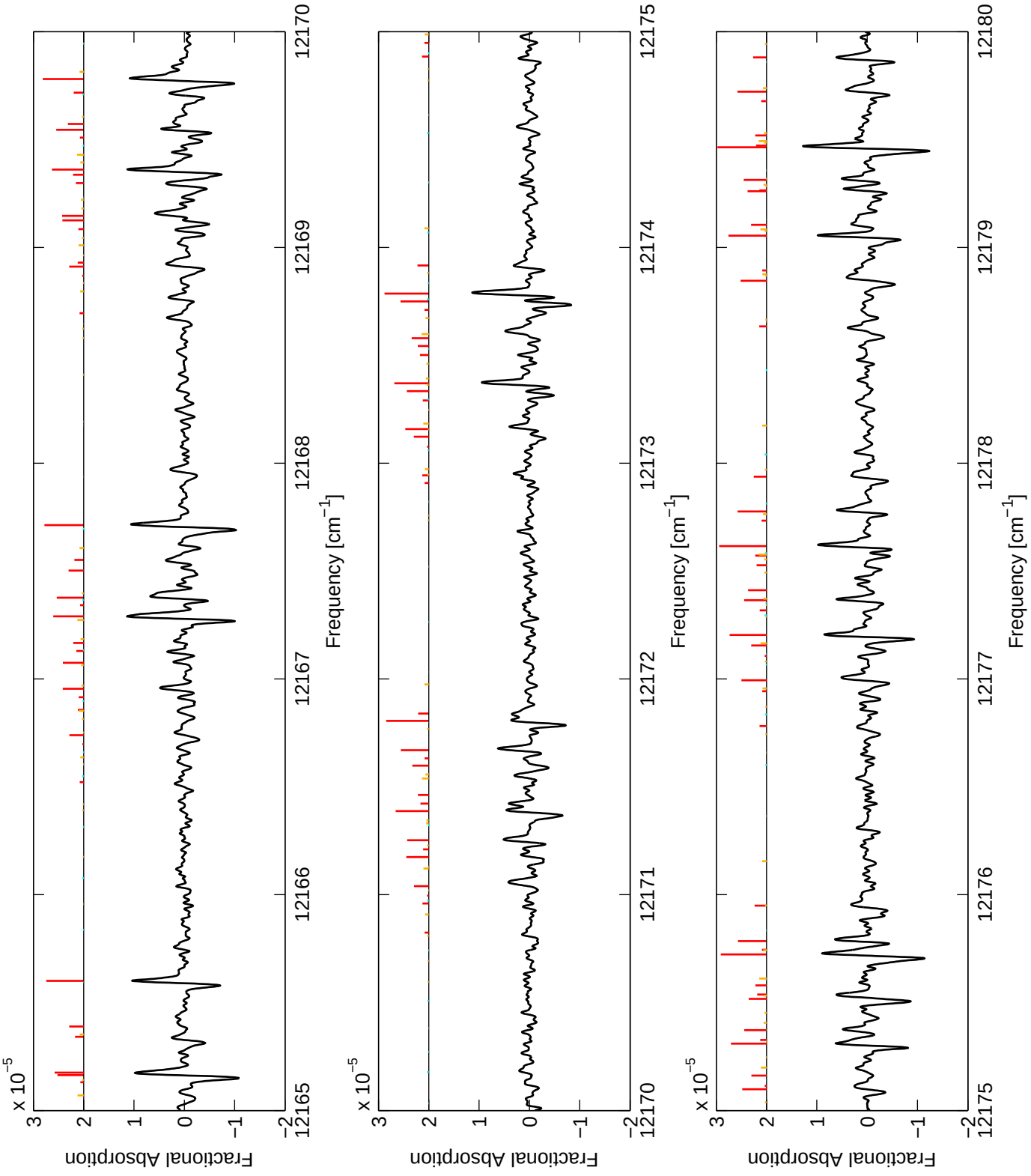
x 10^-5
3
2
1
0
−1
−2
Fractional Absorption
12165
12166
12167
12168
12169
12170
Frequency [cm^-1]
x 10^-5
3
2
1
0
−1
−2
Fractional Absorption
12170
12171
12172
12173
12174
12175
Frequency [cm^-1]
x 10^-5
3
2
1
0
−1
−2
Fractional Absorption
12175
12176
12177
12178
12179
12180
Frequency [cm^-1]

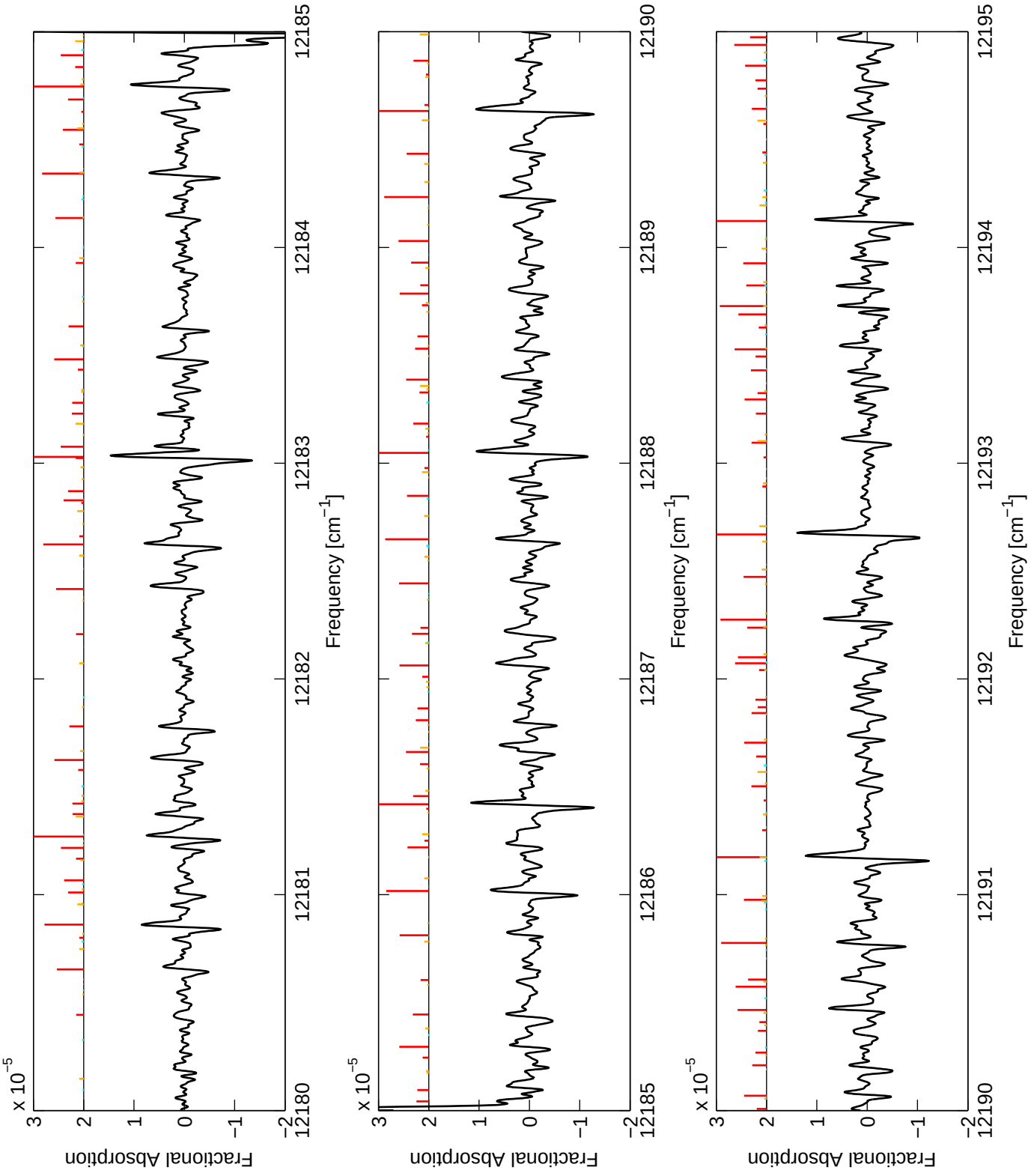
x 10^−5
3
2
1
0
−1
−2
Fractional Absorption
12180
12181
12182
12183
12184
12185
Frequency [cm^−1]
x 10^−5
3
2
1
0
−1
−2
Fractional Absorption
12185
12186
12187
12188
12189
12190
Frequency [cm^−1]
x 10^−5
3
2
1
0
−1
−2
Fractional Absorption
12190
12191
12192
12193
12194
12195
Frequency [cm^−1]

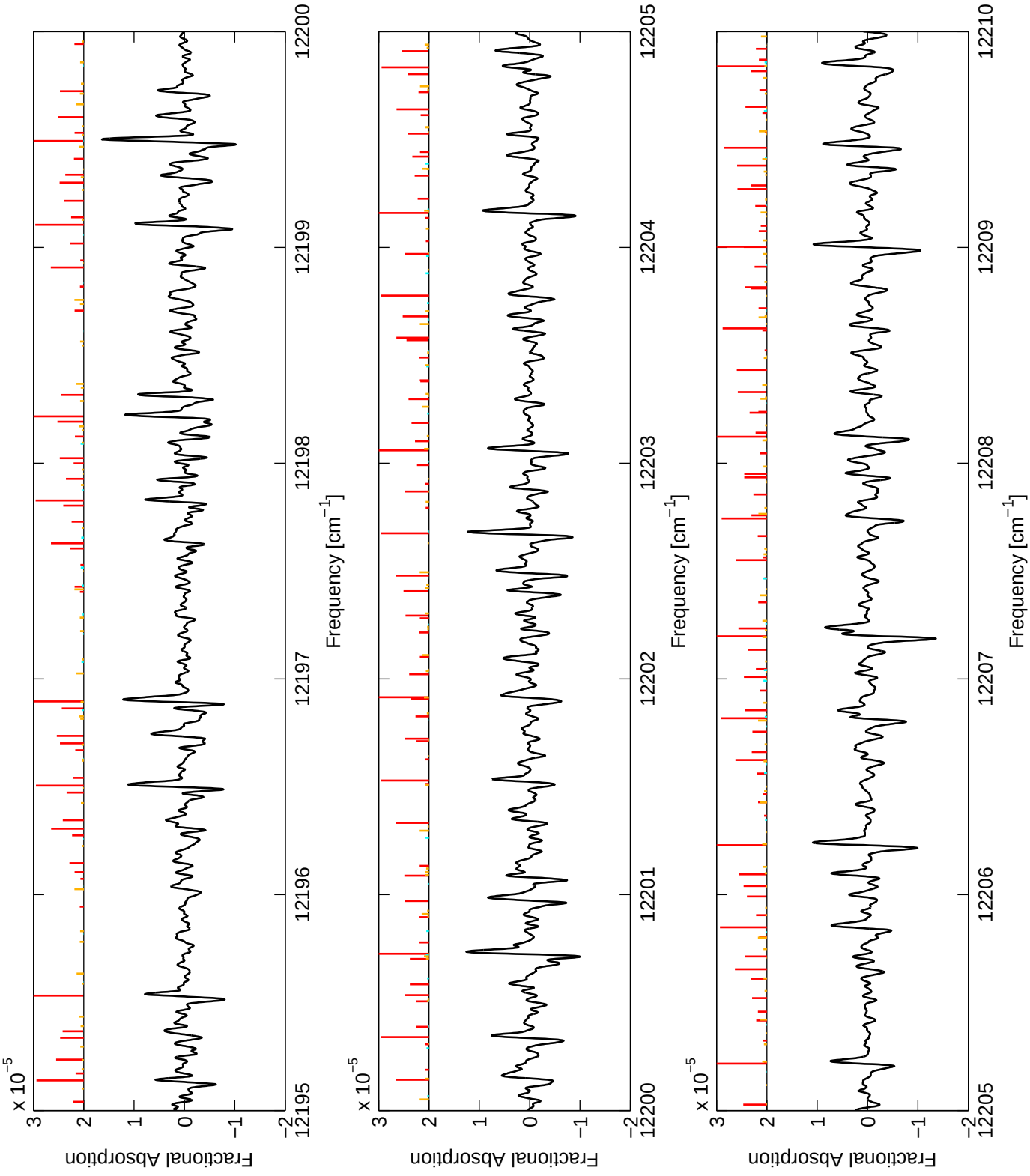
x 10^−5
3
2
1
0
−1
−2
Fractional Absorption
12195
12196
12197
12198
12199
12200
Frequency [cm^−1]
x 10^−5
3
2
1
0
−1
−2
Fractional Absorption
12200
12201
12202
12203
12204
12205
Frequency [cm^−1]
x 10^−5
3
2
1
0
−1
−2
Fractional Absorption
12205
12206
12207
12208
12209
12210
Frequency [cm^−1]

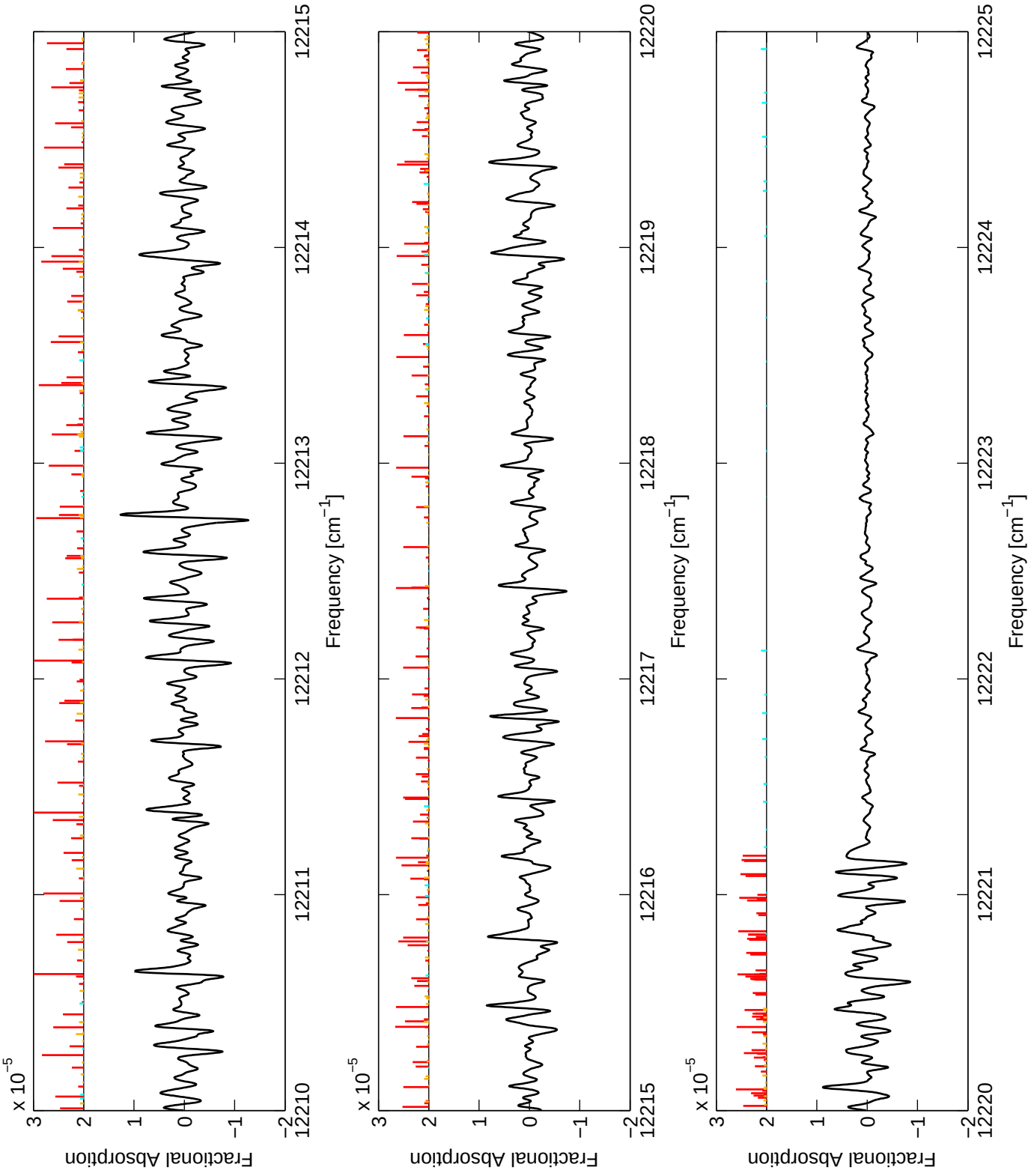
x 10^−5
3
2
1
0
−1
−2
Fractional Absorption
12210
12211
12212
12213
12214
12215
Frequency [cm^−1]
x 10^−5
3
2
1
0
−1
−2
Fractional Absorption
12215
12216
12217
12218
12219
12220
Frequency [cm^−1]
x 10^−5
3
2
1
0
−1
−2
Fractional Absorption
12220
12221
12222
12223
12224
12225
Frequency [cm^−1]

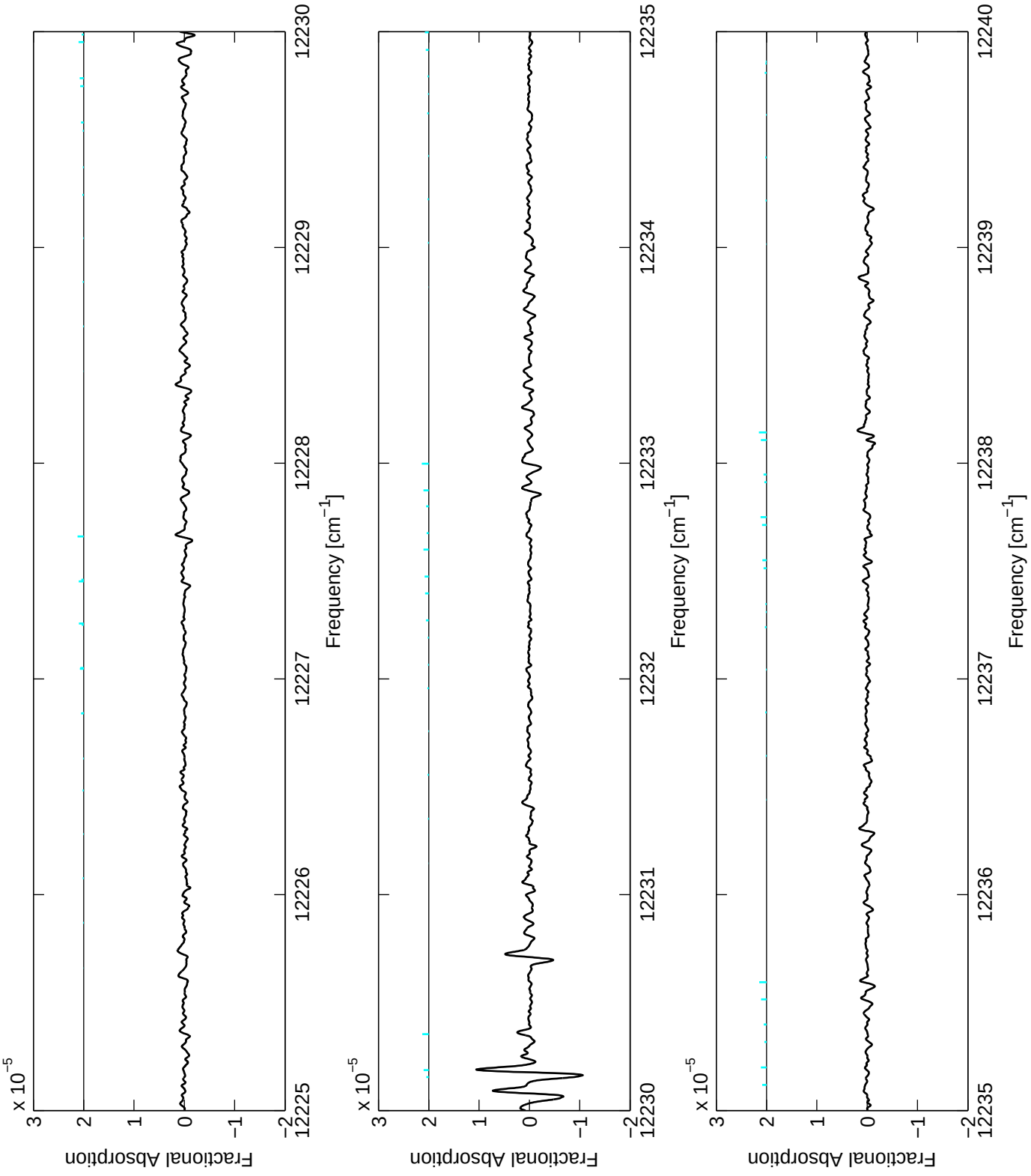
x 10^−5
3
2
1
0
−1
−2
Fractional Absorption
12225
12226
12227
12228
12229
12230
Frequency [cm^−1]
x 10^−5
3
2
1
0
−1
−2
Fractional Absorption
12230
12231
12232
12233
12234
12235
Frequency [cm^−1]
x 10^−5
3
2
1
0
−1
−2
Fractional Absorption
12235
12236
12237
12238
12239
12240
Frequency [cm^−1]

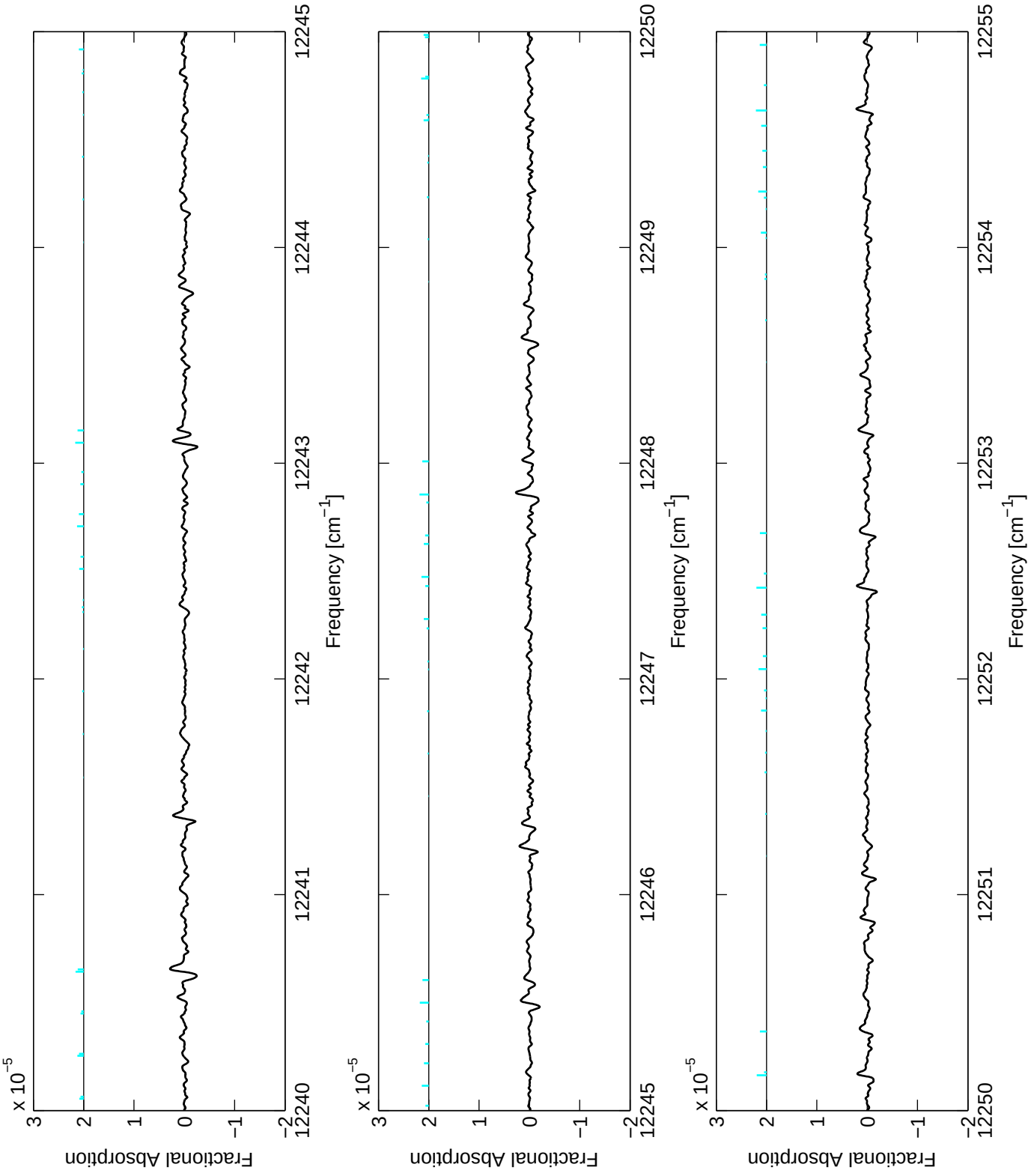
x 10^−5
3
2
1
0
−1
−2
Fractional Absorption
12240
12241
12242
12243
12244
12245
Frequency [cm^−1]
x 10^−5
3
2
1
0
−1
−2
Fractional Absorption
12245
12246
12247
12248
12249
12250
Frequency [cm^−1]
x 10^−5
3
2
1
0
−1
−2
Fractional Absorption
12250
12251
12252
12253
12254
12255
Frequency [cm^−1]

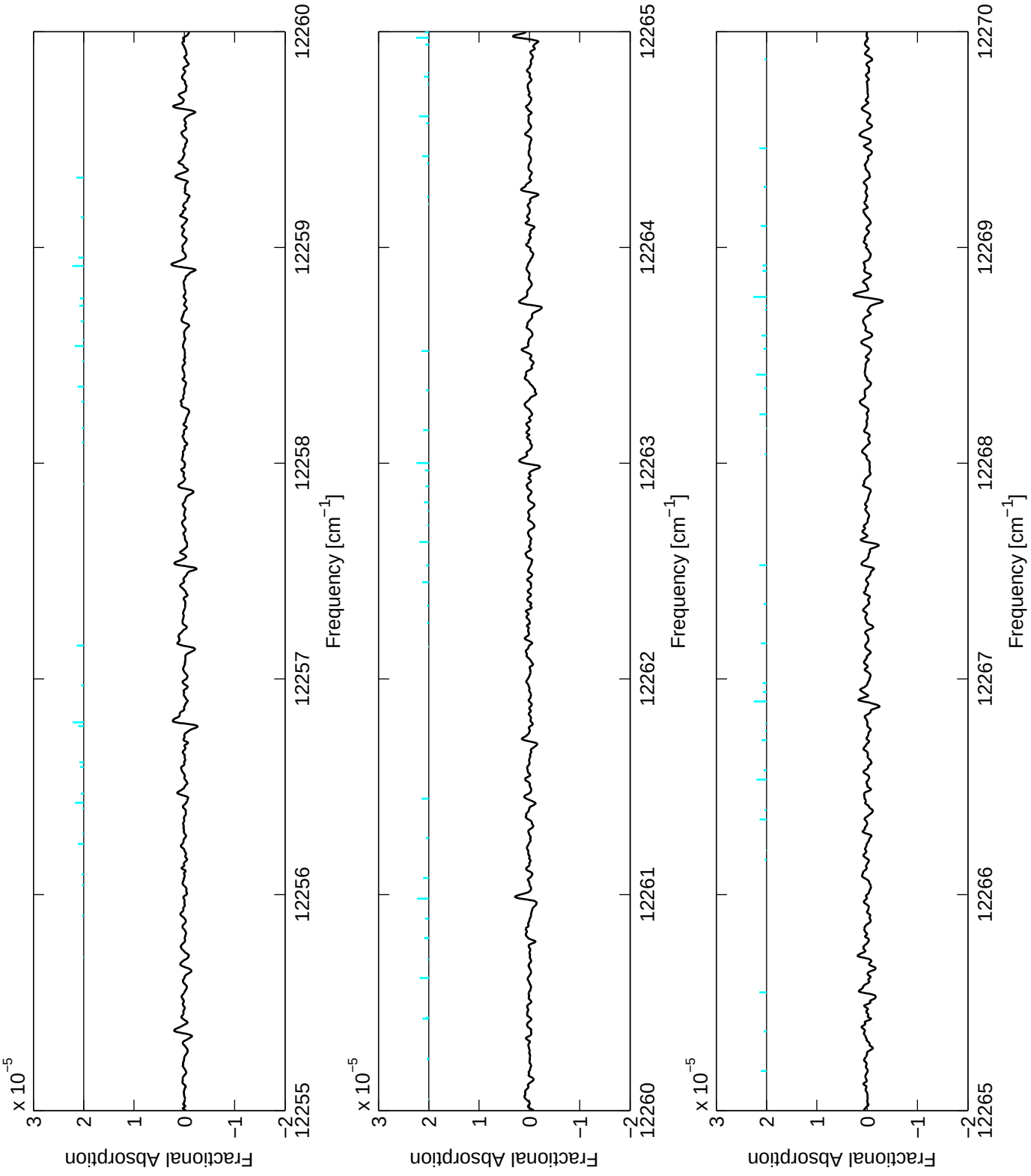
x 10^−5
3
2
1
0
−1
−2
Fractional Absorption
12255
12256
12257
12258
12259
12260
Frequency [cm^−1]
x 10^−5
3
2
1
0
−1
−2
Fractional Absorption
12260
12261
12262
12263
12264
12265
Frequency [cm^−1]
x 10^−5
3
2
1
0
−1
−2
Fractional Absorption
12265
12266
12267
12268
12269
12270
Frequency [cm^−1]

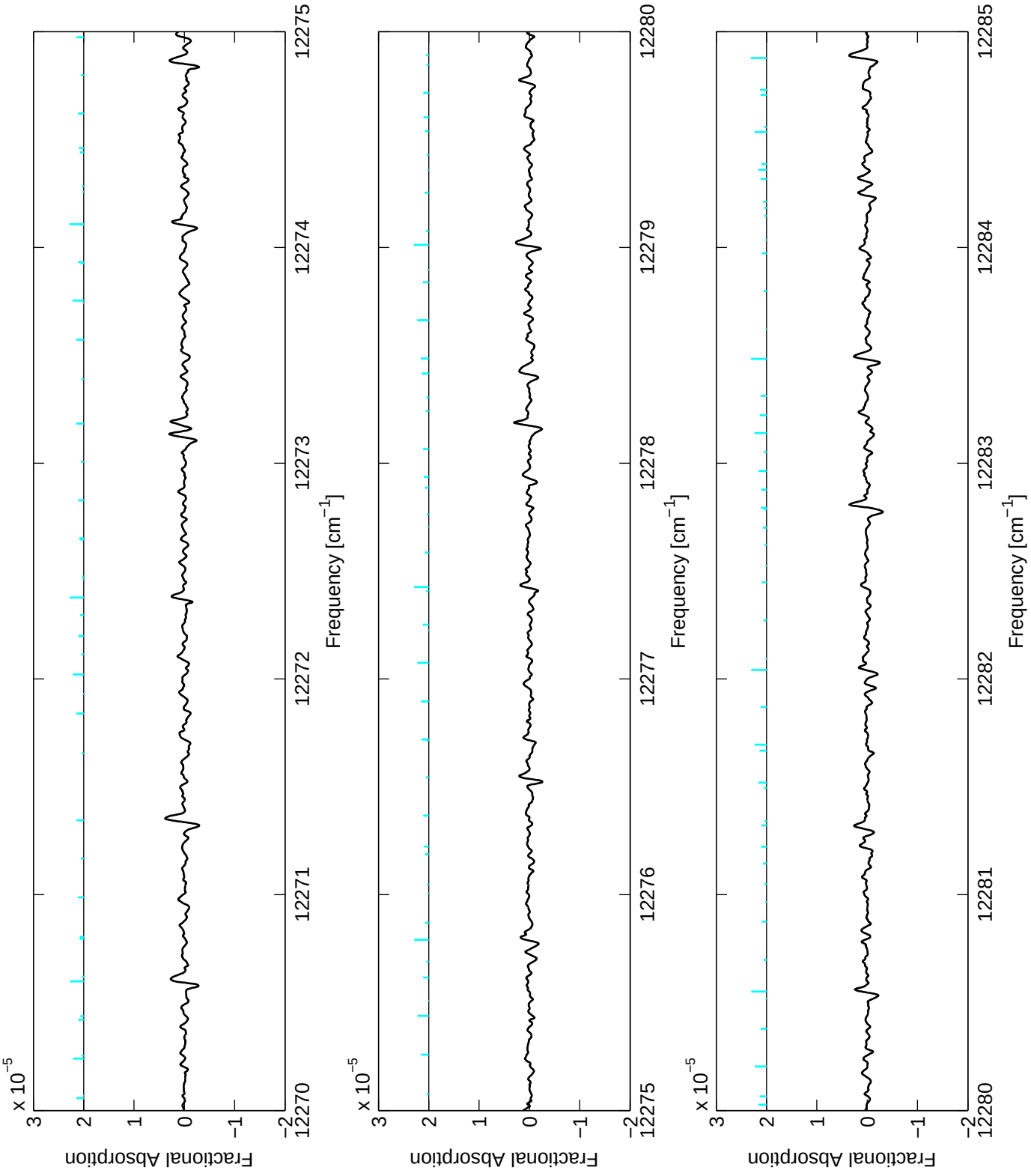
x 10^−5
3
2
1
0
−1
−2
Fractional Absorption
12270
12271
12272
12273
12274
12275
Frequency [cm^−1]
x 10^−5
3
2
1
0
−1
−2
Fractional Absorption
12275
12276
12277
12278
12279
12280
Frequency [cm^−1]
x 10^−5
3
2
1
0
−1
−2
Fractional Absorption
12280
12281
12282
12283
12284
12285
Frequency [cm^−1]

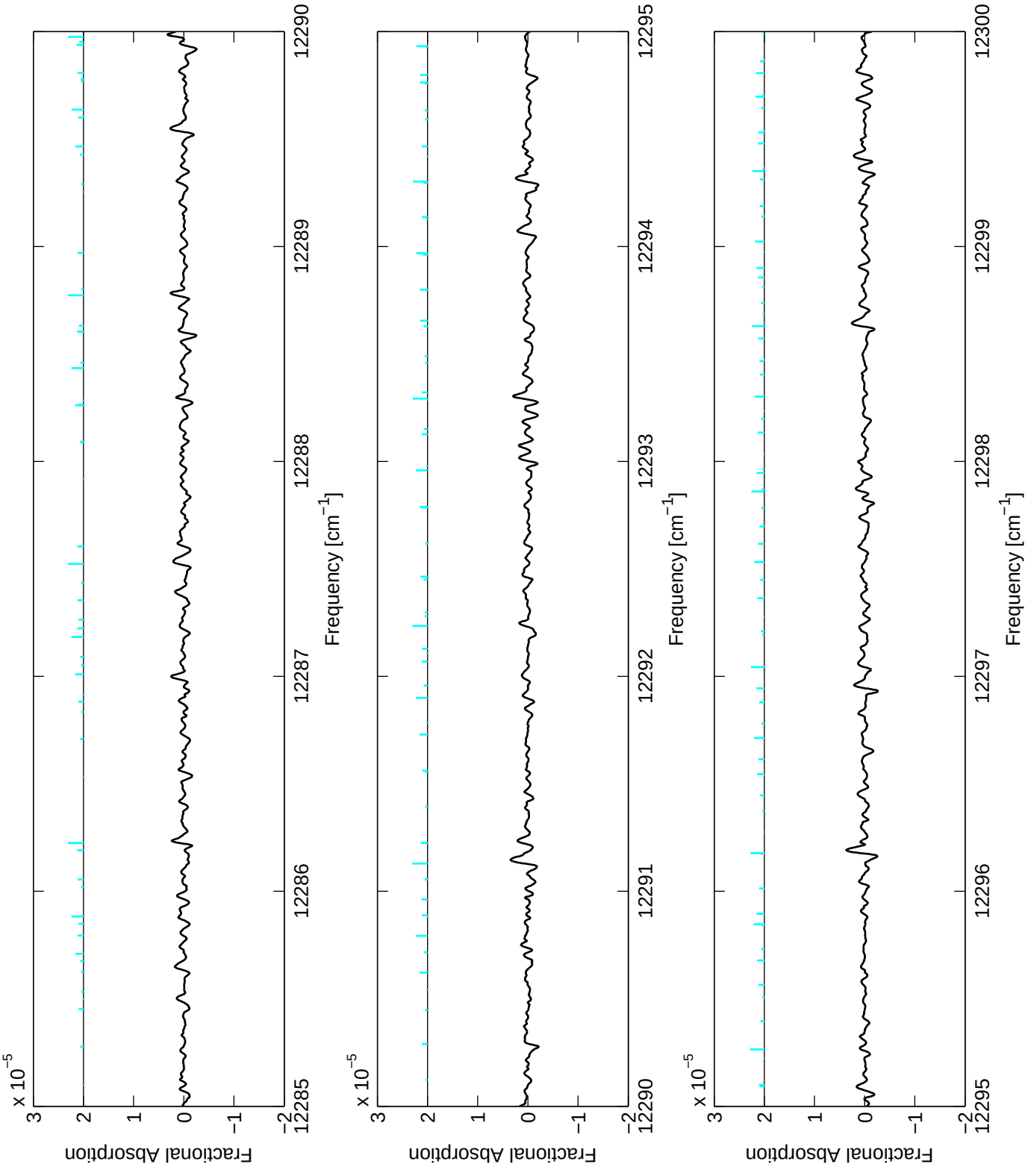
x 10^−5
3
2
1
0
−1
−2
Fractional Absorption
12285
12286
12287
12288
12289
12290
Frequency [cm^−1]
x 10^−5
3
2
1
0
−1
−2
Fractional Absorption
12290
12291
12292
12293
12294
12295
Frequency [cm^−1]
x 10^−5
3
2
1
0
−1
−2
Fractional Absorption
12295
12296
12297
12298
12299
12300
Frequency [cm^−1]

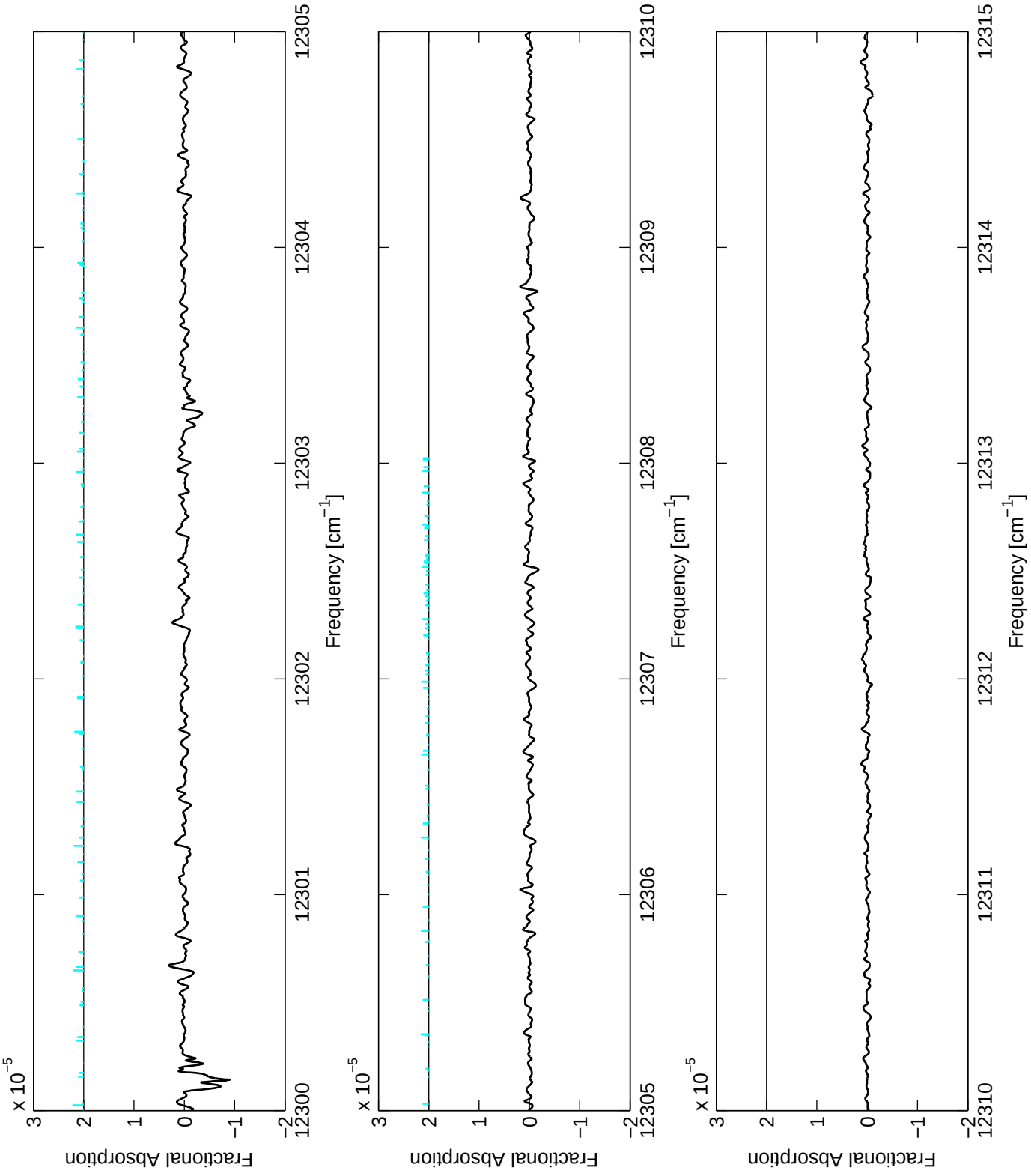
x 10^−5
3
2
1
0
−1
−2
Fractional Absorption
12300
12301
12302
12303
12304
12305
Frequency [cm^−1]
x 10^−5
3
2
1
0
−1
−2
Fractional Absorption
12305
12306
12307
12308
12309
12310
Frequency [cm^−1]
x 10^−5
3
2
1
0
−1
−2
Fractional Absorption
12310
12311
12312
12313
12314
12315
Frequency [cm^−1]

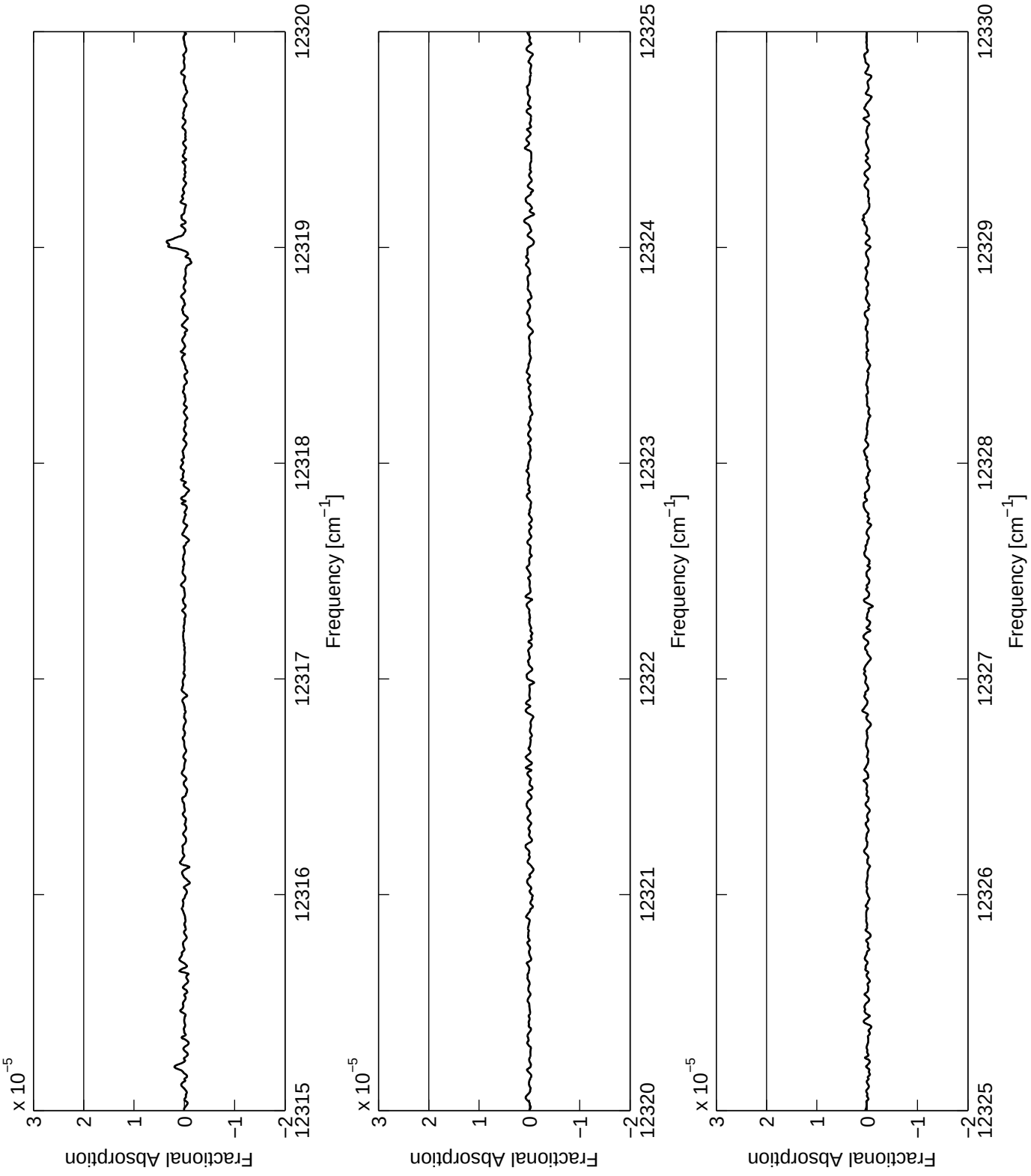
x 10^−5
3
2
1
0
−1
−2
Fractional Absorption
12315
12316
12317
12318
12319
12320
Frequency [cm^−1]
x 10^−5
3
2
1
0
−1
−2
Fractional Absorption
12320
12321
12322
12323
12324
12325
Frequency [cm^−1]
x 10^−5
3
2
1
0
−1
−2
Fractional Absorption
12325
12326
12327
12328
12329
12330
Frequency [cm^−1]

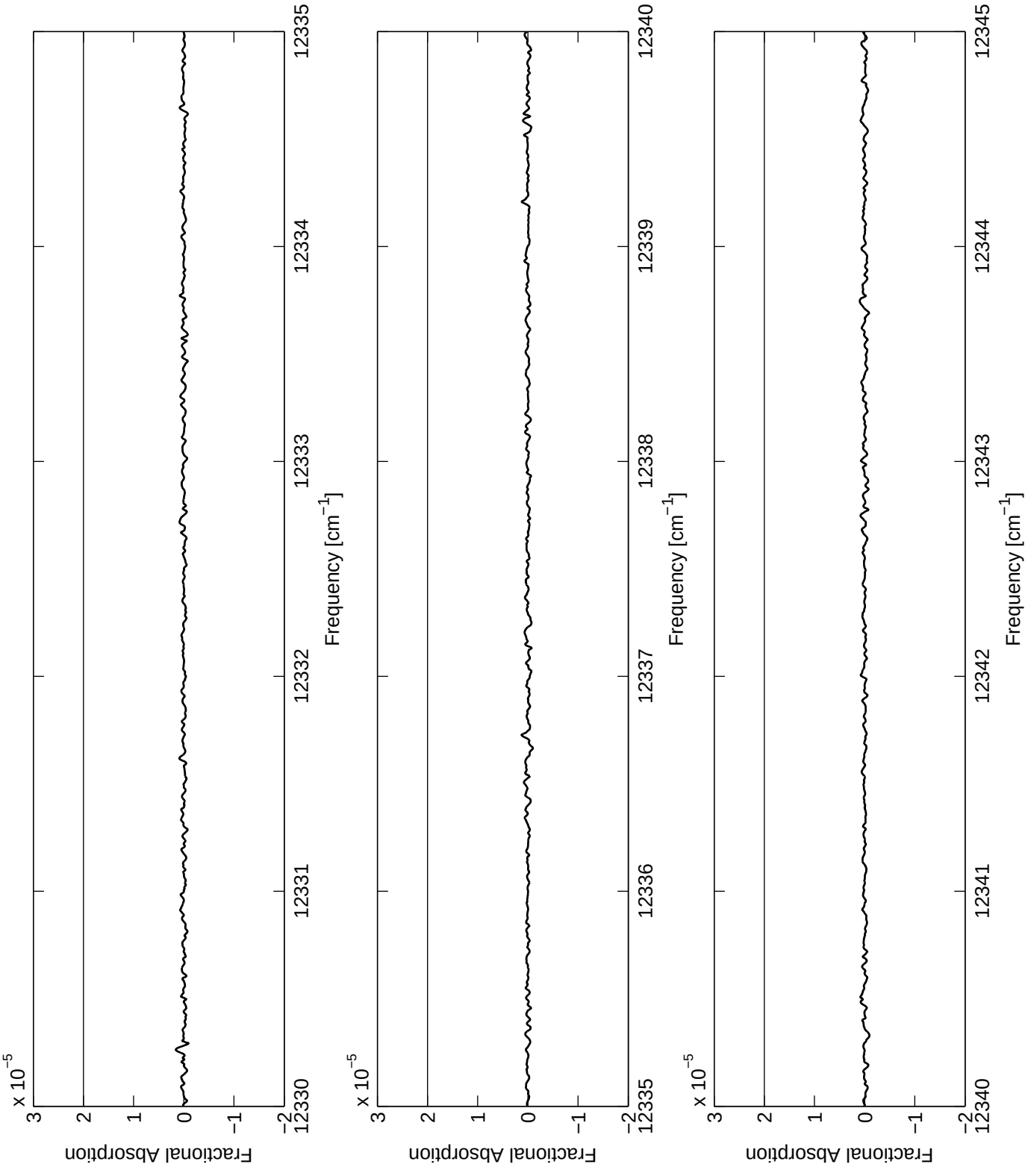
x 10^−5
3
2
1
0
−1
−2
Fractional Absorption
12330
12331
12332
12333
12334
12335
Frequency [cm^−1]
x 10^−5
3
2
1
0
−1
−2
Fractional Absorption
12335
12336
12337
12338
12339
12340
Frequency [cm^−1]
x 10^−5
3
2
1
0
−1
−2
Fractional Absorption
12340
12341
12342
12343
12344
12345
Frequency [cm^−1]

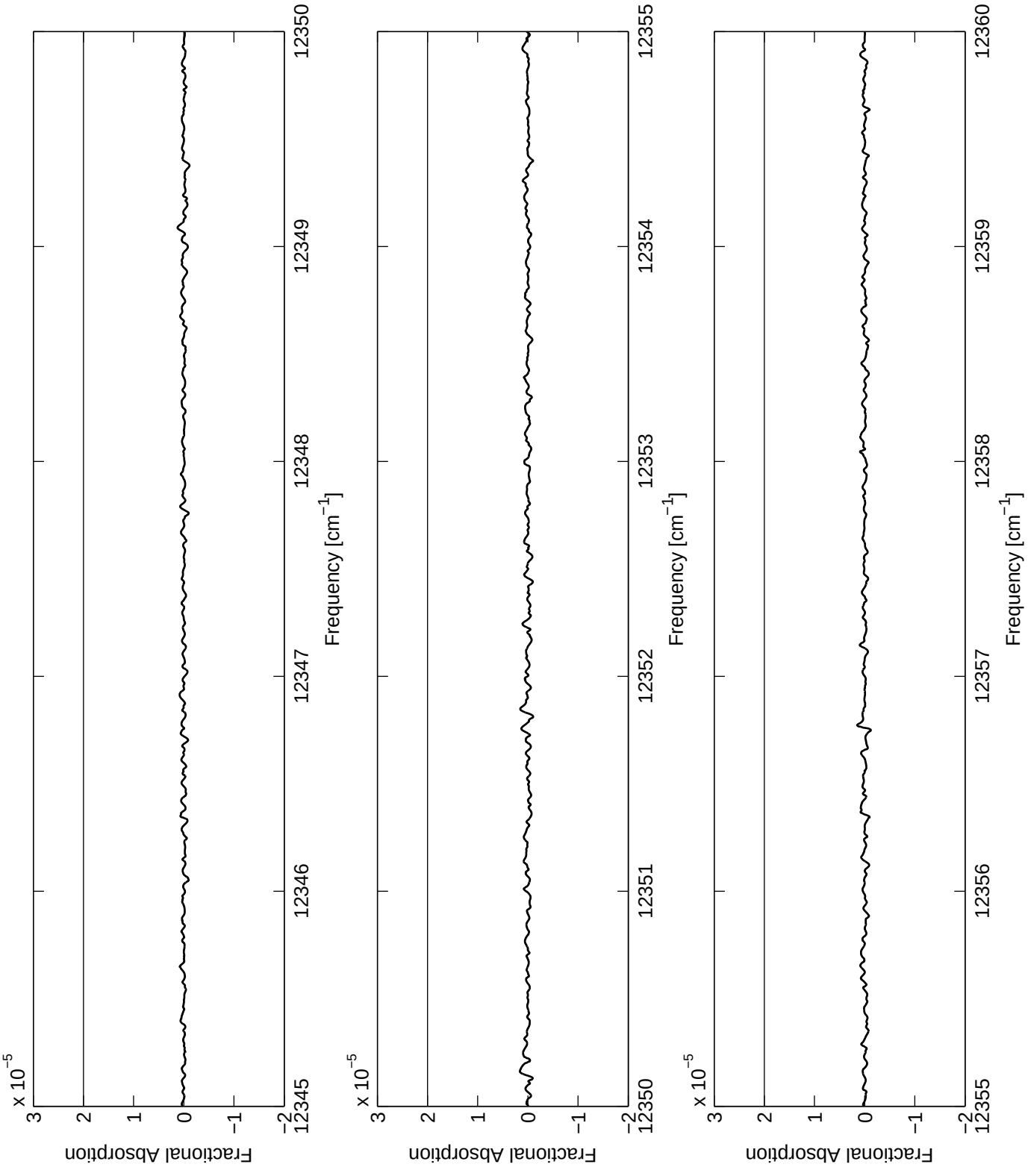
x 10^−5
3
2
1
0
−1
−2
Fractional Absorption
12345
12346
12347
12348
12349
12350
Frequency [cm^−1]
x 10^−5
3
2
1
0
−1
−2
Fractional Absorption
12350
12351
12352
12353
12354
12355
Frequency [cm^−1]
x 10^−5
3
2
1
0
−1
−2
Fractional Absorption
12355
12356
12357
12358
12359
12360
Frequency [cm^−1]

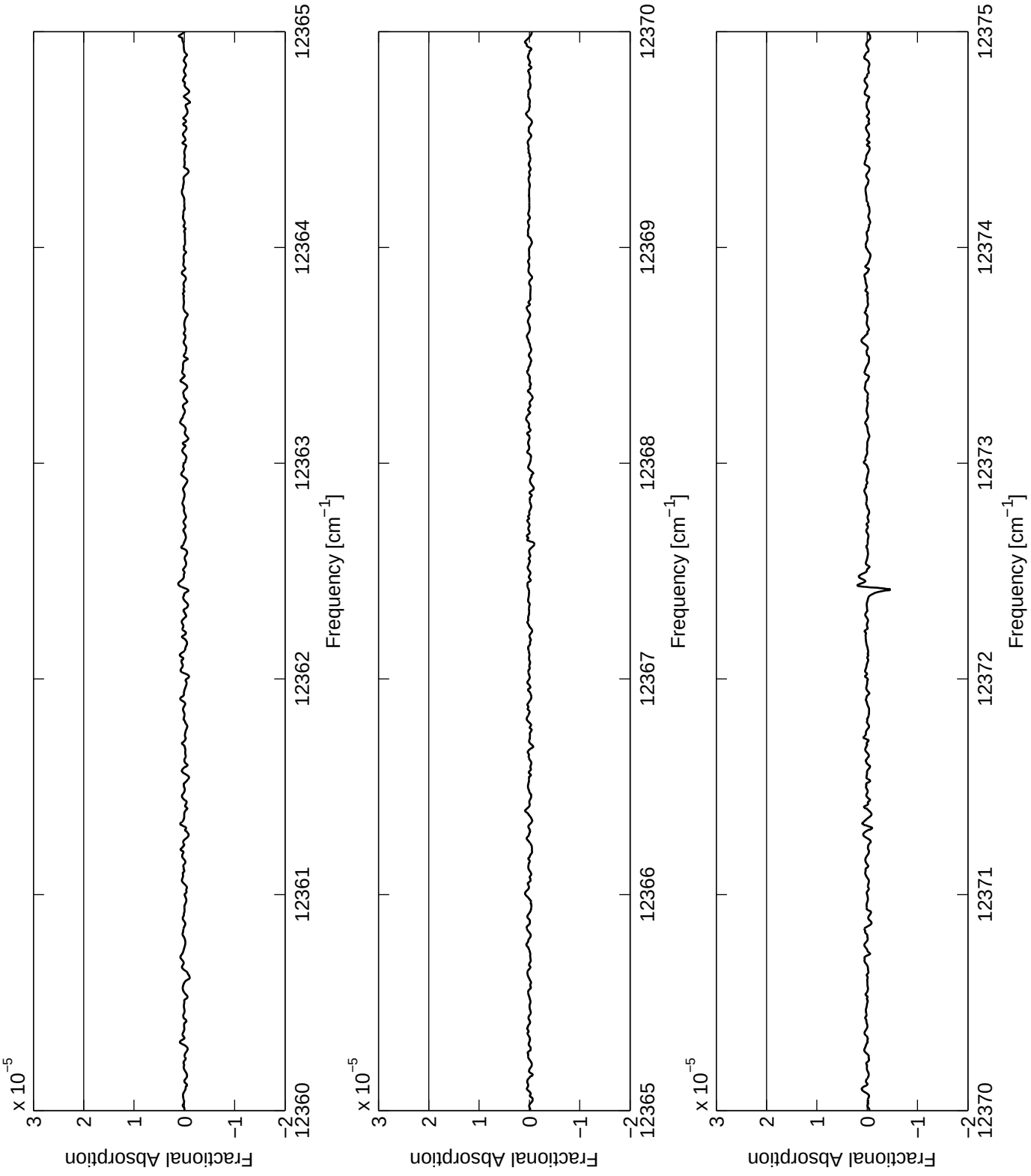
x 10^−5
3
2
1
0
−1
−2
Fractional Absorption
12360
12361
12362
12363
12364
12365
Frequency [cm^−1]
x 10^−5
3
2
1
0
−1
−2
Fractional Absorption
12365
12366
12367
12368
12369
12370
Frequency [cm^−1]
x 10^−5
3
2
1
0
−1
−2
Fractional Absorption
12370
12371
12372
12373
12374
12375
Frequency [cm^−1]

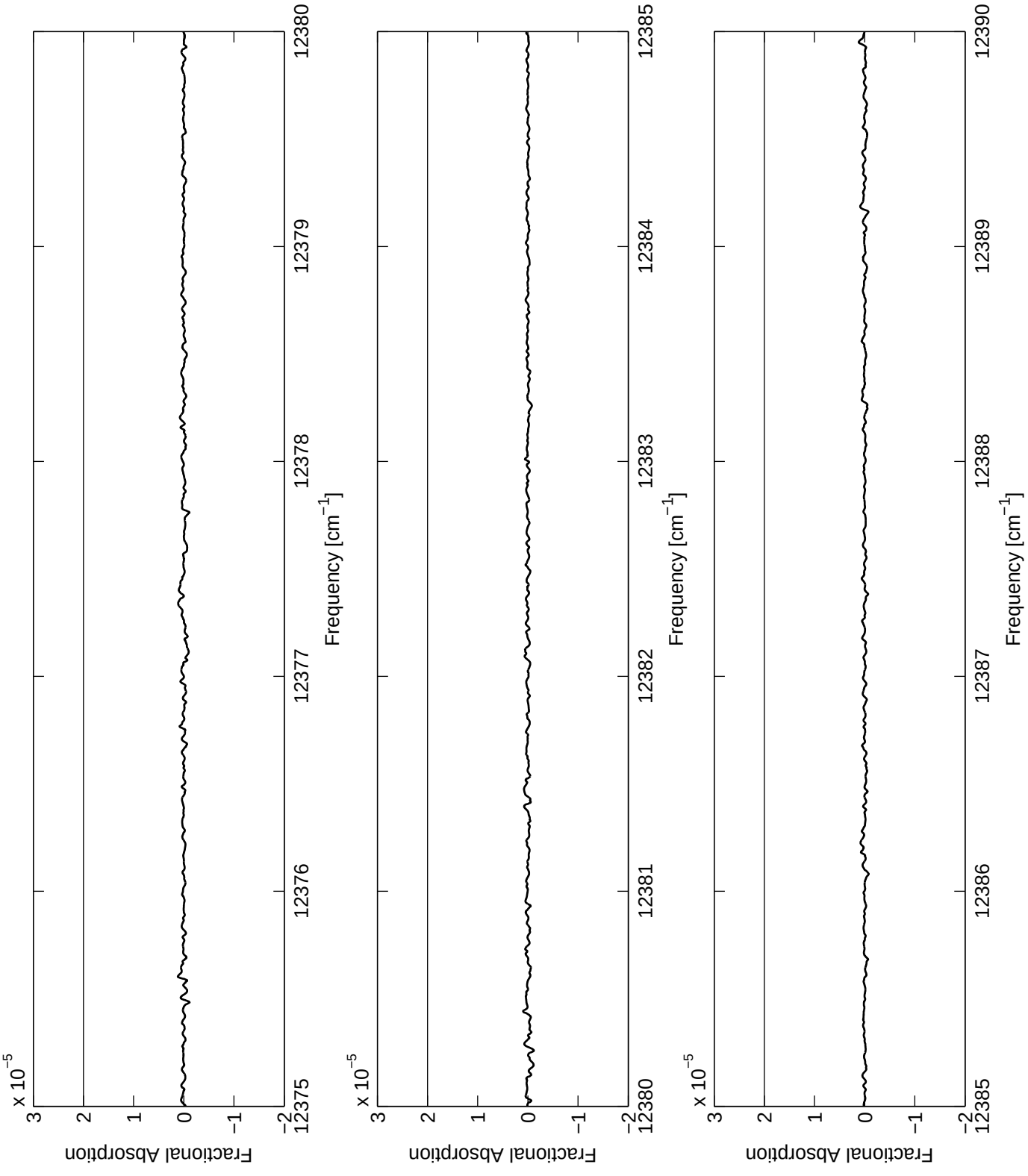
x 10^−5
3
2
1
0
−1
−2
Fractional Absorption
12375
12376
12377
12378
12379
12380
Frequency [cm^−1]
x 10^−5
3
2
1
0
−1
−2
Fractional Absorption
12380
12381
12382
12383
12384
12385
Frequency [cm^−1]
x 10^−5
3
2
1
0
−1
−2
Fractional Absorption
12385
12386
12387
12388
12389
12390
Frequency [cm^−1]

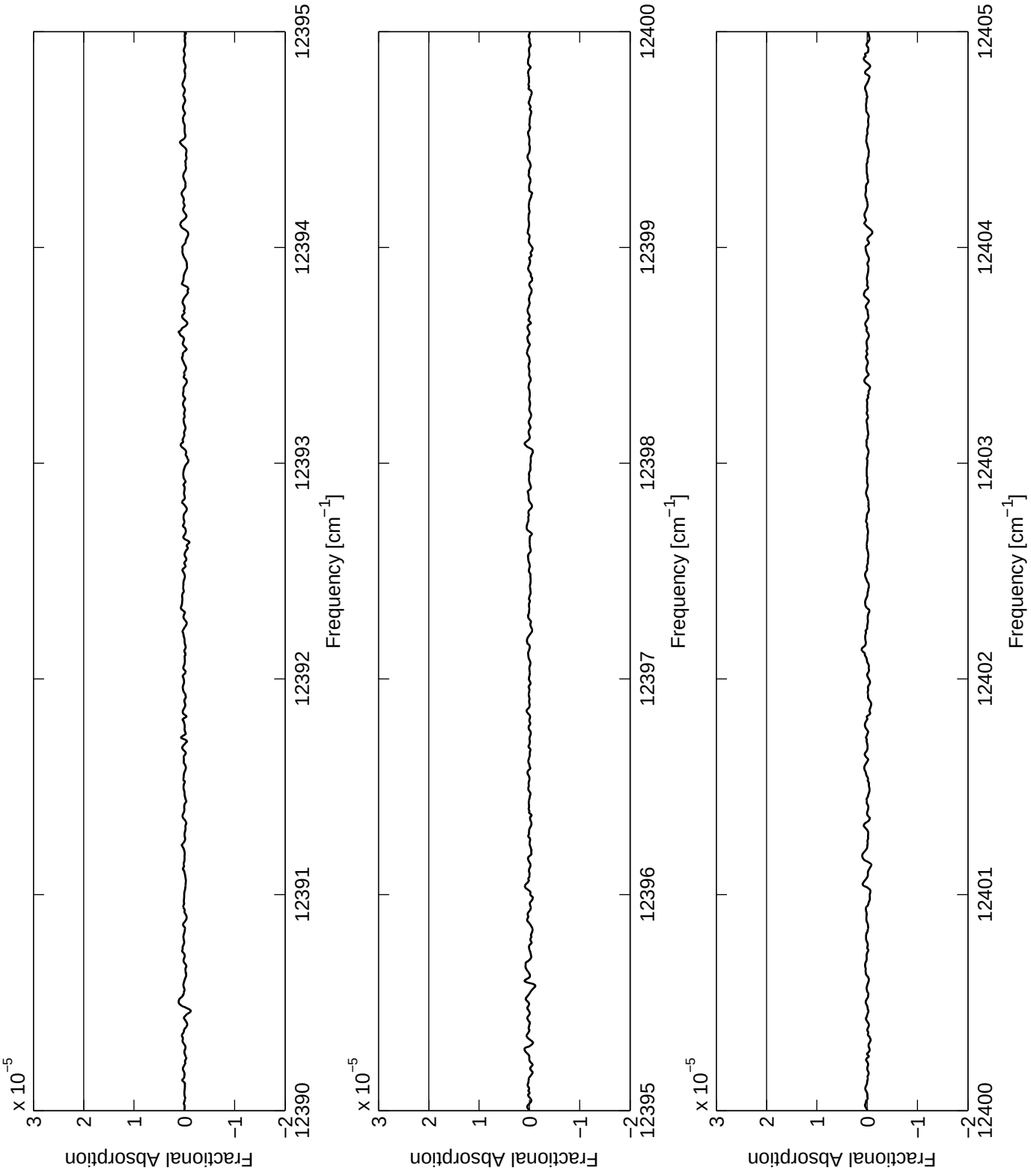
x 10^−5
3
2
1
0
−1
−2
Fractional Absorption
12390
12391
12392
12393
12394
12395
Frequency [cm^−1]
x 10^−5
3
2
1
0
−1
−2
Fractional Absorption
12395
12396
12397
12398
12399
12400
Frequency [cm^−1]
x 10^−5
3
2
1
0
−1
−2
Fractional Absorption
12400
12401
12402
12403
12404
12405
Frequency [cm^−1]

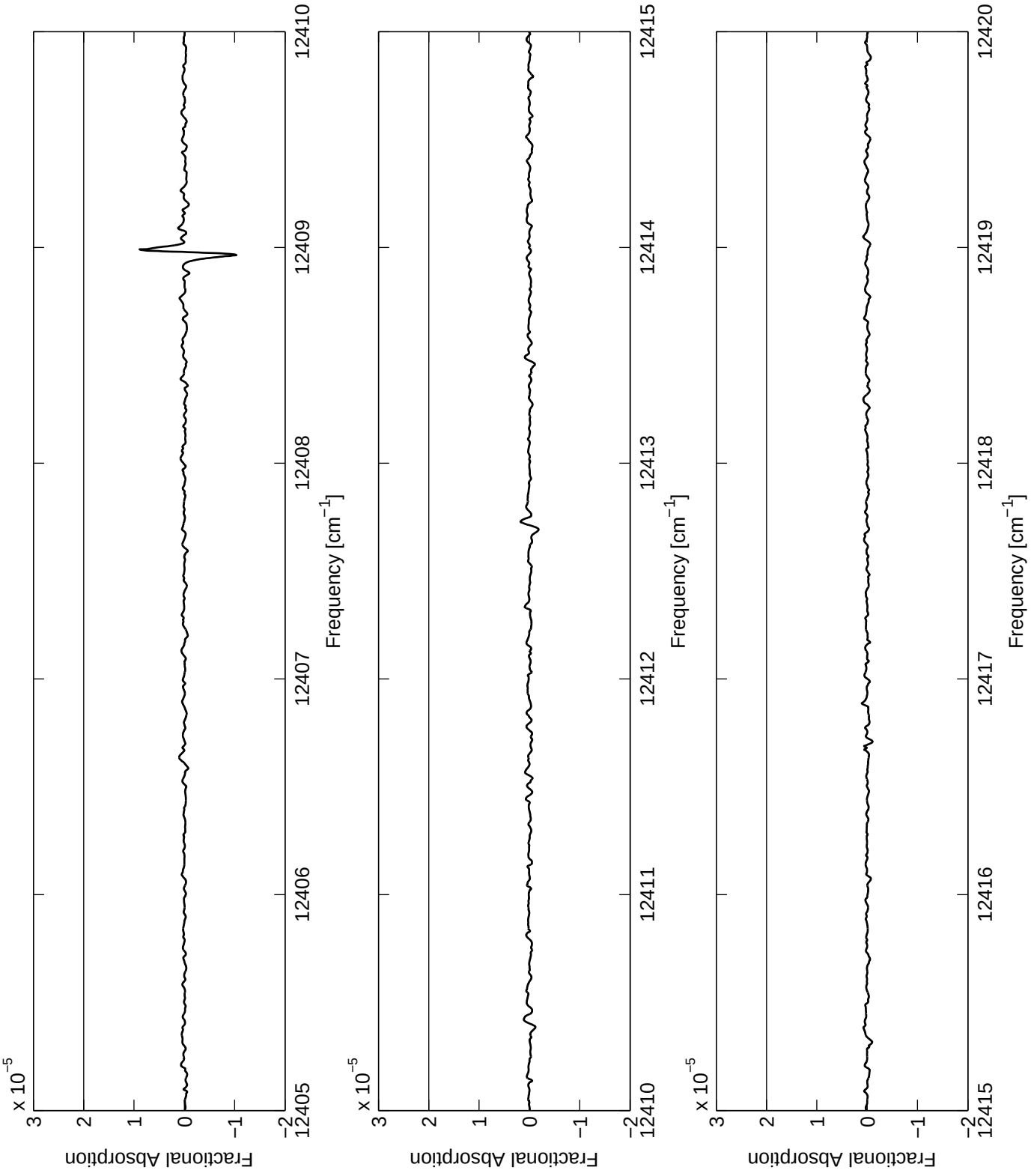
x 10^−5
3
2
1
0
−1
−2
Fractional Absorption
12405
12406
12407
12408
12409
12410
Frequency [cm^−1]
x 10^−5
3
2
1
0
−1
−2
Fractional Absorption
12410
12411
12412
12413
12414
12415
Frequency [cm^−1]
x 10^−5
3
2
1
0
−1
−2
Fractional Absorption
12415
12416
12417
12418
12419
12420
Frequency [cm^−1]

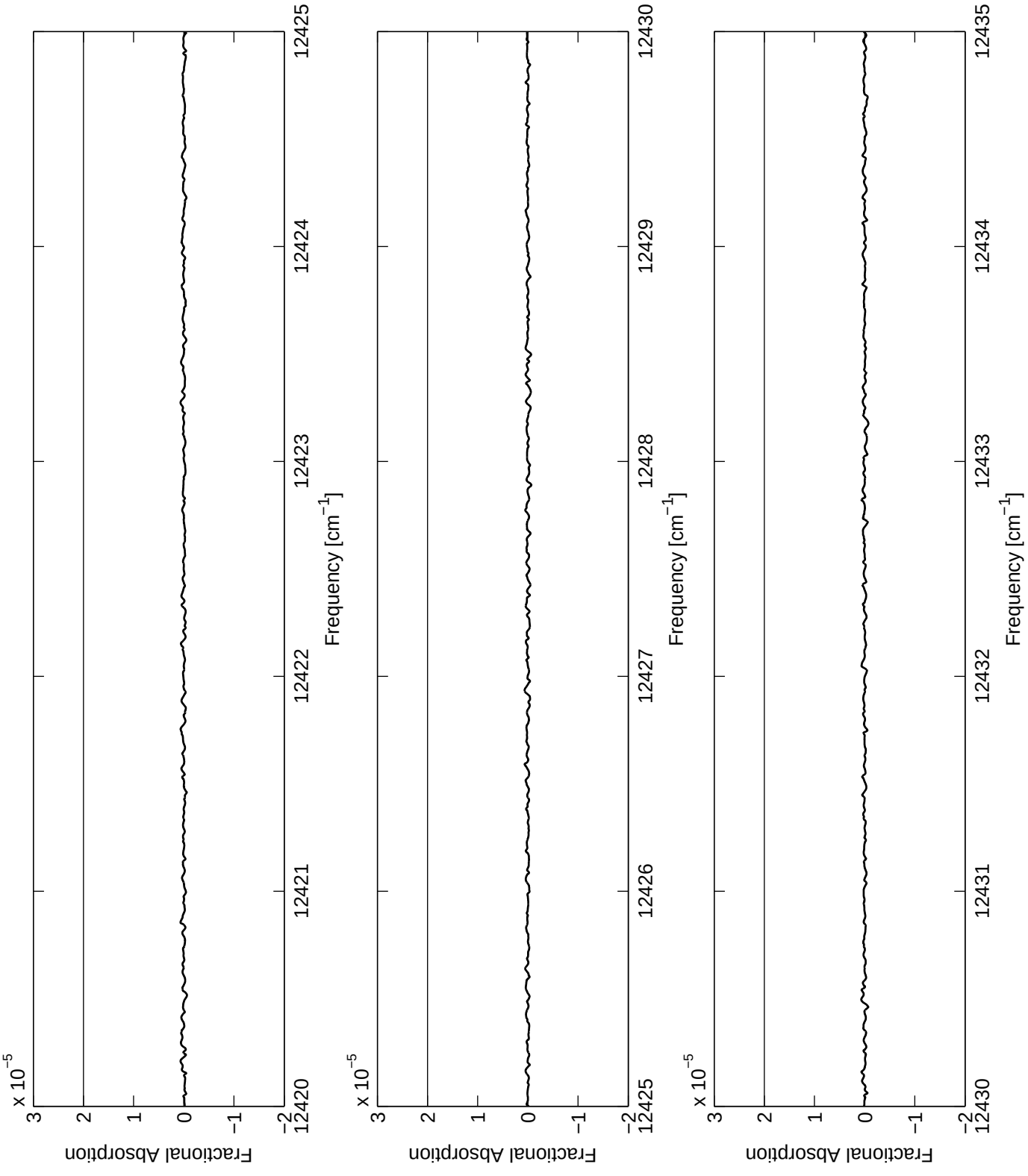
x 10^−5
3
2
1
0
−1
−2
Fractional Absorption
12420
12421
12422
12423
12424
12425
Frequency [cm^−1]
x 10^−5
3
2
1
0
−1
−2
Fractional Absorption
12425
12426
12427
12428
12429
12430
Frequency [cm^−1]
x 10^−5
3
2
1
0
−1
−2
Fractional Absorption
12430
12431
12432
12433
12434
12435
Frequency [cm^−1]

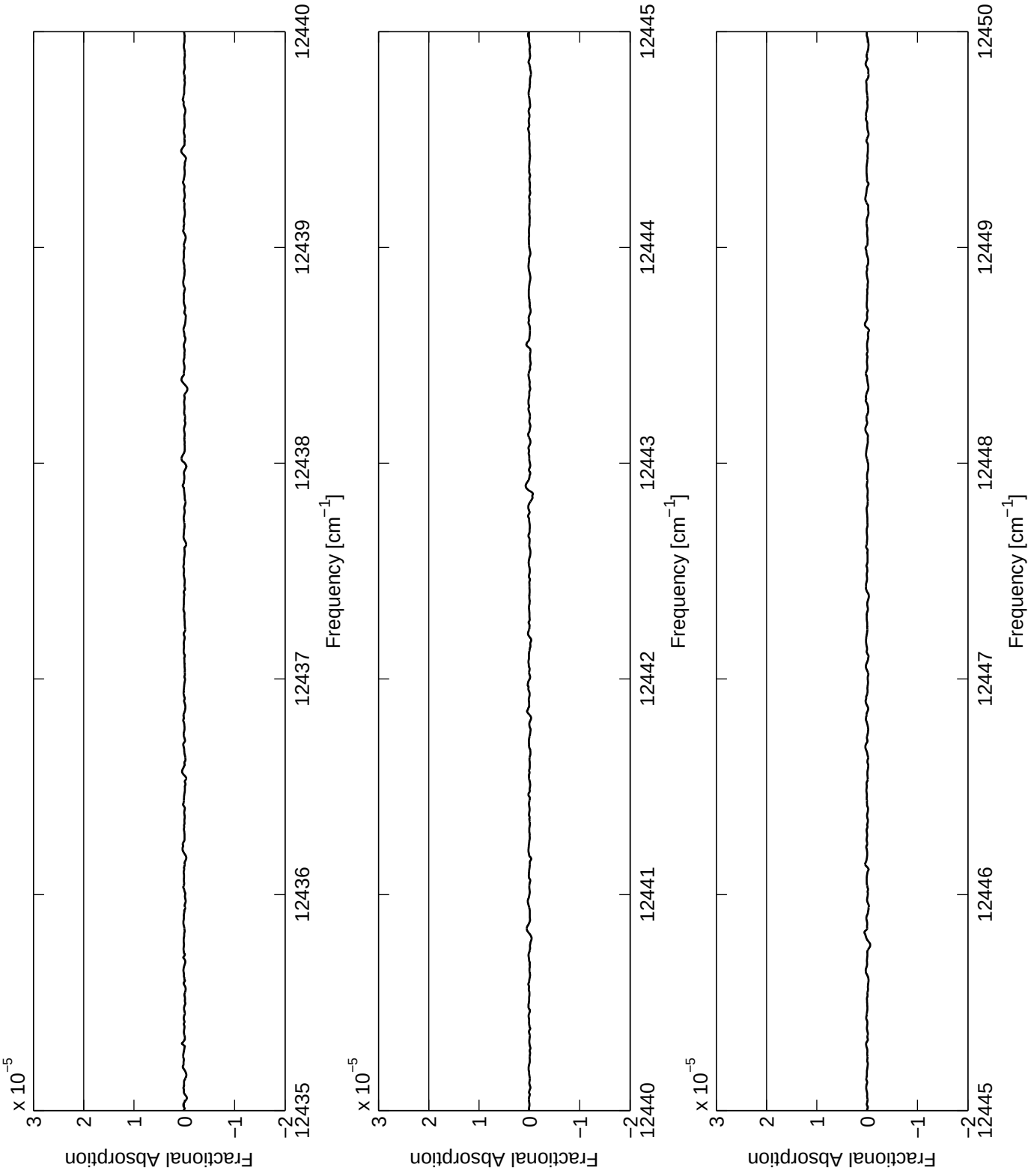
x 10^−5
3
2
1
0
−1
−2
Fractional Absorption
12435
12436
12437
12438
12439
12440
Frequency [cm^−1]
x 10^−5
3
2
1
0
−1
−2
Fractional Absorption
12440
12441
12442
12443
12444
12445
Frequency [cm^−1]
x 10^−5
3
2
1
0
−1
−2
Fractional Absorption
12445
12446
12447
12448
12449
12450
Frequency [cm^−1]

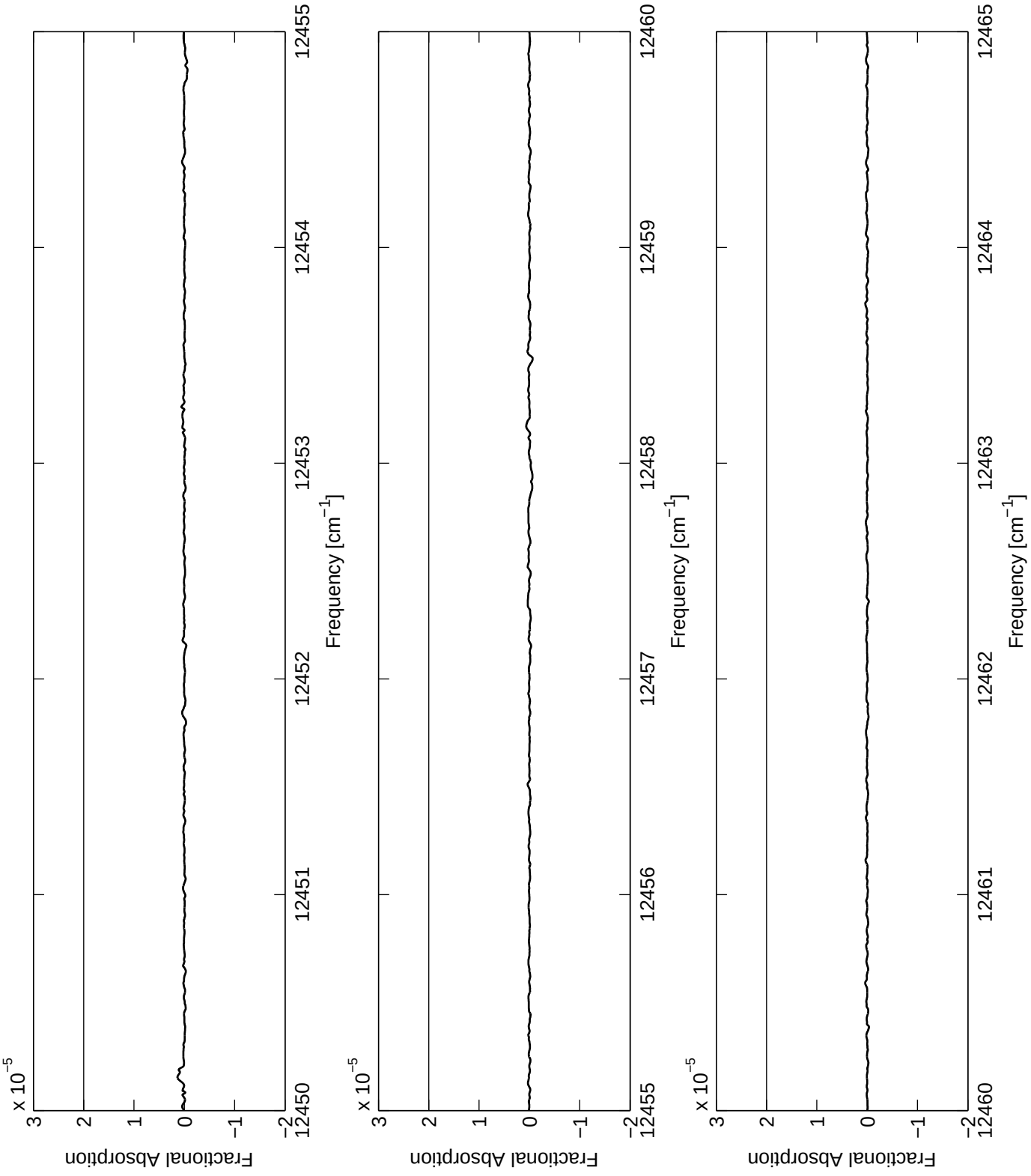
x 10^−5
3
2
1
0
−1
−2
Fractional Absorption
12450
12451
12452
12453
12454
12455
Frequency [cm^−1]
x 10^−5
3
2
1
0
−1
−2
Fractional Absorption
12455
12456
12457
12458
12459
12460
Frequency [cm^−1]
x 10^−5
3
2
1
0
−1
−2
Fractional Absorption
12460
12461
12462
12463
12464
12465
Frequency [cm^−1]

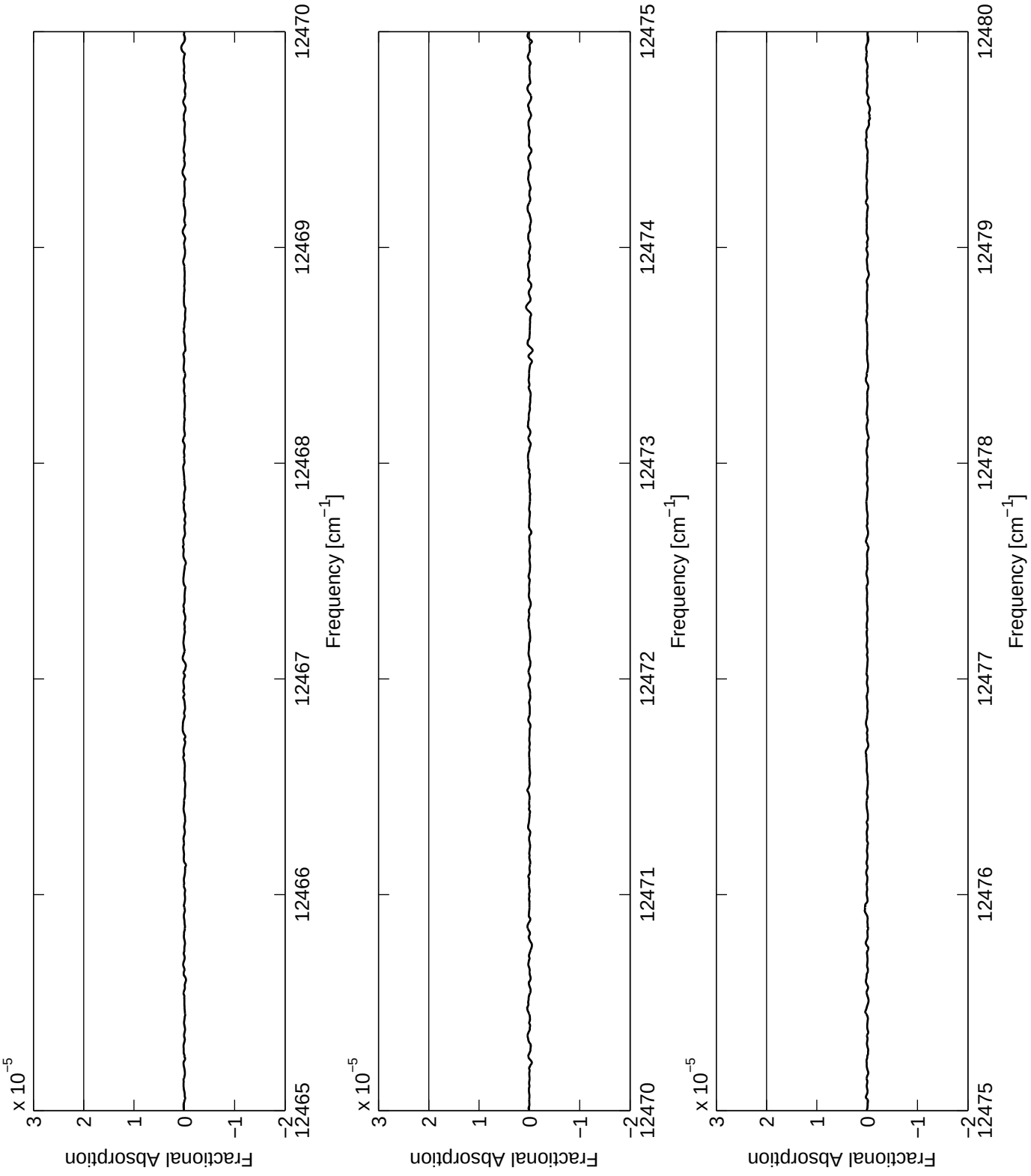
x 10^−5
3
2
1
0
−1
−2
Fractional Absorption
12465
12466
12467
12468
12469
12470
Frequency [cm^−1]
x 10^−5
3
2
1
0
−1
−2
Fractional Absorption
12470
12471
12472
12473
12474
12475
Frequency [cm^−1]
x 10^−5
3
2
1
0
−1
−2
Fractional Absorption
12475
12476
12477
12478
12479
12480
Frequency [cm^−1]

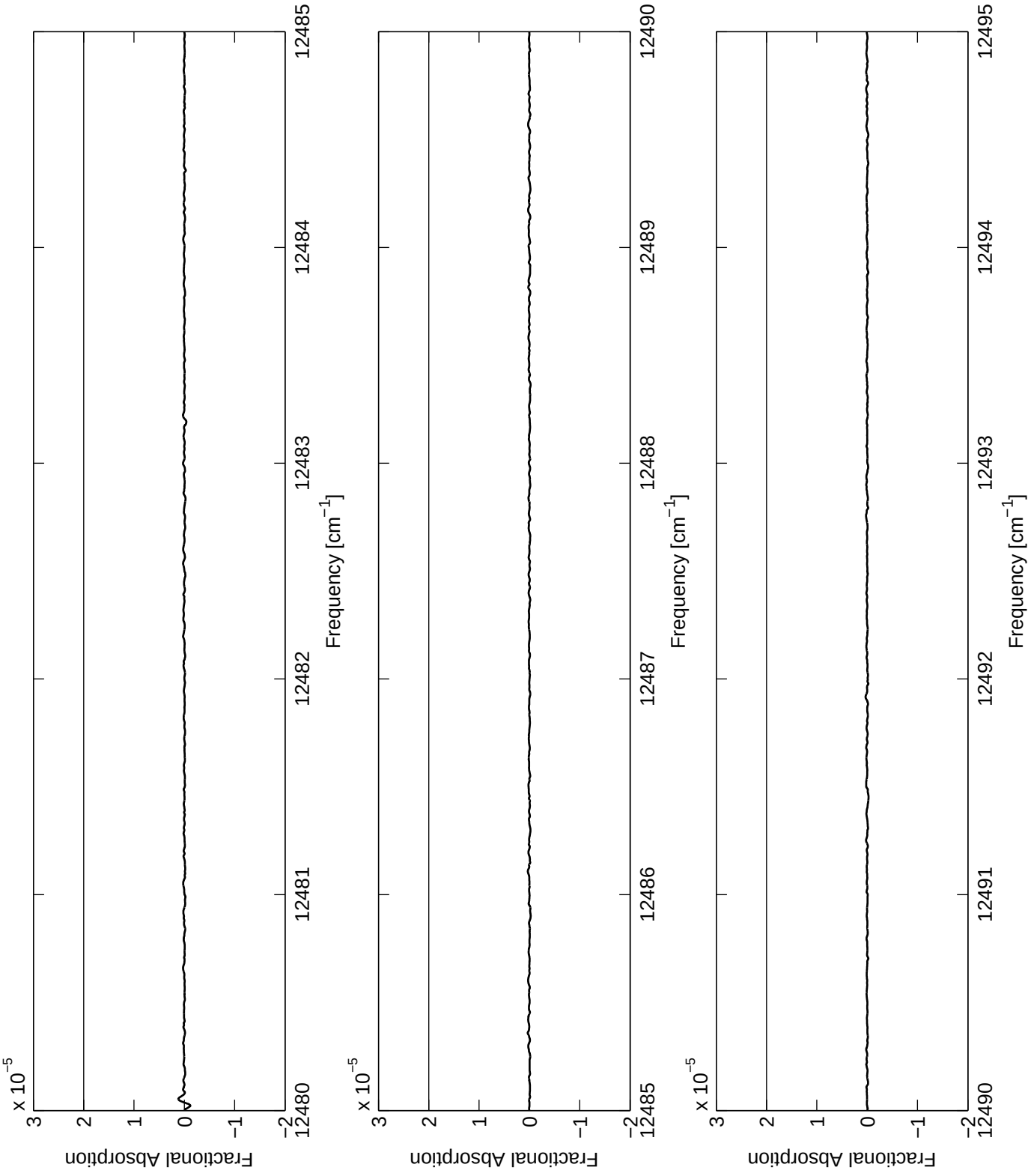
x 10^−5
3
2
1
0
−1
−2
Fractional Absorption
12480
12481
12482
12483
12484
12485
Frequency [cm^−1]
x 10^−5
3
2
1
0
−1
−2
Fractional Absorption
12485
12486
12487
12488
12489
12490
Frequency [cm^−1]
x 10^−5
3
2
1
0
−1
−2
Fractional Absorption
12490
12491
12492
12493
12494
12495
Frequency [cm^−1]

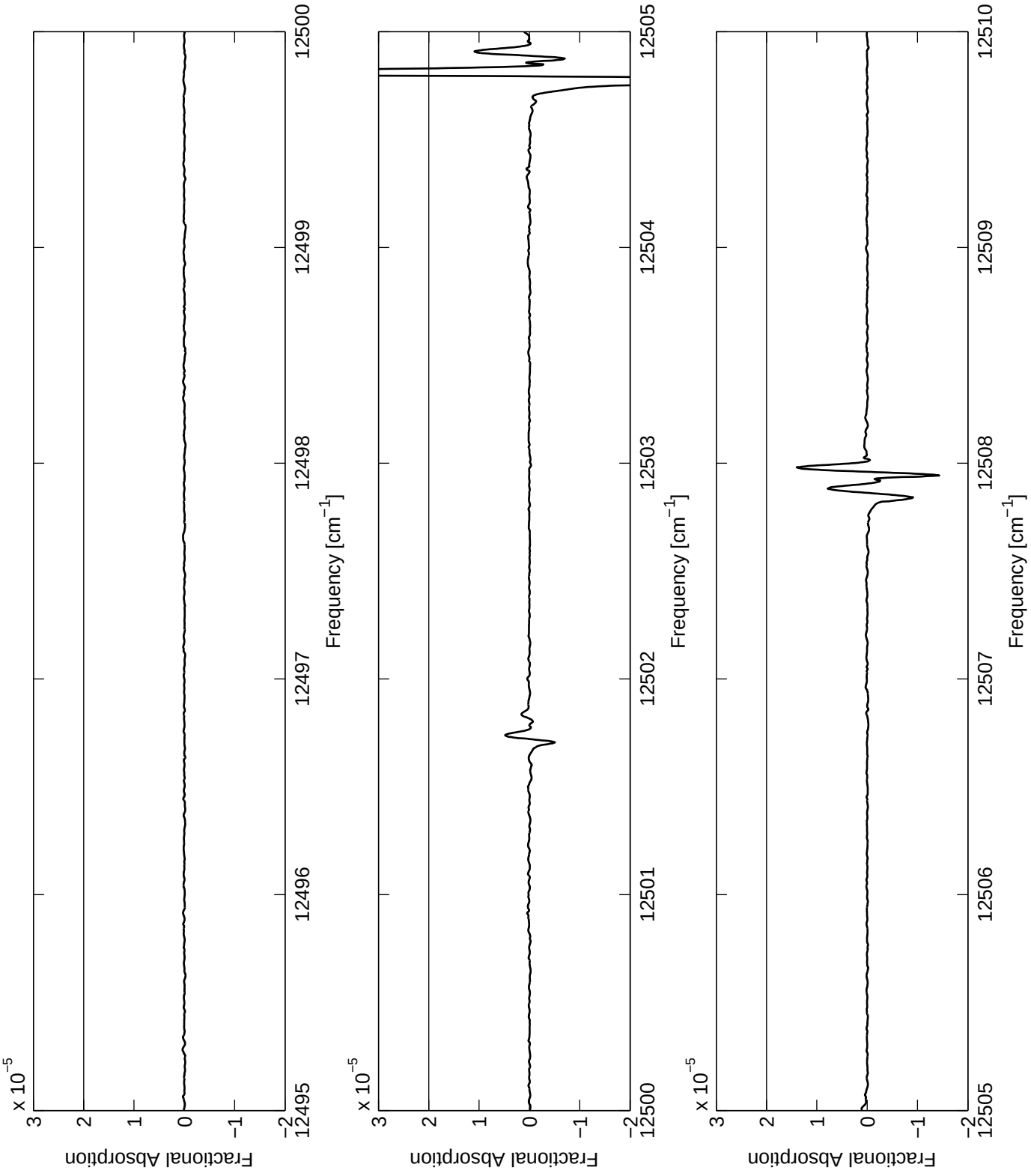
x 10^−5
3
2
1
0
−1
−2
Fractional Absorption
12495
12496
12497
12498
12499
12500
Frequency [cm^−1]
12500
12501
12502
12503
12504
12505
12505
12506
12507
12508
12509
12510

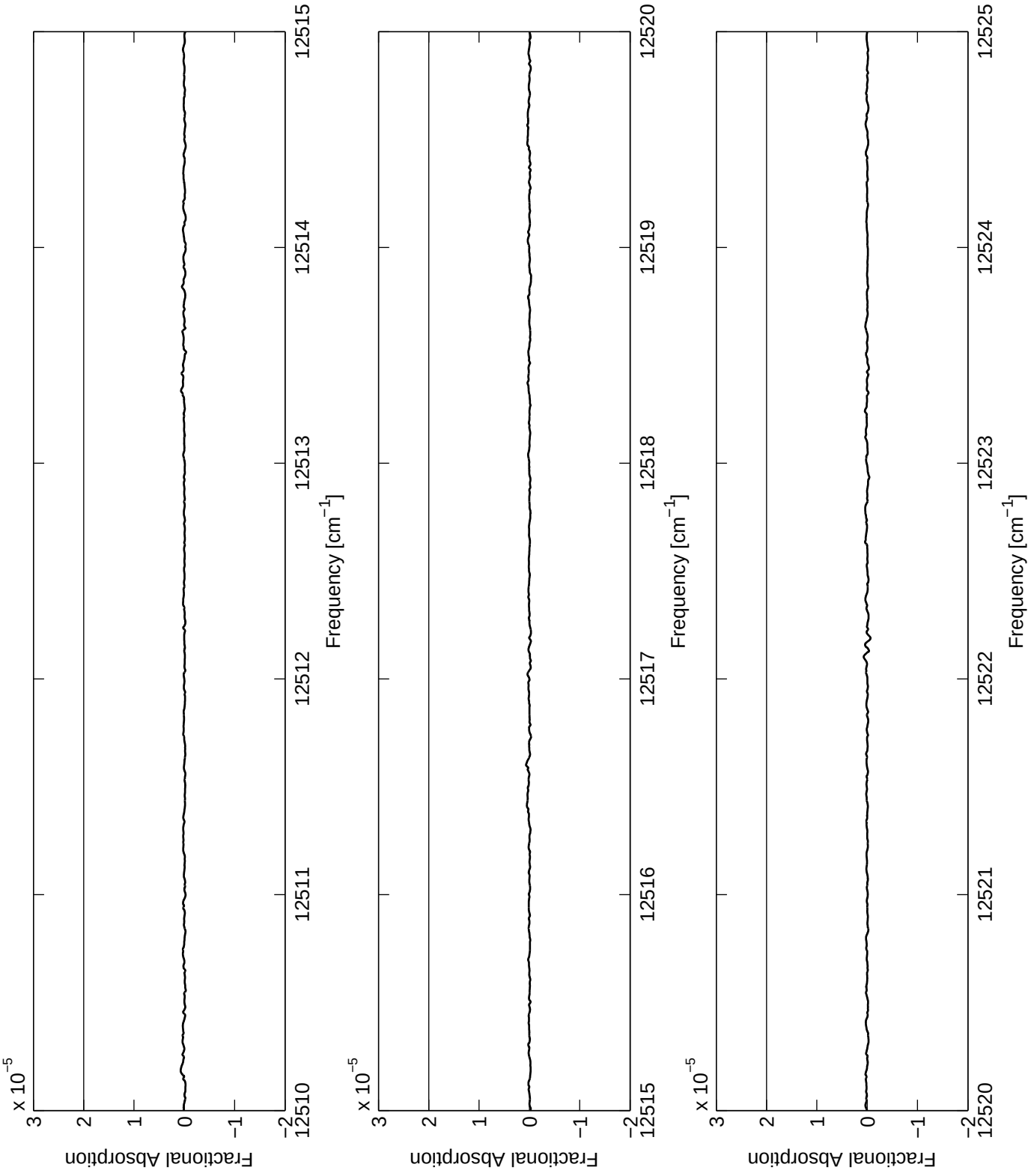
x 10^−5
3
2
1
0
−1
−2
Fractional Absorption
12510
12511
12512
12513
12514
12515
Frequency [cm^−1]
x 10^−5
3
2
1
0
−1
−2
Fractional Absorption
12515
12516
12517
12518
12519
12520
Frequency [cm^−1]
x 10^−5
3
2
1
0
−1
−2
Fractional Absorption
12520
12521
12522
12523
12524
12525
Frequency [cm^−1]

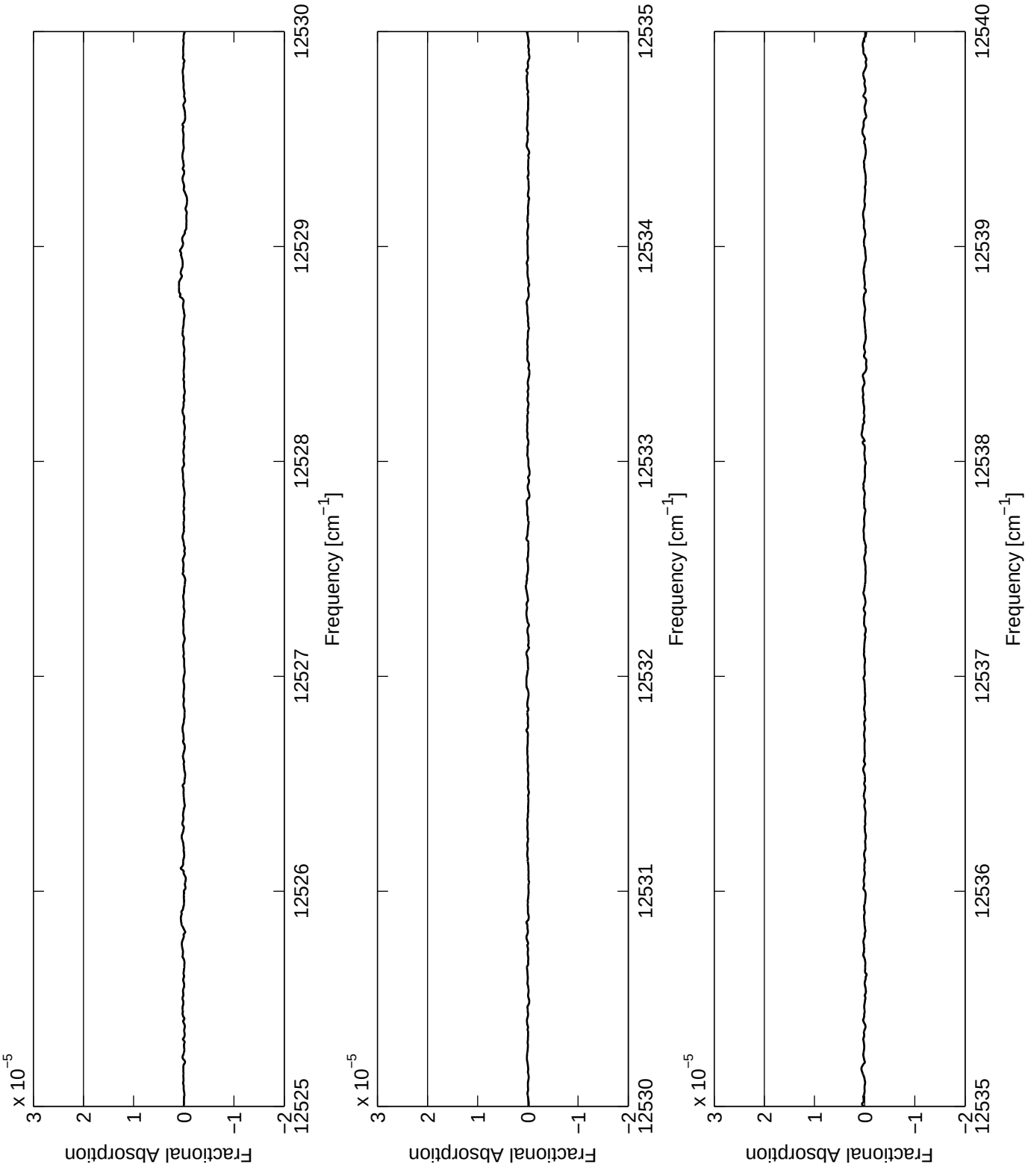
x 10^−5
3
2
1
0
−1
−2
Fractional Absorption
12525
12526
12527
12528
12529
12530
Frequency [cm^−1]
x 10^−5
3
2
1
0
−1
−2
Fractional Absorption
12530
12531
12532
12533
12534
12535
Frequency [cm^−1]
x 10^−5
3
2
1
0
−1
−2
Fractional Absorption
12535
12536
12537
12538
12539
12540
Frequency [cm^−1]

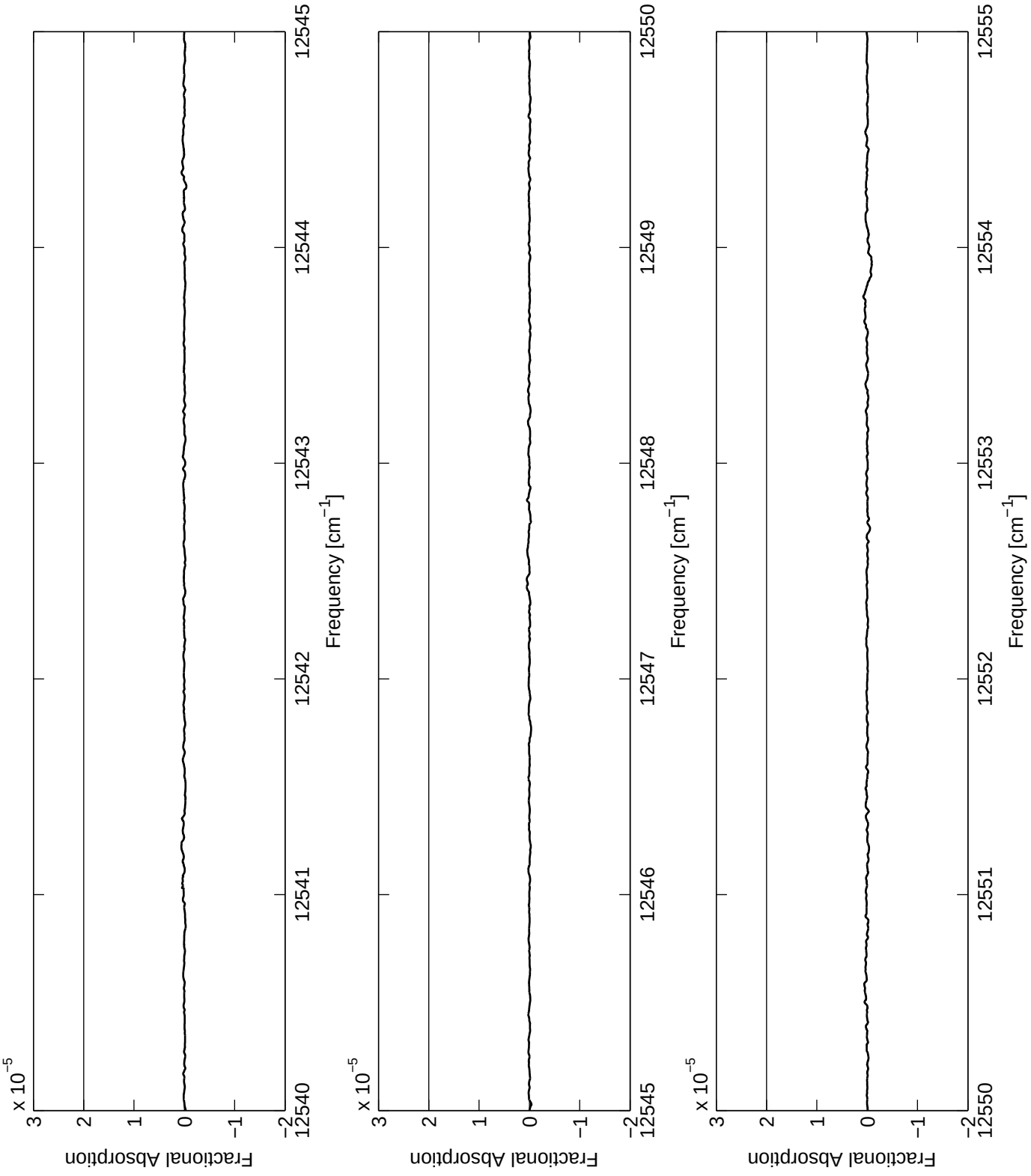
x 10^−5
3
2
1
0
−1
−2
Fractional Absorption
12540
12541
12542
12543
12544
12545
Frequency [cm^−1]
x 10^−5
3
2
1
0
−1
−2
Fractional Absorption
12545
12546
12547
12548
12549
12550
Frequency [cm^−1]
x 10^−5
3
2
1
0
−1
−2
Fractional Absorption
12550
12551
12552
12553
12554
12555
Frequency [cm^−1]

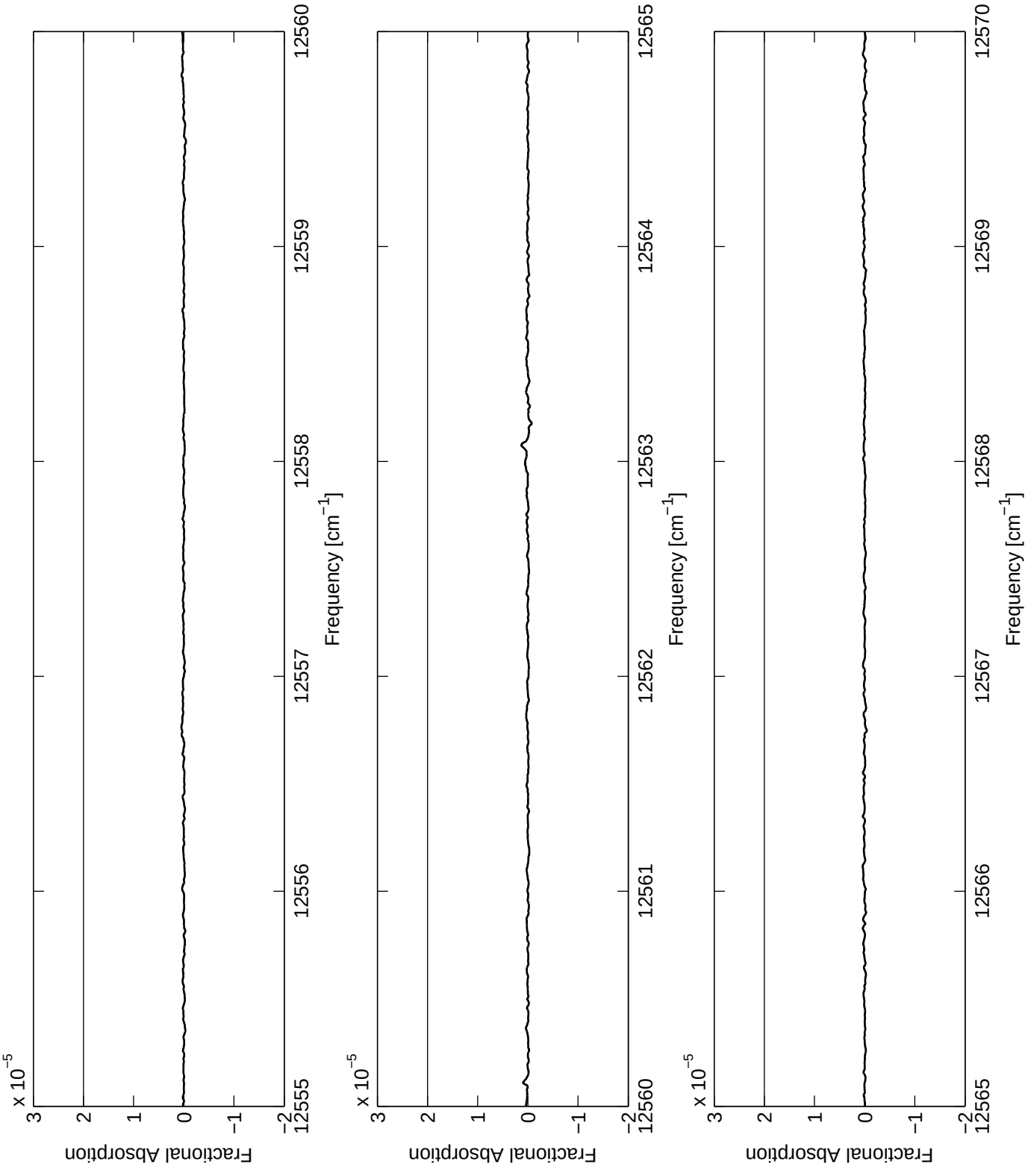
x 10^−5
3
2
1
0
−1
−2
Fractional Absorption
12555
12556
12557
12558
12559
12560
Frequency [cm^−1]
x 10^−5
3
2
1
0
−1
−2
Fractional Absorption
12560
12561
12562
12563
12564
12565
Frequency [cm^−1]
x 10^−5
3
2
1
0
−1
−2
Fractional Absorption
12565
12566
12567
12568
12569
12570
Frequency [cm^−1]

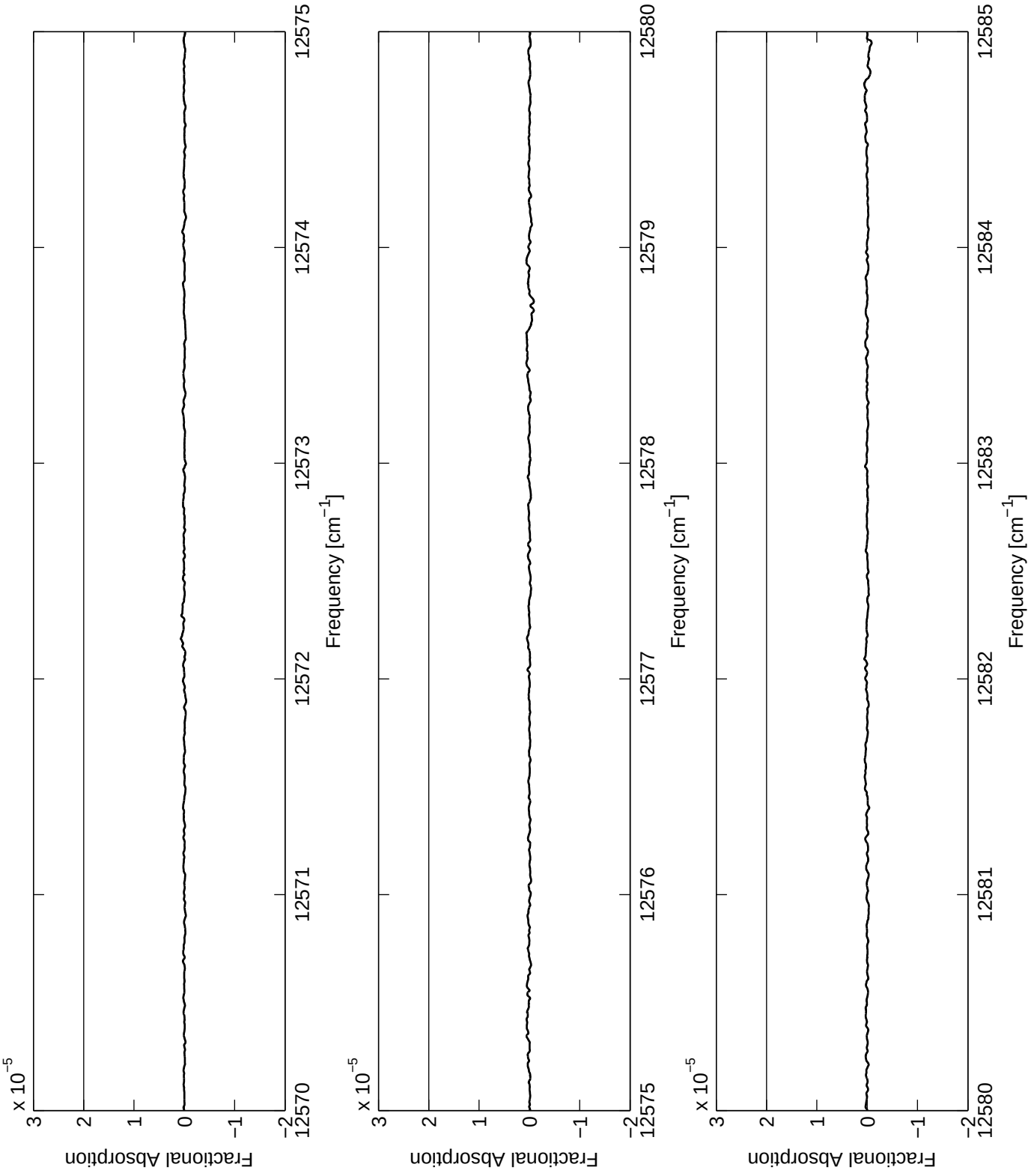
x 10^−5
3
2
1
0
−1
−2
Fractional Absorption
12570
12571
12572
12573
12574
12575
Frequency [cm^−1]
x 10^−5
3
2
1
0
−1
−2
Fractional Absorption
12575
12576
12577
12578
12579
12580
Frequency [cm^−1]
x 10^−5
3
2
1
0
−1
−2
Fractional Absorption
12580
12581
12582
12583
12584
12585
Frequency [cm^−1]

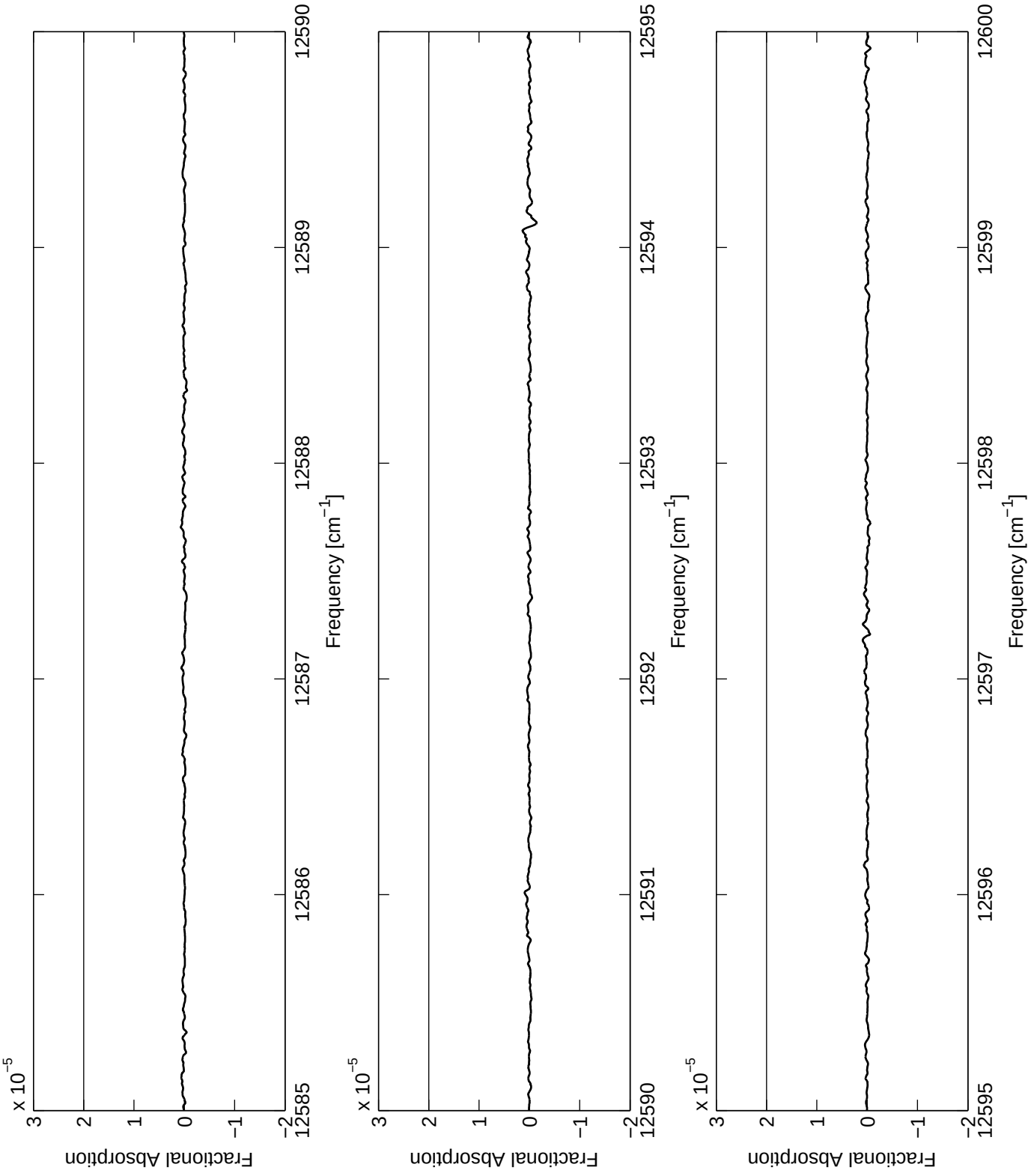
x 10^−5
3
2
1
0
−1
−2
Fractional Absorption
12585
12586
12587
12588
12589
12590
Frequency [cm^−1]
x 10^−5
3
2
1
0
−1
−2
Fractional Absorption
12590
12591
12592
12593
12594
12595
Frequency [cm^−1]
x 10^−5
3
2
1
0
−1
−2
Fractional Absorption
12595
12596
12597
12598
12599
12600
Frequency [cm^−1]

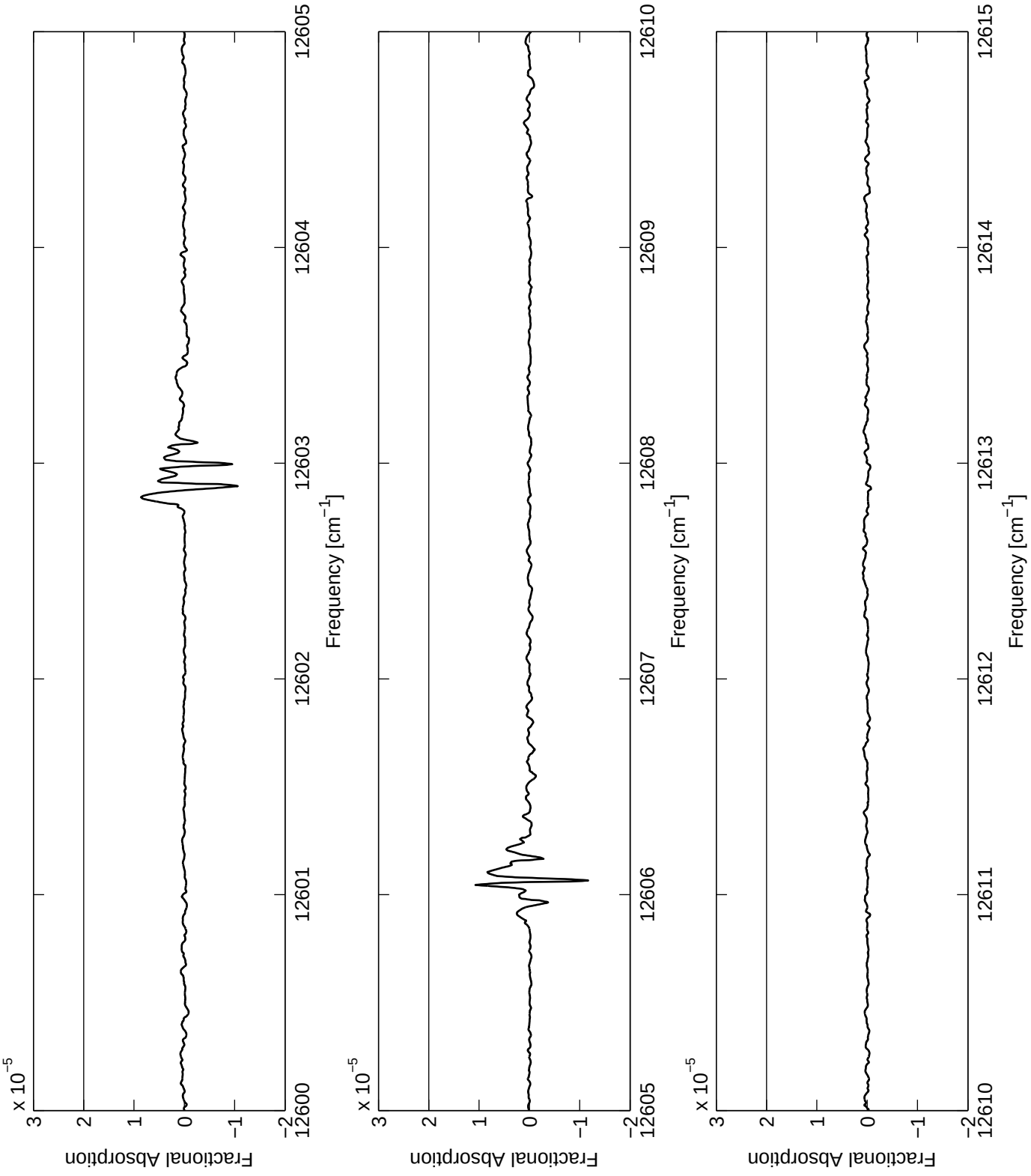
x 10^−5
3
2
1
0
−1
−2
Fractional Absorption
12600
12601
12602
12603
12604
12605
Frequency [cm^−1]
x 10^−5
3
2
1
0
−1
−2
Fractional Absorption
12605
12606
12607
12608
12609
12610
Frequency [cm^−1]
x 10^−5
3
2
1
0
−1
−2
Fractional Absorption
12610
12611
12612
12613
12614
12615
Frequency [cm^−1]

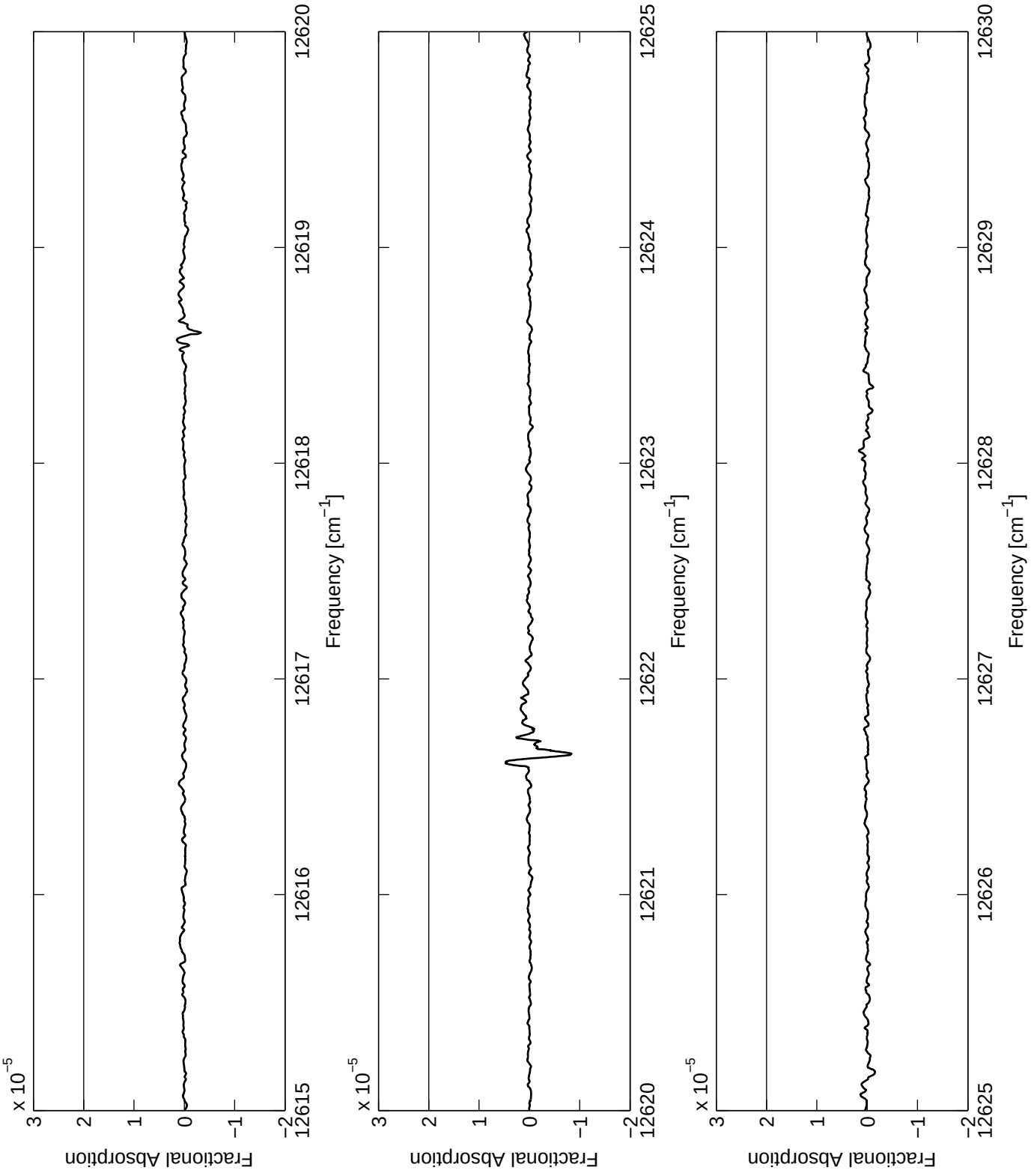
x 10^−5
3
2
1
0
−1
−2
Fractional Absorption
12615
12616
12617
12618
12619
12620
Frequency [cm^−1]
x 10^−5
3
2
1
0
−1
−2
Fractional Absorption
12620
12621
12622
12623
12624
12625
Frequency [cm^−1]
x 10^−5
3
2
1
0
−1
−2
Fractional Absorption
12625
12626
12627
12628
12629
12630
Frequency [cm^−1]

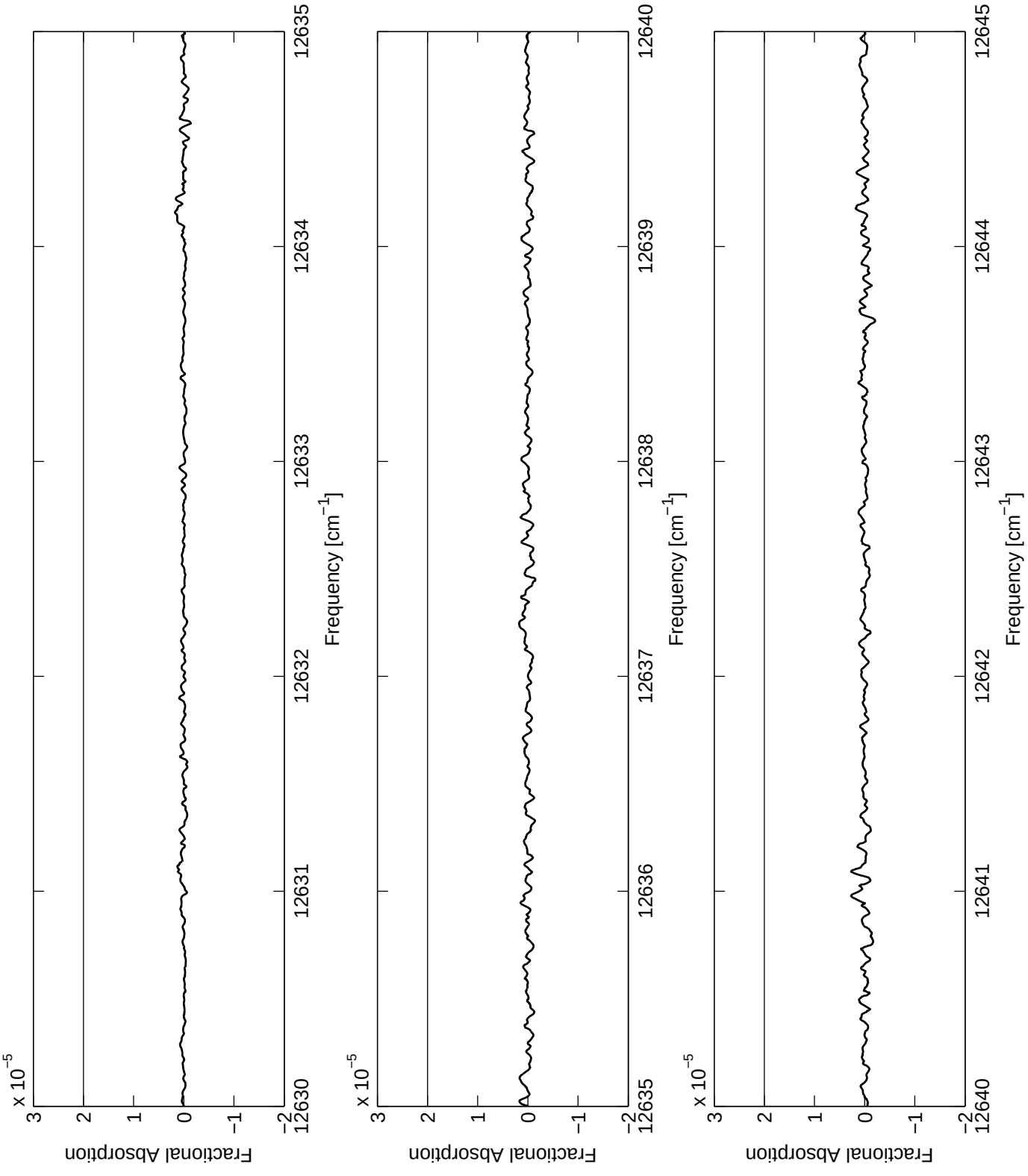
x 10^−5
3
2
1
0
−1
−2
Fractional Absorption
12630
12631
12632
12633
12634
12635
Frequency [cm^−1]
x 10^−5
3
2
1
0
−1
−2
Fractional Absorption
12635
12636
12637
12638
12639
12640
Frequency [cm^−1]
x 10^−5
3
2
1
0
−1
−2
Fractional Absorption
12640
12641
12642
12643
12644
12645
Frequency [cm^−1]

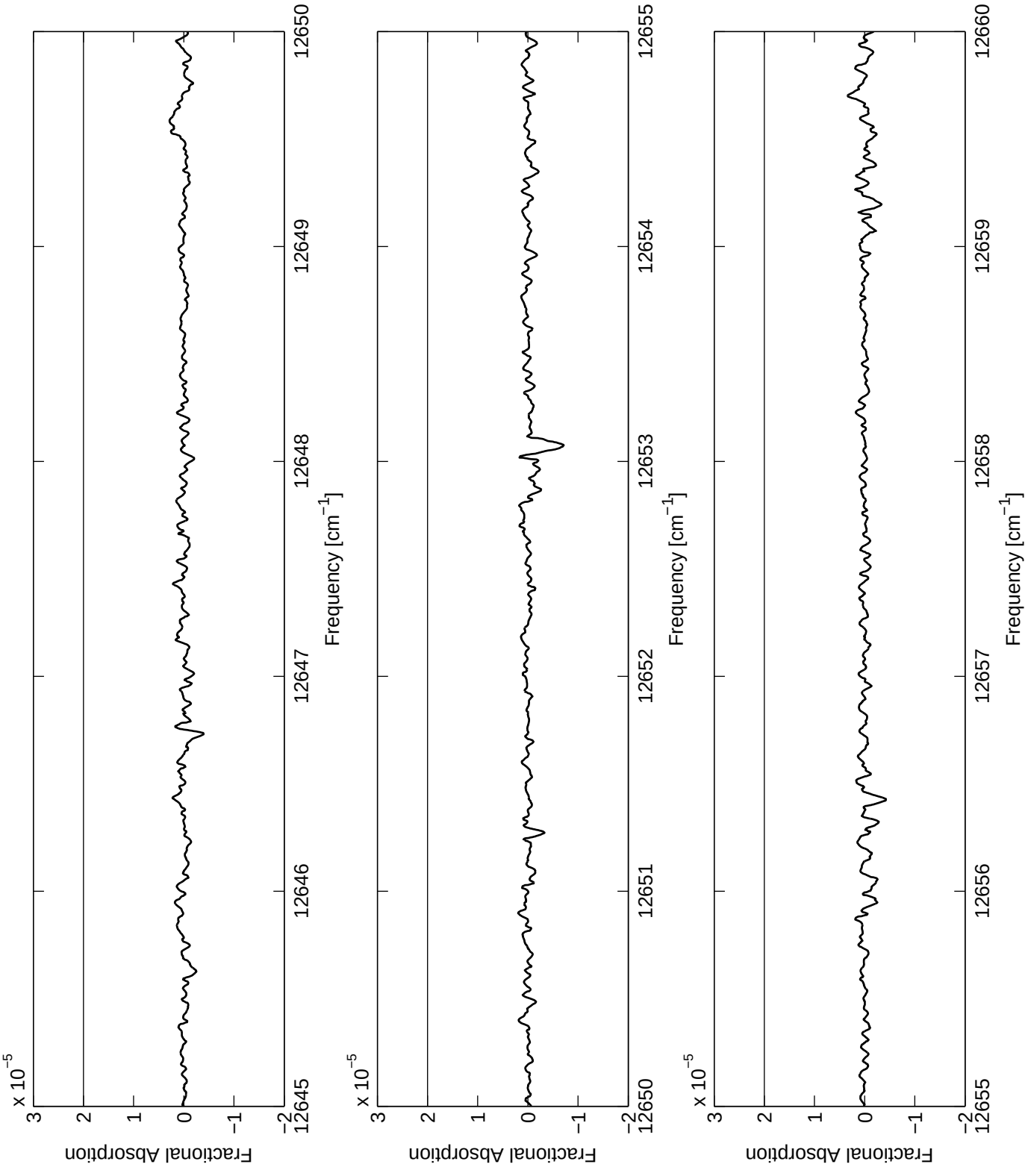
x 10^−5
3
2
1
0
−1
−2
12645
12646
12647
12648
12649
12650
Fractional Absorption
Frequency [cm^−1]
x 10^−5
3
2
1
0
−1
−2
12650
12651
12652
12653
12654
12655
Fractional Absorption
Frequency [cm^−1]
x 10^−5
3
2
1
0
−1
−2
12655
12656
12657
12658
12659
12660
Fractional Absorption
Frequency [cm^−1]

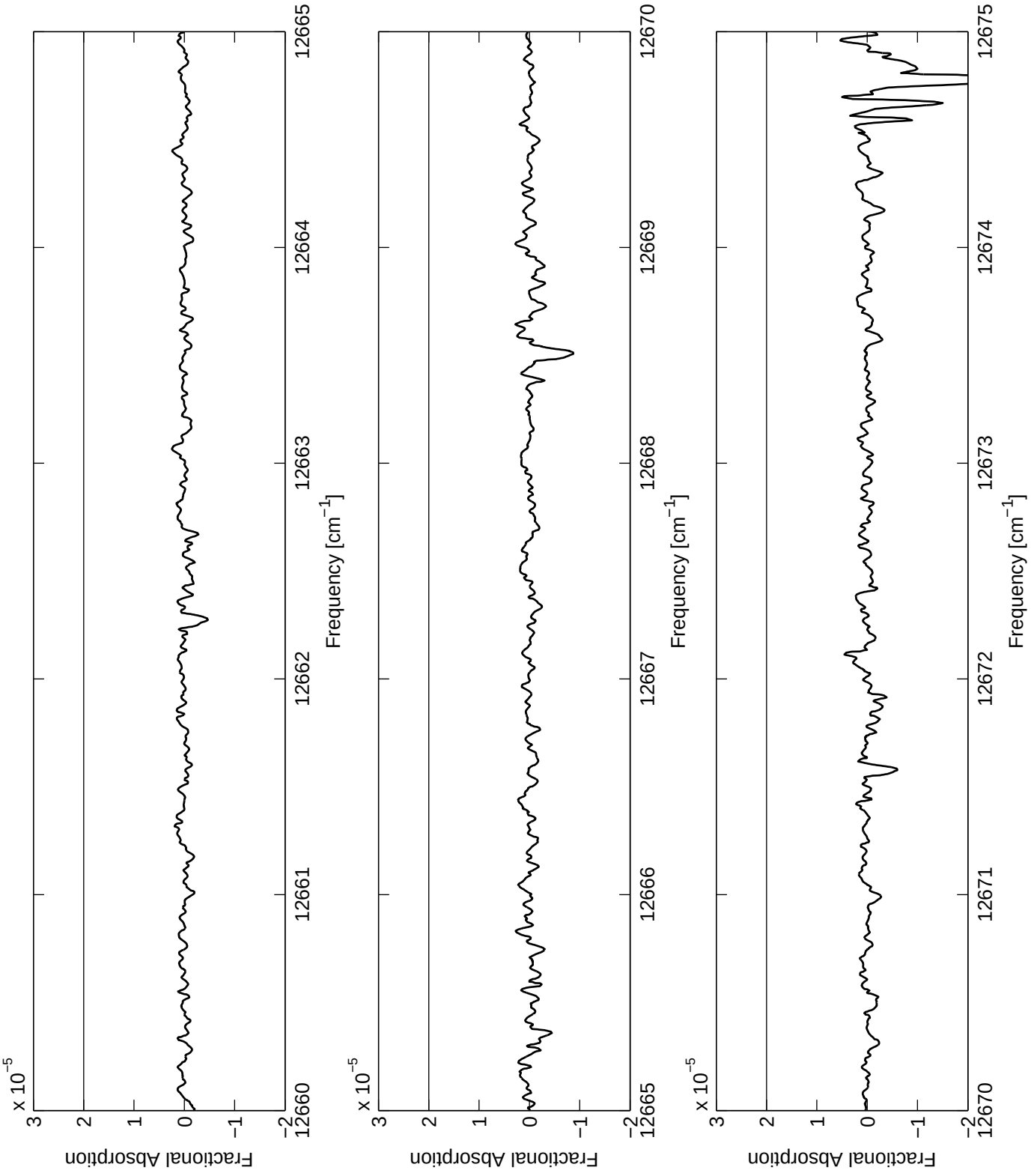
x 10^−5
3
2
1
0
−1
−2
Fractional Absorption
12660
12661
12662
12663
12664
12665
Frequency [cm^−1]
x 10^−5
3
2
1
0
−1
−2
Fractional Absorption
12665
12666
12667
12668
12669
12670
Frequency [cm^−1]
x 10^−5
3
2
1
0
−1
−2
Fractional Absorption
12670
12671
12672
12673
12674
12675
Frequency [cm^−1]

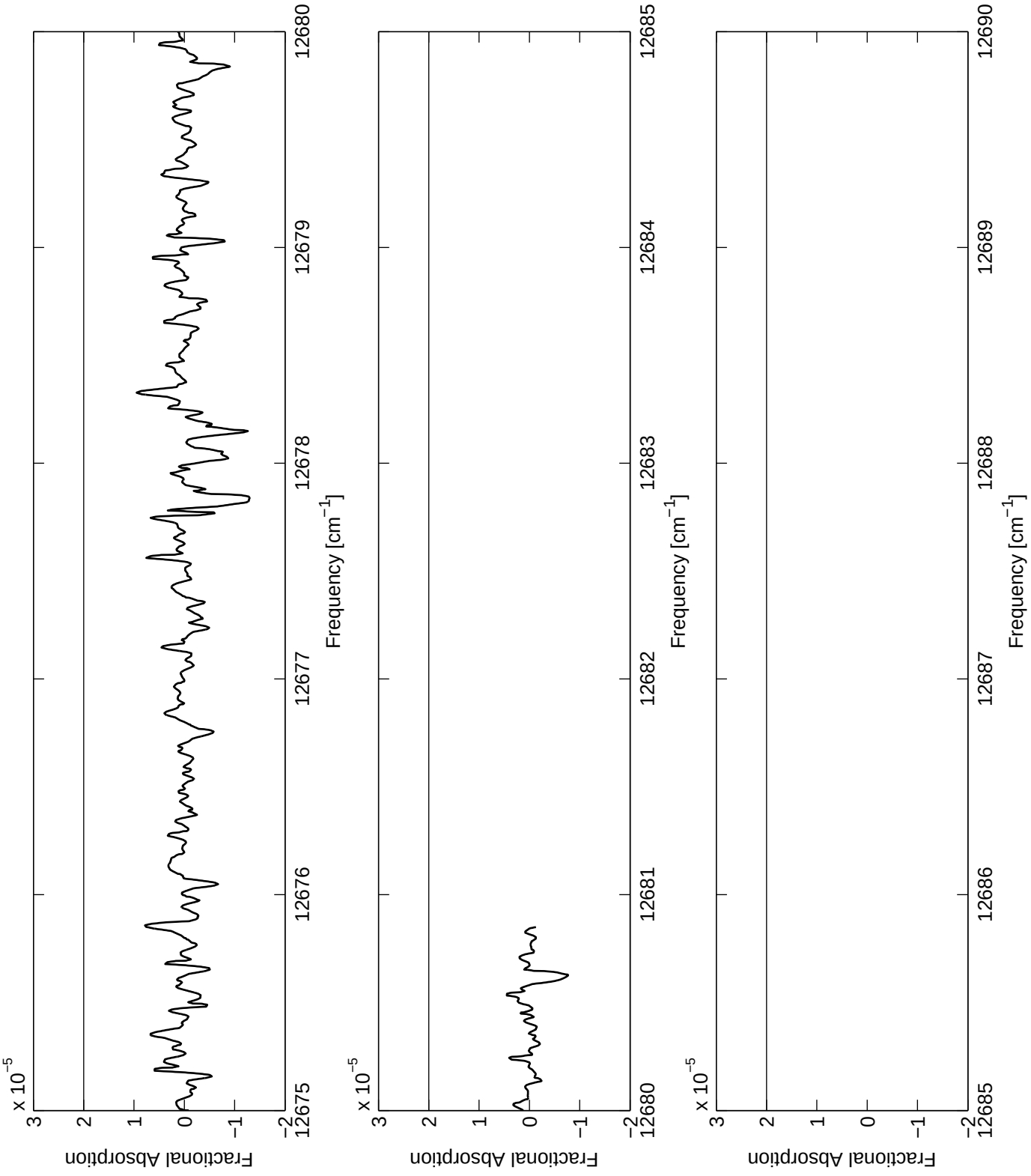
x 10^−5
3
2
1
0
−1
−2
Fractional Absorption
12675
12676
12677
12678
12679
12680
Frequency [cm^−1]
x 10^−5
3
2
1
0
−1
−2
Fractional Absorption
12680
12681
12682
12683
12684
12685
Frequency [cm^−1]
x 10^−5
3
2
1
0
−1
−2
Fractional Absorption
12685
12686
12687
12688
12689
12690
Frequency [cm^−1]

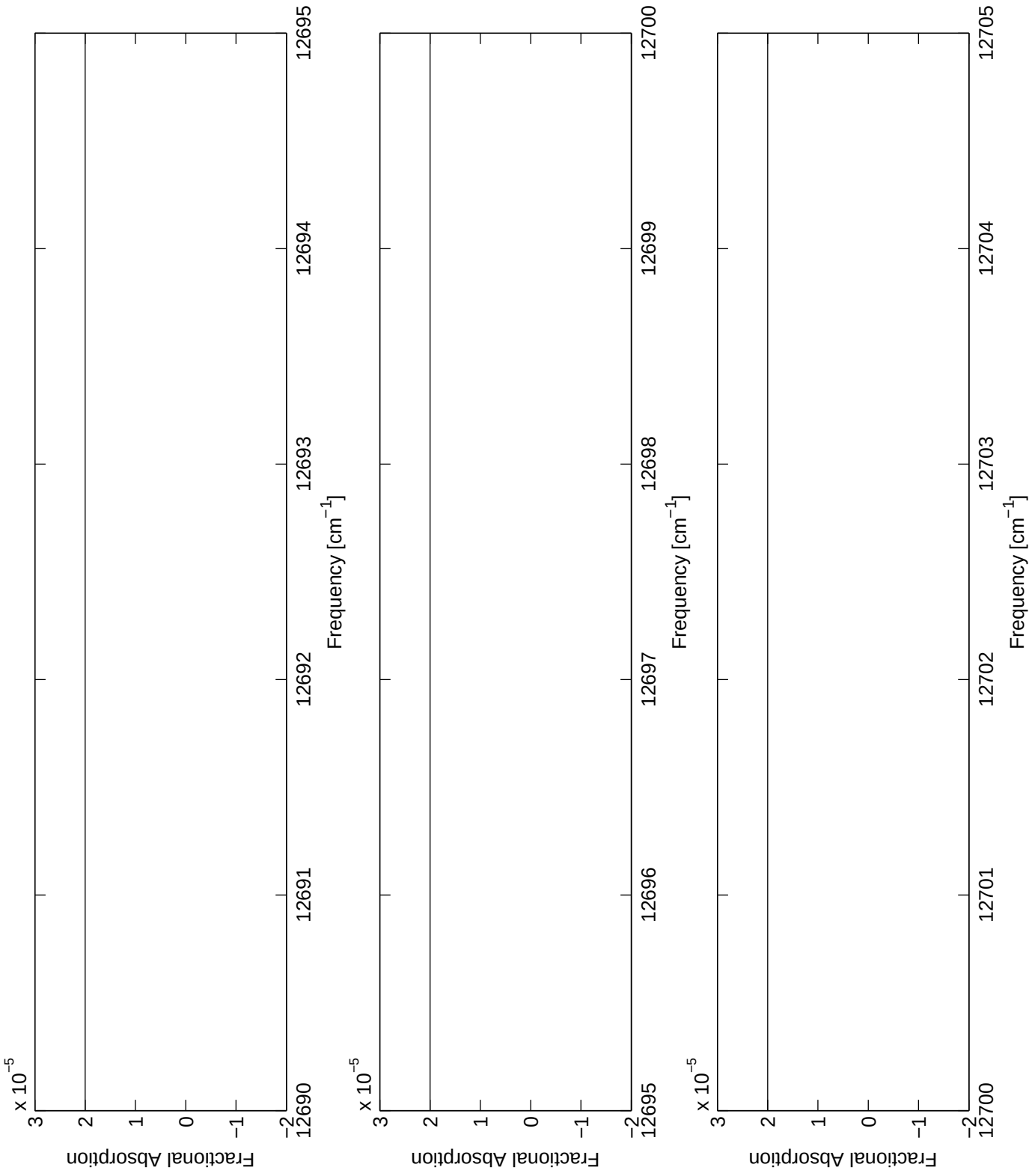
x 10^−5
3
2
1
0
−1
−2
Fractional Absorption
12690
12691
12692
12693
12694
12695
Frequency [cm^−1]
x 10^−5
3
2
1
0
−1
−2
Fractional Absorption
12695
12696
12697
12698
12699
12700
Frequency [cm^−1]
x 10^−5
3
2
1
0
−1
−2
Fractional Absorption
12700
12701
12702
12703
12704
12705
Frequency [cm^−1]